

Misaligned, tilted and distorted: The hard life of Audible Axions

Dissertation submitted for the award of the title
“Doctor of Natural Sciences”
to the faculty of Physics, Mathematics and Computer science of
Johannes Gutenberg-Universität in Mainz

Wolfram Ratzinger
born in Mainz

Mainz, July 26, 2022



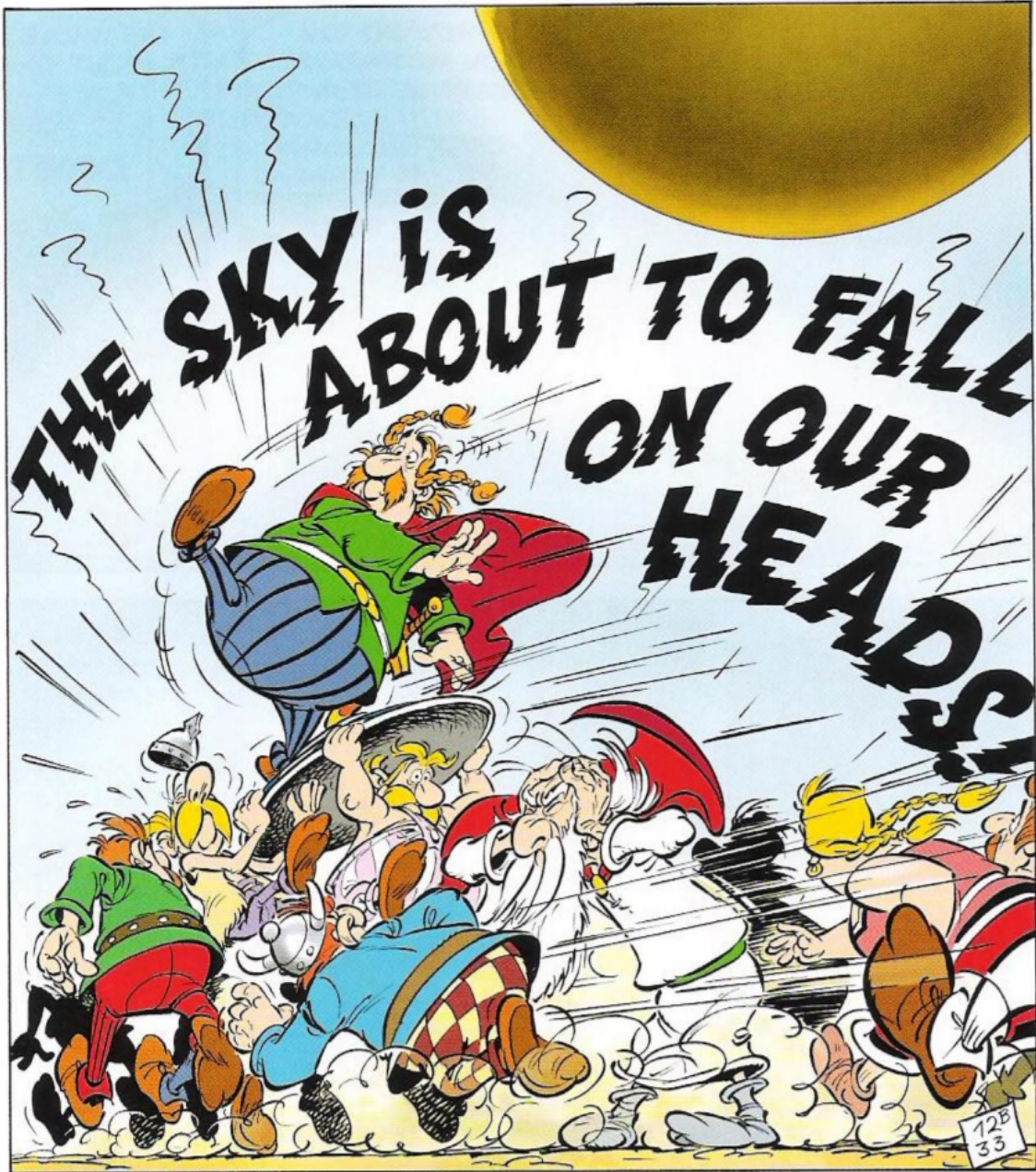
Abstract

The year is 2022DC. Observations in high energy physics, astrophysics and cosmology are entirely explained by the standard model (SM) of particle physics together with the theory of gravity and the Λ CDM model. Well not entirely... There is still a “small” number of unexplained phenomena and tensions on top of dissonances of theoretical nature within the respective theories. Particle accelerators acted as the driving force behind the development of the SM. However, they are seemingly reaching the limits of available technology. Therefore, the search for new messengers of high energy physics is as timely as ever.

Guided by some of these dissonances, namely the strong CP problem and the hierarchy problem, we first take a look at their respective dynamical solutions, the QCD axion and the relaxion. Of particular interest is the phenomenon of axion fragmentation, which is build into the relaxion mechanism but also arises in general axion scenarios. The dynamics of this process feature an instability that leads to the initially homogeneous axion field developing large inhomogenities that eventually come to dominate the axions energy, in particular the initial kinetic energy. Using a lattice simulation allows us to take the inhomogenities fully into account and we are able to show that this energy transfer is even more efficient than previously estimated. We furthermore explore the subsequent cosmology of the axion, in particular the possibility that multiple vacua are populated by the axion.

We then turn our attention to one possible new messenger, gravitational waves (GWs), and present in detail the dynamics of an axion scenario that leads to an observable signal. In this scenario the axion is coupled to a new $U(1)$ gauge boson, the so-called dark photon. The dark photon develops an instability, similar to the one discussed above, due to the coupling to the axion, which results in the exponential production of dark photon quanta. This process is associated with a large anisotropic stress, which sources the GWs. We again study the non-linear dynamics of this process with a lattice simulation to confirm and refine our previous results concerning the viability of this scenario as well as the amplitude of the signal. While the minimal model can indeed lead to a signal detectable by pulsar timing arrays (PTAs), extensions are needed in order to be detectable by planned interferometers. We study two such extensions in detail, one where the axion has a non-vanishing initial velocity and one where the axion is identified with the relaxion that by construction features a time dependent potential.

In the last part of the thesis we focus purely on the phenomenology of new physics with sizeable fluctuations in energy density. Apart from the examples discussed above, phenomena like networks of scaling seeds or first order phase transitions come to mind. We discuss the ability of these new physics scenarios to explain the recent hint of GWs from PTAs such as NANOGrav. The temperature of the SM plasma when these signals are induced is ≈ 1 GeV and below. Since couplings to the SM are highly constrained at such low energies, we primarily focus on purely gravitationally coupled sectors. While we find that currently limits stemming from CMB observations and BBN significantly constrain scenarios with a signal this strong, the prospect of being able to probe such sectors with the constantly culminating PTA data in the near future is exciting. Finally we study the ability of such a dark sector to cause distortions of the CMB spectrum by inducing acoustic waves in the baryon photon fluid. We find that future experiments could detect new physics over large regions of parameter space, some of them also accessible by PTAs, which might mark the dawn of multi-messenger cosmology.



Asterix and the falling sky
Albert Uderzo, 2005

List of publications

This thesis is based on the following publications and preprints. We highlight the authors contribution to each of them.

- E. Morgante, W. Ratzinger, R. Sato and B. Stefanek, *Axion fragmentation on the lattice*, *JHEP* **12** (2021) 037, [[2109.13823](#)], [[1](#)]: All co-authors contributed to the text of the manuscript, while the author together with R. Sato was responsible for the lattice simulations. The analytic estimates were conceived by all authors during discussion, but the author first worked out the NLO estimate in perturbation theory as well as the fluctuations on super-Hubble scales. All plots with one exception have been created by the author. The publication forms the majority of Chapter [III](#).
- C. Machado, W. Ratzinger, P. Schwaller and B. Stefanek, *Gravitational wave probes of axionlike particles* *Phys. Rev. D* **102** (2020), no. 7 075033, [[1912.01007](#)], [[2](#)]: The content of this and the following three publications is based on [[3](#)] that already formed the basis of the authors master thesis. All co-authors contributed to the analytic arguments as well as the text of the manuscript. The author contributed the figures showing the reach of GW searches in the axion parameter space. The numerical results concerning the dark photon mass as well as the GW spectrum and the corresponding figures were created by B. Stefanek and are not part of this text. The publication is part of Chapter [IV](#).
- W. Ratzinger, B. Stefanek and P. Schwaller, *Gravitational Waves from an Axion-Dark Photon System: A Lattice Study*, *SciPost Phys.* **11** (2021) 001, [[2012.11584](#)], [[4](#)]: All co-authors contributed to the text of the manuscript. The author carried out the lattice simulations with a code written from scratch. As a result he created all figures. The publication forms the majority of Chapter [IV](#).
- E. Madge, W. Ratzinger, D. Schmitt and P. Schwaller, *Audible Axions with a Booster: Stochastic Gravitational Waves from Rotating ALPs*, *SciPost Phys.* **12** (2022) 171, [[2111.12730](#)], [[5](#)]: All co-authors contributed to the text of the manuscript. The analytic estimates were also conceived in collaboration. This work formed the basis for D. Schmitts master thesis, which is why he carried out all simulations and created all plots. The technical parts concerning the simulations are therefore shortened in this version. The publication forms Chapter [V](#) and its appendix concerning fragmentation Section [III.7](#).
- A. Banerjee, E. Madge, G. Perez, W. Ratzinger and P. Schwaller, *Gravitational wave echo of relaxation trapping*, *Phys. Rev. D* **104** (2021), no. 5 055026, [[2105.12135](#)], [[6](#)]: All co-authors contributed to the text of the manuscript. The author carried out the estimate of the gravitational wave spectrum together with E. Madge and A. Banerjee. The numerics and parameter scans were done by E. Madge and A. Banerjee, who also created all figures. These parts are therefore shortened again in this text. The publication forms Chapter [VI](#).
- W. Ratzinger and P. Schwaller, *Whispers from the dark side: Confronting light new physics with NANOGrav data*, *SciPost Phys.* **11** (2021) 001, [[2012.11584](#)], [[7](#)]: All co-authors contributed to the text of the manuscript. The author carried out the fits of the spectra and created all figures. Chapter [VII](#) is a revised version of the publication.

- N. Ramberg, W. Ratzinger and P. Schwaller, *Spectral Distortions from Dark Turbulence*, in preparation for publication: The author provided the majority of the manuscript. All calculations were first carried out by him and he created all figures. The publication forms Chapter [VIII](#).

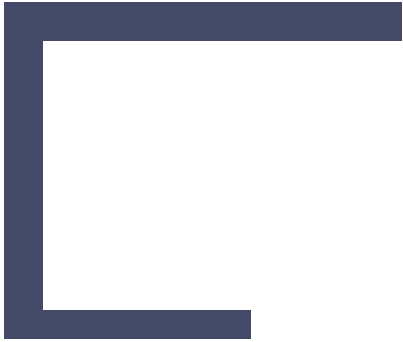
If not mentioned otherwise, all figures shown in this thesis are created by the author. Figures produced by collaborators are indicated as such. The chapters contain excerpts from the respective publication as listed above.

Contents

Abstract	i
List of publications	iii
Prelude	1
I Introduction	3
II Theoretical background	7
II.1 Axions	7
II.2 Gravitational Waves	11
II.3 Harmonic Oscillator with Time-Dependent Frequency	16
Main part I: (Rel-)Axion Fragmentation	18
III (Rel-)Axion Fragmentation	19
III.1 Introduction	19
III.2 Summary of the linear analysis	20
III.3 Lattice analysis	22
III.4 Secondary fluctuations	28
III.5 Formation of bubbles	31
III.6 Relaxion considerations	40
III.7 Gravitational Waves from Axion Fragmentation?	44
III.8 Conclusion	45
Main part II: The Audible Axion	47
IV Lattice Study of the Minimal Model	49
IV.1 Motivation	49
IV.2 Introduction to the Model	50
IV.3 Lattice Formulation and Validation	53
IV.4 Dynamics from the Lattice	54
IV.5 Model Extensions	61
IV.6 Probing Audible Axion Models	63
IV.7 Discussion and Conclusions	66

V	Boosted by an Initial Kick	67
V.1	Motivation	67
V.2	Model Description	67
V.3	Dark Photon Production	70
V.4	Gravitational Wave Spectra	74
V.5	Relic Abundances	76
V.6	Main Results and Summary	80
VI	Rolling down a Slope: The Audible Relaxion	83
VI.1	Introduction	83
VI.2	Setup	83
VI.3	Relics	88
VI.4	Discussion	95
VI.5	Conclusion	99
	Main part III: Interplay of PTAs and Spectral Distortions	101
VII	NANOGrav detection	103
VII.1	Introduction	103
VII.2	The Observation	104
VII.3	Refitting the NANOGrav data	106
VII.4	Audible Axions and NANOGrav	107
VII.5	Phase transitions and NANOGrav	108
VII.6	Discussion and Outlook	111
VIII	Spectral Distortions	113
VIII.1	Introduction	113
VIII.2	Source of μ -distortions through gravitational interaction	114
VIII.3	Analytic Estimation of the Induced Acoustic Energy	120
VIII.4	Detailed analysis of a simple model: $\lambda\phi^4$ -Theory	123
VIII.5	Application to sources of GWs	131
VIII.6	Conclusion	143
	Aftermath	145
IX	Summary and Conclusion	147
A	Redshifting Abundances and Scales	151
A.1	Dark Matter	151
A.2	Dark Radiation	152
A.3	Gravitational Waves	152
A.4	Redshifting Scales	152
B	Lattice Implementation	153

B.1	Lattice Action	153
B.2	Equations of Motion and Integration Scheme	155
B.3	Fourier Transformation and Polarization	156
B.4	Initial Conditions	157
B.5	Lattice Dimensions and Number of Iterations	157
B.6	Gravitational Waves	158
B.7	Energy Density and Shear	160
C	Free Scalar Field	161
	List of abbreviations	175
	Bibliography	177



Prelude



Introduction

Modern high energy physics stands on two pillars: The first is the standard model (SM) of particle physics. Its development started in the 1960s [8–11] guided by the wealth of data stemming from collider experiments. The SM at its core is a quantum field theory that furthermore specifies the field content such that it contains all known particles and their interactions. The last missing piece of the puzzle, the Higgs boson, a massive neutral scalar particle which generates all other particles masses when it undergoes spontaneous symmetry breaking, was finally discovered at the ATLAS and CMS experiments at the LHC in 2012 [12, 13]. Furthermore the SM predictions for particle interactions have been successfully tested in a wide variety of experiments.

The second pillar is gravity and the Λ CDM model of cosmology. It postulates the existence of two forms of energy that the SM particle content does not account for: cold dark matter and dark energy. The resulting expansion history of the universe is able to explain a plethora of phenomena such as big bang nucleosynthesis (BBN), the cosmic microwave background (CMB) and structure formation. Dark matter is furthermore necessary for the understanding of galactic dynamics, with the first hints for dark matter coming from the large velocity dispersion in galaxy clusters [14], over rotation curves [15, 16], to the collision of the bullet cluster, where a displacement of the majority of total mass from the barionic matter in the form of dust after the collision was demonstrated [17].

That said, there are still many open questions in both theories and their interplay. Some stem from observations that can not be explained by the respective theory. For example: Non-vanishing neutrino masses to explain neutrino oscillations [18], evidence for the existence of new physics in the decays of b -quarks [19], the discrepancy in the CMB and the local measurement of the Hubble constant [20] or the depth of the 21cm absorption line caused by Hydrogen right before re-ionization [21]. Other questions are related to the consistency of both theories and their parameters. An example would be so called tuning problems. In a quantum field theory like the SM one follows the approach of writing down the field content as well as the symmetries of the fields. One then expects all operators allowed by these symmetries to be present with comparable strength. This is especially true if the operator is not protected by a symmetry and therefore generated through quantum corrections. In the SM model there are two such tuning problems: The first is the strong CP problem, which relates to the absence of a CP violating operator of the strong interaction (QCD). The strength of this operator is given by an angle θ , so naturally expected to be of $\mathcal{O}(1)$ but is constrained to be $|\theta| < 10^{-10}$ by the absence of a neutron electric dipole moment [22]. The second one is known as the hierarchy problem and deals with the fact that the SM is unanimously viewed as the low energy effective

theory of a (more) complete UV theory e.g. a theory unifying the strong and electro-weak interactions. The non-observation of BSM physics pushes the allowed energy scale of such a theory to higher and higher values. The Higgs mass however is predicted from the parameters of the high energy theory and the cancellation of different contributions at the high scale needed to find a much lower value requires a tuning. In cosmology there exists the similar question of why the scale of the cosmological constant, parameterizing the amount of dark energy, is so much smaller than all other known energy scales. Finally there are questions arising at the intersection of both theories, for example: What is the particle / field nature of dark matter and dark energy? How is the observed discrepancy between matter and anti-matter, the so called baryon asymmetry, generated in the early universe?

There exist many ideas to solve one or multiple of these problems. In the first part of this thesis we investigate a particular solution to the hierarchy problem, the so called self-stopping relaxion. In this kind of model the unnatural small Higgs mass is promoted to a new scalar field, such that the coupling becomes a dynamical degree of freedom. The problem is then solved by setting the field dynamics up in such a way that the field settles at the observed value of the coupling constant. In the dynamics we consider, the field, the so called relaxion, is homogeneous but time dependent in the early universe and therefore scans the Higgs mass. As the Higgs mass approaches the observed value an instability develops in the relaxion, that turns the kinetic energy into relaxion inhomogenities/waves. Subsequently the field stops and the mass is stabilised at its present value. This mechanism was originally considered in [], but there remained questions about the viability of this stopping mechanism. These questions concern the non-perturbative nature of the process once the waves come to dominate the relaxions energy. The methods used in this thesis are able to take these effects fully into account. Furthermore new constraints on this scenario stemming from the embedding into cosmology are presented.

The absence of any clear signal of physics beyond the SM at the LHC, has lead many high energy physicists to turn their attention to cosmology and astronomy and consider these extreme environments as laboratories for new physics. The recent, direct detection of gravitational waves (GWs) by the LIGO collaboration has opened a new avenue in this direction. While the universe becomes opaque to our usual messenger, light, at temperatures above $T \approx 1$ eV, it stays see-through for GWs up to the highest temperatures the post-inflationary universe can possibly reach without being in tension with CMB observations. The catch is that there is no guaranteed source of GWs with large enough amplitudes to ever be observable. One therefore has to wonder which new physics models lead to an observable signal. This motivates us to study a particular coupling between an axion like particle (ALP) and a photon that causes an instability in the dark photon, similar to the one in the relaxion previously discussed. As we will show this mechanism is indeed able to produce a detectable GW signal. We study the relation of this setup to multiple of the previously mentioned questions, such as the nature of dark matter, the baryon asymmetry and again the relaxion mechanism.

While this thesis was conceived, multiple pulsar timing arrays (PTAs), the first of them NANOGrav, published hints for a possible signal of GWs. These arrays monitor the pulses arriving on earth from millisecond pulsars over decades, which enables them to detect GWs as they lead to residuals in the arrival times. While the quadrupolar nature of the GWs is yet to be confirmed by the imprint it leaves when correlating the signal from different pulsars, all operating PTAs see strong hints for such a signal. With the first picture of a super massive black hole at the center of our galaxy and M87 being taken recently [23, 24], the most likely explanation for this signal are inspirals of two such black

holes. It must be said though that this explanation struggles to produce a signal of this strength when compared to today's astrophysics models. This motivates us to take a close look at a variety of new physics models and their ability to produce a primordial GW background that can explain the signal in the final part of this thesis. Further inspiration was provided by [25] that highlighted the possibility to detect GWs with frequencies out of reach of direct GW searches through spectral distortions of the CMB, deviations from a black body spectrum. This motivates a study of spectral distortions caused by the damping of acoustic waves in the baryon-photon fluid that are induced by the previously mentioned new physics models. The size of the spectral distortions generated through this new mechanism is possibly much larger than the ones caused by GWs. We find that the observation of GWs together with observations of spectral distortions provides a powerful tool to constraint or possibly detect purely gravitationally coupled sectors.

Theoretical background

II.1 Axions

In a theory where a global symmetry is broken spontaneously at a scale f , there exists a massless Nambu-Goldstone boson. This particle has the same quantum numbers as the corresponding symmetry transformation. For example, if the current associated with the symmetry is an axial vector, the boson is parity odd. If the symmetry is only an approximate symmetry to begin with, the resulting boson acquires a mass m . The size of the mass is controlled by the parameter explicitly breaking the symmetry and is therefore protected against UV corrections, such that it is technically natural for the mass to be much smaller than the spontaneous breaking scale $f \gg m$. Such a parity odd boson is our notion of an axion or axion-like particle (ALP) in the rest of the thesis.

These particles are a generic prediction of theories aiming to unify the interactions of the SM or even more ambitiously gravity at energy scales far beyond the reach of colliders. For example they are found in string theory as the Kaluza-Klein zero-modes of higher dimensional anti-symmetric tensors required for anomaly cancellation [26–29]. One expects these ALPs to have their corresponding symmetries spontaneously broken at scales f ranging from the grand-unification scale $M_{\text{GUT}} \sim 10^{16}$ GeV to the reduced Planck scale $m_{\text{Pl}} = 2.44 \times 10^{18}$ GeV. In these theories the explicit breaking leading to the mass, can e.g. be realized by instantons, non-perturbative solutions of the theory related to its vacuum structure. These effects can be exponentially small, leading to a large range of possible ALP masses [28]. Interestingly, a generic string compactification is expected to result in a large number ($\gtrsim 10$) of ALPs. This abundance of ALPs motivates searches for more exotic signatures, since some of them might exhibit extraordinary couplings. The exotic signature we will be after in Part II are primordial gravity waves that are sourced due to a strong coupling to a gauge field, which can be easily conceived in this setup [30, 31]. Another possibility to achieve this signature are special axion potentials as discussed in [32, 33].

A particularly intriguing aspect of axions is that they can easily reproduce the observed DM abundance via the misalignment mechanism [34]. If the symmetry corresponding to the axion is spontaneously broken before or during inflation, the axion field takes on a constant value in all of the observable universe $\phi(\mathbf{x}, t_i) = \phi(t_i) = \theta f$ initially, where $\theta \approx 1$ denotes the misalignment angle. The axions motion is overdamped and stays at its initial value as long as the Hubble parameter is larger than the mass $H > m$. Once $H \sim m$ the axion starts oscillating around the minimum of the potential. Due to Hubble friction the amplitude of the oscillation gets damped leading to the energy in the axion red-shifting as $\propto a^{-3}$, where a denotes the scale factor, making the axion a dark matter candidate.

While most of our discussion of the primordial dynamics concerns the generic ALP, we will often come back to examples that are particularly well motivated, since they solve the

naturalness problems of the SM. Naturalness problems concern the question, why certain parameters of a theory take a very specific value. We will in the following concentrate on two of these problems: The QCD θ -angle, which is constrained by measurements to be close to zero, and the Higgs mass that is not protected against UV corrections. The possible solution ALPs provide to these problems is introducing a coupling to the sector in question that promotes the curiously small parameter to a dynamic variable, the field value of the axion. The problem is then solved by setting the dynamics of the field up in such away that today the effective parameter is small. In these setups one exploits the fact that a specific parameter is special in terms of its dynamics. This is opposed to other new physics models, in which a vanishing of the parameter in question enhances as symmetry. This also protects the parameter against quantum corrections and renders the small value technically natural [35]. To put our results in context we briefly review these two tuning problems and their ALP solutions below.

The QCD axion

The original and best known axion is the QCD axion. In QCD, taking into account non-perturbative effects and a general quark mass matrix, a P and CP violating term is present in the Lagrangian:

$$\mathcal{L} \subset \Theta \frac{g^2}{32\pi^2} G^{\mu\nu} \tilde{G}_{\mu\nu}, \quad (\text{II.1})$$

where g denotes the strong coupling constant, $G_{\mu\nu}$ the $SU(3)$ field strength and $\tilde{G}_{\mu\nu} = G^{\alpha\beta} \epsilon_{\mu\nu\alpha\beta}/2$ its dual. The CP violating effects this term induces, in particular the electric dipole moment of the neutron, are constrained by measurements, leading to an upper bound for Θ of $\Theta \lesssim 10^{-10}$ [22].¹ Such a small value is unnatural, since Θ is a dimensionless parameter and one expects $\Theta = \mathcal{O}(1)$. This problem is known as the strong CP problem. It was soon realized that the problem can be solved if the theory features a $U(1)$ symmetry that is anomalous with respect to the strong interactions. For example if one of the quark masses were to vanish e.g. the one of the up quark $m_u = 0$, one recovers symmetry under the axial rotation $u \rightarrow \exp(i\alpha\gamma_5)u$, thus solving the problem. Now the SM doesn't feature a massless quark, but Peccei and Quinn realized that the introduction of any new symmetry anomalous under QCD can still solve the problem [36]. When the new symmetry is broken spontaneously at a scale f , the resulting Nambu-Goldstone boson ϕ couples to the gluon field strength like

$$\mathcal{L} \subset -\frac{\phi}{f} \frac{g^2}{32\pi^2} G^{\mu\nu} \tilde{G}_{\mu\nu}, \quad (\text{II.2})$$

resulting in a new effective vacuum angle $\Theta = \phi/f$ [37]. Once QCD confines, $G^{\mu\nu} \tilde{G}_{\mu\nu}$ acquires a non-zero expectation value due to instanton effects, generating an axion potential. The minima of the potential correspond to $\Theta = \phi/f = 2\pi n$ with $n \in \mathbb{Z}$. The dynamics of the misalignment mechanism discussed above lead to ϕ settling in a minimum and therefore solve the strong CP problem. The curvature of the potential in the minimum gives the mass of the axion. One finds $m = \mathcal{O}(\Lambda_{\text{QCD}}^2/f)$, where Λ_{QCD} is the QCD confinement scale [38]. Throughout the thesis we will use the common approximation of the axion (ϕ) potential by a cosine

$$V = m^2 f^2 \left[1 - \cos\left(\frac{\phi}{f}\right) \right]. \quad (\text{II.3})$$

¹The measurement constraints $\Theta_{\text{eff}} = \Theta + \arg|m_q|$, where m_q is the quark mass matrix. For simplicity

Let us look at one implementation of the axion, the KSVZ axion [39, 40], to make this idea a bit more explicit. We introduce a new scalar Φ and a quark q . The Lagrangian is of the form:

$$\mathcal{L} = \bar{q}i\gamma^\mu D_\mu q - y(\Phi \bar{q}_L q_R + \Phi^* \bar{q}_R q_L) + (\partial_\mu \Phi^*)(\partial^\mu \Phi) + M^2 \Phi^* \Phi - \lambda(\Phi^* \Phi)^2. \quad (\text{II.4})$$

The Φ field acquires a vacuum expectation value $|\langle 0|\Phi|0\rangle| \equiv f = M/\sqrt{2\lambda}$. All newly introduced degrees of freedom therefore acquire a mass of $\mathcal{O}(f)$ and become unobservable if f is huge, except for the axion ϕ that is massless in the classical approximation. The axion ϕ is related to the original Φ via:

$$\Phi(x) = f \exp(i\phi(x)/f). \quad (\text{II.5})$$

If we integrate out the heavy degrees of freedom and only keep ϕ , the anomalous heavy quark loop leads to the coupling of ϕ that we have seen in Eq. (II.2). If the heavy quark is additionally charged under a new dark $U(1)$ gauge symmetry with field strength $X_{\mu\nu}$, the coupling

$$\mathcal{L} \subset -\frac{\phi}{f} \frac{g_X^2}{32\pi^2} X^{\mu\nu} \tilde{X}_{\mu\nu}, \quad (\text{II.6})$$

is introduced as well, where g_X is the coupling constant of the dark photon. We can consider this toy model as a possible UV completion of the effective theory we are discussing in Part II. In the same way as well as through mixing of the axion with pions, the couplings of the axion to the SM gauge bosons are generated.

The Relaxion

The relaxion solves the hierarchy problem also by dynamically selecting a small electro-weak scale, but in this case multiple minima as well as an involved selection mechanism are needed. Let us start by sketching the hierarchy problem. By this point it has become pretty clear that the SM has to be viewed as a low energy effective theory, originating from a (more) complete theory at a higher energy scale Λ . This theory then hopefully answers one or several of the open questions mentioned in the introduction. The energy scale Λ is called the cut-off since above this scale the new degrees of freedom will lead to the break down of the effective theory. It can no longer be used to make accurate predictions of the observables. Given the high energy theory, on the other hand, it is possible to integrate out the heavy degrees of freedom to arrive back at the low energy effective theory. This procedure allows one to identify the field content necessary to describe the low energy phenomena as well as to predict the parameters. Crucially it allows the prediction of the only dimensionful parameter of the SM, the Higgs mass. Famously all other dimensionful observables like the masses of the fermions and weak gauge bosons are generated when the Higgs acquires its vacuum expectation value during the spontaneous breaking of the electro-weak symmetry and are therefore linked to the Higgs mass. The question the hierarchy problem asks in this context is, how this dimensionful parameter ends up being so much smaller than the UV scale Λ . When integrating out the heavy degrees of freedom it is generally expected that the Higgs mass squared picks up several contributions, all of $\mathcal{O}(\Lambda^2)$. This leaves one with the conclusion that to achieve this cancellation a tuning of the high energy theory's parameters to within $\mathcal{O}(m_H^2/\Lambda^2) \ll 1$ is necessary, where m_H is the Higgs mass, in order for all the contributions to cancel to this degree. The tuning that

is needed becomes more and more severe as the UV scale Λ is pushed to higher scales to account for the non-observation of new physics at colliders. For a more detailed argument regarding the hierarchy problem we refer to [41] and references therein.

The relaxion now solves the problem by contributing to the Higgs effective mass through an adequate coupling and with its own dynamics set up to cancel the contributions of $\mathcal{O}(\Lambda)$. This idea was first realized in [42] and the interaction potential between the Higgs H and the relaxion ϕ is given by

$$V(H, \phi) = V_{\text{roll}}(\phi) + \mu_H^2(\phi)|H|^2 + \lambda|H|^4 + V_{\text{br}}(H, \phi), \quad (\text{II.7})$$

where λ is the Higgs' quartic coupling and

$$V_{\text{roll}}(\phi) = -g\Lambda^3\phi, \quad (\text{II.8a})$$

$$\mu_H^2(\phi) = \Lambda^2 - g'\Lambda\phi, \quad (\text{II.8b})$$

$$V_{\text{br}}(H, \phi) = -\frac{\Lambda_{\text{br}}^4}{v_H^2}|H|^2 \cos \frac{\phi}{f}, \quad (\text{II.8c})$$

where, $g' \approx g$ are dimensionless parameters with $g'/(4\pi) < g$, Λ_{br} is the back-reaction scale, $v_H = \langle |H| \rangle = 246 \text{ GeV}$ is the Higgs' vacuum expectation value, and f is the decay constant of the relaxion.

$\mu_H^2(\phi)$ gives the relaxion dependent effective mass of the Higgs. It is now natural to assume that the relaxion starts with a random value, such that the Higgs mass is $\mu_H^2(\phi) = \mathcal{O}(\Lambda^2)$. We furthermore assume that the mass is positive to begin with, so $\phi \approx 0$. The slope of V_{roll} will now lead to the relaxion field rolling towards larger values. Therefore, the Higgs mass becomes 0 and eventually negative. When the Higgs mass becomes negative the minimum of the potential with regards to the Higgs field is no longer at $H = 0$ but at some finite value $|H| > 0$. This leads to the last term turning on $V_{\text{br}}(H, \phi)$. The wiggles that appear on top of the slope finally trap the relaxion and keep it from rolling further. The idea is that this happens at the point when the Higgs expectation value matches the observed one $|H| = v_H$. A second crucial ingredient to trapping the relaxion is some form of friction, since the relaxion picks up a lot of speed whilst rolling down the slope and would otherwise simply overshoot the minima.

In the original idea proposed in [42] this was accomplished by this whole process taking place during inflation. In this period Hubble friction leads to the relaxion field slow rolling with a velocity $\dot{\phi} \approx g\Lambda^3/H_I$. If the Hubble constant of inflation H_I is large the relaxion field will go slow enough to stop in the first minimum it encounters. If $\Lambda_{\text{br}}^4 \approx gf\Lambda^3$ the first minimum provided by the wiggles coincides with the Higgs having its observed value. In this way the mass can be brought down from a cutoff scale of up to $\mathcal{O}(1000)$ TeV as was demonstrated in [42].

It was pointed out in [43, 44] that this exact same setup features a second source of friction. Namely the relaxion field, initially taken to be homogeneous, experiences an instability as it rolls over the forming wiggles. This instability leads to the vacuum fluctuations of the relaxion growing. The energy in these fluctuations is taken from the motion of the homogeneous component of the field, that therefore eventually stops. Taking this process into account relaxation can now also take place after inflation and if it happens during inflation nevertheless the scanning can proceed much faster. This is great news, since in the original model inflation had to last for more than $\mathcal{O}(10^4)$ e-folds, which possibly leads to eternal inflation [45]. The dynamics of this new friction mechanism are however rather

we assume throughout our discussion that $\arg|m_q| = 0$.

complex, since at some point the approximation of the relaxion field as a homogeneous field with small perturbations breaks down. This aspect of the stopping mechanism is studied in Part I.

In Chapter VI we assume that relaxation takes place as originally proposed and take a closer look at the post-inflationary dynamics of the relaxion. If the universe reheats above the electro-weak scale after inflation, the Higgs mass will get a thermal contribution that leads to its expectation value vanishing again. As a consequence the relaxion starts rolling again. We study the conditions that have to be met in order not to ruin the solution to the hierarchy problem and highlight the friction provided by the production of gauge bosons could play in this scenario. We find that apart from this friction potentially saving the mechanism the gravity waves produced in this process can be detectable.

II.2 Gravitational Waves

One of the corner stones to the description of our universe is the cosmological principle. It states that on large scales the universe is homogeneous and isotropic. This principle restricts the metric to a Friedman-Robertson-Walker universe given by

$$ds^2 = a(\tau)^2 (d\tau^2 - d\mathbf{x}^2) = dt^2 - a(t)^2 d\mathbf{x}^2, \quad (\text{II.9})$$

where a denotes the scale factor and t and τ physical and conformal time respectively.² The evolution of the scale factor is determined by the Hubble equation, which is derived from the Einstein equations of general relativity and relates the expansion with the total energy ρ_{tot} of the universe

$$H^2 = \left(\frac{\dot{a}}{a}\right)^2 = \frac{\rho_{\text{tot}}}{3m_{\text{Pl}}^2}. \quad (\text{II.10})$$

Here m_{Pl} denotes the reduced Planck mass. Now our universe is clearly not homogeneous, which necessitates the introduction of perturbations to this idealized solution. The perturbations one considers are however still statistically homogeneous. Furthermore as long as these perturbations are small one can treat them perturbatively. They can be studied by making an ansatz for the metric including perturbations and plugging it into the Einstein equations. At zeroth order in the perturbations we then recover the Hubble equation given above and to first order we find the evolution equations for the perturbations. One particular benefit from this treatment is that these equations are now linear in the perturbations, which leads to the decoupling of the dynamics of mode functions once we Fourier transform in the spacial coordinates. Furthermore one can classify the perturbations of one single mode \mathbf{k} by how they transform when applying rotations around \mathbf{k} . This is done by introducing $m \in \mathbb{N}_0$ reminiscent of the magnetic quantum number.

The cases relevant for cosmology are $m = 0$, so called scalar fluctuations, and $m = 2$, the transverse-traceless fluctuations, which are exactly the gravitational waves (GWs). The scalar part describes the dynamics of density fluctuations and their interaction via the gravitational potentials. We will come back to them in Chapter VIII. Here we give an overview on how to calculate the primordial GW background emitted from turbulent phenomena that will be used throughout most of this thesis.

To get started one replaces the metric found above using conformal time $a^2\eta_{\mu\nu}$ with $a^2(\eta_{\mu\nu} + h_{\mu\nu})$, where $h_{\mu\nu} \ll \mathcal{O}(1)$ is a general perturbation, which is small compared to the Minkowski metric $\eta_{\mu\nu}$. This general perturbation contains scalar, vector and tensor

²In principle the spacial part could be curved, but this curvature is highly constrained [46].

components. To single out the transverse-traceless tensor describing the GW, we only consider the spatial components to be non-zero $h_{ij} \neq 0$. Furthermore, this tensor is taken to be traceless $h_{ii} = 0$ and divergence free $\partial_i h_{ij} = 0$. In this case the linearized Einstein equations state

$$h''_{ij} + 2\frac{a'}{a}h'_{ij} - \nabla^2 h_{ij} = \frac{2}{m_{\text{pl}}^2} \Pi_{ij}, \quad (\text{II.11})$$

where Π_{ij} is the transverse traceless part (satisfies same conditions as h_{ij} , see above) of the perturbations in energy-momentum $\delta T_{\mu\nu}$.

Transverse-Traceless Projector

In Fourier space the conditions for a tensor to be transverse-traceless read $h_{ii}(\tau, \mathbf{k}) = 0$ and $k_i h_{ij}(\tau, \mathbf{k}) = 0$. Since h_{ij} is also part of a metric and therefore symmetric, it follows that we can decompose $h_{ij}(\tau, \mathbf{k})$ as

$$h_{ij}(\tau, \mathbf{k}) = \sum_{\lambda=\pm} \epsilon_i^\lambda(\mathbf{k}) \epsilon_j^\lambda(\mathbf{k}) h^\lambda(\tau, \mathbf{k}), \quad (\text{II.12})$$

where the polarization vectors $\epsilon_i^\lambda(\mathbf{k})$ are given by $k_i \epsilon_i^\lambda(\mathbf{k}) = 0$, $\epsilon_i^{\lambda'*}(\mathbf{k}) \epsilon_i^\lambda(\mathbf{k}) = \delta_{\lambda',\lambda}$ and $\epsilon_{ijk} k_j \epsilon_k^\lambda(\mathbf{k}) = i\lambda \epsilon_i^\lambda(\mathbf{k})$ ³. Notice that $\epsilon_i^\lambda(\mathbf{k}) \epsilon_j^\lambda(\mathbf{k})$ picks up a phase $\exp(i2\lambda\phi)$ under a rotation by an angle ϕ around \mathbf{k} , because each $\epsilon_\lambda(\mathbf{k})$ picks up a phase $\exp(i\lambda\phi)$. We can see that a gravitational wave carries spin $m = 2$ and that $h^\lambda(\tau, \mathbf{k})$ is the mode function with helicity λ .

The polarization of gravitational waves provides an interesting way to experimentally distinguish between different signals. The currently running or planned detectors all rely on the measurement of changes in distance between freely falling masses. In principle, such detectors are able to differentiate between polarizations as Fig. II.1 shows.

Due to $\epsilon_\lambda^* \cdot \epsilon_{\lambda'} = \delta_{\lambda\lambda'}$, we find for the coefficients $h^\lambda(\tau, \mathbf{k}) = \epsilon_i^{\lambda'*}(\mathbf{k}) \epsilon_j^{\lambda*}(\mathbf{k}) h_{ij}(\tau, \mathbf{k})$. In this way we can project out the symmetric transverse traceless part of any tensor with given helicity λ . Starting from perturbations in the energy-momentum tensor δT_{ij} , we can therefore get the anisotropic stress Π_{ij} as

$$\Pi_{ij}(\tau, \mathbf{k}) = \sum_{\lambda=\pm} \epsilon_i^\lambda(\mathbf{k}) \epsilon_j^\lambda(\mathbf{k}) \Pi^\lambda(\tau, \mathbf{k}), \quad (\text{II.13})$$

with $\Pi^\lambda(\tau, \mathbf{k}) = \epsilon_i^{\lambda*}(\mathbf{k}) \epsilon_j^{\lambda*}(\mathbf{k}) \delta T_{ij}(\tau, \mathbf{k})$. At first order in h_{ij} the different helicities evolve independently, as we can see by Fourier transforming Eq. (II.11) and multiplying by $\epsilon_i^{\lambda*}(\mathbf{k}) \epsilon_j^{\lambda*}(\mathbf{k})$:

$$h''_\lambda + 2\frac{a'}{a}h'_\lambda + k^2 h_\lambda = \frac{2}{m_{\text{pl}}^2} \Pi_\lambda \quad (\text{II.14})$$

Energy Density

The quantity commonly used to compare gravitational wave signals is the energy spectrum. But how can we make sense of the energy-momentum in a gravitational

³The symmetric tensors that satisfy $h_{ii}(\tau, \mathbf{k}) = 0$ and $k_i h_{ij}(\tau, \mathbf{k}) = 0$ form a 2 dimensional vector space. $\epsilon_i^+(\mathbf{k}) \epsilon_j^+(\mathbf{k})$ and $\epsilon_i^-(\mathbf{k}) \epsilon_j^-(\mathbf{k})$ are part of it and linear independent and therefore form a basis.

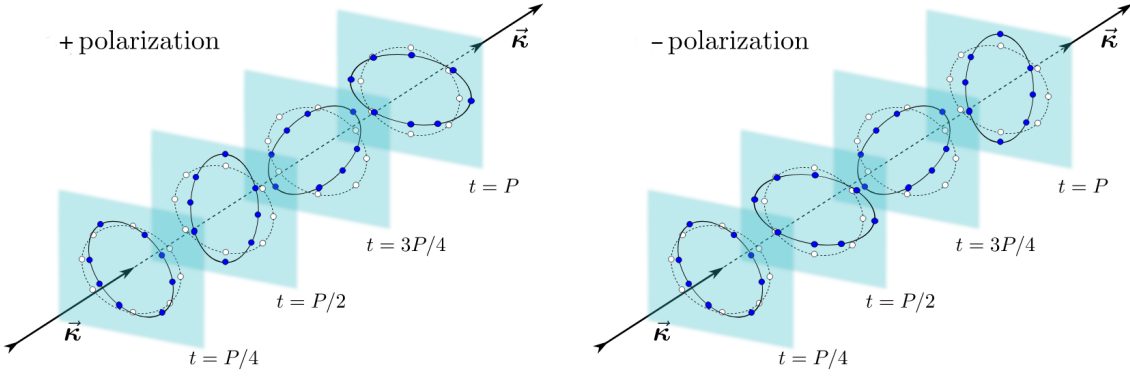


Figure II.1: Polarized gravitational wave hitting a circle of freely falling particles. The circle lies in the blue plane orthogonal to the propagation direction. The solid line with blue dots shows the perturbed circle while the dotted line with white dots is the unperturbed circle before the arrival of the wave. The circle is shown at different times. $P = 2\pi/k$ is the period of the gravitational wave. Illustration borrowed from [47].

wave, a distortion of space-time? Lets examine a localized gravitational wave packet with wavelength λ and width $\delta \gg \lambda$. The energy-momentum is the source in Einsteins field equations. At first order in $h_{\mu\nu}$ we got the linearized Einstein equations, that determine the propagation of the wave packet. Moving onto second order, we find that we can distinguish two types of contributions: The ones that vary on a typical scale λ and describe interactions between gravitational waves e.g. scattering, and the ones that only vary on scales comparable to δ . The second kind behaves exactly like the energy-momentum of e.g. a electromagnetic wave packet, a photon. It vanishes outside the packet and with in it is approximately constant, only varying on scales of the whole package δ rather than single wavelengths λ . Therefore, we identify the second term with the energy-momentum of the gravitational wave. In this case we have [48]

$$T_{\mu\nu}^{\text{GW}} = \frac{m_{\text{pl}}^2}{4} \langle \nabla_\mu h_{ij}^* \nabla_\nu h_{ij} \rangle, \quad (\text{II.15})$$

where ∇_μ denotes the covariant derivative with respect to the background metric $a^2\eta_{\mu\nu}$ and the average has to be taken over several wavelengths, in order to only end up with the slowly varying contributions.

The energy density measured by a co-moving observer is extracted by contracting the energy-momentum-tensor with the 4-velocity of that observer ($u^\mu = (1/a, 0, 0, 0)$ working in conformal time τ).

$$\begin{aligned} \rho &= T_{\mu\nu}^{\text{GW}} u^\mu u^\nu \\ &= \frac{m_{\text{pl}}^2}{4a^2} \langle \nabla_0 h_{\alpha\beta}^* \nabla_0 h^{\alpha\beta} \rangle \\ &\approx \frac{m_{\text{pl}}^2}{4a^2} \langle h_{ij}^* h'_{ij} \rangle \end{aligned} \quad (\text{II.16})$$

where in the last step we have used that ∂_0 and ∇_0 agree for sub-horizon wavelengths since $\Gamma \propto a'/a$. Next, we can Fourier expand h and use that $\langle e^{-i\mathbf{k}\cdot\mathbf{x}+i\mathbf{k}'\cdot\mathbf{x}} \rangle = (2\pi)^3 \delta^{(3)}(\mathbf{k} - \mathbf{k}')$.

We find

$$\rho = \frac{m_{\text{pl}}^2}{4a^2} \int \frac{d^3k}{(2\pi)^3} \langle h_{ij}^{*'}(\tau, \mathbf{k}) h'_{ij}(\tau, \mathbf{k}) \rangle, \quad (\text{II.17})$$

were the remaining brackets denote an average over time. For the spectral density we find

$$\frac{d\rho}{d \log k}(\tau, k) = k \cdot \frac{d\rho}{dk}(\tau, k) = \frac{m_{\text{pl}}^2 k^3}{8\pi^2 a^2} \langle h_{ij}^{*'}(\tau, k) h'_{ij}(\tau, k) \rangle. \quad (\text{II.18})$$

Now that we are in Fourier space again, we can plug in the definition from Eq. (II.12) in order to express the spectral energy density in terms of the mode functions $h_\lambda(\tau, k)$. $h_\lambda(\tau, k)$ is the mode function with helicity λ , allowing us to define the polarized spectra as

$$\frac{d\rho^\lambda}{d \log k}(\tau, k) = \frac{m_{\text{pl}}^2 k^3}{8\pi^2 a^2} \langle h_\lambda^{*'}(k, \tau) h'_\lambda(k, \tau) \rangle. \quad (\text{II.19})$$

The total spectrum is then simply given by summing over the polarizations λ . The determination of this energy density will be the central part of any calculation in the following that tries to assess the detectability of GWs. Throughout this thesis we will use two strategies to do so that we briefly outline here.

Integration in Fourier Space

If the dynamics of the source are already described in Fourier space, the source term $\Pi_\lambda(\mathbf{k}, \tau)$ will also be given in Fourier space. In this case it is easiest to start from Eq. (II.14) and multiply with a , such that we end up with

$$(a h_\lambda)'' + \left(k^2 - \frac{a''}{a}\right) a h_\lambda = \frac{2}{m_{\text{pl}}^2} a \Pi_\lambda \quad (\text{II.20})$$

For sub-horizon wavelengths we have $k^2 \gg a^2 H^2 \approx a''/a$ and can therefore neglect a''/a . In the radiation dominated universe that we will be dealing with throughout this thesis, we have $a(\tau) = 1 + H_{(\tau=0)}\tau$ and therefore a'' even vanishes exact. Formally the equation above is solved by

$$h_\lambda(\tau, \mathbf{k}) = \frac{2}{m_{\text{pl}}^2 a(\tau)} \int_{\tau_i}^{\tau} d\tau' \frac{a(\tau')}{k} \sin(k(\tau - \tau')) \Pi_\lambda(\tau', \mathbf{k}), \quad (\text{II.21})$$

where τ_i denotes a time before the source turned on. The energy spectrum can then be found by plugging this solution into Eq. (II.19), where due to the average in Eq. (II.19) the fast oscillating terms are dropped, in total one finds [3, 49]

$$\frac{d\rho^\lambda}{d \log k}(\tau, k) = \frac{k^3}{4\pi^2 m_{\text{pl}}^2 a^4(\tau)} \int_{\tau_i}^{\tau} d\tau' d\tau'' a(\tau') a(\tau'') \cos(k(\tau' - \tau'')) \Pi_\lambda^*(\tau', k) \Pi_\lambda(\tau'', k). \quad (\text{II.22})$$

Notice that the energy density in gravitational waves scales as a^{-4} and is therefore a form of radiation. Since the sources we consider in the thesis are only efficiently sourcing GWs for a finite amount of time, we can cutoff the integral at some time τ_f when the energy density has converged. From this point onwards we use the equations given in Appendix A

to determine the present day abundance by red-shifting. The quantity commonly used to do so is the energy density normalized by the total energy density, since it is dimensionless and constant during radiation domination up to changes in the relativistic degrees of freedom

$$\Omega_{\text{GW}}^\lambda(\tau, k) = \frac{1}{3m_{\text{pl}}^2 H^2(\tau)} \frac{d\rho^\lambda}{d \log k}(\tau, k). \quad (\text{II.23})$$

Integration in Position Space

The instabilities that we consider below become at some point non-perturbative. When we use the strategy presented above we will always have to make simplifying assumptions about the dynamics of the source to make the description in Fourier space feasible. In some cases we will however solve the full dynamics by integrating the equations of motion in position space. To do so we will have to quantize the space coordinates. We will refer to this as the lattice method. In this case it is best to also solve the dynamics of the GWs on the lattice given by Eq. (II.11). Since the transverse-traceless projector can not readily be applied in position space, we instead use a pseudo stress $\tilde{\Pi}$ that contains all terms of the energy momentum tensor that contribute to the transverse-traceless stress. We can then solve Eq. (II.11) using $\tilde{\Pi}$ instead of Π , Fourier transform the final result and apply the projector. This is mathematically equivalent, since Eq. (II.11) and the projection are linear [50]. Given the solution we again calculate the energy density using Eq. (II.19). The details of the implementation of this method are given in Appendix B.

GW detection

Once one has predicted the GW spectrum, one can evaluate its detectability in current and future experiments. A stochastic GW background can be detected in a given experiment if its signal-to-noise ratio (SNR) ϱ exceeds a threshold value ϱ_{thr} . The SNR is given by [51]

$$\varrho^2 = T_{\text{obs}} \int_{f_{\text{min}}}^{f_{\text{max}}} df \left[\frac{\Omega_{\text{GW}}(f)}{\Omega_n(f)} \right]^2, \quad (\text{II.24})$$

where T_{obs} is the period of observation, $(f_{\text{min}}, f_{\text{max}})$ is the frequency range of the detector and $\Omega_n(f)$ is the detector's noise spectrum converted to fractional energy density. For a cross-correlated measurement in a network of detectors, as for instance a pulsar timing array (PTA), the noise spectrum has to be replaced by the effective noise Ω_{eff} of the network (see [51] for further details), and the SNR is given by Eq. (II.24) with an additional factor of 2.

We will see that the sources considered below don't source a signal strong enough to be detected by the current generation of ground-based interferometers, the LIGO, VIRGO and KAGRA network [52]. But their planned predecessor the Einstein telescope (ET) can test part of the parameter ranges [53]. In the micro-Hertz to Hertz range we furthermore present the projected sensitivities of the planned space-based observatories LISA [54, 55], μAres [56], BBO and DECIGO [57]. Pulsar timing arrays like the planned Square-Kilometre Array (SKA) [58] can detect GWs at even lower frequencies.⁴ In addition, we evaluate current limits from the NANOGrav 11-year dataset [60].

⁴We here assume that the prospective foreground from supermassive black hole binaries can be subtracted. Further details on the sensitivities can be found in [59].

Recently, NANOGrav and other operating pulsar timing arrays have further reported strong evidence for a common-spectrum stochastic process across the pulsars in their data [61–64], which might be due to a GW background. However, a GW detection has not yet been established, due to the lack of conclusive evidence regarding the inter-pulsar correlations of this process. We take a closer look at this possible discovery in Chapter VII, where we present a fitting procedure that allows for a quick parameter estimation given the gravitational wave spectrum of a specific model.

In [25] the possibility of detecting GWs via the CMB spectral distortions they cause was highlighted. In Chapter VIII we consider the possibility of sourcing spectral distortions via gravitationally induced acoustic waves in the baryon-photon fluid. Both these effects are present for the sources of GWs we consider in this thesis and we compare their respective strength.

II.3 Harmonic Oscillator with Time-Dependent Frequency

The dynamics of the models below can be analyzed in the early stages by separating the evolution of homogeneous mean fields and fluctuations that must be quantized. When we perform a Fourier transformation with respect to the spatial coordinates, we find that each mode of these fluctuations obeys the equation of motion of a harmonic oscillator and can be quantized as such. The evolution of the homogeneous mean fields will introduce a time-dependence of the frequencies, leading to a set of harmonic oscillators with time-dependent frequencies. In this case, however, the state of lowest energy changes over time such that it is not obvious how to define the vacuum. In order to solve this problem, we start by quantizing the harmonic oscillator and pay special attention to the time-dependence.

Quantization

The action of a harmonic oscillator with time-dependent frequency reads

$$S = \frac{1}{2} \int dt \left(\dot{\Phi}^2 - \omega^2(t)\Phi^2 \right), \quad (\text{II.25})$$

where $\omega(t)$ denotes the frequency. The equation of motion is

$$\ddot{\Phi} + \omega^2(t)\Phi = 0. \quad (\text{II.26})$$

The system is quantized by promoting Φ and $\Pi = \dot{\Phi}$ to operators $\hat{\Phi}$ and $\hat{\Pi}$ and demanding $[\hat{\Phi}, \hat{\Pi}] = i$. We introduce creation and annihilation operators \hat{a} and \hat{a}^\dagger , that satisfy $[\hat{a}, \hat{a}^\dagger] = 1$. This allows us to express the time dependence of $\hat{\Phi}$ (Heisenberg picture) with a mode function $v(t)$:

$$\hat{\Phi}(t) = v(t)\hat{a} + v^*(t)\hat{a}^\dagger. \quad (\text{II.27})$$

$\hat{\Phi}$ solving the equation of motion Eq. (II.26) is then equivalent to $v(t)$ solving it. From $[\hat{\Phi}, \hat{\Pi}] = i$, we get:

$$i = v(t)\dot{v}^*(t) - v^*(t)\dot{v}(t) = 2i \text{Im}(v(t)\dot{v}^*(t)). \quad (\text{II.28})$$

However, these equations do not uniquely determine $v(t)$. We can derive further restrictions by specifying the vacuum $|0\rangle$, defined by $\hat{a}|0\rangle = 0$. In the time-independent case, we can demand that the vacuum is the eigenstate of the Hamiltonian with the smallest

eigenvalue. This is, in general, impossible since the state of lowest energy is also changing with time. Assuming that for very early times $\omega^2(t)$ approaches a constant value ($\lim_{t \rightarrow -\infty} \omega^2(t) = \omega_0^2$), we can nevertheless define the Bunch Davies Vacuum as the state that minimizes the energy for very early times or, in other words, for early times we describe the system as a harmonic oscillator with constant frequency ω_0 . Its vacuum can then be defined as usual:

$$\begin{aligned} \hat{H} |0\rangle &= \frac{1}{2} [\hat{\Pi}^2 + \omega_0^2 \hat{\Phi}^2] |0\rangle \\ &= \frac{1}{2} [(\dot{v}^*(t))^2 + \omega_0^2 (v^*(t))^2] \hat{a}^\dagger \hat{a}^\dagger |0\rangle + \frac{1}{2} [|\dot{v}(t)|^2 + \omega_0^2 |v(t)|^2] |0\rangle \end{aligned} \quad (\text{II.29})$$

Demanding that $|0\rangle$ is an eigenstate of \hat{H} , we obtain:

$$\begin{aligned} 0 &= \dot{v}^2(t) + \omega_0^2 v^2(t) \\ &= (\dot{v} + i\omega_0 v)(\dot{v} - i\omega_0 v) \end{aligned} \quad (\text{II.30})$$

Only one of the factors above can be set to zero and satisfy Eq. (II.28) which leads to:

$$\dot{v}(t) = -i\omega_0 v(t); \quad (\text{II.31})$$

$$v(t) = \frac{1}{\sqrt{2\omega_0}} e^{-i\omega_0 t} \quad (\text{II.32})$$

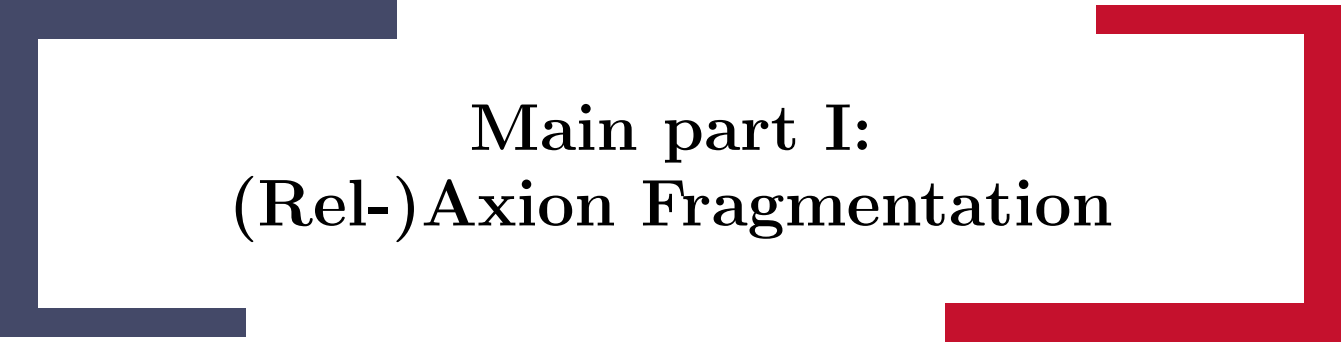
for early times t . Due to the time-dependence, these relations may not hold at later times. Since these equations describe the lowest energy state for early times, as just shown, the system might be in an excited state at later times.

Classical Description after Growth of Mode Functions

Further on in this thesis, the case will be important where the time-dependence of ω^2 leads to an enormous growth of the mode function amplitude. This growth will eventually lead to the break down of the linearized treatment that allowed us to describe the system in terms of its Fourier modes behaving as decoupled harmonic oscillators. The large field amplitudes, however, lead to effects from quantum interference becoming negligible, when calculating total widths to get e.g. a power spectrum. We will be exploiting this fact in the before mentioned lattice method by switching to a classical, stochastic description. This is achieved by turning Φ into a Gaussian random variable

$$\Phi(t) = \text{Re}(v(t))e + \text{Im}(v(t))e', \quad (\text{II.33})$$

where e, e' are independent normalized Gaussian variables $\langle ee \rangle = \langle e'e' \rangle = 1$, $\langle ee' \rangle = 0$. Note that during the growth stage when the perturbative treatment still holds, all the physics is in $v(t)$. Therefore, it makes mathematically no difference at what point we switch to the classical description, as long as it is during the perturbative stage. A special choice is using the classical description from the beginning of the simulation, which is what we refer to when we speak about the Bunch-Davies vacuum as an initial condition for the classical lattice method.

The text is framed by two L-shaped brackets. The left bracket is dark blue, and the right bracket is red. They are positioned on the left and right sides of the text, respectively, with their inner corners facing each other.

**Main part I:
(Rel-)Axion Fragmentation**

(Rel-)Axion Fragmentation

III.1 Introduction

The original relaxion mechanism discussed in Section II.1 relied on Hubble friction during inflation for the relaxion to stop in one of the minima. Without this friction the relaxion does not stop in the first minima it encounters, but rather rolls over many minima and maxima. This, however, gives rise to a new form of friction itself: As the relaxion traverses over the minima, the effective mass given by the curvature of the potential is highly oscillatory. This results in a parametric resonance that leads to exponential growth of fluctuations in the relaxion field for a particular range of momenta [43]. The energy required for this growth is extracted from the motion of the homogeneous mode such that this so-called fragmentation process acts as a source of friction to the rolling of the relaxion. This effect leads to a natural and novel stopping mechanism for the relaxion, the so-called *self-stopping relaxion*, as first pointed out in [43, 44]. Similar self-resonance effects have been considered in the context of axion monodromy inflation [65] and axion monodromy dark matter [33, 66] and can also result in GW production [67].

The necessary ingredients for successful relaxation of the EW scale in the context of the self-stopping relaxion were studied in [44], while Ref. [43] examined the conditions under which ALP fragmentation can efficiently stop the field evolution for generic ALPs. In particular, the time required to stop the field as well as the corresponding field displacement were computed in a linearized analysis, where the equation of motion for the ALP fluctuations can be Fourier transformed into momentum space, with each mode evolving independently. It was shown in [43] that the linear approximation holds for most of the fragmentation process, thus the linearized results for *e.g.*, the stopping time were expected to hold up to $\mathcal{O}(1)$ corrections from non-linearities.

A fully satisfactory description of the system in the non-linear regime requires a detailed lattice study, which we perform in this work. While our motivation is rooted in the relaxion mechanism, our lattice study here is broadly applicable to general ALPs with/without a monodromy-like potential. In particular, another interesting example for the application of the axion fragmentation would be the kinetic misalignment scenario [68–70], which is a novel ALP dark matter production mechanism. In this scenario, the ALP zero mode has initial velocity which is large enough to overcome the potential barrier, and this initial velocity determines the amount of the relic abundance today. A possible mechanism to achieve these initial conditions is discussed in detail in Chapter V. We will briefly discuss the physical consequences of ALP fragmentation in this new production mechanism towards the end of this chapter, in particular commenting on the possibility of emitting detectable GWs. Similar studies have recently appeared in [71], where especially the potential of this mechanism was highlighted to achieve the observed DM abundance in

parameter space with existing or planned direct detection experiments.

We solve the ALP equations of motion in position space on a discretized spacetime lattice using a staggered grid algorithm [72, 73], which reproduces the continuum version of the equations up to an error that is quadratic in the lattice spacing. We generically find that ALP fragmentation is more efficient in the presence of non-linearities, mainly due to the importance of $2 \rightarrow 1$ processes that allow for the growth of modes outside the parametric resonance band. The more efficient fragmentation typically leads to an order of magnitude reduction in the stopping time and field displacement as compared to the results from the linear analysis. As expected, the final ALP spectrum is broadened compared to the linearized analysis, and the final field configuration is highly inhomogeneous as most of the energy in the system is contained in fluctuations corresponding to axion particles. The rest of the features of the linear analysis are qualitatively confirmed, and we comment briefly on the possible formation of domain walls due to the ALP field stopping in different minima on scales separated by more than the inverse stopping time.

Finally we investigate the potential stochastic GW background emitted by fragmentation, if an ALP subject to the kinetic misalignment mechanism constitutes all of DM. A simple argument based on a naive dimensional estimate of the GWs energy density, leads us to the conclusion that no detectable GW background can be sourced without overclosing the universe in the minimal scenario. Further mechanisms to suppress the axions abundance would be needed.

III.2 Summary of the linear analysis

In this section we briefly recall the results of Ref. [43]. We consider a potential of the form

$$V(\phi) = -\mu^3 \phi + \Lambda_b^4 \cos \frac{\phi}{f}. \quad (\text{III.1})$$

This ansatz approximates the relaxion potential of Eq. (II.7) once the Higgs vev has become non-zero. We can then identify $\mu^3 \simeq -g\Lambda^3$ and $\Lambda_b^4 \simeq \Lambda_{\text{br}}^4 |H|^2/v_H^2$, neglecting the dependence of $|H|^2$ on ϕ . This approximation is valid, since in this stopping scenario the relaxion overcomes many minima and maxima, such that the relative change in the barrier size towards the end of its evolution is small. This also means that we are working in the limit $\Lambda_b^4/f \gg \mu^3$ and we define the axion mass $m^2 = \Lambda_b^4/f^2$. Notice that, for $\Lambda_b^4/f \sim \mu^3$, the physical value of the axion mass is smaller than this value. This does not affect our discussion. In the rest of this chapter we will use m or Λ_b interchangeably. We assume that the axion has an initial kinetic energy large enough to overcome the barriers of the potential, $\dot{\phi}^2/2 \gg \Lambda_b^4$. In the relaxion case this velocity is generated through the monodromy $V_{\text{roll}} \approx -\mu^3 \phi$ while the barriers are still absent.

In the kinetic misalignment scenario that we briefly eluded to in the introduction there is no monodromy $\mu = 0$. In this case the initial velocity could be generated via the mechanism discussed in Chapter V or via the alternative presented in [74].

In the linear analysis we decompose the axion field into a homogeneous mode plus small fluctuations:

$$\phi(x, t) = \phi(t) + \delta\phi(x, t) = \phi(t) + \left(\int \frac{d^3k}{(2\pi)^3} a_k u_k(t) e^{ikx} + h.c. \right) \quad (\text{III.2})$$

where a_k are the usual annihilation operators with $[a_k, a_{k'}^\dagger] = (2\pi)^3 \delta^3(k - k')$. As initial condition, we assume the modes are initially in the Bunch-Davies vacuum, where $u_k(t) \approx$

$e^{-ik\tau}/(a\sqrt{2k})$ with τ being the conformal time.¹ The equations of motion for the zero mode $\phi(t)$ and for the mode functions u_k are given by

$$\ddot{\phi} + 3H\dot{\phi} + V'(\phi) + \frac{1}{2}V'''(\phi) \int \frac{d^3k}{(2\pi)^3} |u_k|^2 = 0, \quad (\text{III.3})$$

$$\ddot{u}_k + 3H\dot{u}_k + \left[\frac{k^2}{a^2} + V''(\phi) \right] u_k = 0. \quad (\text{III.4})$$

Equation (III.3) is such that a growth of the mode functions u_k slows down the evolution of the zero mode ϕ . Neglecting cosmic expansion, and in the limit of constant velocity, Eq. (III.4) can be read as a Mathieu equation. This is a special case of the harmonic oscillator with time-dependent frequency as discussed in Section II.3, which features exponentially growing solutions depending on its parameters, namely when k falls in specific bands around $n\dot{\phi}/(2f)$, for integer $n \geq 1$. Modes falling in the $n = 1$ modes grow faster, and the width of the band is larger than for $n \geq 2$, thus we expect these modes to be the principal source of friction to the axion.

For $\dot{\phi}^2/2 \gg \Lambda_b^4$, the $n = 1$ instability band can be written as $|k - k_{\text{cr}}| < \delta k_{\text{cr}}$, with

$$k_{\text{cr}} = \frac{\dot{\phi}}{2f}, \quad \delta k_{\text{cr}} = \frac{\Lambda_b^4}{2f\dot{\phi}}. \quad (\text{III.5})$$

The asymptotic behaviour of u_k at large t is

$$u_k \sim (2k_{\text{cr}})^{-1/2} \exp\left(\sqrt{(\delta k_{\text{cr}})^2 - (k - k_{\text{cr}})^2}t\right) \sin\left(k_{\text{cr}}t + \frac{\pi}{4}\right). \quad (\text{III.6})$$

Due to this exponential growth, the energy density of the fluctuations within the instability band increases. Energy conservation implies that the kinetic energy of the zero mode decreases by the same amount, thus reducing $\dot{\phi}$ and correspondingly shifting the instability band towards smaller k 's. At the linear level, the growth of the modes around k_{cr} stops when they exit the instability band, *i.e.*, when the critical mode has decreased by an amount δk_{cr} . As we will discuss in the following in Sec. III.4, at next to leading order the scattering of two modes of the instability band can enhance modes which are still outside the latter. As a result, these modes enter into the instability band with a larger initial amplitude. Hence, the time needed for their enhancement to level which induces a significant backreaction is shortened, increasing the overall efficiency of the process.

The equation of motion of the fluctuations Eq. (III.4) can be solved, assuming $\ddot{\phi}$ does not vary during the amplification time of a single mode, by means of a WKB approximation in three separate time intervals: first, before the mode k_{cr} enters the instability band; second, when the mode is deep inside the instability band; third, after it has left it. In the two transition regions, when the mode enters and exits the instability band, the solution can be expressed in terms of Airy functions. Continuity of the solution is then used to match the five intervals. The asymptotic solution for u_k , after it has left the instability band, is found to be

$$u_{k_{\text{cr}}}(t) \simeq \frac{1}{a} \sqrt{\frac{2}{k_{\text{cr}}}} \exp\left(\frac{\pi \Lambda_b^8}{4f\dot{\phi}^2 |\ddot{\phi} + H\dot{\phi}|}\right) \sin\left(\frac{1}{a}k_{\text{cr}}t + \delta\right), \quad (\text{III.7})$$

¹Note that Eq. (2.6) in Ref. [43] contains an error in the phase of the Bunch-Davies mode functions, which does not affect the derivation of the subsequent results. In addition, the effects of cosmic expansion are not important since fragmentation is much faster than one Hubble time.

and the time needed for this amplification is

$$\delta t_{\text{amp}} \approx \frac{1}{2\delta k_{\text{cr}}} \log \frac{\dot{\phi}^2}{k_{\text{cr}}^4} = \frac{f\dot{\phi}}{\Lambda_b^4} \log \frac{16f^4}{\dot{\phi}^2}. \quad (\text{III.8})$$

By using energy conservation and Eq. (III.7), the equation of motion for the zero mode can be derived:

$$\dot{\phi}\ddot{\phi} = -3H\dot{\phi}^2 + \mu^3\dot{\phi} - \frac{1}{32\pi^2 f^4} \dot{\phi}^3 |\ddot{\phi} + H\dot{\phi}| \exp\left(\frac{\pi\Lambda_b^8}{2f\dot{\phi}^2|\ddot{\phi} + H\dot{\phi}|\dot{\phi}}\right). \quad (\text{III.9})$$

Equation (III.9) can be integrated exactly for $H = 0$, $\mu = 0$. In particular, one finds that the evolution of the zero mode is stopped by the backreaction after a time

$$\Delta t_{\text{frag}} \simeq \frac{2f\dot{\phi}_0^3}{3\pi\Lambda_b^8} \log \frac{32\pi^2 f^4}{\dot{\phi}_0^2}, \quad (\text{III.10})$$

and the corresponding field excursion is

$$\Delta\phi_{\text{frag}} \simeq \frac{f\dot{\phi}_0^4}{2\pi\Lambda_b^8} \log \frac{32\pi^2 f^4}{\dot{\phi}_0^2}. \quad (\text{III.11})$$

The effect of Hubble friction and of the slope μ is negligible as long as the following equation is satisfied:

$$\mu^3 < 2H\dot{\phi}_0 + \frac{\pi\Lambda_b^8}{2f\dot{\phi}_0^2} \left(W_0 \left(\frac{32\pi^2 f^4}{e\dot{\phi}_0^2} \right) \right)^{-1}. \quad (\text{III.12})$$

Here $W_0(z)$ is the 0-th branch of the product logarithm function. If the slope μ is too large, the field is accelerated and the fragmentation is not efficient enough to stop it, unless Hubble friction balances it. In Sec. III.3 we will check the validity of Eqs. (III.10)–(III.12) with a lattice analysis. Due to the increased efficiency at next-to-leading order (NLO), the time scale and the field excursion of Eqs. (III.10), (III.11) are reduced typically by a factor of a few. Instead, Eq. (III.12) is satisfied with order percent accuracy.

III.3 Lattice analysis

The linear analysis presented above is very useful as it provides simple analytic expressions for the quantities related to the axion evolution. One may wonder, though, whether these results are robust once non-linear effects are taken into account. Even though a strong backreaction is intrinsically related to a breakdown of perturbativity, it is expected that, at NLO, the efficiency of fragmentation is not suppressed in a potential as in Eq. (III.1) [43]. In this section, we discuss the validity of this statement by means of a lattice simulation. The simulation is carried out using a staggered grid quantization of space and time, guaranteeing second order accuracy in the lattice spacing $\mathcal{O}(dx_\mu^2)$. The time integration of the resulting field equations is carried out using a leapfrog algorithm (the algorithm discussed in Sec. B but without the vector field). We vary the side length of the simulated box L as well as the number of lattice sites N to ensure that our results are independent of them, which is the case as long as the critical modes from the start of the simulation when $\langle\dot{\phi}\rangle = \dot{\phi}_0$ up to the end where $\langle\dot{\phi}\rangle < 2mf$ are all covered. This corresponds to $dx = L/\sqrt[3]{N} \ll 2f/\dot{\phi}_0$ and $L \gg 1/m$.

We start neglecting the slope and cosmic expansion, such that $\mu = H = 0$. The most relevant quantities that we want to compute on the lattice are the duration of and the field excursion during the fragmentation process. From the linear analysis, we know that the modes that are inside of the first instability band at the time when the barriers appear, will grow for a time $\delta t_{\text{amp}}|_{\dot{\phi}=\dot{\phi}_0}$ as in Eq. (III.8), where $\dot{\phi}_0$ is the initial velocity. After that time, the instability band moves towards lower k modes due to the backreaction onto the zero mode. We are interested in the time needed to stop the evolution of the zero mode and the corresponding field excursion, which were computed in the linear approximation in Eqs. (III.10) and (III.11) to be

$$\Delta t_{\text{frag}} \simeq \frac{2f\dot{\phi}_0^3}{3\pi\Lambda_b^8} \log \frac{32\pi^2 f^4}{\dot{\phi}_0^2}, \quad \Delta\phi_{\text{frag}} \simeq \frac{f\dot{\phi}_0^4}{2\pi\Lambda_b^8} \log \frac{32\pi^2 f^4}{\dot{\phi}_0^2}, \quad (\text{III.13})$$

where, for the typical relaxion parameters, we find $2/(3\pi) \log(\dots) \sim \mathcal{O}(10)$. Let us also define the quantities

$$t_{\text{nl}} = \frac{f\dot{\phi}_0^3}{\Lambda_b^8}, \quad \phi_{\text{nl}} = \frac{f\dot{\phi}_0^4}{\Lambda_b^8}, \quad (\text{III.14})$$

which control the time and the corresponding distance in field space it takes for the field to come to a complete stop after fluctuations become non-linear. At the non-linear level, we generalize the relations in Eq. (III.13) via the following parameterization

$$\Delta t_{\text{frag}}^{\text{nl}} = \delta t_{\text{amp}} + t_{\text{nl}} \cdot z_t, \quad (\text{III.15})$$

and

$$\Delta\phi_{\text{frag}}^{\text{nl}} = \dot{\phi}_0 \delta t_{\text{amp}} + \phi_{\text{nl}} \cdot z_\phi. \quad (\text{III.16})$$

We show in Fig. III.1 the evolution of $\dot{\phi}(t)$ (top) and $\phi(t)$ (bottom) for different choices of the initial velocity and of the potential parameters. It can be seen that after the short time δt_{amp} in which the axion evolves with an almost constant velocity, the field slows down and stops in a time given in Eq. (III.15) with

$$z_t \approx 2.3, \quad (\text{III.17})$$

for $10m \leq f \leq 10^{10}m$ and $5mf \leq \dot{\phi}_0 \leq 20mf$. Analogously, in the bottom panel we see that

$$z_\phi \approx 1.5. \quad (\text{III.18})$$

These values are shorter by a factor of $\mathcal{O}(10)$ than the ones obtained in the linear analysis. The reason for this enhanced efficiency found in the lattice analysis is mainly due to the NLO correction that will be discussed in detail in Sec. III.4. This difference has a minor impact on the analysis of the relaxion parameter space of Ref. [44] (in which an order of magnitude uncertainty is always assumed), as we will discuss more in Sec. III.6.3.

In Fig. III.2 we show the evolution of the axion field for different choices of the lattice parameters, which demonstrates the stability of our results.

If the fragmentation process takes place after inflation, one may expect the fluctuations to be enhanced during inflation compared to the Bunch-Davies spectrum and be frozen until they re-enter the horizon, with a nearly scale-invariant power spectrum. In Fig. III.3 we show the axion evolution in a run with an initially flat power spectrum, compared to one with the Bunch-Davies spectrum. We fix the normalization of the flat power spectrum in such a way that in the initial resonance band the power spectrum is enhanced with respect to the Bunch-Davies case by $(d\rho/d\log k)_{k_{\text{cr},0}} \approx x \times (d\rho_{BD}/d\log k)_{k_{\text{cr},0}}$, and we

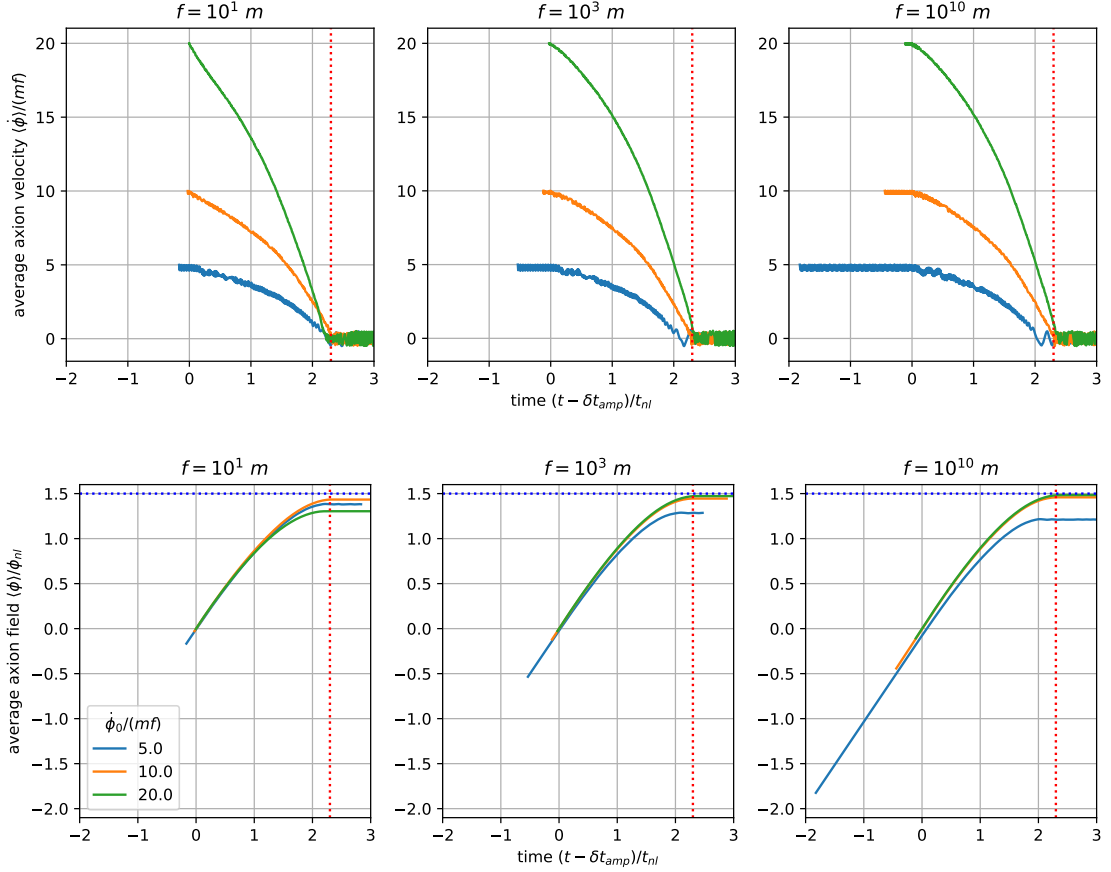


Figure III.1: Field evolution with slope $\mu = 0$ and no expansion for different initial velocities and decay constants f . All simulations were run with $N = 128^3$ lattice sides and length $L = 20/m$ along each side. Top: We clearly see how the stopping process consists of two parts i) a phase where the modes that are initially enhanced by parametric resonance grow from vacuum to an energy density $\rho \approx m^2 f^2$ in a time δt_{amp} and ii) a nonlinear part that lasts a time of $2.3 t_{\text{nl}}$ (marked by the red dotted line). Bottom: We see that in the non-linear regime the fields roll a distance $\approx \phi_{\text{nl}} \cdot 1.5$ (blue dashed line), in the limit of large f and $\dot{\phi}_0$.

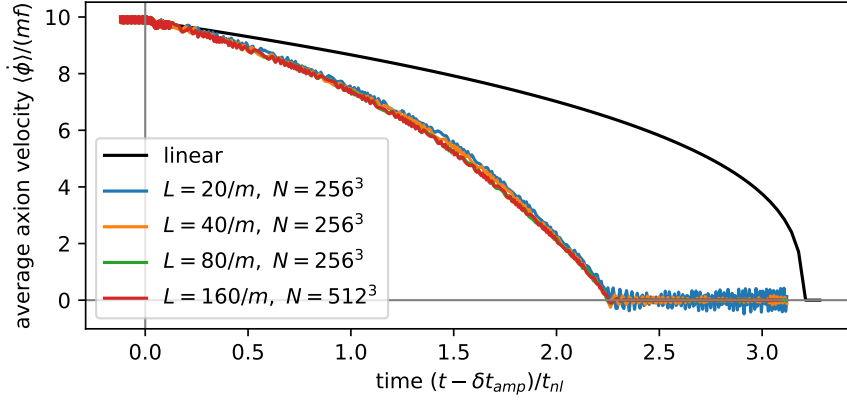


Figure III.2: Average axion velocity for $f = 10^3 m$, $\mu = 0$, and no expansion as obtained from linear analysis (Eq. (III.9)) and from different realizations of the lattice.

take $x = 10^8$ in Fig. III.3. As it can be seen from the figure, the only difference in this case is in the duration of the amplification time δt_{amp} , which now lasts

$$\delta t_{\text{amp}} \rightarrow \delta t_{\text{amp}}^{\text{mod}} \equiv \frac{f \dot{\phi}}{\Lambda_b^4} \log \left(x \times \frac{16 f^4}{\dot{\phi}^2} \right), \quad (\text{III.19})$$

as one would expect. The duration of the non-linear phase $t_{\text{nl}} z_t$ is instead independent of the initial power spectrum. We expect this behavior to not depend on the choice of the power spectrum, but only on the normalization of the initial instability band. This is due to the dominance of induced secondary fluctuations, as will be discussed below in Sec. III.4.

The last quantity that we want to compute on the lattice is the maximal slope of the potential μ_{max} , which is defined from Eq. (III.12) with $H = 0$:

$$\mu^3 < \mu_{\text{max}}^3 \equiv \frac{\pi \Lambda_b^8}{2 f \dot{\phi}_0^2} \left(W_0 \left(\frac{32 \pi^2 f^4}{e \dot{\phi}_0^2} \right) \right)^{-1}. \quad (\text{III.20})$$

For $\mu > \mu_{\text{max}}$, fragmentation is not efficient enough to contrast the acceleration induced by the potential slope. Fig. III.4 shows the evolution of the zero mode for μ around μ_{max} , for different values of f and of the initial velocity. It can be seen that the maximal value of μ for which the field stops respects Eq. (III.20) with a percent accuracy.

In the closing of this section, let us briefly comment on the effect of the Hubble friction. Contrary to the slope term, the Hubble friction acts to slow down the rolling of ϕ . When the Hubble friction is the dominant source of the friction, the fluctuation in ϕ remains small enough to use the linear analysis shown in [43]. In this regime, the two sources of the friction can be written as

$$\left(\frac{d\rho}{dt} \right)_{\text{frag}} = - \frac{\dot{\phi}^3 |\ddot{\phi} + H \dot{\phi}|}{32 \pi^2 f^4} \exp \left(\frac{\pi \Lambda_b^8}{2 f \dot{\phi}^2 |\ddot{\phi} + H \dot{\phi}|} \right), \quad (\text{III.21})$$

$$\left(\frac{d\rho}{dt} \right)_{\text{Hubble}} = -3H \dot{\phi}^2. \quad (\text{III.22})$$

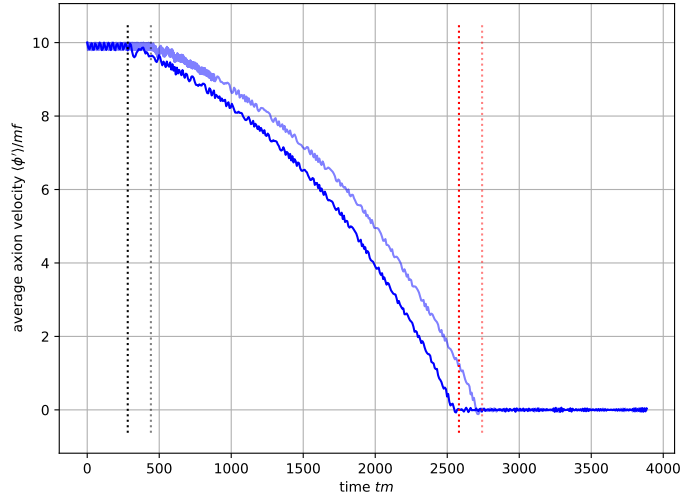


Figure III.3: Evolution of the axion field with $\mu = 0$, $f = 10^{10}m$, $\dot{\phi}_0 = 10mf$, and no expansion for different initial energy spectra. The dark colors correspond to a flat initial energy spectrum (as expected if fluctuations are enhanced during inflation) where the energy in the initial resonance band is enhanced by a factor $d\rho/d\log k(k_{cr,0}) \approx 10^8 d\rho_{BD}/d\log k(k_{cr,0})$ as compared to the Bunch-Davies vacuum (light colors). The gray and black dashed lines mark δt_{amp} and $\delta t_{\text{amp}}^{\text{mod}}$, respectively (see Eq. (III.19)), while the thin and thick red dashed lines correspond to $\delta t_{\text{amp}} + z_t t_{\text{nl}}$ and $\delta t_{\text{amp}}^{\text{mod}} + z_t t_{\text{nl}}$. Both simulations were run with $N = 256^3$ lattice sides and length $L = 80/m$ along each side.

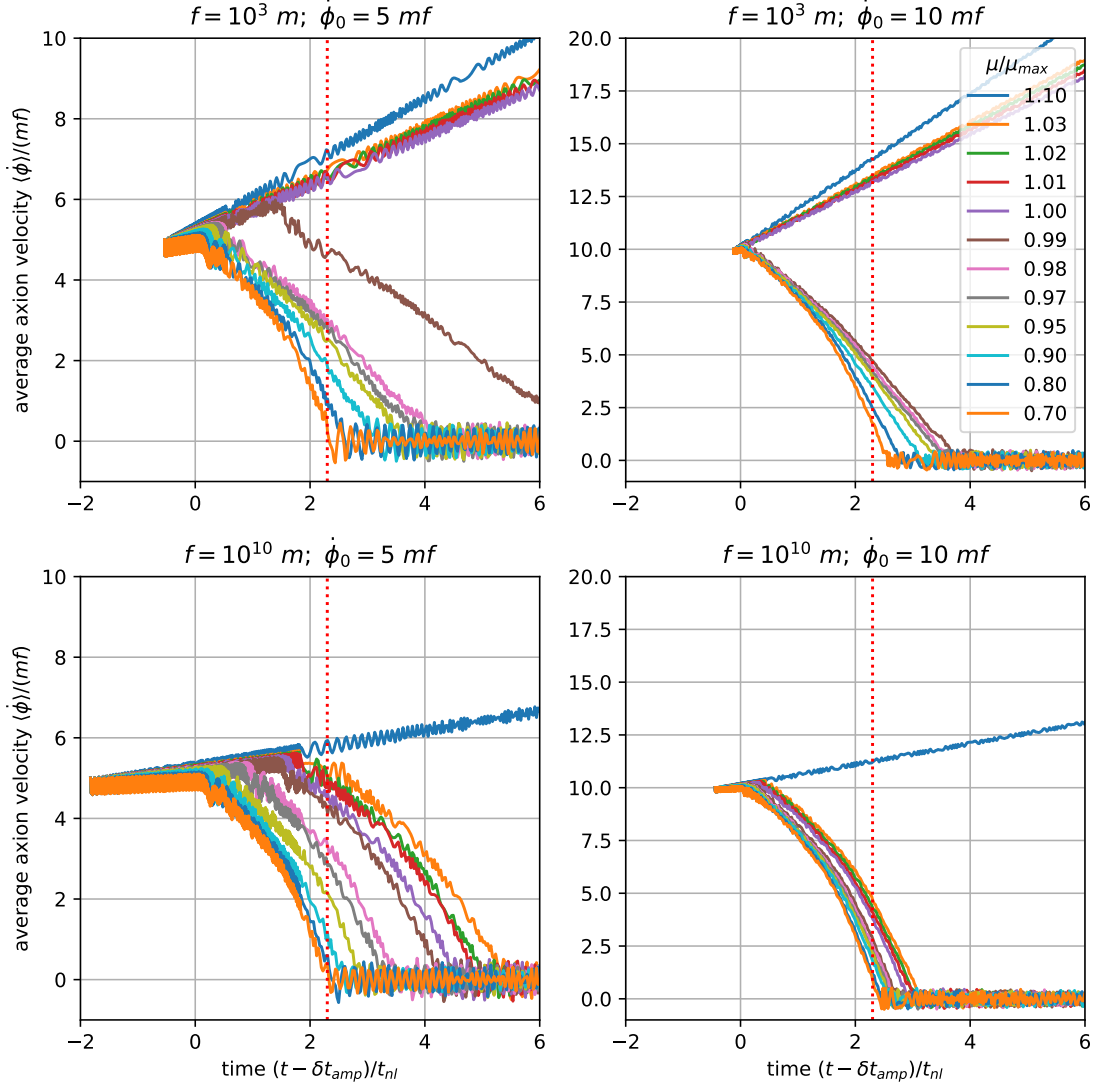


Figure III.4: Average axion velocity varying the slope in the range $0.70 < \mu/\mu_{max} < 1.10$, for $f/m = 10^3$ (top) and 10^{10} (bottom), and $\dot{\phi}_0 = 5mf$ (left) and $10mf$ (right). The red dotted line is at $(t - \delta t_{amp})/t_{nl} = 2.3$.

For the derivation of Eq. (III.21), see Ref. [43]. As long as $|(d\rho/dt)_{\text{frag}}| \ll |(d\rho/dt)_{\text{Hubble}}|$, the fragmentation effect is not important and the time evolution of the zero mode is described by the equation of motion $\ddot{\phi} + 3H\dot{\phi} - \mu^3 - (\Lambda_b^4/f) \sin(\phi/f) = 0$. The fragmentation effect becomes important when $|(d\rho/dt)_{\text{frag}}| \gtrsim |(d\rho/dt)_{\text{Hubble}}|$, which occurs for

$$H \lesssim \mathcal{O}(1) \times \frac{\pi\Lambda_b^8}{f\dot{\phi}^3} \log \frac{32\pi^2 f^4}{\dot{\phi}^2}. \quad (\text{III.23})$$

Here, we assumed $\mu^3 \lesssim \mathcal{O}(1) \times H\dot{\phi}$ otherwise Eq. (III.12) is not satisfied and ϕ keeps rolling. Once this condition is satisfied, $(d\rho/dt)_{\text{frag}}$ quickly dominates over $(d\rho/dt)_{\text{Hubble}}$ because of the exponential factor. Thus, we conclude that Hubble friction is not important once the fragmentation starts, but it controls *when* this happens. For an ALP rolling down its potential, fragmentation starts after H drops below the RHS of Eq. (III.23). In the case of the relaxion, fragmentation starts as soon as the barriers appear, if Eq. (III.23) is satisfied. This justifies our choice of not including cosmic expansion in our lattice simulations.

III.4 Secondary fluctuations

Secondary fluctuations will be sourced as higher order terms in the potential become important once the initial fluctuations in the resonance band have grown. While our lattice analysis takes these effects into account to all orders, we here first outline the approach of calculating them to second order analytically and afterwards compare to the lattice.

To capture the secondary fluctuations, we extend the linear ansatz from Eq. (III.2) by a second order term

$$\phi(x, t) = \phi(t) + \delta\phi(x, t) + \delta^{(2)}\phi(x, t). \quad (\text{III.24})$$

The second order fluctuations $\delta^{(2)}\phi$ are of $\mathcal{O}(\delta\phi^2)$ and initially zero. Plugging this ansatz into the full equation of motion, going to Fourier space, and separating the $\mathcal{O}(\delta\phi^0)$ and $\mathcal{O}(\delta\phi^1)$ pieces we find Eq. (III.4) and also an equation for the $\mathcal{O}(\delta\phi^2)$ terms in the limit of vanishing expansion

$$\delta^{(2)}\ddot{\phi}_k + (k^2 + V''(\phi)) \delta^{(2)}\phi_k = -\frac{1}{2}V'''(\phi) \int \frac{d^3p}{(2\pi)^3} \delta\phi_p \delta\phi_{k-p} =: S_k, \quad (\text{III.25})$$

which is just the equation of a sourced harmonic oscillator. The particle physics interpretation of this result is, that higher order terms in the potential cause scattering of two axions in the excited modes p and $k-p$ into an axion with momentum k .

In order to find an approximate solution to the equation above, we start by noting that the V'' term on the left averages to zero and is therefore only relevant for the modes in the resonance band as long as the axion is rolling. These modes are dominated by the first order perturbations anyhow and we therefore drop the V'' from now on. The equation can then be formally solved to give

$$\delta^{(2)}\phi_k(t) = \int_{t_i}^t dt' \frac{\sin(k(t-t'))}{k} S_k(t'), \quad (\text{III.26})$$

with $t_i \rightarrow -\infty$. The energy density in these modes is given as

$$\langle \rho(x, t) \rangle = \left\langle \frac{1}{2} (\delta^{(2)}\dot{\phi})^2 + (\nabla \delta^{(2)}\phi)^2 \right\rangle \quad (\text{III.27})$$

$$= \frac{1}{2} \int \frac{d^3 k}{(2\pi)^3} \frac{d^3 k'}{(2\pi)^3} e^{-i(\mathbf{k}+\mathbf{k}')\cdot\mathbf{x}} \langle \delta^{(2)} \dot{\phi}_{\mathbf{k}} \delta^{(2)} \dot{\phi}_{\mathbf{k}'} + \mathbf{k} \cdot \mathbf{k}' \delta^{(2)} \phi_{\mathbf{k}} \delta^{(2)} \phi_{\mathbf{k}'} \rangle \quad (\text{III.28})$$

where $\langle \dots \rangle = \langle 0 | \dots | 0 \rangle$. By plugging Eq. (III.26) into (III.27) one obtains

$$\frac{d\rho}{d \log k} = \frac{k^3}{4\pi^2} \int_{t_i}^t dt' dt'' \cos(k(t' - t'')) S^2(k, t', t''), \quad (\text{III.29})$$

where we defined the unequal time correlator (UTC) $S^2(k, t', t'')$ as

$$\langle 0 | S_{\mathbf{k}}(t') S_{-\mathbf{k}'}^*(t'') | 0 \rangle = (2\pi)^3 \delta^{(3)}(\mathbf{k} + \mathbf{k}') S^2(k, t', t''). \quad (\text{III.30})$$

When the axion rolls with a constant velocity $\dot{\phi}_0 = 2fk_{cr}$ the source reads

$$S_{\mathbf{k}}(t) = -\frac{\Lambda_b^4}{f^3} \sin(2k_{cr}t) \int \frac{d^3 p}{(2\pi)^3} \delta\phi_p \delta\phi_{\mathbf{k}-p}. \quad (\text{III.31})$$

In the following we are going to consider the case in which the fluctuations in the resonance band are initially in Bunch-Davies vacuum $\delta\phi_{\mathbf{k}}(t) = a_{\mathbf{k}} u_{\mathbf{k}}(t) + a_{-\mathbf{k}} u_{-\mathbf{k}}^\dagger$ with the mode functions $u_{\mathbf{k}}(t)$ given by Eq. (III.6) for concreteness. When calculating the vacuum expectation value it turns out that only the following combination contributes for finite momenta $k = k' \neq 0$

$$\langle 0 | a_p a_{k-p} a_p^\dagger a_{k-p}^\dagger | 0 \rangle = (2\pi)^6 [\delta^{(3)}(k - p - p') + \delta^{(3)}(p - p')] \delta^{(3)}(k - k') \quad (\text{III.32})$$

and we find for the UTC

$$S^2(k, t', t'') = \frac{\Lambda_b^8}{f^6} \sin(2k_{cr}t') \sin(2k_{cr}t'') \int \frac{d^3 p}{(2\pi)^3} 2 u_p(t') u_{k-p}(t') u_p^*(t'') u_{k-p}^*(t''). \quad (\text{III.33})$$

Since the mode functions only depend on the absolute momentum, we evaluate the momentum integral choosing $|\mathbf{p}|$ and $|\mathbf{k} - \mathbf{p}|$ as our integration variables, together with a trivial angular integration, since the problem is invariant under rotations around \mathbf{k}

$$\int \frac{d^3 p}{(2\pi)^3} = \frac{1}{(2\pi)^2} \int_0^\infty dp \int_{|k-p|}^{k+p} dq \frac{pq}{k}. \quad (\text{III.34})$$

The mode functions given in Eq. (III.6) are sharply peaked around $k = k_{cr}$ and can be approximated as Gaussian in the peak region

$$u_{\mathbf{k}}(t) \approx \frac{1}{\sqrt{2k_{cr}}} \exp\left(\delta k_{cr}t - \frac{(k - k_{cr})^2}{2\delta k_{cr}} t\right) \sin\left(k_{cr}t + \frac{\pi}{4}\right). \quad (\text{III.35})$$

For $k > \sqrt{\delta k_{cr}/(t' + t'')}$ the Gaussian peak lies fully within the momentum integration then and we find

$$S^2(k, t', t'') = \frac{1}{4\pi} \frac{\Lambda_b^8}{f^6} \frac{\delta k_{cr}}{k(t' + t'')} \left[\exp\left(2\delta k_{cr}t'\right) \left(\frac{1}{4} + \frac{1}{2} \sin(2k_{cr}t') - \frac{1}{4} \cos(4k_{cr}t')\right) \right] \cdot \left[t' \rightarrow t'' \right]. \quad (\text{III.36})$$

When we plug this expression back into the equation for the energy density (Eq. (III.29)), all we are left with are the two time integrals. Due to the time-dependent exponential, the integral is dominated by the region $t', t'' \approx t$. We therefore replace $t' + t''$ in the numerator

above by $2t$ and expand $\cos(k(t' - t''))$, which allows us to factorize the two integrals. The integration can be then done explicitly. After dropping all oscillating terms, which have frequencies $2nk_{cr}$, with $n = 1, \dots, 4$, we arrive at

$$\begin{aligned} \frac{d\rho^{(2)}}{d\log k} \approx & \frac{k^2 \delta k_{cr}}{2^9 \pi^3} \frac{\Lambda_b^8}{f^6} \frac{1}{t} \exp\left(4\delta k_{cr} t\right) \theta(2k_{cr} - k) \left[\frac{1}{k^2 + 4\delta k_{cr}^2} + \frac{1}{(k - 2k_{cr})^2 + 4\delta k_{cr}^2} \right. \\ & \left. + \frac{1}{(k + 2k_{cr})^2 + 4\delta k_{cr}^2} + \frac{1}{4} \frac{1}{(k - 4k_{cr})^2 + 4\delta k_{cr}^2} + \frac{1}{4} \frac{1}{(k + 4k_{cr})^2 + 4\delta k_{cr}^2} \right]. \end{aligned} \quad (\text{III.37})$$

In the case of a narrow resonance defined by $\delta k_{cr}/k_{cr} \ll 1$, the first and second term in the square brackets of Eq. (III.37) correspond to secondary resonances at $k = 0$ and $k = 2k_{cr}$. Notice that Eq. (III.37) does not predict any resonance at $k = 4k_{cr}$, due to the finite k range encoded in the θ function. The non-resonant terms are sizeable away from the resonance though, and we included them for completeness.

The first two dominating contributions predict a flat spectrum at low momenta $2\delta k_{cr} \lesssim k \lesssim 2k_{cr}$, and a secondary peak at $k = 2k_{cr}$ corresponding to collinear scattering processes. This expectation is indeed confirmed in Fig. III.5, where we show the axion spectrum as obtained on the lattice for different times. Initially, the axion is taken to be in the Bunch-Davies vacuum shown in black at the bottom of the plot. On the right side of the plot we show a close up of the resonance band around k_{cr} . The exponential growth of the modes in the resonance band with time up to $t \approx t_{\text{amp}}$ is clearly visible as expected from the analytical result Eq. (III.6) (shown in red for comparison). Around $t = 0.7 t_{\text{amp}}$, the energy in the modes with $k < 2k_{cr}$ starts growing at approximately twice the rate of the modes in the resonance band. These are the secondary fluctuations that arise as axions in the resonance band scatter in $2 \rightarrow 1$ processes. The analytic estimate of this effect in Eq. (III.37), shown in orange, predicts the order of magnitude as well as the main features of the spectrum accurately. As t approaches t_{amp} , the energy in higher momentum modes is amplified as well. The secondary peak at $k = 2k_{cr}$ predicted by Eq. (III.37) is clearly visible, as well as the primary one at $k = k_{cr}$. We believe that the additional peaks at higher momenta are due to higher order effects that eventually lead to the breakdown of perturbation theory.

Perturbation theory fully breaks down at t_{amp} when the axion zero mode slows down and the resonance band moves to smaller momenta. The new starting point for the amplification of the modes in the resonance band is not the initial spectrum anymore, but the sum of the initial spectrum and the secondary fluctuations. The time it takes for the energy in the modes to grow sufficiently to slow down the axion zero mode is therefore reduced and the axion stops faster, as we observed in Sec. III.3. This also explains why the stopping process becomes independent of the initial spectrum after t_{amp} : if the initial perturbations are smaller than the induced secondary ones, they are simply negligible after this point.

In Fig. III.6 we show the further evolution of the spectrum. Again it is useful to come up with an expectation in the linear picture to be able to compare to the lattice and understand the effect of higher order processes. In the linear analysis, we can derive a simple analytic formula for the energy spectrum $d\rho/d\log k$. As the axion loses its kinetic energy, the resonance band sweeps from its initial position $k_{cr} = \dot{\phi}_0/2f$ to $k_{cr} = m$, when the axion gets trapped in the wiggles. Assuming the axion deposits its energy only into the resonance band, energy conservation tells us that $\int_{\dot{\phi}_0/2f}^{\dot{\phi}_0/2f} dk d\rho/dk = \dot{\phi}_0^2/2 - \dot{\phi}^2/2$. Then, we obtain [43]

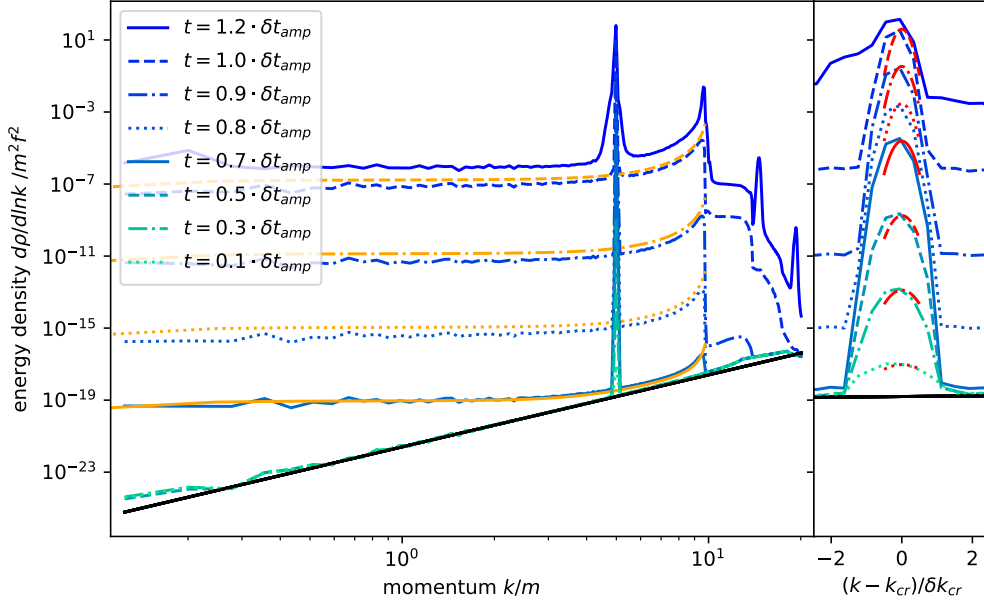


Figure III.5: Early evolution of the axion energy spectrum for $f/m = 10^{10}$, $\dot{\phi}_0 = 10mf$. The blue shaded lines show the spectrum as obtained from a lattice with $N = 512^3$ sites and side length $L = 40/m$. The bottom black line is the analytic expression for the initial Bunch Davies vacuum $\propto k^4$ and the orange lines give the analytic NLO estimate Eq. (III.37) for $t = 0.7 - 1.0 \cdot t_{\text{amp}}$. On the right we magnified the region around the peak $k_{\text{cr}} = 5m$ and show for comparison the analytic LO estimate Eq. (III.6) for $t = 0.1 - 1.0 \cdot t_{\text{amp}}$ in red.

$$\frac{d\rho}{d \log k} = 4f^2 k^2 \quad \text{for} \quad m < k < \frac{\dot{\phi}_0}{2f}. \quad (\text{III.38})$$

This estimation from the linear analysis is shown as the solid black line in Fig. III.6. We see that as the axion slows down, the spectrum is well matched by this estimate for modes with momenta bigger than the current critical momentum. We notice that the simulated spectrum is an $\mathcal{O}(1)$ factor smaller than the estimate. This can be easily understood, since higher order processes keep shuffling the energy into high momentum modes. The spectrum resulting from these processes is clearly visible for modes with $k > \dot{\phi}_0/(2f)$. Once the axion has stopped at $\Delta t_{\text{frag}}^{\text{nl}}$, there is no further energy injected into the axion inhomogeneities. The scattering processes however remain active and result in the peak of the spectrum moving to higher momenta. Such an energy cascade into modes with higher momenta can be understood as the early state of the thermalization [75–77].

III.5 Formation of bubbles

A very important point that needs to be discussed is the possibility that the axion field populates multiple minima in spatially separated regions. If the fragmentation process takes place during inflation, these multiple minima would not be observable as the corresponding regions are stretched by the exponential expansion, and thus in the currently

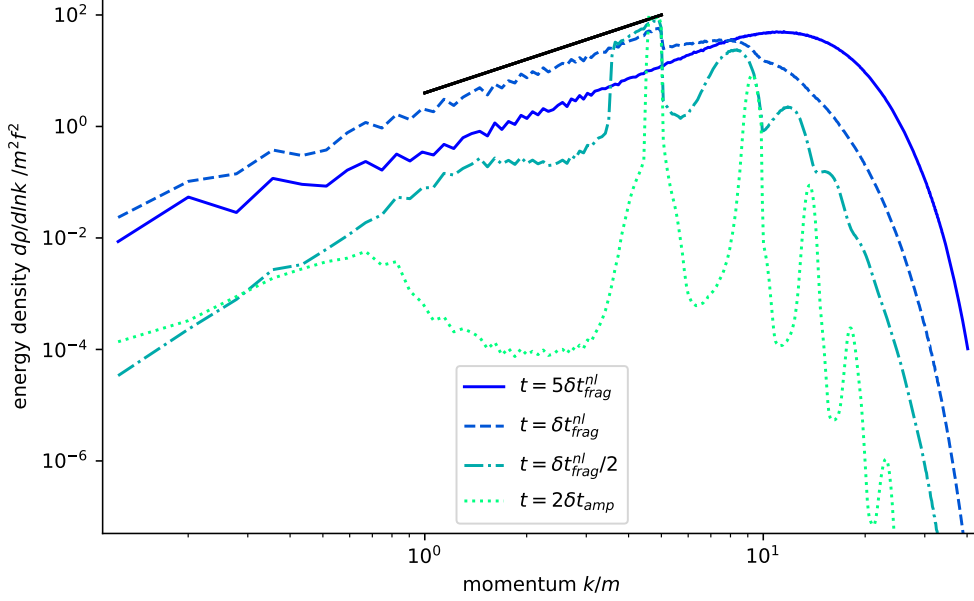


Figure III.6: Evolution of the axion energy spectrum past δt_{amp} for $f/m = 10^{10}$, $\dot{\phi}_0 = 10mf$. The blue shaded lines show the spectrum as obtained from the same lattice as in Fig. III.5. The black line shows the spectrum from the linear analysis given in Eq. (III.38).

visible Universe the vacuum would be unique (unless fragmentation takes place during the last $\mathcal{O}(60)$ e-folds of inflation, in which case the discussion below applies). On the other hand, if fragmentation takes place after inflation, multiple minima can be populated within one Hubble patch. This scenario has multiple consequences, which we list here:

- First of all, if multiple minima are populated, we expect a bubble wall structure to develop. Even if the dynamics is such that the field quickly relaxes to one single minimum within a Hubble volume, the selected minimum need not be the same in different Hubble patches. Hence, as the horizon grows and previously separated patches enter into causal contact, we expect at least one domain wall with an area $\sim H^{-2}$ to be present at any given time in the visible Universe. Depending on its energy, this may be problematic as it could lead to overclosure. This is indeed the case for the self-stopping relaxation, see Sec. III.6.1.
- Secondly, due to the overall slope of the potential $-\mu^3$, different vacua have different vacuum energies. If the energy difference is small, this could lead to an inhomogeneous cosmological constant (CC). If instead the energy difference is large, this would worsen the CC problem in that a fine tuning would be required for the different vacua to average at the correct value.
- Finally, in the case of the relaxation, large spatial inhomogeneities of the field ϕ would lead to an inhomogeneous value of the Higgs VEV. We mention this here for completeness, but we do not expect it to be problematic as the differences in the electroweak VEV would be tiny by construction.

Even though the above possibilities are interesting by themselves, and may be viable depending on the parameters of the model, we will here assume that they do not occur,

and compute the necessary conditions to avoid them. In particular, inhomogeneities may be created on three different length scales, which need to be analyzed separately.

III.5.1 Fluctuations on super-Hubble scales

If the axion is light compared to the Hubble scale during inflation, then it will be excited with a nearly scale invariant spectrum. Due to these fluctuations, we expect patches of the universe with different initial values of the axion field, meaning the axion velocity will also differ at the point when the wiggles in the axion potential appear and fragmentation stops the field shortly after. As we can see from Eq. (III.16), different initial velocities result in the fragmentation process stopping the field at different positions. If these differences are larger than the fundamental period $2\pi f$, this leads to the field stopping in different minima and therefore the existence of superhorizon bubbles. Even if dynamics eventually smooth the field value across the Hubble volume, as the horizon grows more regions in which the field has settled in different minima will enter into causal contact. Therefore, we expect to have multiple minima populated at any time within the visible Universe.

We expect inflation at a scale H_I to result in approximately scale-invariant fluctuations with amplitude $\delta\phi \sim H_I/(2\pi)$ in the field before the scanning process begins. If the height of the barriers does not depend on ϕ (as e.g. for generic ALPs), $H_I \lesssim 2\pi f$ should be imposed to avoid domain wall formation. On the other hand, if the height of the barriers does depend on ϕ (as in the original Graham-Kaplan-Rajendran (GKR) relaxion model Section II.1), the constraint on H_I is relaxed because the fragmentation starts only when ϕ reaches the critical point where the Higgs VEV becomes non-zero and the barriers appear, leading to a reduction in the fluctuations in ϕ .

To get to this result, one has to discuss the evolution of perturbations in the relaxion field prior to the fragmentation. We start with the case in which the relaxation takes place after inflation and only comprises a subdominant fraction of the total energy density. For simplicity we assume that the universe is filled with a fluid with constant equation of state parameter $w > -1$. In this case one can choose the time coordinate such that the Hubble is given as

$$H(t) = \left(\frac{3}{2}(1+w)t \right)^{-1}. \quad (\text{III.39})$$

The relaxion's zero-mode equation of motion in an expanding universe is

$$\ddot{\phi} + 3H\dot{\phi} + V'(\phi) = 0. \quad (\text{III.40})$$

While the relaxion scans the Higgs mass we have $V' = -\mu^3$. We are going to assume that around $\phi = 0$ the correct Higgs mass is reached, wiggles in the potential appear and the relaxion stops shortly after. The solution to the relaxion's equation of motion is then given as

$$\phi(t) = -\Delta\phi_{\text{scan}} + \frac{\mu^3}{2} \frac{1+w}{3+w} t^2 = -\Delta\phi_{\text{scan}} + \frac{\mu^3}{H^2(t)} \frac{2}{9(1+w)(3+w)} \quad (\text{III.41})$$

$$\dot{\phi}(t) = \mu^3 \frac{1+w}{3+w} t = \frac{\mu^3}{H(t)} \frac{2}{3(3+w)} \quad (\text{III.42})$$

where $\Delta\phi_{\text{scan}}$ is the distance the relaxion has to traverse in order to scan the Higgs mass. The Hubble when fragmentation takes place and the initial velocity are then given by

$$H_0 = \sqrt{\frac{2}{9(1+w)(3+w)} \frac{\mu^3}{\Delta\phi_{\text{scan}}}} \quad (\text{III.43})$$

$$\dot{\phi}_0 = \sqrt{\frac{2(1+w)}{(3+w)}} \mu^3 \Delta\phi_{\text{scan}}. \quad (\text{III.44})$$

One can easily check that for $\Delta\phi_{\text{scan}} \lesssim m_{\text{Pl}}$ the relaxion's contribution to the total energy density is indeed subdominant.

To see the effect of isocurvature fluctuations, let us now take the separate universe approach [78] and consider a patch, where the distance the field has to roll is modified by a fluctuation $\Delta\phi_{\text{scan}} \rightarrow \Delta\phi_{\text{scan}} + \delta\phi$. In this patch the scanning process takes longer because the field has to traverse a bigger distance, which will lead to a smaller Hubble when $\phi = 0$ as well as a bigger velocity.

$$\delta H_0 = -H_0 \frac{\delta\phi}{2\Delta\phi_{\text{scan}}} \quad (\text{III.45})$$

$$\delta\dot{\phi}_0 = \dot{\phi}_0 \frac{\delta\phi}{2\Delta\phi_{\text{scan}}} \quad (\text{III.46})$$

Once fragmentation starts, Hubble friction is negligible and the relaxion stops in a fraction of a Hubble time. The effect of the perturbation to the Hubble while fragmentation is active is therefore negligible. The difference in the initial velocity, however, leads to the field rolling further $\Delta\phi_{\text{frag}} \rightarrow \Delta\phi_{\text{frag}} + \delta\phi_{\text{frag}}$, as can be estimated using Eq. (III.16).

$$\delta\phi_{\text{frag}} \simeq 4\Delta\phi_{\text{frag}} \frac{\delta\dot{\phi}_0}{\dot{\phi}_0} = 2\Delta\phi_{\text{frag}} \frac{\delta\phi}{\Delta\phi_{\text{scan}}}, \quad (\text{III.47})$$

where we assumed that the field excursion during the initial amplification is negligible as is the case for the parameter space discussed in [44]. Using that the fluctuations on super-Horizon scales caused by inflation are given by $\delta\phi = H_I/(2\pi)$ and that the fluctuations after stopping should not exceed πf in order to avoid super-Horizon bubbles, we arrive at

$$H_I \lesssim \frac{\pi^2 \Lambda_b^8}{z_\phi \dot{\phi}_0^4} \Delta\phi_{\text{scan}}, \quad (\text{III.48})$$

in order to avoid superhorizon bubbles in this case. The bound in Eq. (III.48) is mild, especially when compared to the original GKR mechanism. As shown in Fig. III.11, H_I can be as large as 10^{16} GeV. In the original GKR relaxion mechanism instead, it can never exceed $\mathcal{O}(10^2)$ GeV and it is typically sub-GeV, or even as low as the meV range [44]. In the case where the axion dominates the total energy and drives inflation or at least a period thereof ($\Delta\phi_{\text{scan}} \gtrsim m_{\text{Pl}}$), this bound disappears since fluctuations in the axion become equivalent to adiabatic fluctuations rather than isocurvature ones.

III.5.2 Critical bubbles

It is useful at this point to take a closer look at the different infrared scales involved in our setup. Regarding the bubbles, we follow Ref. [79] to estimate the width of the bubble wall at rest by minimizing the surface tension, *i.e.*, the energy per unit wall area. While the surface tension arising from the field being displaced from the minimum of the potential grows for larger bubble widths, the tension due to the gradient of the field is reduced. With these considerations, one finds the following estimates for the wall width w and the surface tension σ

$$w \approx 5 m^{-1}, \quad \sigma \approx 10 m f^2. \quad (\text{III.49})$$

Notably, the scales where most of the energy is deposited are smaller than m^{-1} and therefore smaller than the width of a bubble wall. The dynamics of these fluctuations therefore do not resemble the ones of bubbles and we discuss their impact in the next section. Furthermore, one can calculate the critical radius R_{crit} a bubble needs to reach such that the pressure from the non-degeneracy of the vacua driving the expansion of the bubble overcomes the surface tension.

$$R_{\text{crit}} \approx \frac{mf}{\mu^3}. \quad (\text{III.50})$$

The question we would like to answer in this section is whether bubbles with radii bigger than R_{crit} are formed in the stopping process. Those bubbles would keep expanding and it is uncertain whether such a system would finally settle in one common minimum. Unfortunately, it is impossible to answer this question with lattice simulations alone for the following reason: When we choose $\dot{\phi}_0 = \mathcal{O}(10)mf$, such that the field is able to overcome the barriers initially, we need a lattice spacing $\Delta x \approx \mathcal{O}(10^{-2} - 10^{-1})m^{-1}$ in order to resolve the UV dynamics properly. Since current computing power only allow for simulations with $\mathcal{O}(10^3)$ lattice sites along each spatial direction, it is impossible to also include R_{crit} , which in general is much larger than m^{-1} even when choosing $\mu \approx \mu_{\text{max}}$ in Eq. (III.20). We therefore highlight below two observations that we can make on the lattice and extrapolate to argue why there are no expanding bubbles.

Our first observation is that when counting the number of bubbles exceeding a certain volume V_0 once the field has stopped rolling, we find that the number density of such bubbles is exponentially suppressed as one raises V_0 . This is shown in Fig. III.7. It becomes clear, however, that the details of this suppression are very complicated since they show a dependence on time as well as the parameters $\dot{\phi}_0$ and f . Additionally, especially for simulations with large initial velocities $\dot{\phi}_0$, the simulated box cannot be too large without compromising the resolution of the UV physics of fragmentation, resulting in poor statistics for very large bubbles. This being said, we note that the critical volume R_{crit}^3 is much larger than the volumes testable on the lattice and in the case of the relaxation where $\dot{\phi}_0 \gg mf$, we also have $R_{\text{crit}}^3 \gg m^{-3}$ such that we can expect the probability of an expanding bubble forming in the visible universe to be suppressed by a huge exponential factor.

The second argument, which holds for bubbles of slightly larger size, is based on the fact that in parts of space that are separated by more than the time of the first exponential amplification t_{amp} or even the full time it takes the axion to stop t_{frag} , the stopping processes are (partially) independent. They can be viewed as different instances of the same experiment, in which the observable is the rate of energy transfer to the field fluctuations or, equivalently, the minimum in which the field ends up.

If the field ends up in different minima in parts of space where the process takes place independently, we are left with bubbles at the end, as in the super-Hubble case. Such a situation can be avoided if the field average after fragmentation is the same at each instance of the quantum experiment. To check if this is the case, we ran 10 simulations with the same physical parameters $m, f, \dot{\phi}_0$ in boxes with increasing volume $V = L^3$. As Fig. III.8 shows, the spread of minima the field stops in $\sigma_{\phi, \text{frag}}$ reduces as the size of the box is increased. To check whether large, possibly expanding bubbles might exist after the field has stopped we need to extrapolate this result to infrared scales. To do so, we estimate the variance of the total field excursion $\Delta\phi_{\text{frag}}$. We assume that this is entirely due to the variance of t_{amp} and the corresponding field excursion $\dot{\phi}_0 t_{\text{amp}}$.

The time interval t_{amp} lasts until the instability band, whose position depends on the zero-mode velocity, moves to the IR by an amount equal to its initial width. This can be

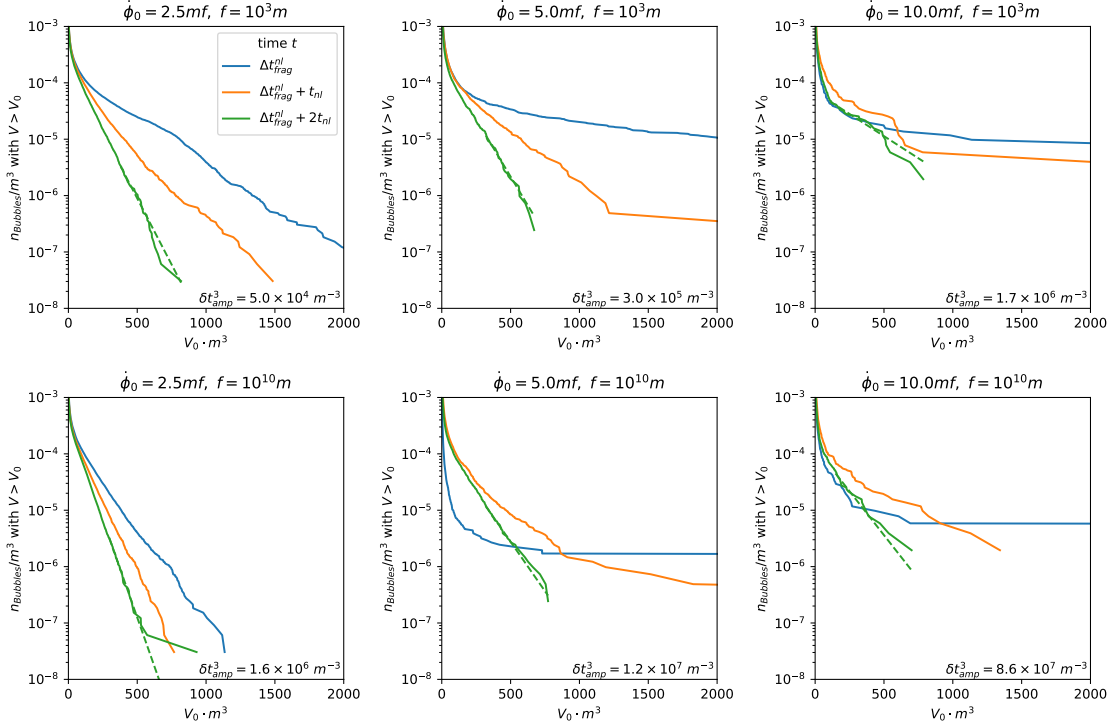


Figure III.7: Dependence of the number density of bubbles with a volume bigger than V_0 for different f and $\dot{\phi}_0$ at three different times. The dashed lines show the fit of an exponential decay $n(V_0) \propto \exp(-\Gamma V_0)$ to the last few data points for each time.

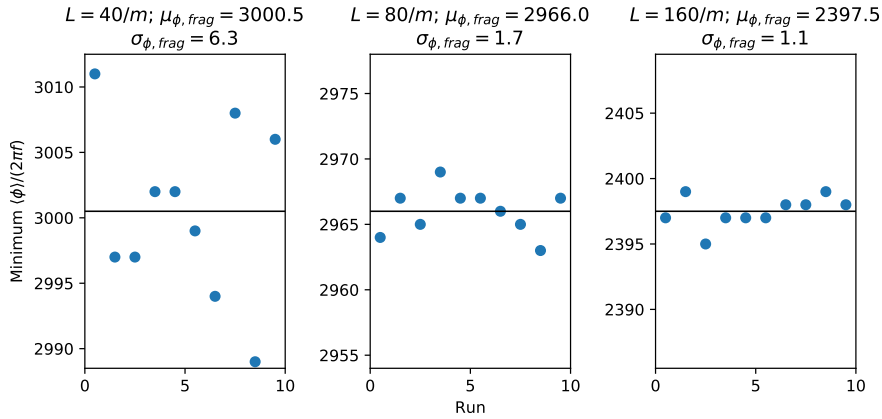


Figure III.8: Spread of the minima the field stops in for $f = 10^{10}m$ and $\dot{\phi}_0 = 10mf$ in different lattice configurations. The y -axis is centered around the average final minimum $\mu_{\phi,\text{frag}}$. Importantly, the spread of the minima $\sigma_{\phi,\text{frag}}$ decreases as the size of the box L is increased.

determined by using energy conservation, and depends on the initial energy of the modes within the instability band (see discussion around Eq. (III.19)). The latter quantity, which we denote by E_0 , is a quantum observable, the variance of which will determine the variance of t_{amp} . We find it reasonable to assume that the variance of Δt_{frag} , and correspondingly $\Delta \phi_{\text{frag}}$, can be entirely ascribed to the variance of t_{amp} , since after this point the process proceeds classically and its duration is fixed by the spectrum within the instability band at t_{amp} .

The time t_{amp} is determined as follows. The energy in the instability band increases as

$$\delta E = E_0 \exp(2\delta k_{\text{cr}} t_{\text{amp}}) - E_0 \approx E_0 \exp(2\delta k_{\text{cr}} t_{\text{amp}}) \quad (\text{III.51})$$

In this time interval, the instability band moves by $-2\delta k_{\text{cr}}$, thus the variation of the kinetic energy K is

$$\delta K = -\frac{dK}{dk_{\text{cr}}} 2\delta k_{\text{cr}} = 2\dot{\phi}_0^2 \frac{\delta k_{\text{cr}}}{k_{\text{cr}}} = 2\Lambda_b^4. \quad (\text{III.52})$$

Energy conservation implies

$$t_{\text{amp}} = \frac{1}{2\delta k_{\text{cr}}} \log\left(\frac{2\Lambda_b^4}{E_0}\right). \quad (\text{III.53})$$

Within this interval, the field evolves by an amount $t_{\text{amp}}\dot{\phi}_0$. Computing the variance, in the probabilistic sense, of t_{amp} is a complicated task. Here, we will limit ourselves to compute its variation assuming E_0 changes by one standard deviation σ_{E_0} :

$$\sigma_{t_{\text{amp}}} \approx \left| \frac{dt_{\text{amp}}}{dE_0} \right| \sigma_{E_0} = \frac{1}{2\delta k_{\text{cr}}} \frac{\sigma_{E_0}}{E_0}. \quad (\text{III.54})$$

Now we need to compute E_0 and σ_{E_0} . E_0 is the expectation value of the initial energy density, obtained recalling that in the Bunch-Davies vacuum $\text{E}[|u_k|^2] = 1/(2k)$

$$E_0 = \int \frac{d^3k}{(2\pi)^3} k^2 \text{E}[|u_k|^2] = \frac{4\pi k_{\text{cr}}^4 (2\delta k_{\text{cr}})}{(2\pi)^3} \text{E}[|u_k|^2] = \frac{k_{\text{cr}}^3 \delta k_{\text{cr}}}{2\pi^2} = \frac{1}{32\pi^2} \frac{\dot{\phi}_0^2 \Lambda_b^4}{f^4} \quad (\text{III.55})$$

To compute σ_{E_0} , we need to know the variance of u_k . u_k is gaussianly distributed, $\mathcal{P}(u_k) \propto \exp(-2k|u_k|^2)$. The modulus follows a Rayleigh distribution, $\mathcal{P}(|u_k|) = 4k|u_k| \exp(-2k|u_k|^2)$, thus

$$\text{E}[|u_k|^2] = 1/(2k) \quad (\text{III.56})$$

$$\text{Var}[|u_k|^2] = 1/(2k)^2 \quad (\text{III.57})$$

The process we are considering takes place in a finite time t_{amp} . In this time, points in space separated by more than $c \cdot t_{\text{amp}}$ can not interfere with each other, hence we can think of enclosing our problem in a box of size $L = c \cdot t_{\text{amp}}$. Momenta are thus discrete and given by

$$\mathbf{k} = \frac{2\pi}{L} \mathbf{i}, \quad (\text{III.58})$$

with $\mathbf{i} = (i_1, i_2, i_3)$, and $i_k \in \mathbb{Z}$. The number of modes inside the instability band $k_{\text{cr}} - \delta k_{\text{cr}} < k < k_{\text{cr}} + \delta k_{\text{cr}}$ is

$$N \approx \frac{4\pi k_{\text{cr}}^2 (2\delta k_{\text{cr}})}{(2\pi/L)^3}. \quad (\text{III.59})$$

Now we can compute the variance, assuming that all modes have the same momentum

and the same variance, which is valid for $2\pi/L \ll \delta k_{\text{cr}} \ll k_{\text{cr}}$:

$$\begin{aligned}
 \text{Var}[E_0] &= \text{Var} \left\{ \frac{1}{(2\pi)^3} \left(\frac{2\pi}{L} \right)^3 \sum k^2 |u_k|^2 \right\} \\
 &= \left[\frac{1}{L^3} k_{\text{cr}}^2 \right]^2 \text{Var} \left[\sum |u_{k_{\text{cr}}}|^2 \right] \\
 &= \left[\frac{1}{L^3} k_{\text{cr}}^2 \right]^2 N \text{Var} [|u_{k_{\text{cr}}}|^2] \\
 &= \frac{1}{4\pi^2 L^3} k_{\text{cr}}^4 \delta k_{\text{cr}}.
 \end{aligned} \tag{III.60}$$

The standard deviation σ_{E_0} is simply $(\text{Var}[E_0])^{1/2}$. Combining Eq. (III.60) with (III.54), we obtain

$$\frac{\sigma_{\phi, \text{frag}}}{2\pi f} = \frac{\dot{\phi}_0 \sigma_{t_{\text{amp}}}}{2\pi f} = \frac{\dot{\phi}_0}{4f L^{3/2} k_{\text{cr}} \delta k_{\text{cr}}^{3/2}}. \tag{III.61}$$

Finally, we can plug in $L = t_{\text{amp}}$:

$$\begin{aligned}
 \frac{\sigma_{\phi, \text{frag}}}{2\pi f} &= \frac{\dot{\phi}_0}{4f k_{\text{cr}} \delta k_{\text{cr}}^{3/2}} (2\delta k_{\text{cr}})^{3/2} \log \left(\frac{2\Lambda_b^4}{E_0} \right)^{-3/2} \\
 &= \frac{1}{2} \log \left(\frac{8\pi f^2}{\dot{\phi}_0} \right)^{-3/2}
 \end{aligned} \tag{III.62}$$

In the parameter space of the self-stopping relaxion, this quantity ranges between 0.01 and 0.001 for $\dot{\phi}_0 = \Lambda^2 = (10^5)^2 \text{ GeV}^2$ and f up to 10^{10} GeV .

Checking Eq. (III.62) on the lattice is not easy, because the lattice size is typically smaller than $c \cdot t_{\text{amp}}$. We can instead compare Eq. (III.61) for a smaller box, of size L , with an estimate of the same quantity obtained by running multiple lattice simulations and computing the standard deviation of $\Delta\phi_{\text{frag}}$. The result of such a comparison is shown in Fig. III.9. We can see that, for relatively small box sizes, the estimate of Eq. (III.61) underestimate the result by a factor of roughly 10, while the dependence on L is compatible with the one obtained from the lattice.

When taking the factor of 10 into account the spread of final field values relative to $2\pi f$ still only takes values between 0.1 and 0.01. This means that for a volume $(ct_{\text{amp}})^3$, different minima occur only at the 10 – 100 σ level. This number cannot be simply translated into a probability, because we do not know the probability distribution to such an accuracy. If it were Gaussian, the probability would be between 10^{-22} and 10^{-2200} . One of course would have to impose that this very rare occurrence does not happen in any of the small volumes that constitute our Universe. Not knowing the actual probability distribution, performing such a calculation is not illuminating, thus we content ourselves with imposing $\sigma_{\phi, \text{frag}}/(2\pi f) \ll 10$ in Eq. (III.62).

III.5.3 Small scale fluctuations

While the majority of the energy is dumped into fluctuations on scales $\leq m^{-1}$, these fluctuations are on scales too small to be thought of as bubbles, since they are smaller than the typical width of a bubble wall of $\mathcal{O}(m^{-1})$. They do however interfere with the previously discussed fluctuations on larger scales, in that they cause a spread of the field.

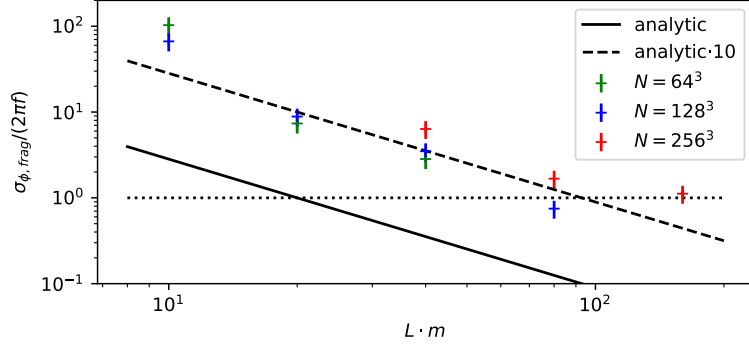


Figure III.9: Dependence of the spread in the final position of the zero-mode of the field $\sigma_{\phi, \text{frag}}$ on the length of the sides of the simulated box L . The different color crosses represent simulations with different numbers of lattice sites, all with $f = 10^{10}m$ and $\dot{\phi}_0 = 10mf$. The solid line corresponds to the analytic estimate of Eq. (III.61), which seems to underestimate the spread by $\mathcal{O}(10)$ but captures the decrease of the spread with increasing length L correctly.

If this spread is comparable or larger than one period of the axion potential $2\pi f$, the dynamics on large scales and of the mean field become less sensitive to the potential. We will argue below, however, that the spread in the axion field is always smaller than $2\pi f$ (although not by much) such that the expected corrections have only a minor influence on the discussion above.

We can estimate the spread of the field by using the analytic final energy spectrum in Eq. (III.38), which for relativistic modes $k > m$ results in the following power spectrum

$$P_\phi(k) = \frac{1}{k^2} \frac{d\rho}{d \log k} = 4f^2 \quad \text{for} \quad m < k < \frac{\dot{\phi}_0}{2f}. \quad (\text{III.63})$$

Integrating this spectrum, we find that the root-mean-square (RMS) of the axion field is given by

$$\delta\phi_{\text{rms}} = \sqrt{\langle \delta\phi^2 \rangle} = 2f \left(\log \frac{\dot{\phi}_0}{2mf} \right)^{1/2}, \quad (\text{III.64})$$

so the spread of the field is indeed comparable to the period of the potential, but very high initial velocities would be required for it to be bigger due to the square root and logarithmic dependence. In the specific case of the relaxion, we find the square root to be in the range $0.2 - 2$, implying that the fluctuations on this scale are indeed smaller than $2\pi f$.

In Fig. III.10, we show the evolution of $\delta\phi_{\text{rms}}$ as the field stops as computed by integration over the modes with $k > m$ in the axion power spectrum obtained from the lattice. We see that $\delta\phi_{\text{rms}}$ starts growing significantly around the time when the production of axion fluctuations starts to slow down the axion zero mode (around 0 with the chosen normalization of the x -axis) and reaches its maximum around the time when the axion stops and no more energy is transferred into axion fluctuations (red vertical line). We note that the maximal $\delta\phi_{\text{rms}}$ is smaller than the analytic estimate in Eq. (III.64) (given by the dotted horizontal lines), and that it further decreases after the axion has stopped rolling. Both of these effects can be attributed to the higher order effects discussed in Sec. III.4,

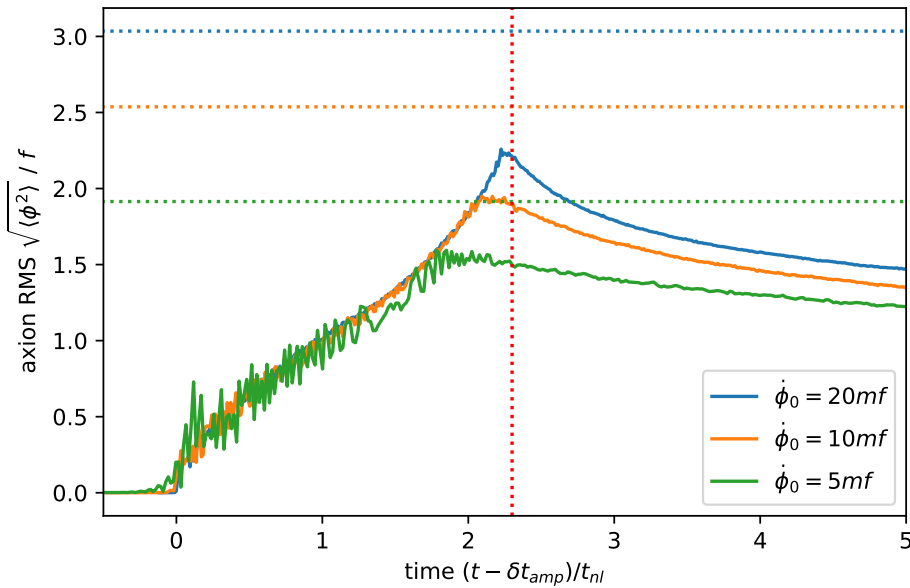


Figure III.10: Evolution of the axion RMS field value caused by modes with $k > m$ as computed by integration of the axion power spectrum obtained from a lattice computation with $N = 256^3$ lattice sites, $L = 40/m$, and $f = 10^{10}m$ (solid lines). The dotted horizontal lines show the analytic estimate from Eq. (III.64). The horizontal, dotted, red line marks the time around which the axion stops as estimated in Sec. III.3.

since the scattering of axions redistributes the energy into higher momentum modes in the non-linear regime. In the relativistic case, the energy density and the power spectrum are related by a factor k^2 , so this leads to a reduction in the integral over the power spectrum (which gives the mean square of the field), while the integral over the energy spectrum is conserved as it must be. In an expanding universe, one additionally has a depletion of the energy, so this effect would be pronounced even more.

Note that the amount by which the analytic result overestimates the peak of the numerical result grows with the initial velocity $\dot{\phi}_0$, signaling that the actual dependence of $\delta\phi_{\text{rms}}$ on the initial velocity is even weaker than predicted by the analytic estimate. We therefore conclude that the spread of the axion field is smaller than $2\pi f$ for a wide range of initial velocities, such that our previous considerations are not significantly affected by the small scale fluctuations.

III.6 Relaxion considerations

In this section, we discuss implications from our lattice results to the relaxion mechanism.

III.6.1 Relaxion bubbles

One of the most interesting features of fragmentation as a stopping mechanism is that the relaxion mechanism does not need strong Hubble friction and therefore the relaxation phase does not need to take place during inflation [44]. The main advantage of a post-inflationary relaxation phase is that some of the issues which are typically associated with the embedding of the relaxion into inflation disappear. In particular, the number of e-folds

does not need to be exceedingly large, but can as well be $\mathcal{O}(10 - 100)$, and the Hubble rate during inflation can be much larger, being only constrained by Eq. (III.48).

However, when relaxation takes place after inflation, there is the possibility of forming relaxion bubbles, *i.e.*, spatially separated patches in which the relaxion field ends up in different minima as discussed in Sec. III.5. The existence of such bubbles would have the following consequences: First, since the Higgs VEV depends on the relaxion field, the EW scale would have slightly different values in each of these regions. This does not seem problematic since a variation in ϕ of size $\Delta\phi \sim 2\pi f$ corresponds to a tiny difference in v_H by construction of the relaxion mechanism. There is however an apparent problem tied to the fact that the difference in potential energy from one minimum of the relaxion potential to the next, namely $2\pi fg\Lambda^3$, is much larger than the measured value of the cosmological constant $\mathcal{O}(10^{-47}) \text{ GeV}^4$. Therefore, even if one assumes that the average value of the CC matches the observed one, the CC would be unacceptably inhomogeneous. We therefore assume that such bubbles do not form, under the criteria derived in Sec. III.5. In addition, the scenario discussed in Sec. III.5 would result in the presence of at least one domain wall of area H^{-2} at any time. The energy density of such an object (given the relaxion parameters) would overclose the universe, which is another reason to impose Eq. (III.48).

III.6.2 Higgs fluctuations

The full potential in the case where ϕ is identified as the relaxion field necessarily includes couplings to the Higgs in order to scan the Higgs mass as well as trigger barriers when the Higgs acquires a non-zero VEV. The required potential can be written as

$$V(\phi, h) = \Lambda^4 - g\Lambda^3\phi + \frac{1}{2}(\Lambda^2 - g'\Lambda\phi)h^2 + \frac{\lambda}{4}h^4 + \Lambda_b^4 \frac{h^2}{v_{\text{EW}}^2} \cos \frac{\phi}{f}. \quad (\text{III.65})$$

As the relaxion rolls over many fundamental periods, the effective Higgs mass

$$\frac{\partial^2 V}{\partial h^2} = \Lambda^2 - g'\Lambda\phi + 3\lambda\langle h^2 \rangle + 2 \left(\frac{\Lambda_b^2}{v_{\text{EW}}} \right)^2 \cos \frac{\phi}{f}, \quad (\text{III.66})$$

is a rapidly oscillating function, leading to an instability that amplifies fluctuations of the Higgs field. Following the analysis of Sec. III.2, there is an instability band for

$$\frac{\dot{\phi}^2}{4f^2} - \frac{\Lambda_b^4}{v_{\text{EW}}^2} < k^2 + m_{\text{eff}}^2 < \frac{\dot{\phi}^2}{4f^2} + \frac{\Lambda_b^4}{v_{\text{EW}}^2}, \quad (\text{III.67})$$

with $m_{\text{eff}}^2 = \Lambda^2 - g'\Lambda\phi + 3\lambda\langle h^2 \rangle \equiv m_h^2(\phi) + 3\lambda\langle h^2 \rangle$. Initially, the Higgs mass $m_h^2(\phi) \sim \Lambda^2$ is large and positive so there is no instability and we have $\langle h^2 \rangle = 0$. However, as the relaxion field scans the potential, the effective Higgs mass decreases and modes will begin to enter the resonance band and grow exponentially. In turn, the quartic induced, effective mass $\propto \langle h^2 \rangle$ grows until the mode again exits the instability band. This interplay between the decrease in effective mass due to the evolution of the relaxion field and the increase due to the quartic induced mass leads to a so-called edge solution where the mode stays fixed at the upper edge of the instability band [80]. Once the edge solution is established, the zero mode obeys the condition

$$m_h^2(\phi) + 3\lambda\langle h^2 \rangle = \frac{\dot{\phi}^2}{4f^2} + \frac{\Lambda_b^4}{v_{\text{EW}}^2}, \quad (\text{III.68})$$

meaning that the typical energy in the Higgs field is

$$\rho_h \sim \lambda \langle h^2 \rangle^2 = \frac{1}{9\lambda} \left(\frac{\dot{\phi}^2}{4f^2} + \frac{\Lambda_b^4}{v_{\text{EW}}^2} - m_h^2(\phi) \right)^2. \quad (\text{III.69})$$

In order to see the effect of the Higgs fluctuations, let us estimate the energy of the Higgs field during the last stage of relaxation where we have $0 \lesssim m_h^2(\phi) \lesssim v_{\text{EW}}^2$. First, we note that $\Lambda_b \lesssim \sqrt{4\pi} v_{\text{EW}}$ is typically expected in simple UV completions, see *e.g.*, App. A of Ref. [44]. Therefore, if $\dot{\phi}/f \ll v_{\text{EW}}$ is satisfied when the edge solution is established, then ρ_h is at most of the order v_{EW}^4 , meaning that the Higgs field cannot absorb a large fraction of the total relaxation kinetic energy and the oscillation of the Higgs zero mode is negligible compared to the Higgs VEV. This condition is indeed satisfied in the most of the viable self-stopping relaxation parameter space previously identified in Ref. [44], meaning that the effect of Higgs fluctuations is small compared to the friction from relaxation fragmentation. Moreover, the regulated growth of the Higgs field due to the quartic leads to an edge solution which is strictly less efficient than the unregulated exponential growth of relaxation fluctuations during the scanning phase. We thus conclude that while growth of Higgs field can occur, it does not significantly alter the success of the self-stopping relaxation mechanism, nor its parameter space.

On the other hand, if $\dot{\phi}/f \gtrsim v_{\text{EW}}$, the amplitude of Higgs zero mode can be larger than v_{EW} before relaxation completes. In this case, the analysis of the relaxation process should involve both the relaxation and the Higgs field, and the stopping condition should be modified. This scenario is interesting, but beyond the scope of this paper. Here, we will simply assume that the condition $\dot{\phi}/f \ll v_{\text{EW}}$ is satisfied and show its impact on the viable self-stopping relaxation parameter space in Sec. III.6.3.

III.6.3 Parameter space

In this section, we want to briefly discuss how the parameter space of the relaxation is modified once the new conditions discussed in this paper are taken into account. For a thorough discussion of all the conditions that the model has to satisfy, we refer the reader to Ref. [44]. There are two modifications with respect to this discussion. First, the lattice simulation of Sec. III.3 and the second order calculation of Sec. III.4 show that fragmentation is more efficient than the purely linear expectation. Second, in order to avoid the growth of Higgs fluctuations, we have to add the condition $\dot{\phi}/f \ll v_{\text{EW}}$ as discussed in Sec. III.6.2.

Concerning the first point, we proceed as in Ref. [44]. There, the parameter space was derived by using Eqs. (III.10) and (III.11), and replacing $\log(\dots) \rightarrow 50$. Analogously, the product \log in Eq. (III.12) was replaced by $W_0(\dots) \rightarrow 50$. Here we proceed analogously by keeping Eqs. (III.10), (III.11), (III.12) but now we replace $\log(\dots) \rightarrow 2$ to account for the shorter stopping time found in the lattice analysis. However, we keep $W_0(\dots) \rightarrow 50$ as in [44], because Eq. (III.12) concerns the onset of fragmentation, which occurs when the fluctuations are still in the linear regime and hence the linear analysis is still valid.

In Fig. III.11, we show a comparison of the parameter space of Ref. [44] (in gray, dashed lines) with that of this work (in red), for three reference scenarios. In the top row, we consider the case of relaxation during inflation. In the center and bottom rows, relaxation takes place after inflation. For this latter case, we superimpose the contours of the maximal allowed value of H_I , according to Eq. (III.48). We fix g/g' as in Ref. [44], while all other parameters are left free to vary. We see that the new results of this paper lead to a slight reduction in the viable parameter space of the self-stopping relaxation model.

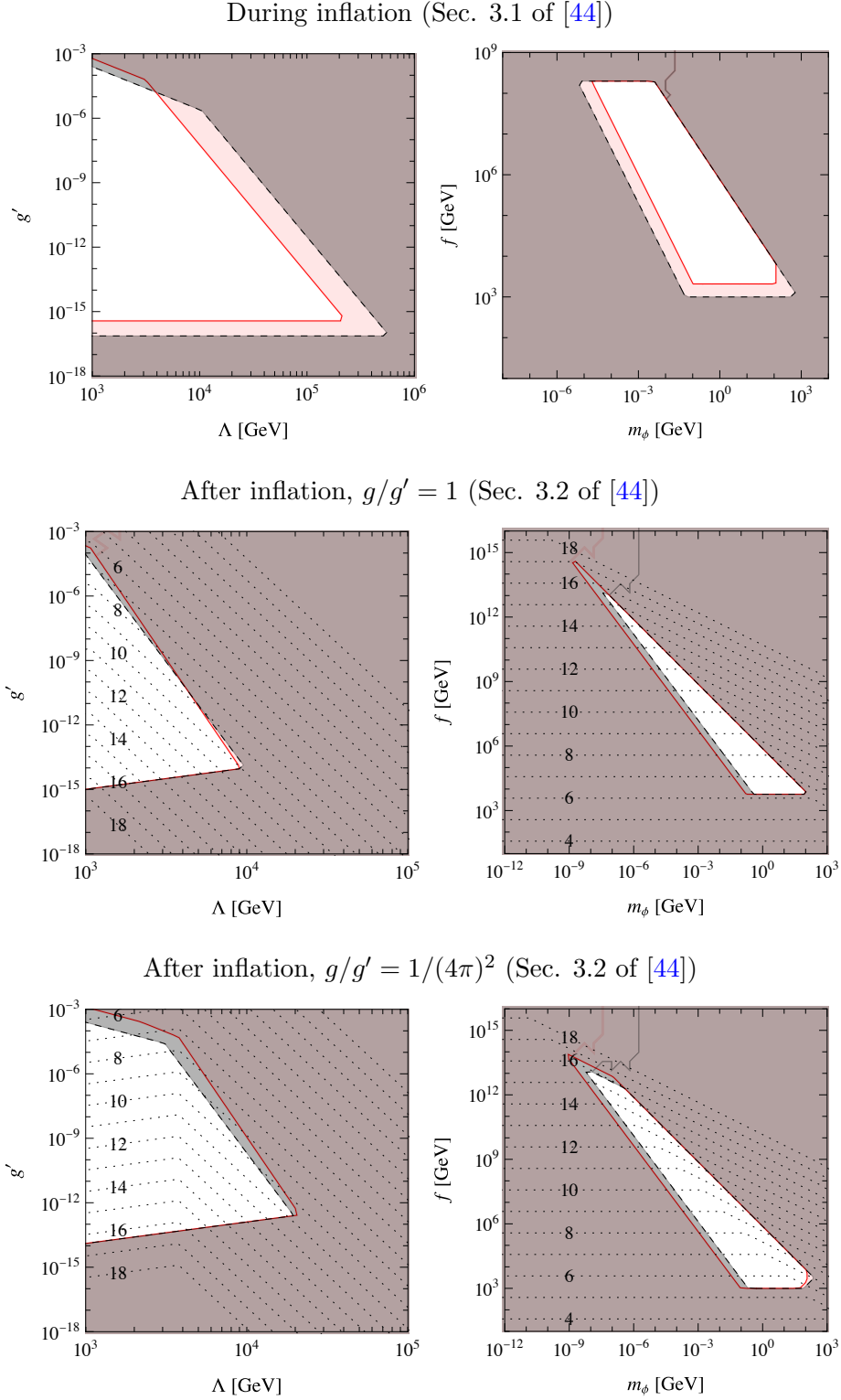


Figure III.11: Parameter space of the relaxion model including the results of this paper (in red), compared to the results of Ref. [44] (in gray, dashed lines). Top: Relaxation during inflation. Center: Relaxation after inflation, with $g/g' = 1$. Bottom: Relaxation after inflation, with $g/g' = 1/(4\pi)^2$. In the center and bottom rows, we superimpose the contours of $\log_{10} H_I^{\max}$, defined according to Eq. (III.48).

III.7 Gravitational Waves from Axion Fragmentation?

Finally we want to investigate whether the fragmentation process discussed above emits a detectable GW signal. When the energy is transferred from the homogeneous axion motion to its fluctuations, the energy density also transitions from being homogeneous to inhomogeneous. This transformation is associated with sizeable energy currents and it is easily conceivable that also anisotropic stress of similar size is present. Therefore, it is clear that GWs will be emitted in this process. We here try to answer the question whether a detectable amount can be sourced without being in conflict with cosmological bounds, namely, the axions relic density overclosing the universe.

While the previous discussion was mainly focused on the relaxion case in which the expansion of the universe could be neglected, for the emission of GWs the relation between the critical scale k_{cr} and the Hubble scale is crucial. From now on k will denote strictly comoving momenta that have to be converted to physical momenta using the scale factor a , while in the relaxion case the distinction was rather loose, since the fragmentation process took place within a fraction of a Hubble time and therefore $a = a_{\text{amp}} \approx a_{\text{frag}} = 1$ was used implicitly for the conversion.

We will here restrict ourselves to a simple analytic argument, why fragmentation processes are not able to produce GWs observable with pulsar timing or laser interferometry without the ALPs relic density overclosing the universe. More detailed discussions can be found in [1, 71]. We use an estimate obtained by naive dimensional analysis for the amount of produced GWs (e.g. [3])

$$\Omega_{\text{GW}}(k_{\text{peak}} \approx k_{\text{cr}}) = c_{\text{eff}} \Omega_{\phi, \text{frag}}^2 \left(\frac{a_{\text{frag}} H_{\text{frag}}}{k_{\text{cr}}} \right)^2, \quad (\text{III.70})$$

where $c_{\text{eff}} = \mathcal{O}(1)$ denotes an efficiency factor for the production of GWs that we set to 1 in the following. We have evaluated all quantities at t_{frag} , since at this point an $\mathcal{O}(1)$ fraction of the axions energy is transferred to inhomogeneities.

The first factor is the amount of energy acting as a source of GWs, in our case the axion's energy. We have $\dot{\phi} \gtrsim mf$ such that the axion actually rolls over the potential barriers and, therefore, $k_{\text{cr}}/(a_{\text{frag}}m) \gtrsim 1$ which implies that the energy density in the excited axion modes redshifts like radiation for some time after GW emission before starting to behave like matter and contributing to DM. Maximizing the amount of energy in the axion without overclosing the Universe therefore amounts to

$$\Omega_{\phi, \text{frag}} \approx \frac{1}{2} \frac{a_{\text{frag}}}{a_{\text{eq}}} \frac{k_{\text{cr}}}{a_{\text{frag}}m} = \frac{k_{\text{cr}}}{2a_{\text{eq}}m}, \quad (\text{III.71})$$

where a_{eq} denotes the scale factor at matter radiation equality. The second factor of Eq. (III.70) includes the characteristic scale of the GW source that also sets the frequency of the waves. In the fragmentation case, it is given by k_{cr} and directly fixed by today's frequency $f_{\text{frag},0} = k_{\text{cr}}/(2\pi a_0)$. In the following we are interested in the maximum GW amplitude we can produce at a frequency given by an experiment under consideration. We therefore consider $f_{\text{frag},0}$ to be fixed. Putting it all together we find

$$\Omega_{\text{GW}} \approx \left(\frac{a_{\text{frag}} H_{\text{frag}}}{a_{\text{eq}} m} \right)^2. \quad (\text{III.72})$$

In this simplified treatment we are only left with two variables: m and a_{frag} , where the latter one fixes H_{frag} given the standard cosmological history. From the formula above it

is clear that we want to minimize m , while maximizing $a_{\text{frag}}H_{\text{frag}}$. This ratio is however limited by a strict hierarchy of scales that is at the heart of the fragmentation process: As previously discussed, we have $k_{\text{cr}}/a_{\text{frag}} \gtrsim m$. Furthermore, one can easily show that $k_{\text{cr}}\delta k_{\text{cr}} = a_{\text{frag}}^2 m^2$, and efficient production of excited axions requires the growth rate $\delta k_{\text{cr}}/a_{\text{frag}}$ to be bigger than the Hubble rate such that we have in total

$$H_{\text{frag}} \lesssim \frac{\delta k_{\text{cr}}}{a_{\text{frag}}} \lesssim m \lesssim \frac{k_{\text{cr}}}{a_{\text{frag}}} . \quad (\text{III.73})$$

It is therefore easy to convince oneself that the GW amplitude is maximized when this hierarchy is as small as possible, which corresponds to all of the scales above being of the same order of magnitude and the axion barely managing to roll over the barriers, $\dot{\phi}^2 \approx m^2 f^2$. From $k_{\text{cr}} \approx a_{\text{frag}}H_{\text{frag}}$ we can determine a_{frag} and express the maximum GW amplitude as a function of solely the GW frequency today. Assuming that the axions energy is subdominant at all times and using that this process takes place before matter radiation equality, we find

$$\Omega_{\text{GW},0} \approx \Omega_{\text{rad},0} \left(\frac{a_{\text{eq}}}{a_0} \right)^2 \left(\frac{H_{\text{eq}}}{f_{\text{frag},0}} \right)^2 = 5 \times 10^{-21} \left(\frac{10^{-8} \text{ Hz}}{f_{\text{frag},0}} \right)^2 , \quad (\text{III.74})$$

where $\Omega_{\text{rad},0}$ is fractional energy in radiation today (see Appendix A for details on red-shifting). This very rough estimate agrees to within one order of magnitude with the one found in [67], although in their setup the above mentioned hierarchy was small by construction and our result can be seen as a generalization. Let us note that in the relaxation case this hierarchy is large [44] and the resulting GWs would be even smaller. From this estimate, it becomes clear that detection in future pulsar timing arrays like SKA with sensitivities down to $\Omega_{\text{GW},0} \approx 10^{-15}$, let alone laser interferometers with similar sensitivity but at higher frequencies, is not possible in a general fragmentation setup without additional suppression of the axion abundance. Finally, let us note that there is in principle a more stringent bound for efficient growth than $H_{\text{frag}} < \delta k_{\text{cr}}/a_{\text{frag}}$ since the critical momentum and, therefore, the amplified modes are red-shifting, as well as the growth time considerations that allowed us to determine t_{frag} in Section III.2.

III.8 Conclusion

In this chapter, we have analyzed axion fragmentation using a classical lattice simulation. We have confirmed that the kinetic energy of the axion zero mode dissipates into fluctuations in a manner similar to the expectations of Ref. [43], with some important modifications coming from non-linearities that can only be captured by the lattice simulation. As shown in Fig. III.2, one such modification is that the dissipation of the zero mode kinetic energy is even more efficient compared to the linear approximation used in Ref. [43] because modes outside of the instability band are populated due to $2 \rightarrow 1$ processes. These secondary fluctuations dominate over the initial fluctuations and thus enhance the dissipation effect in the non-perturbative regime. This is an NLO effect and therefore not included in the analysis of Ref. [43], but is captured to all orders in our lattice simulation. Moreover, since the amplitude of the secondary fluctuations is determined by $2 \rightarrow 1$ processes, the fragmentation process in the non-perturbative regime is insensitive to the particular choice of the initial spectrum of fluctuations as shown in Fig. III.3.

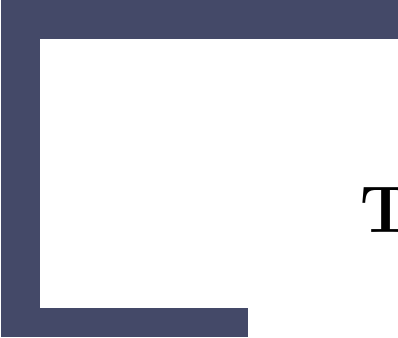
In Sec. III.5, we have discussed the fluctuations after the completion of fragmentation as well as bubble/domain wall formation. Since the typical size of the fluctuation $\langle \delta\phi^2 \rangle$ is of

the order of f^2 , one might worry about problematic domain wall formation. We therefore determined the conditions such that the dynamics of axion fragmentation do not result in domain walls of cosmological size, and we showed that they mainly concern the initial condition of the axion evolution, which are set during inflation, and hence the inflationary Hubble scale H_I .

In Sec. III.6, we examined the consequences of bubble formation as well as the possible excitation of Higgs fluctuations in the relaxion specific case. Bubble formation in the case of the relaxion leads to unacceptable cosmology and thus must be avoided by imposing an upper bound on the scale of inflation. Regarding Higgs fluctuations, we argue that in a large fraction of the viable parameter space for the self-stopping relaxion, the Higgs field cannot absorb a large fraction of the relaxion's kinetic energy and thus the growth of Higgs fluctuations has only a minor impact on the viable parameter space. The new constraints on the parameter space, including the enhanced dissipation of the relaxion's kinetic energy due to NLO effects, are discussed in Sec. III.6.3.

In summary, we have shown directly via lattice simulation that fragmentation is a very efficient mechanism of depleting kinetic energy from an axion field rolling over many oscillations of a periodic potential. In the special case where the axion is identified as the self-stopping relaxion, we have quantified the parameter space where fragmentation as a stopping mechanism leads to successful relaxation of the electroweak scale.

Finally, we investigated whether a detectable GW background can be sourced through fragmentation. We found that the amount of energy in the axion needed to produce GWs with a large enough amplitude, would inevitably lead to the overclosure of the universe, once the axion starts acting as DM.



**Main part II:
The Audible Axion**

Lattice Study of the Minimal Model

IV.1 Motivation

In the previous chapter we investigated the instability that arises in an ALP field with non-standard initial conditions, namely if it rolls over many periods of the potential. We here go back to the standard misalignment scenario but introduce an enhanced coupling of the axion to a hidden $U(1)$ gauge boson. As was shown in Ref. [3], such models can produce a large, stochastic gravitational wave (GW) signal in the early universe. Interestingly this new signal is proportional to the ALPs decay constant f and therefore largest for f close to the Planck scale $f \sim m_{\text{Pl}}$. Such large decay constants are motivated by quantum gravity theories [26–29]. On the other hand all direct couplings to the SM are antiproportional to f and therefore the chances of ever directly detecting such axions are rather slim. As we will show, GWs sourced by a mechanism like this might therefore be the only hope of detecting such axions over a wide range of parameter space.

The coupling of the axion to the dark $U(1)$ induces a tachyonic instability when the ALP begins to oscillate for a specific range of “dark photon” momenta controlled by the ALP mass m . Dark photon modes in this range have their underlying vacuum fluctuations ($\rho_{\text{vac}} \sim m^4$) exponentially amplified until their energy density becomes of order that of the ALP ($\rho_{\text{ALP}} \sim m^2 f^2$). To do so the modes grow by a factor of $\mathcal{O}(f^2/m^2)$. This growth results in a highly anisotropic dark photon energy distribution that sources GWs. Furthermore, the amplification of vacuum fluctuations occurs in a parity-asymmetric way due the non-vanishing expectation value of the parity-violating ALP-dark photon operator. As a result, the produced GW spectrum is typically highly chiral in the peak region and is expected to be a smoking gun for such models.

While the majority of the chapter is devoted to a detailed understanding of the dynamics in the minimal setup only containing the axion and a massless dark photon, we also comment on the implications of a dark photon mass, kinetic mixing between the dark and SM photon as well as possible implications, if the axion is indeed the QCD one. We find that the mass can be neglected during the production of dark photons as long as it is small enough to not interfere with the tachyonic instability. As for the mixing with or coupling to the SM fields, we find that all possible effects are suppressed by thermal masses that the SM particles pick up. This justifies our negligence of all these effects when we study the dynamics in the following.

As dark photon production occurs at the expense of energy in the ALP field, some parameter space where the ALP relic abundance would normally overclose the universe can be opened up. However, care here is required as these dynamics also backreact on the ALP field due to inverse decay and scattering processes involving ALPs and dark photons. These processes introduce a limit to how much energy can be transferred from the ALP to

dark photons, and introduce anisotropies in the initially homogeneous ALP field. Thus, linear analyses of the system such as that of Ref. [3] break down and one must perform a detailed lattice study to correctly capture the dynamics. This fact was previously pointed out in Refs. [81–83], where it was found that the ALP relic abundance can be suppressed at most by a factor of $\mathcal{O}(10^{-2})$.

In this work, we perform our own lattice study in order to further understand the non-perturbative dynamics of the system and its impact on the GW spectrum. We solve the equations of motion for the full axion, dark photon, and GW system in position space on a discretized spacetime lattice. In particular, our implementation is based on the staggered grid algorithm of Refs. [72, 73] which ensures that the discretized theory respects all the same symmetries of the continuous one, importantly including gauge invariance and the shift symmetry of the ALP. Additionally, our entire lattice implementation reproduces the continuum version of the theory up to an error which is quadratic in the lattice spacing. We are able to confirm previous work suggesting that the ALP relic abundance can be suppressed by roughly 2 orders of magnitude, in addition to robustly establishing the existence of the GW spectrum predicted in Ref. [3]. We find that the main changes to the GW spectrum when compared to the results of the linear analysis are: i) an enhancement of power at higher momenta due to $2 \rightarrow 1$ processes not present in the linear analysis and ii) a dependence of the polarization of the GW spectrum on the ALP-dark photon coupling α . The second point is expected since the two dark photon helicities are coupled through the ALP, so depending on the value of α the polarization tends to be washed out or “frozen-in” at some value depending on when backscattering processes decouple. We discuss extensions to the original model which allow for additional suppression of the ALP relic abundance and show the viable parameter space in the f vs. m plane.

IV.2 Introduction to the Model

Let us start with an overview of the Audible Axion model introduced in Ref. [3]. The simplest version of the model consisted of an axion field ϕ and a massless dark photon X_μ of an unbroken $U(1)_X$ Abelian gauge group

$$\mathcal{S} = \int d^4x \sqrt{-g} \left[\frac{1}{2} \partial_\mu \phi \partial^\mu \phi - V(\phi) - \frac{1}{4} X_{\mu\nu} X^{\mu\nu} - \frac{\alpha}{4f} \phi X_{\mu\nu} \tilde{X}^{\mu\nu} \right], \quad (\text{IV.1})$$

where the parameter f is the scale at which the global PQ symmetry corresponding to the Nambu-Goldstone field ϕ is spontaneously broken. The dark photon field strength is $X_{\mu\nu}$ with $\tilde{X}^{\mu\nu} = \epsilon^{\mu\nu\alpha\beta} X_{\alpha\beta}/2$ its dual¹. The strength of the axion-dark photon coupling is parameterized by α , which in general can be larger than the fundamental $U(1)_X$ coupling. We also assume the PQ symmetry is explicitly broken at the scale $\Lambda \sim \sqrt{mf}$, generating the potential $V(\phi)$, a mass m for the axion, and breaking the continuous shift symmetry of the ALP down to a discrete one, $\phi \rightarrow \phi + 2\pi n$. The potential should be invariant under this discrete shift symmetry, thus for simplicity we choose

$$V(\phi) = m^2 f^2 \left(1 - \cos \frac{\phi}{f} \right), \quad (\text{IV.2})$$

unless otherwise specified.

Let us for now limit the analysis to the case of a massless dark photon, which allows us to work in temporal gauge $X_0 = 0$. In an expanding background $ds^2 = a^2(\tau)(d\tau^2 - d\mathbf{x}^2)$,

¹Our convention is $\epsilon^{0123} = 1/\sqrt{-g}$

the equations of motion governing the system are

$$\phi'' + 2aH\phi' - \nabla^2\phi + a^2V'(\phi) - \frac{\alpha}{fa^2}\mathbf{X}' \cdot (\nabla \times \mathbf{X}) = 0, \quad (\text{IV.3})$$

$$\mathbf{X}'' + \nabla \times (\nabla \times \mathbf{X}) + \frac{\alpha}{f}[\phi'(\nabla \times \mathbf{X}) - \nabla\phi \cdot \mathbf{X}'] = 0, \quad (\text{IV.4})$$

where primes denote derivatives with respect to conformal time τ and $H = a'/a^2$ is the Hubble rate. Additionally, one has the Gauss constraint

$$\nabla \cdot [\mathbf{X}' + \frac{\alpha}{f}\phi(\nabla \times \mathbf{X})] = 0. \quad (\text{IV.5})$$

We assume the PQ symmetry is broken before the end of inflation $f > H_I$, leading to an axion field that is spatially homogeneous over the visible universe. As in the standard misalignment scenario (see Section II.1 and [34]), the initial field value of the axion is drawn from a uniform random distribution $\theta = \phi_0/f \in [-\pi, \pi]$, where $\theta \sim \mathcal{O}(1)$ is the initial misalignment angle. While $H > m$ is satisfied, Hubble friction is important and the axion field is overdamped, thus the initial velocity tracks the slow-roll attractor. As is well known, massless vector modes are not excited during inflation so we take the dark photon to be in the Bunch-Davies vacuum initially. We further assume that the universe is radiation-dominated by the SM plasma with the axion contributing sub-dominantly to the total energy density.

With these initial conditions, one can study the axion-dark photon system by initially neglecting any spatial dependence of the axion $\phi(\tau, \mathbf{x}) \rightarrow \phi(\tau)$. In this limit, the equation of motion for the dark photon in momentum space becomes

$$X_{\pm}''(\tau, \mathbf{k}) + \omega_{\pm}^2(k, \tau)X_{\pm}(\tau, \mathbf{k}) = 0; \quad \omega_{\pm}^2(k, \tau) = k^2 \pm k\frac{\alpha}{f}\phi'(\tau), \quad (\text{IV.6})$$

where X_{\pm} are the mode functions of the two circular polarizations of the dark photon. The modification of the dispersion relation caused by the interaction leads to the modes with momenta $0 < k < \alpha|\phi'|/(2f)$ of the polarization $-\text{sgn}(\phi')$ experiencing a tachyonic instability once the axion starts to freely oscillate. We define the start of oscillations $a = a_{\text{osc}}$ by the condition $H = m$. Due to this instability, the energy in the dark photon quickly grows from the vacuum value $k^4 \sim m^4$ to an $\mathcal{O}(1)$ fraction of the axion energy $\propto m^2 f^2$.

Tachyonic production is efficient if the mode functions grow more than an $\mathcal{O}(1)$ factor during one oscillation of the axion. Since the axions velocity at the beginning of oscillations is given as $|\phi'| \approx \theta m f a_{\text{osc}}$ and that the period of the axion oscillation is $\Delta\tau \approx 1/m$ one can show that $\theta\alpha > 1$ is required in order to have efficient particle production. Since $\theta \approx 1$ this leads to $\alpha > 1$, which can be obtained in several UV completions, see e.g. [30, 31, 84]. The analytic understanding of the dynamics in the regime where the homogeneous axion still dominates the energy density has been improved in Ref. [85] and we summarise the relevant results in Section IV.4.2. Most importantly they allow for a precise estimation of the time when the dark photon starts to dominate in energy at a_* .

At this point, one expects a backreaction of the dark photon onto the axion dynamics and for the axion field to develop anisotropies. Thus, one must study the system on the lattice in order to correctly capture the dynamics. In our previous work we simplified the backreaction onto the axion by assuming that it stays homogeneous while only the amplitude of the oscillations is reduced to enforce conservation of energy (see also Refs. [2, 3, 86]). When studying the dynamics in detail in Sec. IV.3, we will refer to this treatment as linear analysis and compare our results with it. When the dark photon comes to

dominate the energy density of the system, the distribution of the energy also becomes inhomogeneous. The energy-momentum currents that are associated with this transition cause an anisotropic stress that can cause a detectable gravity wave (GW) signal if the energy in the axion - dark photon system makes up a sizeable fraction of the total energy in the universe at the time. Calculating this signal and estimating its detectability is one of the key goals of the simulations carried out here.

Before we do so we will discuss some possible extensions of the minimal model that might arise in a given UV completion.

IV.2.1 Finite dark photon mass

First, we consider the possibility of a non-zero mass for the dark photon which could arise through a dark Higgs or Stueckelberg mechanism. This is of special phenomenological interest since it allows the dark photon to be a viable dark matter candidate. The main effect of m_X is to further modify the dark photon dispersion relation

$$\omega_{\pm}^2(k, \tau) = k^2 \pm k \frac{\alpha}{f} \phi'(\tau) + a^2(\tau) m_X^2, \quad (\text{IV.7})$$

which can reduce the efficiency of or prevent tachyonic growth. To further quantify this statement, we go back to the previously mentioned argument that the tachyonic growth of the mode functions becomes inefficient if they grow less than $\mathcal{O}(1)$ during one oscillation of the axion field. This happens when $-\omega_{\pm}^2 < (am)^2$ is satisfied for all modes k . From this we can deduce that one must require $m_X \lesssim \theta \alpha m / 2$ in order to have tachyonic production. Below when studying the viability of dark photon dark matter we focus on dark photon masses well below this bound which will not affect the success of our mechanism.

IV.2.2 Kinetic Mixing

Next, we examine whether the relevant photon-dark photon kinetic mixing operator

$$\Delta \mathcal{L} = -\frac{\epsilon}{2} F_{\mu\nu} X^{\mu\nu}, \quad (\text{IV.8})$$

affects our mechanism. Indeed, this operator will inevitably be generated by renormalization group flow if there exist states which carry both electromagnetic and $U(1)_X$ charge [87]. If kinetic mixing leads to an effective coupling of the dark photon to the SM radiation bath, one might worry that it induces a large thermal mass for the dark photon that prevents tachyonic growth.

In the case of an exactly massless dark photon $m_X = 0$, the kinetic mixing term is unphysical as it can be removed via the field redefinition $X' = X + \epsilon A$ and $A' = A / \sqrt{1 - \epsilon^2}$ that leaves the coupling of the SM photon to the electromagnetic current unchanged. Thus, it is clear that only the field combination that couples to the SM plasma A' develops a thermal mass.

However, for $m_X \neq 0$, the mixing is physical. Diagonalizing the kinetic terms by performing the same field redefinition now leads to a non-diagonal mass matrix which, in addition to the thermal mass Π induced by the SM plasma for A' , must be included in the dispersion relation

$$\left[\omega^2 + k^2 + \begin{pmatrix} \epsilon'^2 m_X^2 + \Pi & -\epsilon' m_X^2 \\ -\epsilon' m_X^2 & m_X^2 \end{pmatrix} \right] \begin{pmatrix} A'^{\mu} \\ X'^{\mu} \end{pmatrix} = 0, \quad (\text{IV.9})$$

with $\epsilon' = \epsilon/\sqrt{1-\epsilon^2}$. The photon thermal mass is of order $\Pi \approx e^2 T^2$, which at the time when the axion begins to oscillate evaluates to $\Pi \approx e^2 m M_P$. As discussed in Section IV.2.1, the existence of the tachyonic instability requires $m_X \lesssim \theta \alpha m/2$. Furthermore, the momenta that experience tachyonic growth are those with $k \lesssim \theta \alpha m$, so we are deeply in the regime where $m_X^2, k^2 \ll \Pi$. In this limit, the effective mass matrix in Eq. (IV.9) always has a small eigenvalue $m_X^2(1 + \mathcal{O}(\epsilon^2))$ which is independent of T^2 , despite the kinetic mixing [88]². Thus, we conclude that the field combination associated with the dark photon X' does not acquire a thermal mass via kinetic mixing, so we are subject only to the usual constraints on ϵ , see e.g. Refs. [89–102].

IV.2.3 QCD Axion

Finally, we examine the case where the ALP ϕ is taken to be the QCD axion itself, which is the focus of Ref. [86]. In this limit, m and f are not independent parameters but are instead related by $m^2 f^2 = \chi_{\text{QCD}}$, where $\chi_{\text{QCD}} = (75.5 \text{ MeV})^4$ is the QCD topological susceptibility. In particular, the QCD axion has the following couplings to SM gauge bosons

$$\Delta\mathcal{L} = \frac{\alpha_s}{8\pi f} \phi G_{\mu\nu}^a \tilde{G}^{a\mu\nu} + \frac{g_{\phi\gamma\gamma}}{4} \phi F^{\mu\nu} \tilde{F}_{\mu\nu}, \quad (\text{IV.10})$$

where $G_{\mu\nu}^a$ and $F_{\mu\nu}$ are the gluon and photon field strengths, respectively, and $g_{\phi\gamma\gamma}$ is a model dependent coupling, e.g. $g_{\phi\gamma\gamma} = -1.92 \alpha_{\text{EM}}/(2\pi f)$ in the KSVZ model [103, 104]. These couplings are of the same form as the one of the axion to the dark photon and one might therefore expect that these fields also experience tachyonic instabilities. Those are however regulated by plasma effects. The photon acquires a Debye mass of order $\Pi \sim e^2 T^2$ via hard thermal loops, preventing tachyonic growth [105, 106]. Similarly, the gluon self-coupling induces a magnetic mass $m(T) \sim g^2 T$ [107–109]. The fact that the tachyonic growth is prevented once the gauge field in question couples to plasma lead us to consider a dark photon in the first place. This allows one to formulate further constraints on the dark sector, in order for the dynamics of the dark photon to not alter from the once in the minimal model that we discuss below: The dark sector can not be populated by a plasma of particles that are charged under the dark $U(1)$ nor can it have charged degrees of freedom lighter than $m^2 \lesssim e_X E_X \approx e_X m f$, where E_X is the dark, electrical field strength, since otherwise this light degree of freedom is produced via the Schwinger effect. This scenario has been studied for a case were the axion also drives inflation in Ref. [110].

As a final consideration, model dependent couplings of ϕ to SM fermions also exist. However, the production of fermions is not exponential due to Pauli-blocking. Thus, the exponential production of dark photons dominates over SM channels.

IV.3 Lattice Formulation and Validation

We solve the full equations of motion of the coupled axion and dark photon system by discretizing space and time. To ensure that we recover the correct theory in the continuum limit, the discretized theory must have the same symmetry structure as the continuum one. Ideally, the discretization should reproduce the continuum theory up to an error which is high order in the lattice spacing to ensure fast convergence. Our implementation meets the following requirements:

²This result, while perhaps surprising at first, becomes clear when we consider the limit $m_X \rightarrow 0$, where the dark photon must decouple.

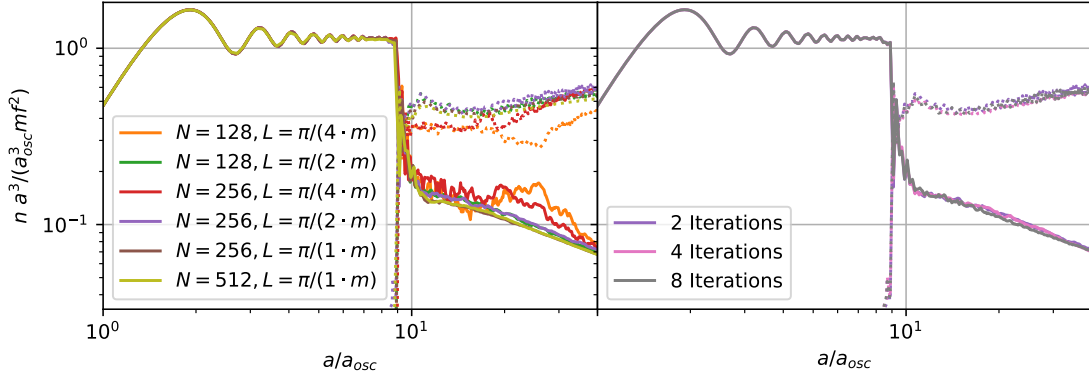


Figure IV.1: Comoving axion (solid) and dark photon (dotted) number densities for different choices of the lattice parameters with $\alpha = 60$ and $\theta = 1$ held fixed. In the left panel, L and N are varied while the number of iterations in the implicit scheme is held fixed at 2. Similarly, the right panel fixes $N = 256$, $L = \pi/(2m)$ and varies the number of iterations in the implicit scheme. The different choices agree to within $\sim 10\%$ except in the case of the smallest length $L = \pi/(4m)$.

- The continuum versions of the equations are reproduced up to $\mathcal{O}(dx_\mu^2)$, where dx_μ denotes the spatial and temporal distance between lattice sites.
- The discretization admits gauge invariance.
- The shift symmetry $\phi \rightarrow \phi + \epsilon$ of the continuum theory is respected on the lattice. This is equivalent to the discretized version of $X_{\mu\nu}\tilde{X}^{\mu\nu} = \partial_\mu(2X_\nu\partial_\alpha X_\beta\epsilon^{\mu\nu\alpha\beta})$ being a total (lattice) derivative.

We implement these features using an implicit, staggered grid algorithm closely following Refs. [72, 73]. The equations of motion for the transverse-traceless metric fluctuations are solved to obtain the GW spectrum following Refs. [111, 112], where an algorithm is implemented that also reproduces the continuum up to $\mathcal{O}(dx_\mu^2)$.

We simulate a comoving volume L^3 with side length $L = \pi/m$ and $N = 512$ lattice sites along each direction with periodic boundary conditions such that we cover comoving momenta $2 \leq k/(ma_{\text{osc}}) \leq 512$. This comfortably covers the range of momenta experiencing tachyonic growth, $k \sim \theta\alpha ma_{\text{osc}}/2$ for $\theta = \mathcal{O}(1)$ and $\alpha \sim 40 - 100$ ³. The lattice parameters are thus L , N , and the number of iterations in the implicit scheme. We varied these parameters to ensure that none of our results depend on them, see Fig. IV.1 where we show the evolution of the axion and dark photon number densities for different lattice parameters. To keep the computational cost down, we only go to second order (2 iterations) in the implicit scheme used to solve the equations of motion as justified in the right panel of Fig. IV.1. For a detailed description of the lattice numerics, see Appendix B.

IV.4 Dynamics from the Lattice

The lattice simulation was performed with $m = 10^{-2}$ eV and $f = 10^{17}$ GeV held fixed for all runs. We then use the scaling relations described in Section IV.4.3 to adapt the results

³For benchmark points with $\theta = 3$, a smaller box $L = \pi/(3m)$ was used in order to resolve the UV

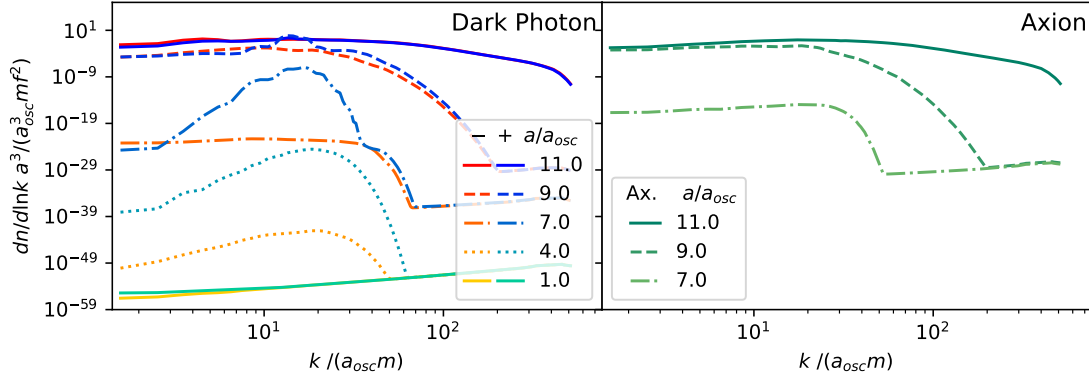


Figure IV.2: Early evolution of the dark photon (left) and axion (right) spectra. The model parameters are $\alpha = 60$ and $\theta = 1$. The “+” polarization is the first to experience tachyonic instability.

to other values of the model parameters. In the left panel of Fig. IV.2, we show the early evolution of the comoving dark photon number density for $\alpha = 60$ and $\theta = 1$, where the linear analysis holds. We define the start of oscillations $a = a_{osc}$ by the condition $H = m$, with the dark photon initially in the Bunch-Davies vacuum such that $dn/d\ln k \propto k^3$.

At the second time step $a/a_{osc} = 4$, the dark photon spectra perfectly agrees with the expectation from the linear analysis: during the first period of oscillation we have $\phi' \approx \theta m f a_{osc}$ and therefore according to Eq. IV.6 the modes in the range $k \in [0, \alpha|\phi'|/f] \approx [0, \alpha\theta m a_{osc}]$ experience a tachyonic instability. These are indeed the modes that are enhanced at $a/a_{osc} = 4$ compared to the Bunch-Davies vacuum. In the first half period of oscillation, the axion velocity does not change sign and therefore only one helicity experiences tachyonic growth. Without loss of generality, we label the first helicity to experience tachyonic growth as “+” throughout this work. In the second half period, the “-” polarization is excited. However, the damping of the axion velocity due to Hubble friction results in a smaller range of tachyonic modes. Since the growth rate depends exponentially on the axion velocity, the amplitude of the “-” polarization is exponentially suppressed compared to the “+” polarization.

In the next time step at $a/a_{osc} = 7$, we see the position of the peak move towards lower momenta. This is expected since the axion velocity is further decreased by Hubble friction. Additionally, we see a second contribution to the dark photon spectrum appearing that is plateau shaped and falls off at an $O(1)$ multiple of the original peak momentum. Looking over to the right side of Fig. IV.2, we note that the appearance of this plateau happens at the same time as inhomogeneities in the axion field arise with a similar spectrum. From a particle point of view the origin of this feature is clear, as the axion-dark photon coupling allows for the (back-)scattering of two photons into an axion. The kinematics of this process dictate that the resulting spectrum should fall off at twice the dark photon peak momentum, which is what we observe. The plateau in the dark photon spectrum arises from further back-scattering of dark photons into finite momentum axions and is expected to be unpolarized. These effects are similar to the once we discussed for axion fragmentation above in Chapter III, where we were able to derive an analytic expression for the second order fluctuations and therefore were able to back up the particle physics

dynamics properly. When attempting to capture the late time behavior of the axion abundance in Fig. IV.4, we used $N = 128$ and $L = \pi/(2 \cdot m)$ as the simulation must be run longer.

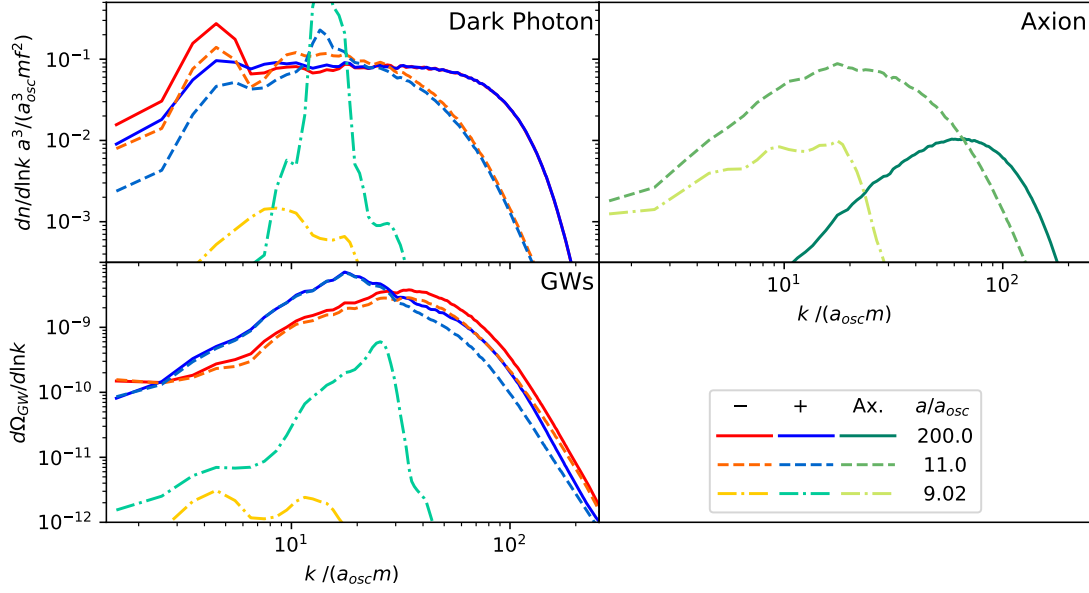


Figure IV.3: Evolution of the spectra in the non-linear regime. The model parameters are $\alpha = 60$ and $\theta = 1$. The “+” polarization is the first to experience tachyonic instability. The dark photon and axion panels correspond to those in Fig. IV.2 but within a much smaller range of energy densities.

picture. Such a perturbative treatment would be much harder here since there exist no closed analytic expression for the first order perturbations.

The next time of interest is a_* when the energy in the dark photon and axion become comparable in size $\rho_X \sim \rho_\phi$ and therefore any perturbative scheme breaks down. This roughly corresponds to $a/a_{osc} = 9$ where we see the peak from tachyonic growth and the plateau from back-scattering becoming comparable in size. The UV cutoff of the plateau also moves toward higher momenta and becomes less steep, which in the particle picture results from multiple scattering processes becoming more important as the number densities grow.

The last time step at $a/a_{osc} = 11$ is some time after the two energy densities become comparable in size. Before we take a closer look at the evolution during this period, let us make two technical comments. We chose a vanishing initial spectrum for the axion which stays zero during the first two time steps to within working precision. In general, the initial axion spectrum would depend on the inflation history. However, the axion spectrum resulting from backscattering processes is uncorrelated with and can be simply added to any initial spectrum that might exist from inflation. The second point concerns the UV behavior of the spectra at $a/a_{osc} = 7, 9$. This behavior corresponds to rounding errors due to the fact that we are dealing with field amplitudes differing by $\approx \log_{10}(f/m) = 29$ orders of magnitude while using double precision floats with a precision of only 16 orders of magnitude. One expects the errors to take a random value in position space, uncorrelated from site to site. We have checked that this results in the UV part of the spectrum behaving as $\propto k^3$ in momentum space.

Fig. IV.3 shows a close up of the last two time steps from Fig. IV.2 as well as the final spectra taken at $a/a_{osc} = 200$. Also shown is the evolution of the spectrum of gravitational waves. The close up reveals that at $a/a_{osc} = 9$ when $\rho_X = \rho_\phi/2$, the dark photon spectrum

is still dominated by the sharp, polarized peak resulting from the tachyonic instability. This initial peak and its polarization are however quickly washed out through scattering effects, resulting in a flat, unpolarized plateau. The UV cutoff of the plateau behavior is extended to slightly higher momenta after the two energy densities become comparable due to multiple scattering processes. Interestingly, another peak at lower momenta appears in the final spectrum that is dominated by the “-” polarization. We believe this peak, also present in the study of Ref. [83], is due to the tachyonic enhancement that occurs as the axion zero mode settles down to the minimum with roughly constant velocity. The axion velocity at this point is already significantly reduced by the production of dark photons and the resulting peak is therefore at smaller momenta.

IV.4.1 Relic Abundance Suppression

Shortly after the dark photon energy density becomes comparable to that of the axion, the axion velocity becomes too small to allow for efficient production of dark photons through the tachyonic instability. In the linear analysis, dark photon production continued nonetheless due to a narrow parametric resonance resulting from the coherent oscillation of the homogeneous axion field. This effect could lead to a suppression of the axion relic abundance by more than 10 orders of magnitude relative to the case without any particle production.

On the lattice however, we see the axion spectrum right after the energy densities become comparable at $a/a_{osc} = 11$ has a broad peak as shown in Fig. IV.3. At late times, this peak moves to slightly higher momenta (similar to the dark photon), while IR power is suppressed. Low momentum axions correspond to nearly homogeneous field configurations in position space and it therefore seems plausible that the suppression of the axion abundance at low momenta is due to a parametric resonance. However, it is clear that the axion abundance at high momenta is not suppressed and that high momentum axions are still being produced at late times. This severely limits the amount by which the total axion abundance can be suppressed.

In particular, we find that the relic abundance suppression relative to the case without particle production is typically limited to 10^{-2} , in good agreement with Ref. [81]. This can be seen clearly in Fig. IV.4, we show the evolution of the comoving axion energy density as calculated on the lattice compared the result from the linear analysis. They start to differ shortly after the initial backreaction, when the linear analysis predicts a much stronger depletion of the axion abundance due to the parametric resonance driven by the zero-momentum condensate. On the lattice, the axion abundance is dominated by relativistic axions, so the axion energy density scales as radiation until their momenta drops below the axion mass, locking in a suppression of about 10^{-2} compared to the scenario without particle production.

As shown in Fig. IV.5, we find that the amount of suppression has only weak dependence on θ and α in the regime where dark photon production is efficient ($\theta\alpha \gtrsim 30$) and friction from particle production does not cause the axion to slow-roll ($\theta\alpha \lesssim 200$). In Ref. [81], a similar study was performed in the QCD axion case (where the axion mass poses a time dependence) that comes to roughly the same conclusion. The lattice computation results in a more predictable relic abundance compared to the linear analysis, where the final abundance depended chaotically on the initial conditions [86]. Since an axion overabundance limits the parameter space with detectable gravitational waves, we discuss two potential paths to further suppress the axion abundance in Sec. IV.5.

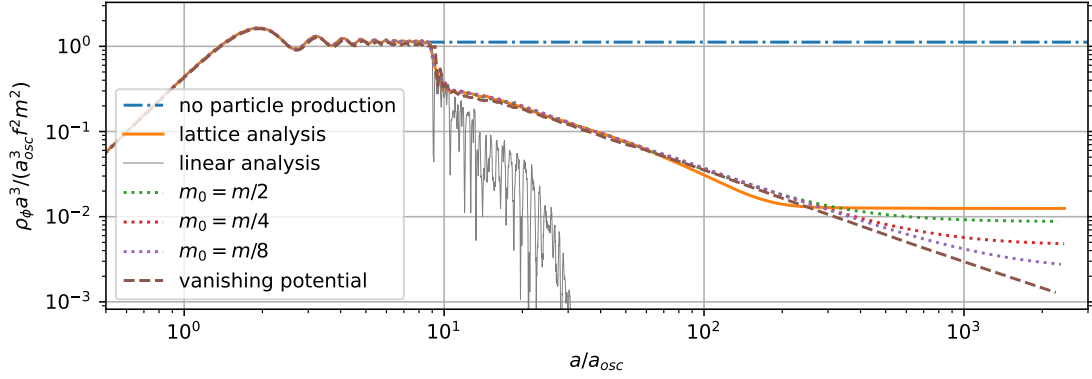


Figure IV.4: Evolution of the comoving axion energy density for $\theta = 1$. Around $a = a_{osc}$, the axion starts oscillating and scaling like matter $\rho_\phi \approx a^{-3} m^2 f^2$. Without particle production, this scaling would persist (blue dot-dashed line) yielding the standard abundance from misalignment. For $\alpha = 60$, the backreaction of dark photon production becomes strong around $a/a_{osc} \sim 9$. The thin gray line shows the result from the linear analysis, while the solid orange line gives the lattice result. The lattice result shows a suppression of the final axion abundance by $\approx 10^{-2}$ compared to the case with no particle production, in stark contrast to the linear analysis which suggests a much stronger suppression. The dotted lines show possible further suppression in case where the final mass is adiabatically reduced, while the brown dashed line corresponds to a time dependent potential that vanishes around $a/a_{osc} = 100$ (see Sec. IV.5 for details).

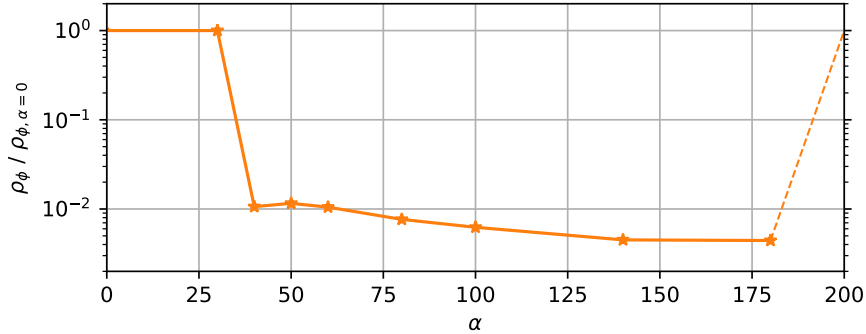


Figure IV.5: Suppression of the axion relic abundance for different values of α and fixed $\theta = 1$ compared to the standard misalignment case where $\alpha = 0$ and there is no dark photon production. We see that $\theta\alpha \gtrsim 30$ is required for efficient dark photon production. For values of $\theta\alpha \gtrsim 200$, friction from particle production causes the axion to slow-roll and behave as vacuum energy, thus it will quickly come to dominate the energy density of the universe. As we ignore the effect of the axion-dark photon system on the gravitational background, this regime is beyond the scope of our simulation, and we simply sketch the expected sharp loss of suppression in this region with the dashed line.

IV.4.2 Scaling Relations

Before moving on let us briefly discuss the dependence of the axion and dark photon abundance on the parameters of the model. In the regime of small misalignment angles $\theta \lesssim \pi/2$, where the quadratic approximation for the potential holds we find that the axion

number density is well approximated as

$$n_\phi = \theta^2 m f^2 \left(\frac{a_{osc}}{a} \right)^3, \quad (\text{IV.11})$$

after the onset of oscillation. Our analysis shows that the final abundance is suppressed by a factor typically of order 10^{-2} through the dark photon production as discussed above. The abundance of dark photons is set during the initial backreaction at time t_* , when the majority of energy is transferred from the axion to the dark photon. Afterwards, it scales as

$$\rho_X = \rho_\phi|_{t=t_*} \left(\frac{a_*}{a} \right)^4 = \theta^2 m^2 f^2 \frac{a_*}{a_{osc}} \left(\frac{a_{osc}}{a} \right)^4. \quad (\text{IV.12})$$

The linear analysis describes the dynamics with great precision leading up to the backreaction and can be used to find an analytic estimate for a_*/a_{osc} . To do so, we assume that the energy in the dark photon is dominated by the fastest growing mode $k_* = \alpha|\phi'|/(2f) \approx \alpha\theta/2 (a_{osc}/a_*)^{3/2} a_* m$ and the energy in the dark photon is therefore given as $\rho_X^* \approx (k_*/a_*)^4 |v_*/v_{BD}|^2$, where v_* is the dark photon mode function corresponding to k_* at t_* and v_{BD} the Bunch-Davies mode function. Using the analytic estimate for the mode function v_* found in Ref. [85], we can rewrite $\rho_X^* \approx \rho_\phi^*$ in the form of a transcendental equation for a_*/a_{osc}

$$\begin{aligned} \log \left(\frac{f}{\theta \alpha^2 m} \left(\frac{a_*}{a_{osc}} \right)^{3/2} \right) &= \frac{\alpha \theta}{\sqrt{2}} \left(\frac{a_{osc}}{a_*} \right)^{1/4} \\ &\times \left[0.6 - 0.82 \sqrt{\frac{a_{osc}}{2a_*}} - 0.49 \sqrt{\frac{a_*}{2a_{osc}}} + 0.45 \frac{a_*}{a_{osc}} - 0.05 \sqrt{\frac{a_*^3}{2a_{osc}^3}} \right]. \end{aligned} \quad (\text{IV.13})$$

We compared these two equations to our results on the lattice and found that they track the scaling to within a factor 2 for $40 \leq \theta\alpha \leq 100$. For $\theta\alpha \gtrsim 100$ the backreaction occurs within the first period of oscillation and keeps the axion from efficiently rolling towards $\phi = 0$. This leads to a prolonged emission of dark photons that is not taken into account by these relations.

IV.4.3 Gravitational Wave Spectrum

Since the gravitational wave spectrum is dominantly produced in the short period after the energy densities of the axion and dark photon become comparable, the main features of the GW spectrum computed in the linear analysis of Ref. [3] survive on the lattice. In particular, the linear analysis leads to the expectation that the GW signal resulting from a polarized vector carries the same polarization as its source. Looking at the bottom panel of Fig. IV.3, we see that the GW spectrum is indeed strongly polarized at $a/a_{osc} = 9$, since up to this point the anisotropic stress is dominated by the highly polarized dark photon. On the lattice, we are now consistently including the axion scalar perturbations as a GW source. This can lead to a washout of polarization in the final spectrum, although as we will see some parts of the GW spectrum can remain strongly polarized.

In Ref. [3], we presented some basic scaling relations which allow for the estimation of the peak amplitude and frequency of the GW spectrum via naive dimensional analysis (NDA)

$$k_{\text{peak}} \sim 2k_* \approx \theta \alpha m \sqrt{\frac{a_{osc}}{a_*}} a_{osc}$$

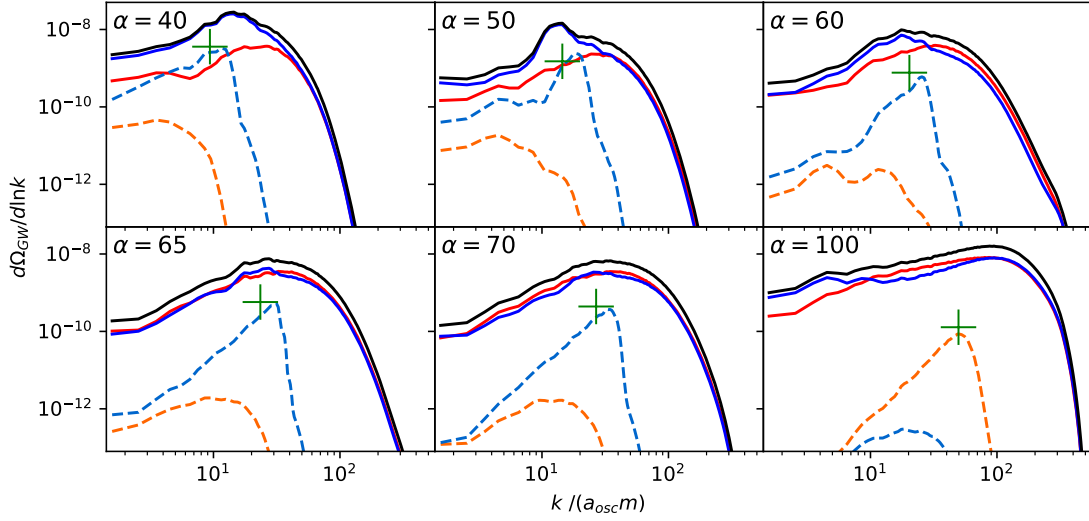


Figure IV.6: Gravitational wave spectra computed on the lattice for different values of α with $\theta = 1$ held fixed. The light dashed lines show the two polarizations (red, blue) when $\rho_X = \rho_\phi/2$ (roughly the end of the perturbative regime). The solid lines are the final spectra taken at $a/a_{osc} = 40$ when the GW spectrum has fully converged. The solid black line gives the sum of the two polarizations in the final spectrum and green crosses mark the NDA scaling relation from Eq. IV.14 with $c_{\text{eff}} = 1$. The source material includes the final spectra in tabulated form.

$$\Omega_{\text{GW}}(k_{\text{peak}}) = c_{\text{eff}} (\Omega_\phi^*)^2 \left(\frac{a_* H_*}{k_*} \right)^2 = \frac{c_{\text{eff}}}{9} \left(\frac{f}{m_{\text{Pl}}} \right)^4 \left(\frac{\theta}{\alpha} \right)^2 \frac{a_*}{a_{osc}}, \quad (\text{IV.14})$$

where c_{eff} is a factor quantifying the efficiency of GW emission and stars denote the corresponding quantity at the time of the initial backreaction t_* where the GW spectrum is dominantly produced.

In Figs. IV.6 and IV.7, we show the GW spectrum computed on the lattice for several values of θ and α , where the NDA prediction from the scaling relation Eq. (IV.14) with $c_{\text{eff}} = 1$ is indicated by a green cross. We report a final GW spectrum at $a/a_{osc} = 40$ at which point the GW signal has fully converged for all choices of the model parameters. Also shown is the spectrum at the end of the perturbative phase $t = t_*$ when $\rho_X = \rho_\phi/2$ for the first time. We see that the NDA scaling relation predicts the peak of the spectrum at $t = t_*$ to within a factor of 2, but in general fails to predict the peak of the final spectrum⁴. We suspect that $2 \rightarrow 1$ scattering processes in the phase $t > t_*$ are prolonged for large values of θ and α , leading to larger signal amplitudes and peak momenta. These processes also tend to smooth out and broaden the dark photon and axion spectra, which in turn leads to the appearance of a softened UV cutoff in the GW spectrum, as compared to the rapid exponential falloff we found in the linear analysis. The IR behavior for modes $k/(ma_{osc}) \lesssim 1$ with wavelengths larger than the lattice size L is expected to approach k^3 scaling from causality.

Another important difference between the linear and lattice studies is that while the peak of the GW spectrum at the end of the perturbative phase t_* is highly polarized, the polarization of the peak of the final spectrum on the lattice shows a strong dependence

⁴For large $\theta \sim 3$, the scaling relation also differs from the early spectrum because the approximation of

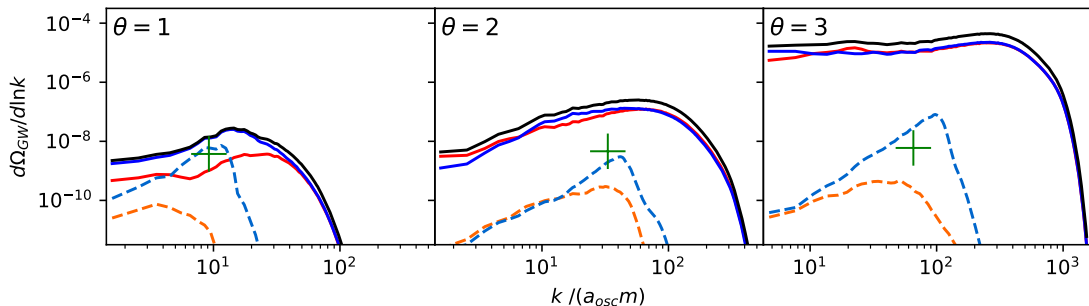


Figure IV.7: Same as Fig. IV.6 except $\alpha = 40$ is held fixed while θ is varied. In the case of $\theta = 3$ we chose a smaller sized box $L = \pi/(3ma_{osc})$ to better resolve the UV part of the spectrum.

on θ and α . In particular, we see the polarization of the final spectrum is diminished for $\theta\alpha \gtrsim 60$. For $\theta\alpha \lesssim 60$ the GW amplitude grows by a factor of $\lesssim 10$ in the late stages $t > t_*$, while for $\theta\alpha \gtrsim 60$ the final spectrum can surpass the spectrum at t_* by up to 3 orders of magnitude. The fact that the peak is largely unpolarized in cases where it is predominantly sourced after t_* fits well with our earlier observation that the polarization in the dark photon spectrum is washed out after t_* due to backscattering processes coupling the two dark photon helicities. The unpolarized dark photon and axion spectra thus lead to unpolarized gravitational waves. A similar suppression of polarization for large coupling constants α has been observed in models of natural steep inflation [113], while a study that appeared during the completion of this work found that the final polarization is limited to 10% roughly independent of θ and α [83]. That study considered $40 \leq \theta\alpha \leq 60$, which is the region where, in contrast, we find up to 90% polarization in the peak region. In addition, while the peak amplitude and momentum agree with our findings within roughly a factor of two, the overall shape of the spectra show significant differences.

As a final point, for $\theta\alpha \gtrsim 100$, the backreaction becomes sizeable within the first period of oscillation and the regimes of tachyonic growth and non-perturbative interaction of fluctuations are not well separated. This leads to the initially subdominant helicity surpassing the dominant one already by $t = t_*$ in the case of $\theta = 1$, $\alpha = 100$ and some strongly polarized features in the IR tail of the final spectra.

IV.5 Model Extensions

As previously discussed, the axion relic density can be suppressed by only two orders of magnitude via production of dark photons once inhomogeneities in the axion field are taken into account. Overproduction of DM thus renders a sizeable part of the parameter space leading to detectable gravitational waves inconsistent with cosmology. Solutions which simply reduce the initial axion abundance such as tuning the initial misalignment angle are inappropriate in our case, as they also suppress the GW source. Instead, a mechanism is needed that reduces the axion abundance once the tachyonic phase of dark photon production (responsible for the majority of the GW signal) has ended. This could be achieved if the axion potential is in some way time-dependent or flattens out around the minimum. In both cases, the axion mass can be suppressed at late times. Let us first

the cosine potential as quadratic fails, invalidating the analytic solution found in Ref. [85].

explore the latter scenario in the context of a monodromy-inspired potential [114–119]

$$V(\phi) = \frac{1}{2}m^2 f^2 \left(\frac{\phi}{f}\right)^2 - m_w^2 f_w^2 \left[1 - \cos\left(\frac{\phi}{f_w}\right)\right], \quad (\text{IV.15})$$

where the first term corresponds to Eq. (IV.2) expanded to quadratic order in ϕ/f , and we take $f_w < f$. Expanding for small ϕ , the ALP mass at late times is given by

$$m_0^2 = m^2 - m_w^2, \quad (\text{IV.16})$$

which can be small if $m_w \sim m$. Defining $m_w^2 = m^2(1 - \epsilon^2)$ with $\epsilon \ll 1$ and $\varphi = \phi/f$, we can write

$$\frac{V(\varphi)}{m^2 f^2} = \frac{1}{2}\varphi^2 - \frac{f_w^2}{f^2}(1 - \epsilon^2) \left[1 - \cos\left(f\frac{\varphi}{f_w}\right)\right]. \quad (\text{IV.17})$$

In this form, we can easily see that when $\varphi \sim \theta \sim \mathcal{O}(1)$, the argument of the cosine term is large and its overall contribution to V is suppressed by f_w^2/f^2 . Thus, ALP dynamics in this regime are controlled by the φ^2 term and the axion mass is approximately m . However, once the ALP amplitude becomes of order $\varphi \lesssim f_w/f$, we can expand the cosine and see that the ALP mass changes from m to the final mass m_0 . Our simulations confirm that during this process the axion number density is conserved to a good approximation, leading to a suppression of the axion relic abundance which is linear in the ratio m_0/m as shown in Fig. IV.4.

A similar setup was considered in [66, 67], which relied on the anharmonic part of the potential for self-resonant axion (and GW) production. In that case, taking ϵ small necessarily leads to a weak resonance unless the initial axion field value is very large. As we rely on the axion-dark photon coupling for particle production (which simply requires a non-vanishing ϕ'), this incompatibility does not hold here. Indeed, the model given by Eq. (IV.15) combined with a strong axion-dark photon coupling leads to sizeable GW production even for $\phi_0/f \sim 1$. We estimated in Ref. [3] that tachyonic production stops once the scale factor has grown by $a/a_{osc} = (\alpha\theta/2)^{2/3}$. Since the axion amplitude damps at least as fast as $a^{-3/2}$ (it falls off even faster when including friction from particle production), one finds

$$\frac{1}{f_w} \gtrsim \frac{\alpha}{2f}, \quad (\text{IV.18})$$

is required in order to have tachyonic particle production complete before the cosine substructure is resolved. Interestingly, this suggests a possible embedding of the model into a monodromy construction where the axion couples to the dark photon as f_w^{-1} , with different UV origins for the quadratic and cosine terms in Eq. (IV.15), as in Refs. [120, 121]. Large α in such a construction could be understood in terms of the separation of scales f/f_w .

Another way to reduce the axion relic abundance is via a time-dependent potential. One possibility is that the axion mass at early times comes dominantly from a potential induced via $U(1)_X$ monopoles through the Witten effect [122, 123]. In this case, the axion potential is proportional to the monopole number density and thus decays as a^{-3} .

Finally, one could entertain the possibility that the axion is exactly massless at late times [124]. This would occur if the axion potential arises from some QCD-like dynamics, where the dark quarks temporarily acquire mass from the VEV of a dark Higgs field that later vanishes [125]. In such a case, the late time axion potential vanishes in exactly the same way as in QCD with one massless quark, and the axion relic abundance is subject only to N_{eff} constraints.

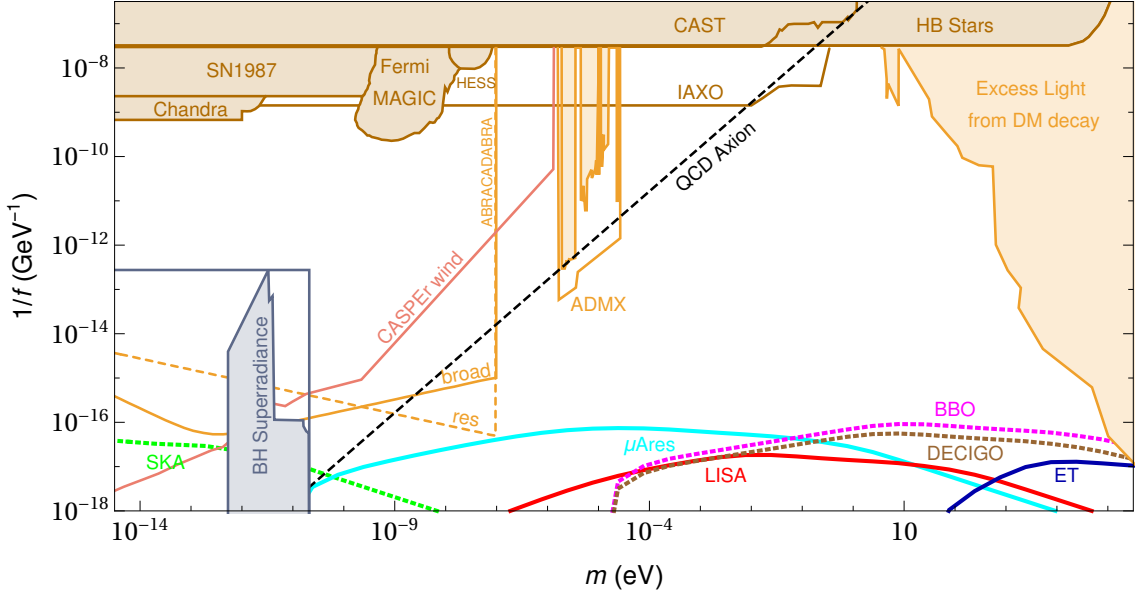


Figure IV.8: Axion and ALP parameter space in the mass vs. inverse decay constant plane. Regions below the colored curves are in reach of future ground-based (ET) and satellite-based (LISA, BBO, DECIGO) GW detectors, or future pulsar timing arrays (SKA). Shaded regions are excluded by existing constraints, while unshaded regions show the sensitivity of various other planned experiments. Black hole superradiance excludes the grey shaded region, and future black hole observations could extend this region to the grey line. The location of the QCD axion band is indicated by the black dashed line.

A detailed discussion of two more involved scenarios is subject of the following chapters. One of them revolves around the previously discussed relaxion (Chapter VI), while the other one acquires the energy for production of dark photons not from the axions potential. Instead a mechanism is introduced that leads to an initial velocity of the axion, commonly referred to as kinetic misalignment (Chapter V).

IV.6 Probing Audible Axion Models

With the results of the previous section, we can now identify the regions of parameter space that may be probed by future GW experiments. Detectability requires an SNR above a certain experiment dependent threshold. Here, we use the values and method of Ref. [59]. We include the regions that result in detectable GW signals as well as cosmological bounds on the model for fixed $\alpha = 100$ and $\theta = 1$. The GW detectability curves were computed using the GW spectrum obtained from the lattice, with the IR scaling for $k \lesssim ma_{\text{osc}}$ taken to be $\propto k^3$ as expected from causality. Our results are shown in Fig. IV.8, where the detectable regions lie below the curves labeled as SKA, LISA, BBO, DECIGO and ET, respectively⁵. Interestingly, GW experiments are most sensitive for large values of the decay constant f corresponding to very weakly coupled axions. These probes are therefore highly complementary to other existing limits (orange shaded) or planned searches (orange lines), which are typically more sensitive for larger couplings. An exception is the constraint coming from black hole superradiance (gray

⁵For experiments which probe the axion-photon coupling $g_{\phi\gamma\gamma}$, we assume the KSVZ relation $g_{\phi\gamma\gamma} = -1.92 \alpha_{\text{EM}} / (2\pi f)$ to convert between $g_{\phi\gamma\gamma}$ and $1/f$.

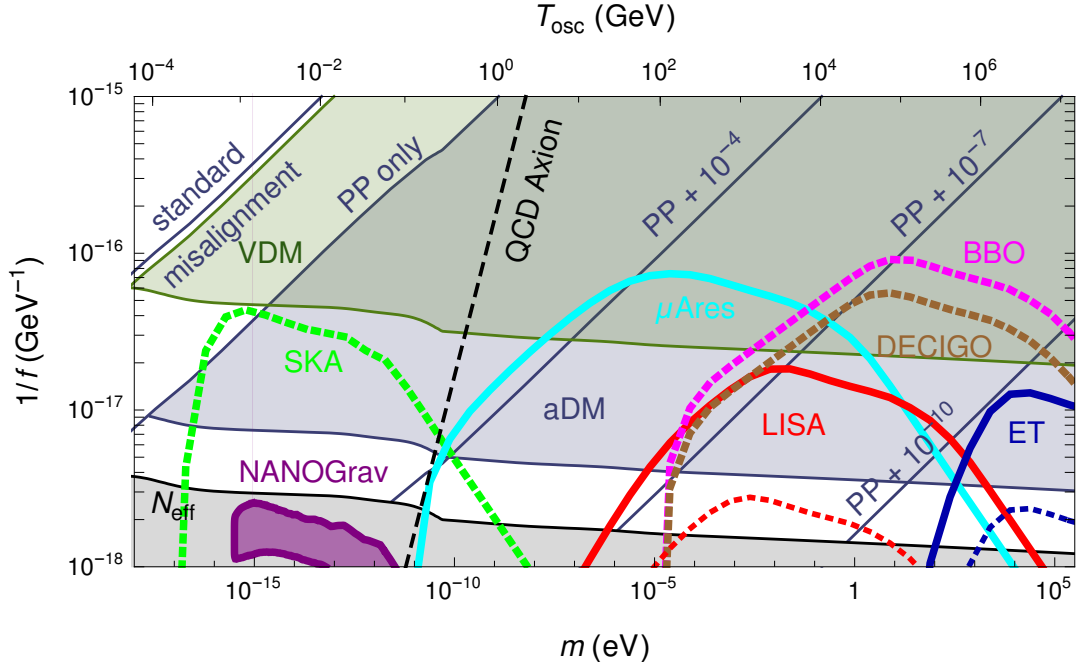


Figure IV.9: ALP parameter space in the mass vs. inverse decay constant plane with $\alpha = 100$ and $\theta = 1$ held fixed. The parameter space below the bright colored curves could be probed by future GW experiments, such as pulsar timing arrays (SKA) as well as space- (LISA, DECIGO, BBO, μ Ares) and Earth-based (ET) interferometers. In addition, we also show the region where LISA (dashed red) or ET (dashed blue) can potentially detect the chirality of the GW signal. The purple region is where the model could account for the recently reported NANOGrav signal. The gray region is excluded in case of a relativistic dark photon by bounds on N_{eff} , while in the green region a massive dark photon can be a viable DM candidate. The solid diagonal lines refer to axion dark matter scenarios in which, from left to right, there is no particle production (standard misalignment), only the suppression from particle production $\approx 10^{-2}$ (PP only), or further suppression η from model extensions (PP + η). In the blue shaded area, the axion is cool enough to be DM, assuming sufficient suppression of the relic abundance.

shaded), which is also most reliable for large decay constant f and also indirectly relies on GW observations [126, 127]. It should also be emphasized that the GW signal regions do not depend on the axion relic abundance today, and therefore do not require the axion to account for all of DM. The non-decoupling behavior of the GW signal is due to the fact that larger f corresponds to more energy in the axion field $\Omega_{\phi}^{\text{osc}} \propto m^2 \theta^2 f^2$ which is available to be converted into gravitational radiation. This holds as long as the initial misalignment angle θ takes on natural values of $\mathcal{O}(1)$ ⁶.

In Fig. IV.9, we show a close up of the parameter space that leads to detectable signals, as well as bounds arising from cosmology. To do so, we use the improved scaling relations from Section IV.4.2 to calculate the axion and dark photon relic abundance and apply the bounds from Appendix A.

The blue shaded region in Fig. IV.9 corresponds to the parameter space where the axion possibly comprises all of DM. The left diagonal bound of the region matches the dark

⁶Additionally, we are always assuming $m_X \lesssim m/2$ and $\alpha \sim 10 - 100$ such that the particle production process is efficient, see e.g. Refs. [3, 86].

matter abundance assuming a suppression of two orders of magnitude from particle production. The region near this line, where no further suppression is needed, can be probed by SKA for $m \sim 10^{-16} - 10^{-14}$ eV and $f \sim 5 \times 10^{16}$ GeV. As discussed in Section IV.4, the axion transitions from the condensate into non-zero momentum states in the process of dark photon production. Axion dark matter can therefore be warm in this scenario. Requiring axion dark matter to be cool enough to form structures gives the lower bound on the blue shaded region. Observable GW signals in the space (ground)-based interferometers require an additional suppression of the axion abundance by 4 to 7 (10) orders of magnitude in order to avoid overclosure. As discussed in Section IV.5 this can be achieved in simple extensions of our model.

In the case where the dark photon has a sufficiently small mass such that it is relativistic at late times, it contributes to the number of effective relativistic degrees of freedom N_{eff} . Requiring the N_{eff} bounds to be satisfied leads to the gray shaded exclusion region in Fig. IV.9. We find that the bounds from N_{eff} are in tension with the NANOGrav signal originating from this model, and similarly for any spectral distortions that might be probed by the future Voyage2050 mission. Although there has been recent interest in similar models with ultralight scalars and their GW signals in the context of the Hubble tension [128] as well as Quintessence [129], none of these studies incorporate the scalar perturbations in a consistent manner. Their inclusion might considerably strengthen the bounds from CMB fluctuations and therefore lead to a non-trivial probe of the model via CMB spectral distortions. If the dark photon mass is larger but still less than the axion mass in order to not interfere with the tachyonic production, the dark photon can be a viable vector dark matter (VDM) candidate [82, 130–132] in the green shaded region of Fig. IV.9. The origin of the lower bound is again where the dark photon DM would be too warm to be compatible with structure formation.

A smoking gun for Audible Axion models is the chiral nature of the GW spectrum as discussed above. This can provide powerful background rejection, since SGWBs from astrophysical sources are not expected to carry a net polarization. It has been pointed out that the dipolar anisotropy induced by the Doppler shift due to the relative motion of our solar system with respect to the cosmic reference frame can be exploited to allow planar detectors to detect net circular polarization [133–137]. In particular, LISA and ET would be able to detect net circular polarization with an SNR of $\mathcal{O}(1)$ for a SGWB with amplitude $h^2\Omega_{\text{GW}} \sim 10^{-11}$ [138]. In Fig. IV.9, we indicate using dashed lines the region in parameter space where the signal is strong enough such that LISA and ET can pick up on the polarization following the analysis of Ref. [138] assuming full polarization. Of course, if a network of non-coplanar detectors is available in a particular frequency range, GW polarization can be detected without paying the $\mathcal{O}(10^{-3})$ suppression factor due to our peculiar velocity [133, 139]. As previously discussed the simplifying assumption of full polarization is only justified for small values of α and θ near the peak. The resulting lines should therefore only be considered as an indication, for which parts of parameter space the partially polarized spectrum of this model from other unpolarized signals, especially for parameter points where $\theta\alpha \lesssim 60$, where the signal is more than 90% polarized.

In Fig. IV.9 we have further included the 2σ -region where the Audible Axion can account for the recently reported hint of a GW signal by NANOGrav. Unfortunately this region is in conflict with the N_{eff} bound. In Part III we discuss how to derive this region and furthermore comment on further tests of the model for axion masses below 10^{-16} eV using CMB fluctuations, polarization and spectral distortions.

IV.7 Discussion and Conclusions

The nature of dark matter and how it is produced in the early universe remains a mystery. Axions or ALPs are viable candidates, and coupled to a dark photon they can induce a tachyonic instability, efficiently transferring energy from the axion to the dark photon and thereby widening the viable parameter space for ALP dark matter [86]. In Ref. [3] we showed that this process can be accompanied by the production of a stochastic GW background, which as we showed here renders the model testable for large decay constants. We furthermore argued that effects like a dark photon mass, kinetic mixing with the SM photon as well as couplings to other SM fields that one expects to arise from realistic UV completions do not interfere with the production of the dark photon.

Backscattering of dark photons into axions is essential to understand the final ALP relic abundance, however, capturing this non-linear effect requires simulating the system on a lattice. In this work, we present results of a lattice simulation of the axion-dark photon system on a 512^3 lattice and obtain the resulting gravitational wave spectrum. Our formulation manifestly preserves the shift symmetry and gauge invariance of the continuum theory. We confirm the findings of Refs. [81–83] that the ALP relic abundance cannot be suppressed by more than about two orders of magnitude relative to the ordinary misalignment mechanism with no particle production.

For the GW signal, we find that the inclusion of backscatterings and GWs sourced from axion anisotropies broadens the spectrum towards the UV, while the peak frequency and amplitude are roughly consistent with the results from the linear analysis [3]. Furthermore, we find that the polarization of the GW spectrum now depends non-trivially on the coupling strength α and initial misalignment angle θ . While the signal remains strongly polarized for smaller couplings, for $\theta\alpha \gtrsim 60$ the polarization is washed out due to backscatterings which couple the dark photon helicities. At even larger couplings, the polarization can flip from the initially dominant one and exhibit a non-trivial frequency dependence. If these features could be observed experimentally, they would provide additional information on the model parameters and potentially even the initial conditions after inflation.

As discussed in detail above, a large fraction of the parameter space of interest for experimental GW detection is inconsistent with the observed DM relic abundance. In Section IV.5, we sketch two simple extensions of the model that could potentially resolve this tension, which essentially come down to decreasing the axion mass after GW production, such that the experimental signatures remain unchanged. In the more radical approach, where the axion is rendered massless at late times, the dark photon can be given a small mass and play the role of dark matter. While much of the parameter space requires extending the model, a window remains for pulsar timing arrays to probe the original, minimal model.

Boosted by an Initial Kick

V.1 Motivation

As discussed above the audible axion scenario only produces an observable GW signal for very large axion decay constants, $f_\phi \gtrsim 10^{17}$ GeV, since otherwise the energy in the axion is not sufficient to source enough GWs. For large regions of the parameter space the large energy density of the axion however limits the viability of the mechanism, since the axion DM abundance tends to overclose the universe.

This leads us to consider the case where the axion is initially equipped with a large amount of kinetic energy, as we already did in the context of fragmentation in Chapter III, now in combination with the coupling to the dark photon. In that case, both the axion mass and decay constant become relatively unconstrained. As we will see it is furthermore possible to achieve the tachyonic instability with small values of the coupling $\alpha \ll 1$ that one naively expects from perturbation theory.

This work is based on the kinetic misalignment scenario [68, 69, 140], but should easily also apply to other models such as trapped misalignment [70, 74]. Kinetically misaligned axions are attractive for model building and phenomenology [141, 142], since they can explain the baryon asymmetry [140, 143–146] and modify the spectrum of long lasting primordial GW sources [147–149]. Furthermore, in combination with dark photons, GWs are produced along with vector dark matter. This was already noted in Ref. [150], where a rough estimate of the corresponding GW spectrum was presented. Here, we provide a more elaborate assessment of the GW background from kinetically misaligned audible axions. We compute the GW spectrum numerically in the linear analysis and identify the regions of parameter space that may be probed by future GW experiments. We furthermore evaluate the cosmological constraints on the model and identify the regions where either the axion or the dark photon are viable DM candidates. Our main results are the GW spectrum shown in Fig. V.2, as well as Fig. V.4 which highlights the large range of viable axion DM parameter space that can be probed using GWs.

V.2 Model Description

Let us be oblivious for a second to where the axion’s velocity is coming from and consider the dynamics as described by the action in Eq. (IV.1). In this case we can go back to the dispersion relation for the dark photon coupled to the axion Eq. (IV.6) and find that if we choose the initial velocity large enough, a tachyonic instability can be achieved no matter what value of coupling α or decay constant f .

There is however one subtlety concerning this scenario: If the axion’s kinetic energy dominates over the potential, the energy redshifts as $\rho_\phi = \frac{1}{2a^2} \dot{\phi}^2 \propto a^{-6}$. The typical dark

photon growth rate therefore scales as $\omega \propto \frac{\alpha}{f} \phi' \propto a^{-2}$. To see whether tachyonic production is efficient, this rate needs to be compared to the comoving Hubble rate¹, which redshifts during radiation domination as $aH \propto a^{-1}$. Since the Hubble rate decreases more slowly, tachyonic production is either efficient right away or never, allowing for no sensible $\tau \rightarrow 0$ limit. This goes to show that the dynamics of dark photon production cannot be studied independently of the process causing the initial velocity. We therefore study a concrete implementation in the following.

V.2.1 Generation of finite ALP Velocity

Kinetic misalignment was proposed in [68, 140] as a mechanism to generate a finite ALP velocity. This scenario is inspired by Affleck-Dine baryogenesis [151, 152], where rotations of scalar particles are induced via higher-dimensional operators. To begin with, we identify the axion $\phi = \theta S$ as the angular component of a complex scalar field

$$P = \frac{1}{\sqrt{2}} S \exp(i\theta) . \quad (\text{V.1})$$

The radial component S is called saxion² in the following and determines the effective decay constant $f_{\text{eff}} = S$, which is identical to the ALP decay constant f_ϕ when S takes its vacuum expectation value (VEV) at $\langle S \rangle = f_\phi$. As a concrete realization, we choose a quartic potential

$$V(P) = \lambda^2 \left(|P|^2 - \frac{f_\phi^2}{2} \right)^2 + V_{\mathcal{PQ}} \quad (\text{V.2})$$

for the field P , where the coupling constant is defined as $\lambda = m_{S,0}/(\sqrt{2}f_\phi)$, with $m_{S,0}$ being the vacuum mass of the saxion. We assume that the $U(1)_{\mathcal{PQ}}$ symmetry is explicitly broken in the UV by the higher-dimensional operator

$$V_{\mathcal{PQ}} = \frac{AP^n}{n m_{\mathcal{PQ}}^{n-3}} + \text{h.c.} \quad (\text{V.3})$$

Here, A denotes the dimensionful coupling and n gives the mass dimension. These terms may be motivated by quantum gravitational effects at high energies for instance, or if the $U(1)_{\mathcal{PQ}}$ symmetry is generated as an accidental symmetry via other exact symmetries. The crucial point is that $V_{\mathcal{PQ}}$ generates an angular gradient in the potential at large field values, which may induce a rotation of P that is related to a \mathcal{PQ} charge density

$$n_{\mathcal{PQ}} = i\dot{P}^* P - i\dot{P} P^* = S^2 \dot{\theta} \quad (\text{V.4})$$

Hence, the angular motion corresponds to a non-zero ALP kinetic energy. As the impact of the higher-dimensional term vanishes rapidly due to cosmic expansion, the $U(1)_{\mathcal{PQ}}$ symmetry is effectively restored as the Universe cools down. Due to charge conservation, the ALP continues to rotate around its potential.

V.2.2 Initial Conditions

We assume that the radial component S is driven to large field values during inflation. This is a valid assumption if the quartic potential is sufficiently flat or $m_{S,0} \ll H_I$, with

¹In the previous chapter we compared the growth rate to the mass of the axion, which was always larger than the Hubble rate, once the axion started rolling. This bound was therefore satisfied trivially.

²Despite following the common nomenclature, we do not assume supersymmetry in this work.

$H_I \leq 6 \times 10^{13}$ GeV being the maximum Hubble scale during inflation [153]. Since this is given in the entire parameter space we consider, we take the saxion to be initially displaced from its minimum at a value S_i , which we treat as a free parameter in the following. In a radiation dominated universe, P starts to roll when the Hubble parameter decreases to the order of the effective saxion mass at S_i , which reads

$$m_{S_i} = \sqrt{\frac{\partial^2 V}{\partial S^2}} \Big|_{S=S_i} = \sqrt{3\lambda} S_i \quad . \quad (\text{V.5})$$

We denote with the subscript S_i the quantities when the saxion becomes free to oscillate once $3H_{S_i} = m_{S_i}$. The key quantity to compute is the angular velocity that arises via the angular gradient induced by $V_{\mathcal{P}\mathcal{Q}}$. In order to do so, we follow the approach from Refs. [68, 140] and introduce the quantity

$$\epsilon \equiv \frac{n_{\mathcal{P}\mathcal{Q}}}{n_S} \quad , \quad (\text{V.6})$$

that parameterizes the ratio of the charge density in the rotation and the saxion number density, which is given as $n_{S_i} = V_0(S_i)/m_{S_i}$. Hence, ϵ gives a measure of the shape of the path that P follows, with $\epsilon = 1$ corresponding to a purely circular trajectory. Thus the axion velocity right after the kick by $V_{\mathcal{P}\mathcal{Q}}$ may be expressed as

$$\dot{\phi}_{S_i} = \frac{\epsilon}{4\sqrt{3}} \lambda S_i^2 \quad . \quad (\text{V.7})$$

It can be shown that ϵ is related to the dimensionful coupling A and the mass dimension n of $V_{\mathcal{P}\mathcal{Q}}$ as well as the initial angle θ_i , assuming that P starts at rest. However, in this work we set $\epsilon = 1$ for simplicity. As before we consider the dark photon to be in Bunch-Davies vacuum initially.

V.2.3 Dynamics

Before investigating the process of dark photon and gravitational wave production, it is worth to study the scaling behaviour of the system during the different stages of the evolution. As long as $S \gg f_\phi$, P rotates in a quartic potential, hence mimicking the scaling behaviour of radiation, and it follows that

$$\dot{\phi} \propto a^{-2}, \quad \rho_\phi \propto a^{-4}, \quad S \propto a^{-1}. \quad (\text{V.8})$$

During this phase of the evolution, $\Omega_\phi = \text{const.}$ up to changes in the relativistic degrees of freedom, unless photon production becomes effective. As the value of the saxion field decreases while the Universe expands, the radius of the circular trajectory approaches the ALP decay constant. When $S = f_\phi$, P enters the minimum of the potential. We then obtain a kination-like scaling behaviour

$$\dot{\phi} \propto a^{-3}, \quad \rho_\phi \propto a^{-6}, \quad S = \text{const.} \quad (\text{V.9})$$

From this moment, the radial degree of freedom takes a constant value. We thus regard the ALP independently. The usual, cosine-like ALP potential as given by Eq. (II.3) then corresponds to a tilt of the total potential from Eq. (V.2). When the kinetic energy of the ALP becomes comparable to the height of the potential barriers $V_{\text{max}} = 2m_\phi^2 f_\phi^2$, the system enters a phase of matter-like scaling. Hence, the respective scale factor dependencies read

$$\dot{\phi} \propto a^{-3/2}, \quad \rho_\phi \propto a^{-3}, \quad (\text{V.10})$$

when the axion is trapped and behaves like DM as oscillations around the minimum start.

V.2.4 Model Constraints

As before we consider the case that the energy in the dark sector is subdominant at all times. For this condition to be met initially we require

$$S_i \lesssim m_{\text{Pl}}. \quad (\text{V.11})$$

Additionally, we may define the parameter range where kinetic misalignment is active. That is the case if the kinetic energy of the rotation dominates over the height of the potential barriers of the usual axion potential (Eq. (IV.2)) when the axion enters the bottom of the Mexican hat at $a_{S=f_\phi} = a_{S_i} \cdot S_i/f_\phi$. With the use of Eq. (V.7), this constraint may be translated to $\epsilon m_{S,0} \gtrsim 20m_\phi$ under the assumption that the tachyonic window has not opened yet, since dark photon production would act as friction decreasing the ALP velocity.

Before including the dark vector dynamics in the next section, let us comment on the validity of the axion-dark photon coupling within the present framework. An effective operator as given in Eq. (IV.1) may be generated by integrating out a heavy fermion ψ charged both under $U(1)_X$ and $U(1)_{\text{PQ}}$,

$$\mathcal{L} \supset y_\psi P \bar{\psi} \psi + \text{h.c.} . \quad (\text{V.12})$$

Requiring that the fermion is heavy enough to not be produced thermally sets a lower bound on y_ψ . Through loop corrections a large value of y_ψ also leads to a large value of λ and therefore to a possible conflict with our initial conditions if the initial saxion mass m_{S_i} is larger than the Hubble rate during inflation. Combining these constraints we obtain

$$\left(\frac{30}{16\pi^4 g_{\rho, S_i}} \right)^{1/4} \left(\frac{m_{\text{Pl}}}{S_i} \right)^{1/2} < 1, \quad (\text{V.13})$$

which gives a lower bound on the initial saxion field value, with a weak dependence on the saxion mass through the energetic degrees of freedom at the time the saxion starts to roll.

V.3 Dark Photon Production

In this section, we introduce the dark photons under the assumption of a finite ALP velocity. In particular, we study the conditions for successful tachyonic growth and give an analytic estimate of their growth time. In addition, we provide the results of the numerical simulation.

V.3.1 Tachyonic Instability

Now that we know the dynamics of the saxion and axion respectively, we can estimate the conditions for efficient dark photon production. To do so, we generalise the dispersion relation Eq. (IV.6) by taking into account that the radial component of the complex field P is no longer fixed at f_ϕ

$$\omega_\pm^2(k, \tau) = k^2 \pm k \frac{\alpha}{S} \phi'. \quad (\text{V.14})$$

Just like in the standard audible axion case discussed above, the fastest growing mode and the corresponding comoving growth rate are given by $k_{\text{peak}}(\tau) = \frac{\alpha}{2S(\tau)} |\phi'(\tau)|$. For tachyonic production to be efficient, the physical rate k_{peak}/a needs to be larger than the

Hubble rate H . While the saxion rolls down the quartic part of the potential, we have $S \propto a^{-1}$ and $\dot{\phi} \propto a^{-2}$ such that the growth rate scales as

$$k_{\text{peak}}/a = \frac{\alpha}{2S(\tau)} |\dot{\phi}(\tau)| = \frac{\alpha}{2S_i} |\dot{\phi}_{S_i}| \frac{a_{S_i}}{a} \propto a^{-1}, \quad (\text{V.15})$$

which is slower than the Hubble rate during radiation domination, $H \propto a^{-2}$. On the other hand, once the saxion has settled in its minimum with $S = f_\phi$, the kination scaling sets in and the growth rate is diminishing faster than the Hubble rate

$$k_{\text{peak}}/a = \frac{\alpha}{2f_\phi} |\dot{\phi}(\tau)| = \frac{\alpha}{2f_\phi} |\dot{\phi}_{S=f_\phi}| \left(\frac{aS=f_\phi}{a} \right)^3 \propto a^{-3}. \quad (\text{V.16})$$

Using the scaling of the Hubble rate H , that additionally takes into account changes in degrees of freedom, we can calculate the scale factor a_* at which the tachyonic window opens up

$$\frac{a_*}{a_{S_i}} = \frac{8}{\alpha\epsilon} \left(\frac{g_{\rho,*}}{g_{\rho,S_i}} \right)^{1/2} \left(\frac{g_{s,S_i}}{g_{s,*}} \right)^{2/3}, \quad (\text{V.17})$$

where g_ρ and g_s denote the effective degrees of freedom with respect to energy and entropy at the corresponding times. Since $\epsilon \leq 1$ and the fine structure constant is also expected to be small, we find that, initially, there is no tachyonic photon production. We can then distinguish three cases:

1. $a_* < a_{S=f_\phi}$: Dark photon production becomes efficient before the saxion takes on its VEV. In this case we expect efficient production at least until $S \approx f_\phi$, when the growth rate starts diluting faster than the Hubble rate.
2. $a_* \sim a_{S=f_\phi}$: In this case we only expect a very short period of tachyonic particle production, since, right after the window opens, it closes again due to the onset of the kination regime. Whether an $\mathcal{O}(1)$ fraction of the axion energy can be transmitted to the dark photon, which is required for GW emission, strongly depends on the exact time it takes the photon modes to grow, which we will study in the next section.
3. $a_* > a_{S=f_\phi}$: In this case the phase in which the growth rate increases relative to the Hubble rate is too short, such that kination sets in before the tachyonic window opens. Therefore, the production of photons is never efficient and only axion fragmentation might take place as discussed in Chapter III.

It is therefore clear that there exist a threshold α_{min} above which the tachyonic window opens. This threshold can be found from $a_* = a_{S=f_\phi}$ to be

$$\alpha_{\text{min}} = \frac{8}{\epsilon} \left(\frac{g_{\rho,*}}{g_{\rho,S_i}} \right)^{1/2} \left(\frac{g_{s,S_i}}{g_{s,*}} \right)^{2/3} \frac{f_\phi}{S_i}. \quad (\text{V.18})$$

Since $f_\phi \ll S_i$ and with $\epsilon = \mathcal{O}(0.1 - 1)$ there is a large parameter space in the kinetic misalignment scenario, where tachyonic production is possible without requiring $\alpha > 1$ as in the original audible axion scenario. Although large values of α can be achieved as shown in Refs. [86, 154], the small value of α allows for simpler UV completions.

V.3.2 Growth Time

So far we have only discussed when tachyonic production of dark photons starts. For efficient GW production it is however necessary that the majority of the axion energy is transferred to the photon. Since we assume there is initially no photon population except for vacuum fluctuations, there elapses some time between the onset of tachyonic production at τ_* and the emission of GWs at τ_{GW} .

While the dark photon is in the Bunch-Davies vacuum the energy in the resonance band is

$$\rho_{X,*} = \frac{1}{a_*^4} \frac{k_{\text{peak},*}^4}{16\pi^2} \quad (\text{V.19})$$

This energy needs to grow up to $\rho_{\phi,*} = \frac{1}{2}\dot{\phi}_*^2$ before GWs are emitted. The resulting time delay can be estimated as

$$\frac{\delta\tau}{\tau_*} = \frac{a_* H_*}{2k_{\text{peak},*}} \log\left(\frac{\rho_{\phi,*}}{\rho_{X,*}}\right) = \frac{1}{2} \log\left(\frac{\rho_{\phi,*}}{\rho_{X,*}}\right). \quad (\text{V.20})$$

If the Universe is dominated by a radiation bath, this can be re-expressed as the redshift $a_{\text{GW}}/a_* = 1 + \frac{\delta\tau}{\tau_*}$.

In Fig. V.1 we show the results of a simulation that was started at a_* , right as the dark photon production becomes efficient. We can see the growth rate k_{peak}/a starting to dominate over the Hubble rate. Around a_{GW} , as calculated with the formula above and marked by the black dotted line, the growth rate deviates from the analytic estimate, as a result of the axion slowing down due to the friction from dark photon production. This effect also becomes apparent in the bottom panel, where we can see the dark photons energy dominating over the axion soon after a_{GW} . After this point, the growth rate oscillates. Its mean, however, takes on a constant ratio with respect to the Hubble rate. This can be understood as the growth rate regulating itself: A large growth rate results in more efficient dark photon production, more friction on the axion and therefore a decrease in the growth rate.

Eventually, the saxion settles down at its VEV f_ϕ at $a_{S=f_\phi}$ marked by the black, dash-dotted line. From here on out, the dark photon growth rate starts to decrease compared to the Hubble, due to the stronger effect of Hubble friction during kination scaling, and dark photon production becomes ineffective. As a consequence, we can see the energy densities taking on the expected scaling behaviors before we eventually stop the simulation, once the growth rate becomes smaller than the Hubble.

Before we conclude this section, let us briefly comment on the dark photon abundance and the resulting N_{eff} bound. Even if one makes the assumption that all of the axions energy is converted to dark photons, one finds that the contribution to N_{eff} is small compared to the current bounds as long as one stays within the bounds of $\epsilon < 1$ and $S_i < m_{\text{Pl}}$.

V.3.3 Simulation

For our numerical analysis we adopt the linear analysis developed in Ref. [3]. We solve the coupled system of 10^5 dark photon modes with linearly spaced momenta in the range $0 < k \leq \alpha\phi'_*/S_*$, which corresponds to the tachyonic window at the start of the simulation at $a = a_*$, and the homogeneous axion field ϕ . For the saxion field we assume however, that it follows the analytic scaling. That is

$$S(\tau) = \begin{cases} \frac{a_*}{a(\tau)} S_* & a(\tau) < a_{S=f_\phi} \\ f_\phi & a(\tau) \geq a_{S=f_\phi} \end{cases}. \quad (\text{V.21})$$

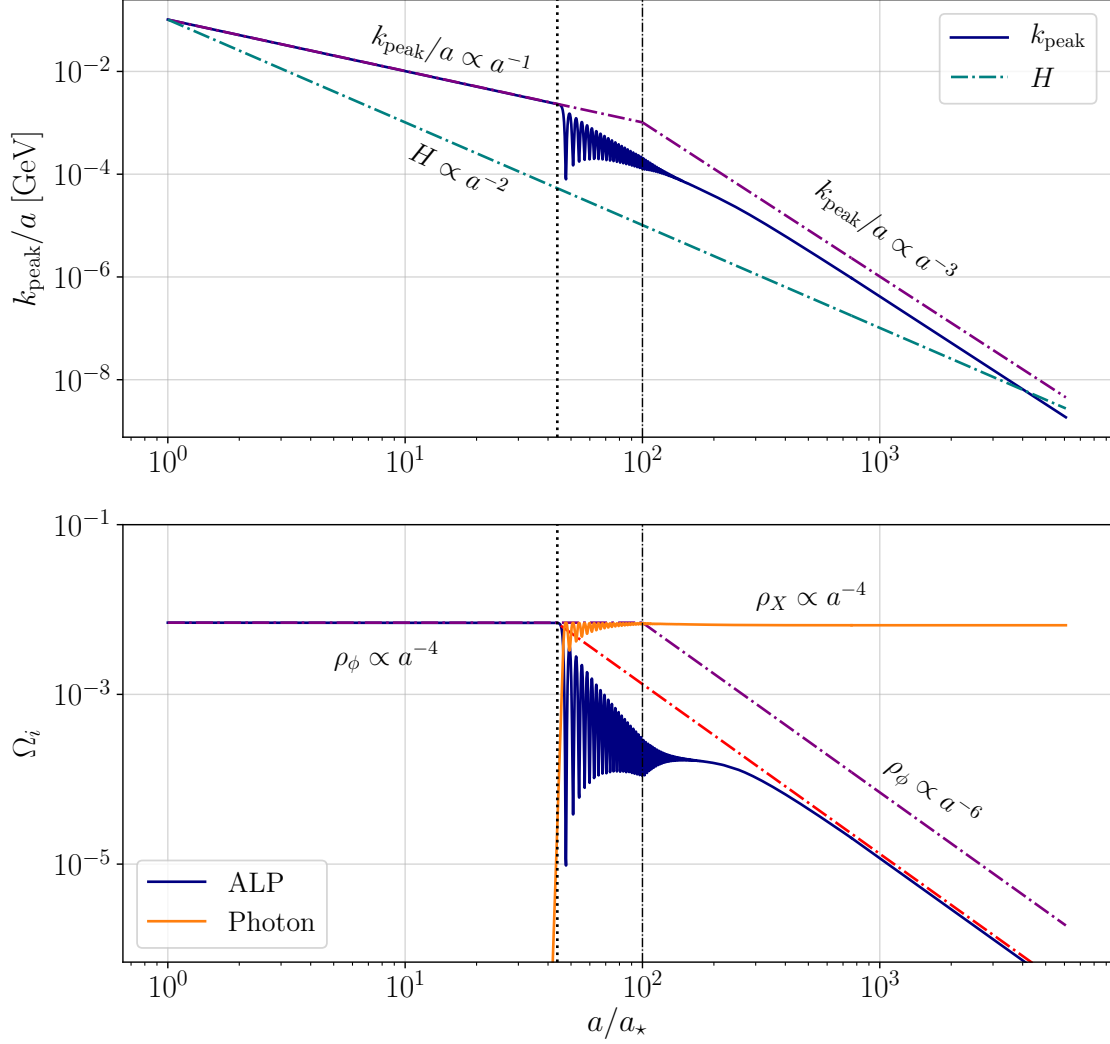


Figure V.1: Comparison of rates and energy densities between a numerical simulation and analytic scaling relations for $S_i = 2 \times 10^{18}$ GeV, $m_{S,0} = 1$ GeV, $f_\phi = 5 \times 10^{13}$ GeV, $\alpha = 0.02$ and $\epsilon = 1$. We start the simulation when the Hubble rate coincides with the dark photon growth rate k_{peak}/a at $a = a_*$. In the top panel we show the growth rate in dark blue dominating over the Hubble rate. At $a_{\text{GW}}/a_* \approx 43$ marked by the black dotted line, the growth rate deviates from the analytic scaling behavior shown as the purple, dash-dotted line. The reason for this discrepancy can be found in the bottom panel, where we can see the dark photon energy becoming comparable to the one of the axion around this time. Friction from dark photon production becomes efficient and the growth rate, which is proportional to the axions velocity, decreases faster as by the scaling only considering Hubble friction. The dash-dotted black line marks the saxion field settling at its VEV f_ϕ at $a_{S=f_\phi}$. Afterwards the photon production quickly becomes inefficient and all quantities take on their respective scaling behaviors, although with the growth rate and axion energy reduced due to friction from the photons. The relic ALP abundance after dark photon production is well matched by the red dash-dotted line, which denotes a kination-like scaling starting at a_{GW} . Since we observe this behavior throughout all our simulations, we will use this as an analytic estimate of the minimum relic ALP abundance in Section V.5.1. Simulation and figure created by D. Schmitt.

The axion EOM then takes the form

$$\phi'' + n(\tau)aH\phi' + a^2\frac{\partial V}{\partial\phi} = -\frac{\alpha}{S(\tau)}a^2\langle 0|\mathbf{E}\cdot\mathbf{B}|0\rangle, \quad (\text{V.22})$$

where we take

$$n(\tau) = \begin{cases} 1 & \text{if } a(\tau) < a_{S=f_\phi}, \\ 2 & \text{if } a(\tau) \geq a_{S=f_\phi}, \end{cases} \quad (\text{V.23})$$

in order to account for the effect of the radial saxion mode on the circular motion before the saxion settles. Note further that, for the back-reaction of the photon modes on the axion, we have to take the expectation value, since we are only considering the motion of the homogeneous axion field, $\mathbf{E}\cdot\mathbf{B} \rightarrow \langle 0|\mathbf{E}\cdot\mathbf{B}|0\rangle$. As shown in Refs. [3, 86], this expectation value can be expressed as an integral including the mode functions, which in our simulation is approximated by summing over the simulated mode functions.

Let us briefly comment on the two main assumptions that we made in our analysis. The first is that the motion of the saxion field S can be treated independently. Imagine for simplicity a scenario where the full field $P = S/\sqrt{2} \exp(i\phi/S)$ is on a circular track with the radius S slowly changing due to Hubble friction, initially. Even in this idealized scenario the field would leave this circular track once friction from photon production diminishes the rotational momentum. However the main characteristics of the photon and GW spectrum would be set before these effects become sizeable. Furthermore, once the saxion S starts varying rapidly, the effective field theory (EFT) in which the degrees of freedom leading to the coupling between the axion and photons, presumably fermions, have been integrated out is not valid anymore. At this point, also our semi-classical treatment of the system breaks down and, to our knowledge, there is no method to treat such a system so far. We therefore stick to the pragmatic approach here of calculating what we can, knowing that the main observables, the features of the GW spectrum, will be estimated correctly.

The second assumption is that the axion stays homogeneous throughout the evolution. Since the dark electric and magnetic fields are inhomogeneous, as becomes clear from their non-vanishing momenta in Fourier space, the backreaction onto the axion will introduce inhomogeneities. The effects of this deviation from our assumption have been studied in detail in the previous section as well as Refs. [4, 81–83, 113]. As we saw before including the inhomogeneities has some minor influence on the GW spectrum but more crucially allows one to accurately calculate the axion abundance. In Section V.5.1 we therefore only give a lower and upper bound. Perhaps one might think that the second point can be fixed by running a lattice simulation as in the previous chapter. However, related to the first point, it is not clear how to integrate the radial motion in such an analysis. If one simply neglects it or makes simplifying assumptions like we did in the linear analysis, one has to wonder whether one really gained any precision, which is why we decided to leave it at the linear analysis.

V.4 Gravitational Wave Spectra

As we have seen in the previous chapter, the exponential growth of the dark photons mode functions is associated with a sizeable anisotropic stress that leads to the emission of GWs. Below we first give an analytic estimate of the signal amplitude and compare to the results of the simulation.

V.4.1 Analytic Estimates

As discussed in Section V.3.2, GW emission occurs at the time τ_{GW} , which is delayed from the time τ_* , at which the tachyonic production starts, by the growth time of the dark photon modes. Assuming that the SGWB is generated instantaneously at τ_{GW} , a simple estimate of the peak position of the resulting GW spectrum can be obtained as follows.

Following again the discussion in Ref. [3] the GW peak is approximately given by twice the dark photon peak momentum at the time of GW production, so that we obtain the GW peak momentum \tilde{k}_{GW} ,

$$\tilde{k}_{\text{GW}} \approx 2 k_{\text{peak}} = \frac{\alpha^2 \epsilon^2}{32\sqrt{6}} \frac{m_{S,0} S_i}{f_\phi} \left(\frac{g_{\rho, S_i}}{g_{\rho, \text{GW}}} \right)^{\frac{1}{2}} \left(\frac{g_{s, \text{GW}}}{g_{s, S_i}} \right)^{\frac{2}{3}} \frac{\tau_*}{\tau_{\text{GW}}} a_{\text{GW}}, \quad (\text{V.24})$$

where we assumed that GW emission occurs before the saxion reaches its minimum, i.e. $S > f_\phi$, so that k_{peak}/a_* is given by Eq. (V.15). Note that $S_i \sim m_{\text{Pl}}$ is required to obtain a sufficiently large angular velocity to generate an observable GW signal, whereas occurrence of tachyonic production constrains α/f_ϕ . Hence, the peak momentum is predominantly set by the saxion mass parameter $m_{S,0}$.

As before we estimate the GW amplitude at the peak of the spectrum as [3, 155, 156]

$$\Omega_{\text{GW}} = c_{\text{eff}} \Omega_{\phi, \text{GW}}^2 \left(\frac{H_{\text{GW}}}{\tilde{k}_{\text{GW}}^{\text{phys.}}} \right)^2 = c_{\text{eff}} \left(\frac{\epsilon S_i}{m_{\text{Pl}}} \right)^4 \left(\frac{a_*}{a_{\text{GW}}} \right)^2 \frac{g_{\rho, S_i}^2}{g_{\rho, \text{GW}} g_{\rho, *}} \left(\frac{g_{s, \text{GW}} g_{s, *}}{g_{s, S_i}^2} \right)^{\frac{4}{3}}, \quad (\text{V.25})$$

where the factor c_{eff} accounts for the efficiency of converting the energy initially stored in the axion into GWs. The second part of the equation is obtained using that efficient dark photon production starts when the tachyonic window opens at $a_* H_* = k_{\text{peak}}$, as well as that the axion energy density $\rho_\phi = \frac{1}{2} \dot{\phi}^2$ redshifts as radiation for $S > f_\phi$. The present day values for the frequency of the GW as well as their amplitude are obtained by redshifting using the formulas in Appendix A. Note that, fixing $\epsilon = 1$ at its maximal value, the energy budget, and, correspondingly, the peak amplitude, are predominantly determined by the initial saxion field value S_i , with only a weak dependence on other model parameters through the effective degrees of freedom and the growth time delay τ_{GW}/τ_* .

Similar to the audible axion scenario discussed above, we expect the spectrum to drop sharply above the peak, as the generation of GWs with momenta $|\mathbf{k}| > \tilde{k}_{\text{GW}}$ requires that also the contributing dark photon modes have momenta $|\mathbf{q}|, |\mathbf{k} - \mathbf{q}| > k_{\text{peak}}$. Furthermore, as only one dark photon polarization is produced, the GW spectrum will also be chiral. In the low frequency tail, on the other hand, for frequencies corresponding to momenta on super-horizon scales at production, the spectrum should behave as k^3 based on causality arguments [48, 157] (cf. also Ref. [150]).

V.4.2 Numerical Calculation

To corroborate the analytic estimates from Section V.4.1, and to further obtain the spectral shape of the generated SGWB, the GW spectrum is also calculated numerically from the simulation discussed in Section V.3.3, using a subset of 200 of the 10^5 simulated modes. The computation follows the procedure in Ref. [3].

The left panel of Fig. V.2 shows the resulting GW spectrum at the time of emission. The solid line depicts the total spectrum, whereas the dot-dashed lines indicate the respective contributions from the positive and negative GW helicity. As expected, the resulting spectrum is dominated by the positive helicity contribution, corresponding to the sign of

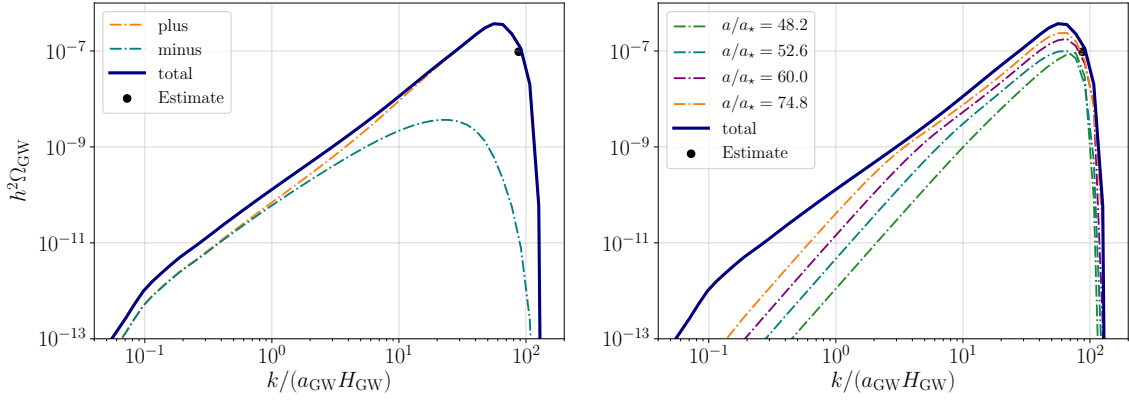


Figure V.2: GW spectrum as a function of the physical momentum k/a_{GW} normalized to the Hubble rate at emission calculated from the same simulation as Fig. V.1. The black dots indicates the estimate in Eq. (V.25). **Left:** GW spectrum at the time of emission. The solid blue curve depicts the total spectrum, whereas the dot-dashed orange and cyan curves correspond to positive and negative GW helicities, respectively. **Right:** Total GW spectrum at different times. Figure created by D. Schmitt.

the initial axion velocity. The GW helicity picks up contributions from the photon helicity as well as orbital angular momentum, which is why the spectrum is only partially polarized as described in Ref. [3]. Although as we saw in the previous chapter no conclusion can be made about the size of the polarization without accounting for the inhomogeneities in the axion field. The analytic estimate Eq. (V.25) provides a good approximation of the peak position, assuming an efficiency factor of $c_{\text{eff}} = 1$. The right panel of the figure illustrates the time dependence of the GW spectrum, showing the spectrum at different stages during the simulation. As can be seen from the figure, efficient GW emission occurs early on, with comparably little additional GWs emitted at later times. The GW peak is already pronounced at $a/a_* = 48.2$, which agrees well with the estimate of the GW emission time $a_{\text{GW}}/a_* \sim 43$ obtained in Section V.3.2.

To allow for an efficient evaluation of the detectability over the parameter space without the necessity to run the numerical simulation for every single parameter point, we use the analytic estimates in Eq. (V.24) and Eq. (V.25) to infer the spectrum from the one shown in Fig. V.2.³

V.5 Relic Abundances

In the following, we compute the relic ALP abundance. Here, we distinguish the cases where the pseudoscalar represents an ALP or the QCD axion itself, respectively. In addition, we consider the possibility for the dark vectors to constitute dark matter and the conditions for successful axiogenesis.

V.5.1 ALP Dark Matter

As discussed in Section V.2.3, assuming a slight tilt in the potential of the complex scalar P , the potential effectively behaves as a cosine potential for the axion, cf. Eq. (IV.2),

³We here don't use the spectrum from the simulation directly as in Section IV.6, but instead use a fit to the peak consisting of a powerlaw in the IR and an exponential decay in the UV. The details can be found in the original publication [5].

once its kinetic energy has been diluted and becomes comparable to the height of the potential barriers, $\dot{\phi}/2 = 2m_\phi^2 f_\phi^2$. The circular motion of the ALP then ends, and it starts to oscillate around the minimum of the cosine potential. Its energy density subsequently scales like matter, rendering the kinetically misaligned axion a candidate for DM, similar to the standard misalignment case.

As discussed before the axion abundance can only be reliably estimated using a lattice simulation. Here, we limit ourselves to the estimation of a maximum and suppressed abundance scenario.

Maximum abundance:

In this case, we ignore the energy transfer from the ALP to the dark photon. The relic abundance is then exclusively determined by the dynamics described in Section V.2.3. The ALP kinetic energy scales kination-like between the time the saxion settles at its minimum to the start of the oscillations when $\dot{\phi}_{\text{osc}}^2/2 = 2m_\phi^2 f_\phi^2$, hence,

$$\left(\frac{a_{S=f_\phi}}{a_{\text{osc}}}\right)^3 = \frac{2m_\phi f_\phi}{\dot{\phi}_{S_i}} \left(\frac{a_{S=f_\phi}}{a_{S_i}}\right)^2. \quad (\text{V.26})$$

The maximal fractional energy density of the ALP at MR equality thus becomes

$$\begin{aligned} \Omega_{\phi,\text{eq,max}} &= \frac{\rho_{\phi,S_i}}{\rho_{\text{rad,eq}}} \left(\frac{a_{S_i}}{a_{S=f_\phi}}\right)^4 \left(\frac{a_{S=f_\phi}}{a_{\text{osc}}}\right)^6 \left(\frac{a_{\text{osc}}}{a_{\text{eq}}}\right)^3 = \frac{m_\phi f_\phi \dot{\phi}_{S_i}}{\rho_{\text{rad,eq}}} \frac{a_{S=f_\phi}}{a_{S_i}} \left(\frac{a_{S_i}}{a_{\text{eq}}}\right)^3 \\ &\simeq 0.23 g_{\rho,S_i}^{-1/4} \frac{g_{s,\text{eq}}}{g_{\rho,\text{eq}}} \epsilon \left(\frac{S_i}{m_{\text{Pl}}}\right)^{3/2} \left(\frac{f_\phi}{m_{S,0}}\right)^{1/2} \frac{m_\phi}{T_{\text{eq}}}, \end{aligned} \quad (\text{V.27})$$

where we make the approximation $g_{\rho,S_i} = g_{s,S_i}$, which is a valid assumption in all of the considered parameter space.

Suppressed abundance:

In reality, a fraction of the ALP energy density is transferred to the dark gauge field such that the final relic abundance is suppressed. As observed in our simulations (cf. Fig. V.1), the relic ALP abundance after the tachyonic phase may be well approximated by an earlier onset of the kination-like scaling behavior at a_{GW} instead of $a_{S=f_\phi}$, and correspondingly an earlier start of the axion oscillations. Our estimate for the suppressed abundance is hence obtained replacing $a_{S=f_\phi}$ in Eq. (V.26) and the first line of Eq. (V.27) by a_{GW} . Therefore,

$$\Omega_{\phi,\text{eq,min}} = \Omega_{\phi,\text{eq,max}} \frac{a_{\text{GW}}}{a_{S=f_\phi}} = \Omega_{\phi,\text{eq,max}} \frac{f_\phi}{S_i} \frac{a_*}{a_{S_i}} \frac{a_{\text{GW}}}{a_*}, \quad (\text{V.28})$$

where the last two terms are given in Eq. (V.17) and Section V.3.2.

V.5.2 QCD Axion and Axionogenesis

If we take the ALP to be the QCD axion, we have to keep in mind that the zero temperature mass $m_{\phi,0}$ and decay constant f_ϕ are no longer independent parameters, but related by the QCD topological susceptibility [158] via

$$m_{\phi,0} = \frac{(78 \text{ MeV})^2}{f_\phi}. \quad (\text{V.29})$$

In addition, the interaction with the thermal bath induces a suppression of the axion potential, potentially delaying the onset of oscillations. If the temperature at which axion oscillations start is smaller than the QCD scale, $T_{\text{osc}} < T_{\text{QCD}} \approx 200$ MeV, the discussion from the previous section applies. However, if $T_{\text{osc}} > T_{\text{QCD}}$, the QCD axion undergoes an extended phase of kination-like scaling compared to the ALP from Section V.5.1, since oscillations are then delayed until T_{QCD} . As the kinetic energy then is negligible comparable to the height of the potential barriers, the energy density in the ALP field at T_{QCD} is determined by the potential energy. Hence, in this scenario the relic axion abundance is the same as obtained from the conventional misalignment mechanism [159].

As previously pointed out [140], the rotating QCD axion provides the possibility of successful electroweak baryogenesis. The PQ asymmetry stored in the rotation is transferred to the quark sector via QCD sphalerons. Subsequently, the chiral asymmetry is translated into the $B + L$ asymmetry by electroweak sphaleron transitions that become strongly suppressed at the electroweak phase transition (EWPT). Hence, the rotating axion constantly sources the baryon asymmetry which freezes in once the electroweak symmetry spontaneously breaks. Following the result from Ref. [140], the normalized baryon asymmetry induced by the rotation is given by

$$Y_B = \frac{n_B}{s} = \frac{45 c_B}{2 g_{s,\text{ws}} \pi^2 T} \Big|_{T=T_{\text{ws}}}, \quad (\text{V.30})$$

where $c_B \simeq 0.1 - 0.15 c_W$, with c_W being the weak anomaly coefficient. The observed baryon asymmetry reads $Y_B^{\text{obs}} = 8.7 \times 10^{-11}$ [46], which may immediately be converted to the required angular velocity

$$\dot{\theta}_{\text{ws}} = \frac{\dot{\phi}_{\text{ws}}}{S} = \frac{2 g_{s,\text{ws}} \pi^2}{45 c_B} Y_B^{\text{obs}} T_{\text{ws}} = 5.1 \times 10^{-6} \times \frac{0.1}{c_B} \text{ GeV}, \quad (\text{V.31})$$

at $T_{\text{ws}} \sim 130$ GeV, which denotes the temperature where weak sphaleron transitions become ineffective. Since $T_{\text{ws}} > T_{\text{QCD}}$, the axion potential is flat when the baryon asymmetry freezes in, hence the pseudoscalar exhibits either a radiation- or kination-like scaling.

Therefore there are four cases that one has to distinguish when calculating $\dot{\theta}_{\text{ws}}$. In the first scenario the EWPT takes place before the saxion reaches its vev and one only has to consider the radiation like scaling of the velocity $\dot{\theta} \propto a^2$ between T_{S_i} and T_{ws} . If the it takes place after one additionally has to account for the phase of kination between $T_{S=f_\phi}$ and T_{ws} . From these two one obtains the other ones by taking into account whether dark photon production becomes efficient before T_{ws} . Similar to the axion relic abundance our simulations can't be trusted when it comes to predicting the axion velocity in this case. We again consider two limiting cases. The first one labeled *max* neglects the backreaction altogether and coincides with the estimates given above. In the second case labeled *min* we consider the axion velocity scaling to be kination like between T_{GW} and T_{ws} , just like in our estimates of the axion relic abundance.

We may now explore the parameter space that reproduces the observed baryon asymmetry. Since the GW amplitude mainly depends on the initial value of the radial degree of freedom, we fix $S_i = 2 \times 10^{18}$ GeV in the following to ensure the resulting signal lays within the reach of future observatories. Figure V.3 depicts the compatible region in the $f_\phi - m_{S,0}$ plane which are then the decisive parameters regarding the GW peak frequency. In terms of the gauge coupling, we fix $\alpha = 10^{-7}$, since a large coupling leads to an earlier onset of dark photon production, hence a larger decrease of the axion velocity such that the generated baryon asymmetry is not sufficient. As a consequence of this small coupling, the axion decay constant is constrained to $f_\phi \lesssim 4 \times 10^8$ GeV to have successful GW

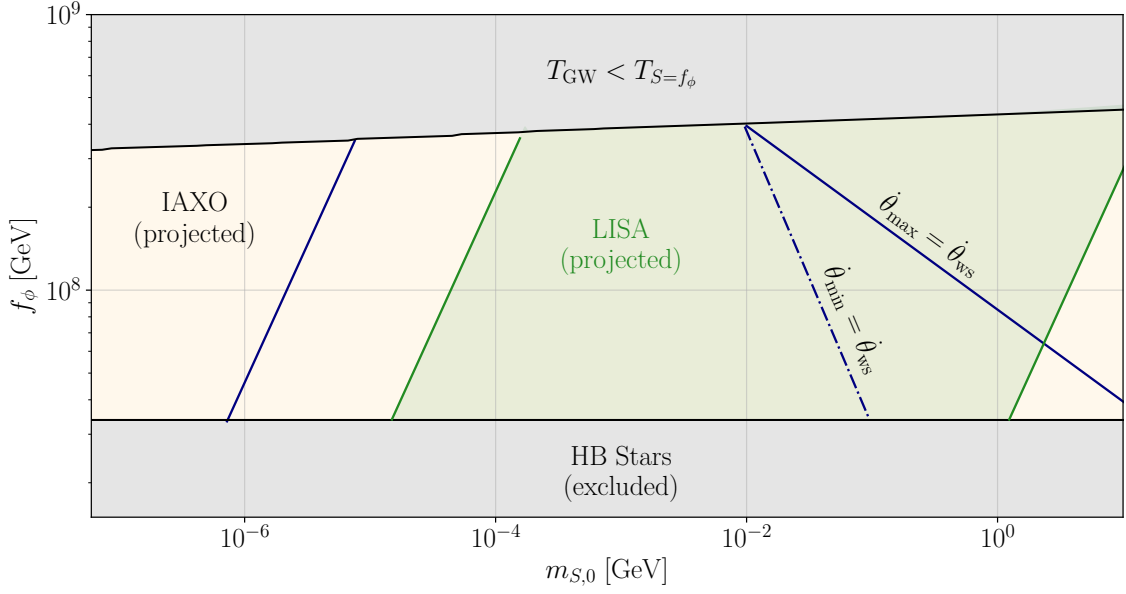


Figure V.3: Parameter space of the QCD axion for fixed benchmark parameters $S_i = 2 \times 10^{18}$ GeV and $\alpha = 10^{-7}$. On the blue lines the correct baryon symmetry is induced by weak sphaleron (WS) processes at the time of the electroweak phase transition. For large saxion masses this happens during or after the production of dark photons, where the predictability of our perturbative method is limited, which is why we show two limiting scenarios (straight and dash-dotted). In the future, the relevant parameter space may be probed by both direct axion searches such as the IAXO experiment (yellow shaded region), as well as the GW observatory LISA (green-shaded region) and potential follow-up experiments like μ ARES. Note that for the chosen parameters, the relic axion abundance corresponds to the one obtained from conventional misalignment and therefore only constitutes part of DM in the shown parameter region. Figure created by D. Schmitt.

emission. The straight blue lines in Fig. V.3 denote where the axion rotation may source the baryon asymmetry under the assumption of maximum velocity, hence no dark photon production.

For $m_{S,0} \gtrsim 5 \times 10^{-5}$ GeV, the EWPT takes place during the kination-like phase, since $T_{S=f_\phi} > T_{\text{ws}}$. Therefore the scaling behaviour changes between small and large saxion masses, considering the maximum velocity case. Regarding the minimum velocity scenario depicted by the dash-dotted line, we find that for successful axiogenesis, the baryon asymmetry needs to freeze in during GW production, hence $T_{S=f_\phi} < T_{\text{ws}}$ in this case. Regarding the prospect of observation, we find that most of the parameter space where axiogenesis is viable may be probed by LISA, as the green shaded region suggests. In addition, also the future projects BBO, B-DECIGO, and DECIGO are sensitive to the large $-m_{S,0}$ region. The small $-m_{S,0}$ part of the shown parameter space, however, may be targeted by the projected observatory μARES . In all of the shown parameter range the QCD potential appears so late, that the axion abundance is purely given through the normal misalignment mechanism. Assuming a misalignment angle $\theta_i = \mathcal{O}(1)$, the axion produces the correct DM abundance for $f_\phi \sim 3 \times 10^{11}$ GeV. We therefore expect the axion to only contribute a small fraction of the total DM density in the given scenario.

In order to check whether this parameter space can be tested by direct searches we relate f_ϕ to the coupling to the SM photon γ through the relation $g_{a\gamma\gamma} = -1.92/(2\pi)\alpha_{\text{em}}f_\phi^{-1}$ in the case of the KSVZ axion, with $\alpha_{\text{em}} = 1/137$. We then find that Primakoff axion losses in horizontal branch (HB) stars limit $f_\phi \gtrsim 3.4 \times 10^7$ GeV [160].⁴ Interestingly, the entire parameter region may be probed by the planned axion helioscope IAXO [161] for the chosen benchmark. Our model is therefore able to generate GWs over the entire range of decay constants, and we provide a multi-messenger approach for axion searches in the future, opening up parameter space that is simultaneously testable by both GWs as well as direct detection experiments.

V.5.3 Vector Dark Matter

If the dark photon is massive, it may in principle also constitute DM. This scenario is again subject to the previously discussed constraints, that the dark photon mass has to be small enough to not interfere with the tachyonic instability (Section IV.2.1) and the dark photons velocity stemming from the non-zero momentum has to be small enough to allow for structure formation (see Appendix A). The dark photon abundance is set around τ_{GW} by the axion transmitting the majority of its energy. This again allows one to estimate the relic abundance using that the dark photons number density is conserved past this point. By combining our findings for the dark photon relic abundance with the bound that its velocity must be small enough, we find

$$\epsilon S_i \lesssim 0.05 m_{\text{Pl}} \left(\frac{g_{\epsilon,\text{eq}}}{g_{\epsilon,S_i}} \right)^{1/2} \left(\frac{g_{s,S_i}}{g_{s,\text{eq}}} \right)^{2/3} \quad (\text{V.32})$$

as the condition on the initial saxion value in the scenario where it amounts to all of DM.

V.6 Main Results and Summary

Given the GW spectrum from Section V.4 and the relic abundances computed in Section V.5, we now evaluate the prospect of the presented model to both produce detectable

⁴Note that we do not include the potentially stronger bounds on the ALP coupling to nucleons from

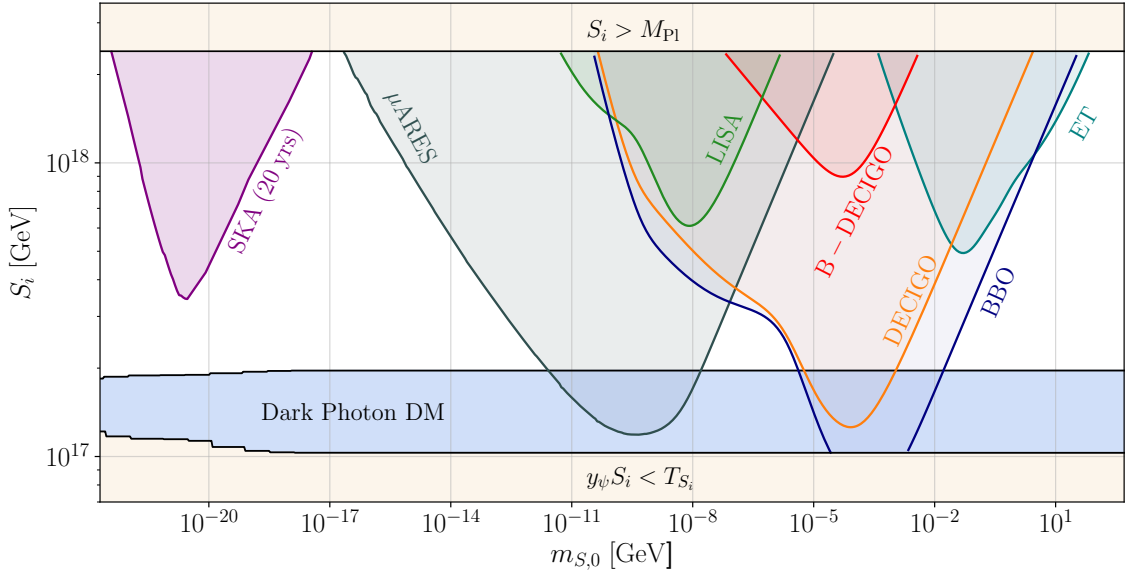


Figure V.4: The parameter regions in the $S_i - m_{S,0}$ plane that are testable in the future, for the benchmark parameters $f_\phi = 10^{12}$ GeV and $\alpha = 0.02$. Since the GW amplitude is independent of f_ϕ , the presented model provides detectable signals for any value of f_ϕ . Hence, also the parameter region that is subject to direct axion searches may be probed via GWs in the future. In the entire parameter space, the ALP can constitute DM, since the GW production is independent of m_ϕ . The blue shaded region marks where the dark photons, if they were massive, are sufficiently cold to be DM, but also do not overclose the Universe at T_{eq} . Figure created by D. Schmitt.

signals as well as provide viable DM candidates.

In Fig. V.4, we present the regions in the $S_i - m_{S,0}$ plane that may be probed by next-generation GW observatories. Here, we fix $f_\phi = 10^{12}$ GeV and $\alpha = 0.02$. As shown in Section IV.4.3, the amplitude of the GWs mainly depends on the initial value of the radial component S_i which sets the energy budget available to be converted into gravitational radiation. We find that $S_i \gtrsim 10^{17}$ GeV is required for the GWs to be within the reach of future detectors. For smaller values of S_i , it is also not ensured that the EFT is valid, since fermions with mass $y_\psi S_i$ are produced thermally then. The fact that S_i has to be close to the Planck scale can be understood from the fact that the energy sourcing the GWs now stems from the potential of the full complex field, rather than just its phase, the ALP. This lifts the constraint from the original audible axion model (Chapter IV) that f_ϕ has to be large and we now find a probeable parameter region for any f_ϕ as long as α is large enough to allow for efficient dark photon production. Smaller values of f_ϕ open up the possibility for multi-messenger ALP searches, as the ALP can be found in direct searches while sourcing detectable GWs (see discussion around Fig. V.3).

The frequency of the resulting GW spectrum is controlled by the gauge coupling α , the ALP decay constant f_ϕ and the saxion vacuum mass $m_{S,0}$. For the chosen parameters in Fig. V.4, detectable GWs are produced between 10^{-23} GeV $< m_{S,0} < 10^2$ GeV, where the low masses may be probed by PTAs and the larger masses lie within the reach of future interferometers. In Section V.5, we have computed upper and lower limits for a potentially massive dark photon to constitute DM. This bound evaluates to $S_i \lesssim 2 \times 10^{17}$ GeV, as

SN1987A, since they are less robust [160].

denoted by the blue shaded region in Fig. V.4. In that regime, the dark photons neither overclose the Universe at matter-radiation equality, nor violate the bounds from structure formation.

The ALP is however a viable dark matter candidate in all of the shown parameter space, simply because the ALP mass m_ϕ neither influences the GW frequency nor amplitude. Therefore there always exist a mass m_ϕ , such that the ALP abundance matches the observed DM density. Due to the uncertainties in calculating the ALP abundance discussed in Section V.5.1, we can however only determine a range for this value of m_ϕ . Notice that this is in stark contrast to the minimal audible axion model from Chapter IV, where the ALP mass controlled the frequency of the GWs as well as the relic abundance. This lead to the ALP over-closing the universe in the majority of parameter space with detectable GWs.

Rolling down a Slope: The Audible Relaxion

VI.1 Introduction

In this final section dealing with an ALP coupled to a dark photon, we will study in more detail the scenario, where a temperature and therefore time dependent ALP potential elevates the tension between observable GWs and an overproduction of ALP DM. We already alluded briefly to this idea in Section IV.5. While the idea must have seemed somewhat ad hoc in this context, exactly this situation arises in the original proposal [42] of the relaxion scenario out-lined in Section II.1: The Higgs mass is scanned during inflation. If the reheating temperature is higher than the electroweak scale, the Higgs vacuum expectation value (vev) vanishes after reheating, due to thermal corrections to the potential of the Higgs field, and as a consequence the barriers in the relaxion potential vanish as well. As a consequence the relaxion starts rolling down the slope again. Since the Hubble friction that kept the field from rolling fast during inflation is much reduced now after reheating, it is crucial that the barriers reappear quickly enough to keep the relaxion from going to the next minimum, in which case there would be nothing to keep the relaxion from rolling indefinitely and ruining the solution to the hierarchy problem. Not only does this scenario provide a time dependent potential, from a model building point of view it also motivates the introduction of a coupling between the relaxion and a dark photon as by means of generating additional friction. This additional friction can prevent the relaxion from crossing to the next minimum and therefore opens up new viable parameter space. In the following we discuss in detail the post-inflationary evolution of the relaxion assuming that the electroweak scale has been scanned during inflation and highlight the roll of a potential coupling to a dark photon. We evaluate the resulting GW signal and its detectability in the relaxion parameter space.

VI.2 Setup

In this section, we consider the relaxion ϕ coupled to a dark photon field X_μ introduced in Section II.1 and Chapter IV respectively. For convenience let us remind the reader of the main ingredients,

$$-\mathcal{L} \supset V(H, \phi) + \frac{\alpha}{4} \frac{\phi}{f_\phi} X_{\mu\nu} \tilde{X}^{\mu\nu}, \quad (\text{VI.1})$$

with the potential of the relaxion field ϕ and Higgs doublet H given by

$$V(H, \phi) = V_{\text{roll}}(\phi) + \mu_H^2(\phi) |H|^2 + \lambda |H|^4 + V_{\text{br}}(H, \phi), \quad (\text{VI.2})$$

where λ is the Higgs' quartic coupling and

$$V_{\text{roll}}(\phi) = -g\Lambda^3\phi, \quad (\text{VI.3a})$$

$$\mu_H^2(\phi) = \Lambda^2 - g'\Lambda\phi, \quad (\text{VI.3b})$$

$$V_{\text{br}}(H, \phi) = -\frac{\Lambda_{\text{br}}^4}{v_H^2}|H|^2 \cos \frac{\phi}{f_\phi}, \quad (\text{VI.3c})$$

where, $g \approx g'$ are dimensionless parameters, Λ is the Higgs mass cut-off scale, Λ_{br} is the back-reaction scale, $v_H = \langle |H| \rangle = 246 \text{ GeV}$ is the Higgs' vacuum expectation value, and f_ϕ is the decay constant of the relaxion.

We assume that during inflation the relaxion rolled down the linear slope of its potential V_{roll} and scanned the Higgs mass parameter $\mu^2(\phi)$. Once μ^2 crossed zero, the Higgs acquired a non-vanishing vacuum expectation value (vev), triggering the breaking of the EW gauge symmetry. The Higgs' vev then creates wiggles in the relaxion potential via V_{br} . Once the Higgs back-reaction balances the rolling potential, the relaxion is trapped in the first minimum it encounters. Choosing $g\Lambda^3 f_\phi \sim \Lambda_{\text{br}}^4$, we end up with a weak-scale expectation value for the Higgs boson, solving the hierarchy problem. The relaxion mass and the relaxion-Higgs mixing angle are then given as [162, 163]

$$m_\phi^2 \simeq \frac{\Lambda_{\text{br}}^6}{f_\phi^2 \Lambda v_H}, \quad \sin \theta_{h\phi} \simeq \sqrt{2} \left(\frac{m_\phi^4 f_\phi \Lambda^2}{v_H m_h^6} \right)^{\frac{1}{3}}, \quad (\text{VI.4})$$

in terms of the fundamental parameters. Here, $m_h = 125 \text{ GeV}$ is the Higgs mass.

VI.2.1 Relaxion and dark photon evolution

After reheating, the EW symmetry will be restored due to thermal corrections to the potential, provided that the reheating temperature is above the EW phase transition temperature. Reheating temperatures above the EW scale are well motivated by a large class of Inflation models (see e.g. [164] and Refs. therein) and also needed in most models that explain the observed baryon abundance (see e.g. [165] and Refs. therein). As a consequence, the relaxion will start rolling again, leading to exponential production of dark photon modes. The evolution of the relaxion field is given by the differential equation

$$\theta'' + 2aH\theta' + \frac{a^2}{f_\phi^2} \frac{\partial V_{\text{roll}}}{\partial \theta} = -\frac{a^2}{f_\phi^2} \frac{\alpha}{4a^4} \langle X_{\mu\nu} \tilde{X}^{\mu\nu} \rangle, \quad (\text{VI.5})$$

where $\theta = \phi/f_\phi$, and primes denote derivatives with respect to conformal time τ with $a d\tau = dt$. In the following we will assume that all dynamics take place during radiation domination, in which case the relationship $\tau = 1/(aH)$ holds. Furthermore we will work in the linear analysis, assuming that the relaxion field stays homogeneous, which necessitates taking the expectation value above (see Section V.3.3 for details).

Let us for now only consider the minimal scenario, in which the dark photon is not present. In this case the above equation can be solved to give the relaxions velocity

$$\theta'(\tau) = \frac{\Lambda_{\text{br}}^4}{5f_\phi^2} \left(\frac{a_{\text{rh}}}{\tau_{\text{rh}}} \right)^2 \tau^3 \left[1 - \left(\frac{\tau_{\text{rh}}}{\tau} \right)^5 \right], \quad (\text{VI.6})$$

after reheating at τ_{rh} , when the relaxion was at rest ($\theta'(\tau_{\text{rh}}) = 0$). Once the universe has cooled sufficiently, the EW phase transition occurs and the wiggles of the back-reaction

potential reappear. We can now calculate the total displacement of the relaxion due to rolling up to the time when the barriers reappear at τ_{ra}

$$\Delta\theta = \int_{\tau_{\text{rh}}}^{\tau_{\text{ra}}} d\tau \theta' \approx \frac{\Lambda_{\text{br}}^4}{20f_\phi^2} \frac{a_{\text{rh}}^2 \tau_{\text{ra}}^4}{\tau_{\text{rh}}^2} = \frac{m_\phi^2 \Lambda v_H}{20H_{\text{ra}}^2 \Lambda_{\text{br}}^2}. \quad (\text{VI.7})$$

In order for the relaxion to remain trapped in this minimum, we need to require that the displacement is less than the distance between the minimum and the next maximum, $\Delta\theta \lesssim 2\delta$, where $\delta = \Lambda_{\text{br}}^2/(\Lambda v_H)$ [162, 166]. This sets an upper bound on the relaxion mass $m_\phi \lesssim \sqrt{40}H_{\text{ra}}\delta$.

Now let us see how the inclusion of the dark photon changes the evolution. As discussed in the previous chapters the relaxions velocity will modify the dispersion relation of the dark photon, which for the positive and negative helicity modes $X_\pm(k, \tau)$ becomes (see Eq. (IV.6))

$$\omega_\pm^2(k, \tau) = k^2 \pm k\alpha\theta'. \quad (\text{VI.8})$$

As evident from Eq. (VI.8), dark photon modes with $0 < k < \alpha\theta'$ are tachyonic for one polarization and will experience exponential growth compared to the vacuum fluctuations. The resulting dark photon spectrum then features anisotropies in its energy-momentum tensor which will act as a source for GW production, leading to a stochastic GW background as we already saw in Chapters IV and V. Since only modes of the helicity with the same sign as the relaxion velocity can become tachyonic, the rolling relaxion will produce a circular polarized dark photon background. In our case, as we choose $\theta' > 0$, only the positive-helicity modes are exponentially produced. The solution to the equations of motion for these modes is given in the WKB approximation by

$$X_+(k, \tau) = \frac{e^{g(k, \tau)}}{\sqrt{2\Omega(k, \tau)}}, \quad (\text{VI.9})$$

where $\Omega^2(k, \tau) = k\alpha|\theta'(\tau)| - k^2 > 0$ is the corresponding tachyonic frequency, and $g(k, \tau) = \int^\tau d\tau' \Omega(k, \tau')$. The approximation holds for $|\Omega'/\Omega^2| \ll 1$.

Subsequently, due to the exponential production, the dark photons energy becomes comparable to the kinetic energy in the relaxion, at which point the friction provided by the dark photon becomes significant and the evolution of θ starts to differ from Eq. (VI.6). Similar to the argument provided in Section V.3.2, the time-scale τ_{pp} at which the friction from particle production kicks in can be determined by equating the friction term with the slope of the potential

$$\frac{\langle X_{\mu\nu} \tilde{X}^{\mu\nu} \rangle(\tau_{\text{pp}})}{4a^4(\tau_{\text{pp}})} \approx \frac{\tilde{k}^4 e^{2g(\tilde{k}, \tilde{\tau})}}{4\pi^2 a^4} \sim \frac{\Lambda_{\text{br}}^4}{\alpha}, \quad (\text{VI.10})$$

where \tilde{k} is the mode that dominates the $\langle X \tilde{X} \rangle$ term given by $\partial g(k, \tau)/\partial k|_{\tilde{k}} = 0$. After τ_{pp} the slope of the potential and the back-reaction from the dark photon balance each other and the relaxion field velocity becomes proportional to the Hubble rate evolving as [166, 167]

$$\theta'(\tau) \approx \frac{\xi}{\alpha} a(\tau) H(\tau) \left(1 + \epsilon \log \frac{\tau}{\tau_{\text{pp}}} \right) \approx \frac{\xi}{\alpha\tau}, \quad (\text{VI.11})$$

with a small logarithmic correction ($\epsilon \ll 1$). Here we defined the parameter $\xi = \frac{\alpha|\theta'|}{aH}$ at τ_{pp} . From Eq. (VI.10) one obtains $\xi \sim \mathcal{O}(10 - 100)$ with a mere logarithmic dependence

on the relaxion parameters [167]. The dominating k -mode at each epoch is then given as $\tilde{k} \sim \alpha\theta'(t) \sim \xi aH$.

The rolling of the relaxion between reheating and T_{ra} still leads to a displacement from the minimum in which it originally settled during inflation. The displacement can be approximated as

$$\Delta\theta = \int_{\tau_{\text{rh}}}^{\tau_{\text{ra}}} d\tau \theta' \approx \frac{\xi}{4\alpha} \left[1 + \log \frac{H_{\text{pp}}^2}{H_{\text{ra}}^2} \right]. \quad (\text{VI.12})$$

Again we need to require that this displacement is small enough for the relaxion to stay trapped in the original minimum, $\Delta\theta \lesssim 2\delta$. For too small of a coupling, the dark photon friction is insufficient to prevent the relaxion from rolling into one of the neighbouring minima. However, instead of limiting the viable relaxion mass, we get a lower limit on the coupling to the dark photons in this case. This inevitably opens up new parameter space in which the Higgs scale can be relaxed successfully.

If the relaxion would pass this first maximum, it then would need to traverse $\Delta\theta \sim \mathcal{O}(n)$ to end up in the n -th minimum, where $n = 1$ denotes the minimum in which it stopped during inflation. This possibility is not strictly ruled out, extending the parameter space of the theory. However, going beyond the first minimum requires a careful adjustment of the initial conditions to let the relaxion stop exactly at the bottom of the n -th minimum at reappearance. Otherwise, the time required for the relaxion to reach the bottom would exceed the age of the Universe. We thus simply assume that α takes on the minimal value $\alpha = \xi/(2\delta)$ in the following, such that the relaxion is still re-trapped in the original minimum.¹

VI.2.2 Dark photon spectrum

In order to be able to calculate the GW signal we need the evolution of the dark photon mode function that experienced tachyonic growth: $X_+(k, \tau)$ with $k < k_{\text{pp}} = \alpha\theta'|_{\tau_{\text{pp}}}$ the largest k to become tachyonic. At any time, the peak of the dark photon spectrum is given by the mode that experiences maximal growth with $k = k_{\text{m}}(\tau) = |\alpha\theta'|/2$. We therefore take the ansatz

$$X_+(k, \tau) = \begin{cases} \mathcal{A}_k \cos(k\tau - \xi) & \text{for } k_{\text{m}} < k < k_{\text{pp}}, \\ 0 & \text{otherwise,} \end{cases} \quad (\text{VI.13})$$

where we neglect the negative-helicity modes as well as all modes that did not experience maximal growth yet, since these are exponentially suppressed.

The dark photon energy density due to the tachyonic instability is estimated as

$$\rho_X = \int_{k_{\text{m}}}^{k_{\text{pp}}} \frac{dk k^2}{4\pi^2 a^4} (|X'|^2 + k^2|X|^2) = \int_{k_{\text{m}}}^{k_{\text{pp}}} \frac{dk}{k} \frac{|\mathcal{A}_k|^2 k^5}{4\pi^2 a^4}. \quad (\text{VI.14})$$

On the other hand, we can determine the energy density of the dark photons from the energy that gets transmitted as the relaxion rolls down the slope as

$$\rho_X = - \int_{\tau_{\text{pp}}}^{\tau} d\eta \frac{a^4(\eta)}{a^4(\tau)} \frac{\partial V}{\partial \theta} \frac{\partial \theta}{\partial \eta} \approx \int_{k_{\text{m}}}^{k_{\text{pp}}} \frac{dk}{k} \frac{k_{\text{m}}^4 \xi \Lambda_{\text{br}}^4}{k^4 \alpha}, \quad (\text{VI.15})$$

¹Just like the minimal scenario discussed in Chapter IV, large couplings α are required in this construction. As $\delta = \frac{\Lambda_{\text{br}}^2}{\Lambda v_H} < \frac{v_H}{\Lambda}$, this implies $\alpha \gtrsim 10^2 \left(\frac{\Lambda}{1 \text{ TeV}} \right) \left(\frac{\xi}{10} \right)$. Such large couplings can be obtained in a

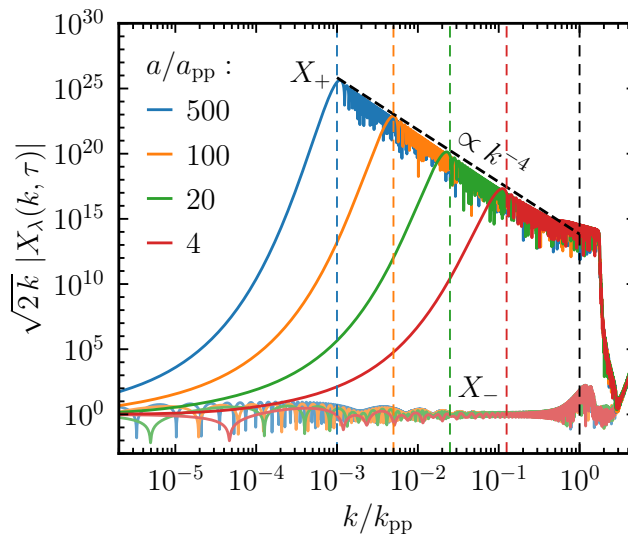


Figure VI.1: Simulated (coloured lines) and expected (dashed black line) amplitude of the dark photon modes at different times. The deep (light) coloured lines correspond to the positive (negative) helicity. At each time, the expected peak momentum is indicated by the vertical dashed line in the corresponding colour, whereas the black-dashed vertical line indicates the upper bound $k < k_{\text{pp}}$ on the tachyonic dark photon momentum. Figure created by E. Madge.

where we assumed that at each time energy is dominantly transferred into the maximally growing mode, which goes like $k_m \propto 1/\tau$. Hence, we can rewrite $\mathcal{A}_k = \mathcal{A}_X k^{-9/2}$ with

$$\mathcal{A}_X = \frac{\pi}{2} \Lambda_{\text{br}}^2 \sqrt{\frac{\xi}{\alpha}} a_{\text{ra}}^2 k_{\text{ra}}^2, \quad (\text{VI.16})$$

where k_{ra} is the mode that exits the tachyonic band at reappearance, $k_{\text{ra}} = \xi/\tau_{\text{ra}}$, completing our estimate of the dark photon spectrum in Eq. (VI.14).

To corroborate our estimation, we have simulated the dark photon and relaxion evolution after reheating, solving the equations of motion (VI.5) and (VI.8) numerically, using 5000 logarithmically-spaced, discretized momenta (see Section V.3.3 and [3] for details). In Fig. VI.1 we present the result of the numeric simulation for the dark photon modes as a function of the momentum k . The simulation assumes $m_\phi = 1 \text{ meV}$, $f_\phi = 2.35 \times 10^{13} \text{ GeV}$, $\Lambda = 100 \text{ TeV}$ and $\xi = 77$. The value of α has been determined numerically from Eq. (VI.10) [166]. We show the spectrum at $a/a_{\text{pp}} = 4$ (red), 20 (green), 100 (orange) and 500 (blue), where the full and light coloured lines correspond to the positive and negative helicity, respectively. As expected, the positive helicity modes dominate over the negative helicity by far. Furthermore, the amplitude for positive helicities indeed follows a $k^{-9/2}$ law (cf. Eq. (VI.14), i.e. $\sqrt{2k}|X_+|$ goes as k^{-4}) between the momentum k_{pp} that exits the tachyonic band at particle production and the peak momentum $k_m(\tau)$ that experiences the largest growth rate at the respective time. The peak momenta and k_{pp} are indicated by the coloured and black, dashed vertical lines respectively.

technically natural way for example via the clockwork mechanism [168–171].

VI.3 Relics

VI.3.1 Gravitational Waves

Let us now consider the stochastic GW background generated from anisotropies in the energy-momentum tensor of the dark photon produced during the post-Inflationary evolution of the relaxion. In particular, we here focus on the GWs sourced during the rolling of the relaxion between reheating and the EW phase transition. Since we now have an estimate of the dark photon spectrum we can come up with an analytical estimate of the energy density in GW using the method as in [3].

This method corresponds to the integration of the GWs equation of motion in Fourier space as we already lined out in Section II.2. The equation of motion is given by

$$(\partial_\tau^2 + k^2) a(\tau) h_{ij}(\mathbf{k}, \tau) = \frac{2a(\tau)}{m_{\text{Pl}}^2} \Pi_{ij}(\mathbf{k}, \tau), \quad (\text{VI.17})$$

where $k = |\mathbf{k}|$ is the comoving wave number. The anisotropic stress tensor Π_{ij} sourcing the GWs is related to the energy-momentum tensor T_{ij} , via $\Pi_{ij}(\mathbf{k}, \tau) = \Lambda_{ij}^{ab}(\mathbf{k}) T_{ab}(\mathbf{k}, \tau)$, where $\Lambda_{ij}^{ab} = P_i^a P_j^b - \frac{1}{2} P_{ij} P^{ab}$ with $P_{ij} = \delta_{ij} - k_i k_j / k^2$ is the projector that extracts the transverse and traceless part [48]. The equations of motion are then solved by (neglecting the a'' term which vanishes in a radiation dominated universe i.e. for $a \propto \tau$)

$$h_{ij}(\mathbf{k}, \tau) = \frac{2}{m_{\text{Pl}}^2} \int_{\tau_i}^{\tau} d\tau' \frac{a(\tau')}{a(\tau)} \Pi_{ij}(\mathbf{k}, \tau') \mathcal{G}(k, \tau, \tau'), \quad (\text{VI.18})$$

where $\mathcal{G}(k, \tau, \tau') = \sin[k(\tau - \tau')]/k$ is the causal Green's function. Since the anisotropic stress Π we are going to consider here stems from the dark photon field, which is initially in the Bunch-Davies vacuum and therefore a quantum field, the anisotropic stress and any other derived quantity is an operator, which we denote by the hat (e.g. $\hat{\Pi}$).

Given the evolution of the GWs their energy density spectrum can be calculated as [48]

$$\frac{d\rho_{\text{GW}}}{d \log k}(k, \tau) = \frac{m_{\text{Pl}}^2 k^3}{8\pi^2 a^2} \sum_{ij} \langle |h'_{ij}(\mathbf{k}, \tau)|^2 \rangle \quad (\text{VI.19})$$

$$= \frac{k^3}{4\pi^2 m_{\text{Pl}}^2 a^4(\tau)} \int_{\tau_i}^{\tau} d\tau' \int_{\tau_i}^{\tau} d\tau'' a(\tau') a(\tau'') \cos[k(\tau' - \tau'')] \Pi^2(k, \tau', \tau''), \quad (\text{VI.20})$$

where τ_i is the time at which the GW source starts operating and $\Pi^2(k, \tau', \tau'')$ is the unequal time correlator of the anisotropic stress, defined as

$$\langle 0 | \hat{\Pi}^{ab}(\mathbf{k}, \tau) \hat{\Pi}_{ab}^*(\mathbf{k}', \tau') | 0 \rangle = (2\pi)^3 \delta(\mathbf{k} - \mathbf{k}') \Pi^2(k, \tau, \tau').$$

In our case, the GWs are generated between reheating and reappearance, hence $\tau_i = \tau_{\text{rh}}$ and $\tau \leq \tau_{\text{ra}}$. As the GWs produced before the relaxion reaches its terminal velocity will however be subdominant, we can take $\tau_i = \tau_{\text{pp}}$, so that to first approximation the GW signature becomes independent of the temperature to which the Universe was reheated. The dark photon anisotropic stress sourcing the GWs can be written in terms of the dark electric and magnetic fields as

$$\hat{\Pi}_{ab}(\mathbf{k}, \tau) = -\frac{\Lambda_{ab}^{ij}(\mathbf{k})}{a^2(\tau)} \int \frac{d^3 q}{(2\pi)^3} [\hat{E}_i(\mathbf{q}, \tau) \hat{E}_j(\mathbf{k} - \mathbf{q}, \tau) + \hat{B}_i(\mathbf{q}, \tau) \hat{B}_j(\mathbf{k} - \mathbf{q}, \tau)]. \quad (\text{VI.21})$$

As discussed in the previous section the dark photon is dominated by one polarization that we take as the + one. In this case the dark electric and magnetic field operator can be rewritten as

$$\hat{\mathbf{E}}(\mathbf{k}, \tau) = X'_+(k, \tau) \varepsilon_+(\mathbf{k}) \hat{a}_+(\mathbf{k}) + \text{h.c.}, \quad (\text{VI.22a})$$

$$\hat{\mathbf{B}}(\mathbf{k}, \tau) = k X_+(k, \tau) \varepsilon_+(\mathbf{k}) \hat{a}_+(\mathbf{k}) + \text{h.c.}, \quad (\text{VI.22b})$$

where $X_+(k, \tau)$ are the mode functions we estimated in the previous section, $\varepsilon_+(\mathbf{k})$ is the + helicity polarization vector and $\hat{a}_+(\mathbf{k})$ is the annihilation operator of the mode.

From here Eq. (VI.22) has to be plugged into Eq. (VI.21) and Eq. (VI.20) to obtain the spectrum

$$\frac{d\rho_{\text{GW}}}{d \log k} = \frac{k^3}{2\pi^2 m_{\text{Pl}}^2 a_{\text{ra}}^4} \int \frac{d^3 q}{(2\pi)^3} |\Sigma_{ab}(\mathbf{k}, \mathbf{q})|^2 (|I_c(\mathbf{k}, \mathbf{q})|^2 + |I_s(\mathbf{k}, \mathbf{q})|^2). \quad (\text{VI.23})$$

The algebra in terms of the creation and annihilation operators here is the same as in Section III.4. In Section III.4 we furthermore saw that if the Green's function is a sine, one can factorize the two time-integrals. The same was done here with $I_{c/s}$ denoting

$$I_{c/s}(\mathbf{k}, \mathbf{q}) = - \int_{\tau_{\text{pp}}}^{\tau_{\text{ra}}} \frac{d\tau}{a(\tau)} \left\{ \begin{array}{l} \cos(k\tau) \\ \sin(k\tau) \end{array} \right\} \chi(q, l, \tau) \quad (\text{VI.24})$$

where $\chi(\mathbf{k}, \mathbf{q}, \tau) = X'_+(q, \tau) X'_+(l, \tau) + q X_+(q, \tau) l X_+(l, \tau)$ and $l = |\mathbf{k} - \mathbf{q}|$. Using the dark photon spectrum Eq. (VI.14) we obtain

$$\chi(q, l, \tau) = \frac{\mathcal{A}_X^2 \cos[(q-l)\tau]}{(ql)^{\frac{7}{2}}} \quad (\text{VI.25})$$

for $\min(q, l) > k_{\text{m}}(\tau)$.

A new aspect of this calculation is the algebra involving the polarization vectors and transverse-traceless projector. As it turns out, this part can be factored out as well and is captured by $|\Sigma_{ab}(\mathbf{k}, \mathbf{q})|^2 = \varepsilon^{a+*} \varepsilon^{b+*}(\mathbf{k} - \mathbf{q}) \Lambda_{ab}^{ij}(\mathbf{k}) \varepsilon_i^+(\mathbf{q}) \varepsilon_j^+(\mathbf{k} - \mathbf{q})$.

It is beneficial to express the momenta in terms of k_{ra} and rewrite the energy density as

$$\frac{d\rho_{\text{GW}}}{d \log k} = \frac{\Lambda_{\text{br}}^8 \xi^2}{\alpha^2 H_{\text{ra}}^2 m_{\text{Pl}}^2} x^3 \int_{\frac{1}{2}}^{\infty} dr \int_{-1}^1 d \cos \theta \frac{|\Sigma_{ab}(x, r, \cos \theta)|^2}{512 r^5 s^7} \left(|\tilde{I}_c(x, r, s, \xi)|^2 + |\tilde{I}_s(x, r, s, \xi)|^2 \right)^2 \Theta(s - 1/2), \quad (\text{VI.26})$$

where the remaining integrals only depend on $x = k/k_{\text{ra}}$ and ξ . We here defined $r = q/k_{\text{ra}}$ and $s = l/k_{\text{ra}}$. The polarization part can now be evaluated to give (see e.g. [3])

$$|\Sigma_{ab}|^2 = \sum_{\lambda=\pm} \left[\frac{1 + \lambda \cos \theta}{2} \right]^2 \left[\frac{1 + \lambda \frac{x-r \cos \theta}{s}}{2} \right]^2, \quad (\text{VI.27})$$

where λ now denotes the GW helicity, and the time integrals are given as

$$\tilde{I}_{c/s} = \begin{cases} \text{Ci}[(x+r-s)\xi] - \text{Ci}\left[\frac{(x+r-s)\xi}{2 \min(r,s)}\right] + (r \leftrightarrow s) \\ \text{Si}[(x+r-s)\xi] - \text{Si}\left[\frac{(x+r-s)\xi}{2 \min(r,s)}\right] + (r \leftrightarrow s) \end{cases} \quad (\text{VI.28})$$

where Ci and Si are the cosine and sine integral function,

$$\text{Ci}(z) = \int_z^\infty dt \frac{\cos t}{t}, \quad \text{Si}(z) = \int_0^z dt \frac{\sin t}{t}. \quad (\text{VI.29})$$

To get closer to a full analytic approximation, we evaluate the expression in Eq. (VI.26) close to the peak at k_{peak} as well as determining the IR and UV behavior:

Since the GW momentum is given by the sum of two dark photon momenta, $\mathbf{k} = \mathbf{q} + \mathbf{l}$, and since the time-integrals are dominated by the late-time behaviour, the peak of the GW spectrum will roughly be given by twice the peak momentum of the dark photon spectrum at reappearance, i.e. we take $k_{\text{peak}} = k_{\text{ra}}$. As the arguments of the cosine and sine integrals in Eq. (VI.28) are proportional to $\xi \sim \mathcal{O}(10 - 100)$, we can expand for large ξ . Assuming that the cosine and sine terms remaining in the expansion oscillate quickly and therefore average to zero, the corresponding amplitude for $x = 1$ then evaluates to

$$\frac{d\rho_{\text{GW}}^{\text{peak}}}{d \log k} = \left[\frac{1}{4\xi^2} + \mathcal{O}(\xi^{-4}) \right] \frac{\xi^2}{\alpha^2} \frac{\Lambda_{\text{br}}^8}{H_{\text{ra}}^2 m_{\text{Pl}}^2}. \quad (\text{VI.30})$$

For $k \gg k_{\text{ra}}$ or equivalently $x \gg 1$, we have $x + r - s = r(1 + \cos \theta) + \mathcal{O}(x^{-1})$ and $x - r + s = 2x + \mathcal{O}(1)$. The ($r \leftrightarrow s$) part of Eq. (VI.28) is hence suppressed by $1/x$ and only the first two terms contribute. The r or equivalently q integration is dominated by $r \approx 1$. This can be interpreted as the UV tail of the spectrum being dominantly sourced by the interference of a mode close to the peak of the photon spectrum $q \approx k_{\text{ra}}$ and a UV mode $l \approx k$. Again expanding for large ξ , we obtain that the spectrum behaves as

$$\frac{d\rho_{\text{GW}}^{\text{UV}}}{d \log k} = \left[\frac{5}{192\xi^2} + \mathcal{O}(\xi^{-4}) \right] \frac{\xi^2}{\alpha^2} \frac{\Lambda_{\text{br}}^8}{H_{\text{ra}}^2 m_{\text{Pl}}^2} \frac{k_{\text{ra}}^4}{k^4}. \quad (\text{VI.31})$$

The IR tail $k \ll k_{\text{ra}}$, on the other hand, is sourced by two modes close to the peak of the photon spectrum and their momenta canceling each other, to give a small k . The arguments of the cosine and sine integrals become proportional to $x \pm r \mp s = x(1 \pm \cos \theta) + \mathcal{O}(x^2)$, so that we can expand the integrals for low arguments, yielding the IR behaviour

$$\frac{d\rho_{\text{GW}}^{\text{IR}}}{d \log k} = \frac{64}{19965} \frac{\xi^2}{\alpha^2} \frac{\Lambda_{\text{br}}^8}{H_{\text{ra}}^2 m_{\text{Pl}}^2} \frac{k^3}{k_{\text{ra}}^3}. \quad (\text{VI.32})$$

As can be seen from Eq. (VI.27), at low momentum, $x \ll 1$, where we have $s \sim r$, both GW helicities contribute equally, whereas at high momentum, where $x \gg 1$ and hence $s \sim x$, the negative helicity is suppressed by a factor of $1/k^2$ compared to the positive one. So similar to cases discussed in Chapter IV and Chapter V, we obtain a GW spectrum with an unpolarized low-frequency tail and a chiral spectrum above the peak in the linear analysis. As we saw in Chapter IV this behavior might be modified though when taking into account the full back-reaction onto the relaxion.

Our approximation to the full spectrum is now obtained by combining these results. Neglecting GW production after reappearance, the energy density will subsequently simply redshift as $\rho_{\text{GW}} \sim a^{-4}$ (see Section V.5 for details), so that the spectrum today as a function of the present day frequency f can be written as

$$\Omega_{\text{GW}}(f) = \Omega_{\text{GW}}^{\text{peak}} \mathcal{S}_\xi(f/f_{\text{peak}}) \quad (\text{VI.33})$$

with the peak frequency, obtained by redshifting k_{peak}

$$f_{\text{peak}} = \frac{k_{\text{ra}}}{2\pi a_0} = \frac{\alpha|\theta'_{\text{ra}}|}{2\pi a_0} = \frac{a_{\text{ra}} \xi H_{\text{ra}}}{a_0 2\pi}, \quad (\text{VI.34})$$

and the peak amplitude given as

$$\Omega_{\text{GW}}^{\text{peak}} = \frac{1}{\rho_c^0} \frac{a_{\text{ra}}^4}{a_0^4} \frac{1}{m_{\text{Pl}}^2 H_{\text{ra}}^2} \frac{\Lambda_{\text{br}}^8}{4\alpha^2} = \frac{3\rho_c^{\text{ra}} a_{\text{ra}}^4}{4\rho_c^0 a_0^4} \cdot \left(\frac{\Lambda_{\text{br}}^4 \theta'_{\text{ra}} \tau_{\text{ra}}}{\rho_c^{\text{ra}}} \right)^2 \cdot \frac{1}{\xi^2} = \frac{1}{\rho_c^0} \frac{a_{\text{ra}}^4}{a_0^4} \frac{m_\phi^4 f_\phi^4}{m_{\text{Pl}}^2 \xi^2 H_{\text{ra}}^2}. \quad (\text{VI.35})$$

We here used Eq. (VI.11) as well as $\xi \simeq 2\delta\alpha$ and $\Lambda_{\text{br}}^4 = m_\phi^2 f_\phi^2 / \delta$ in the last steps of our simplifications. In the second to last step we have written $\Omega_{\text{GW}}^{\text{peak}}$ in a suggestive way that allows us to reconcile our result with the naive dimensional analysis introduced in the audible axion context in Eq. (IV.14). While the first factor only contains the redshift as well as an $\mathcal{O}(1)$ factor, the second factor can be interpreted as the energy sourcing the GWs squared Ω_{source}^2 , since the relaxion rolls down the potential with slope Λ_{br}^4 and traverses a distance $\approx \theta'_{\text{ra}} \tau_{\text{ra}}$ in the Hubble time before the wiggles reappear such that $\Omega_{\text{source}} = \Omega_X \approx \Lambda_{\text{br}}^4 \theta'_{\text{ra}} \tau_{\text{ra}}$. The third factor captures the suppression from the characteristic scale k_{ra} lying inside the horizon at production $\xi = k_{\text{ra}} / (a_{\text{ra}} H_{\text{ra}})$.

By evaluating the above expressions we find the following useful estimates

$$f_{\text{peak}} \sim \frac{a_{\text{ra}}}{a_0} \xi H_{\text{ra}} \sim 1 \mu\text{Hz} \left(\frac{\xi}{25} \right) \left(\frac{T_{\text{ra}}}{1 \text{ GeV}} \right), \quad (\text{VI.36})$$

$$\begin{aligned} \Omega_{\text{GW}}^{\text{peak}} &\sim 10^{-10} \left(\frac{25}{\xi} \right)^2 \left(\frac{m_\phi}{0.1 \text{ eV}} \frac{f_\phi}{10^{10} \text{ GeV}} \right)^4 \left(\frac{1 \text{ GeV}}{T_{\text{ra}}} \right)^8 \\ &\sim 10^{-12} \left(\frac{25}{\xi} \right)^2 \left(\frac{0.1 \text{ eV} \sin \theta_{\phi h}}{m_\phi} \frac{1}{10^{-13}} \right)^{12} \left(\frac{\text{TeV GeV}}{\Lambda T_{\text{ra}}} \right)^8. \end{aligned} \quad (\text{VI.37})$$

The spectral shape \mathcal{S}_ξ in Eq. (VI.33) is obtained by combining the results that we found in the different limits inversely, in such a way that the peak lies at $x = 1$. These considerations lead us to

$$\mathcal{S}_\xi(x) = \frac{1}{1 + \frac{48}{5}(x-1)^4 + \frac{19965}{256\xi^2}(x^{-3} + 3x - 4)}. \quad (\text{VI.38})$$

In Fig. VI.2 we show the GW spectrum from our numeric simulation (cf. Fig. VI.1), assuming a reappearance temperature of $T_{\text{ra}} = 150 \text{ GeV}$ (blue) and 750 GeV (orange), corresponding to $a/a_{\text{ra}} = 500$ and $a/a_{\text{ra}} = 100$, respectively. Eq. (VI.33) (light lines) overestimates the simulated spectra by an $\mathcal{O}(1-10)$ factor, but captures the main features of the spectrum well. In the following we use the analytic estimate to evaluate the detectability of the signal by present and future GW searches.

VI.3.2 Relaxion dark matter

After the reappearance of the Higgs back-reaction potential, the displaced relaxion begins to oscillate around the minimum of its potential, providing a candidate for ultra-light dark matter (DM) as discussed in [166]. Assuming the maximal displacement of $\Delta\theta = 2\delta$, the relaxion relic abundance is given by

$$\Omega_\phi = \frac{2 m_\phi^2 f_\phi^2 \delta^2}{3 m_{\text{Pl}}^2 H_0^2} \frac{g_{*s}(T_0) T_0^3}{g_{*s}(T_{\text{osc}}) T_{\text{osc}}^3}, \quad (\text{VI.39})$$

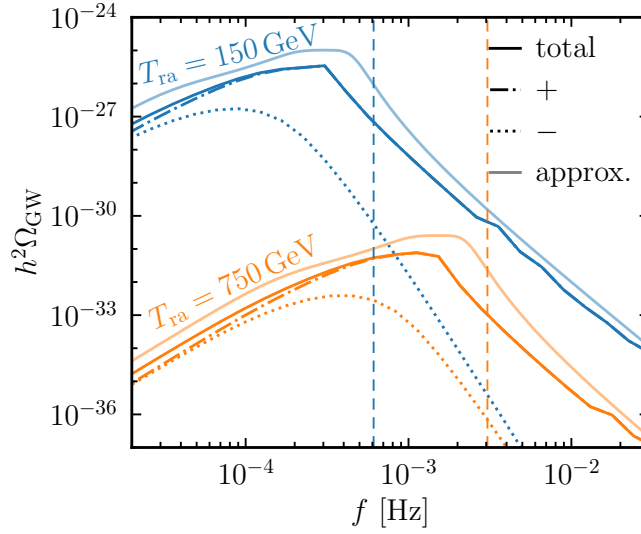


Figure VI.2: Simulation (full colours) and analytic approximation (light colours) of the GW spectrum for a reappearance temperature of $T_{\text{ra}} = 150$ GeV (blue) and 750 GeV (orange). The vertical dashed lines indicate the expected peak frequency, whereas the dash-dotted and dotted curves correspond to the positive and negative helicity contributions to the simulated spectrum. Figure created by E. Madge.

where, $T_{\text{osc}} \sim \min[T_{\text{ra}}, \sqrt{m_\phi m_{\text{Pl}}}]$ is the temperature when the relaxion starts to oscillate. Requiring that the relaxion provides all of DM, i.e. $\Omega_\phi h^2 = 0.12$ [172], the relaxion decay constant can be expressed as

$$f_\phi \sim 5 \times 10^9 \text{ GeV} \left(\frac{\Lambda}{1 \text{ TeV}} \right)^{\frac{2}{5}} \left(\frac{T_{\text{osc}}}{1 \text{ GeV}} \right)^{\frac{9}{10}} \left(\frac{0.1 \text{ eV}}{m_\phi} \right). \quad (\text{VI.40})$$

The possible decay channels of the relaxion are into two photons and two dark photons, $\Gamma_\phi = \Gamma_{\gamma\gamma} + \Gamma_{XX}$. The decay rate into a dark photon pair is given by

$$\Gamma_{XX} = \frac{\alpha^2}{64\pi} \frac{m_\phi^3}{f_\phi^2}, \quad (\text{VI.41})$$

while the decay width of $\phi \rightarrow \gamma\gamma$ is subdominant compared to that of $\phi \rightarrow XX$ as it is suppressed by the square of the relaxion-Higgs mixing angle [166], which in turn is bounded from above by $\sin \theta_{h\phi} \lesssim v_H/f_\phi$ [163]. The relaxion lifetime hence becomes

$$\tau_\phi \sim 20 \text{ Gyr} \left(\frac{25}{\xi} \right)^2 \left(\frac{T_{\text{osc}}}{1 \text{ GeV}} \right)^3 \left(\frac{0.1 \text{ eV}}{m_\phi} \right)^5, \quad (\text{VI.42})$$

where we have chosen $\alpha = \xi/(2\delta)$. Since the decay of DM into relativistic particles affects the spectrum of the cosmic microwave background (CMB) at low- ℓ multipoles, the lifetime is constrained as $\tau_\phi > 160 \text{ Gyr}$ [173].

As shown in Chapter IV, for $\alpha(\Delta\theta)_{\text{sep}} \sim \mathcal{O}(10^2)$, the oscillating axion may introduce a second phase of tachyonic dark photon production, that could suppress the DM abundance by up to two orders of magnitude. This condition is satisfied in parts of the parameter space where the field displacement is maximal, since there $\alpha \sim \mathcal{O}(\xi/\delta)$ and $\xi \sim \mathcal{O}(10-10^2)$, and introduces some uncertainty in our estimate of the DM abundance in those regions.

VI.3.3 Constraints

A successful cosmological relaxation of the Higgs mass requires the Inflation sector to dominate the total energy density, $3H_I^2 m_{\text{Pl}}^2 \gtrsim \Lambda^4$, as well as that the classical motion of the relaxion dominates over quantum fluctuation during Inflation, $(\Delta\phi)_{\text{cl}} \gtrsim H_I/2\pi$. Here, H_I is the Hubble scale during Inflation. Combining these two constraints we get an upper bound on the cut-off scale Λ ,

$$\Lambda \lesssim \left(\frac{2\pi\sqrt{3} m_{\text{Pl}}^3 \Lambda_{\text{br}}^4}{f} \right)^{1/6}. \quad (\text{VI.43})$$

As we are considering a Higgs dependent back-reaction potential, we also require $\Lambda_{\text{br}} \lesssim v_H$ [42, 163]. The allowed range of the effective cut-off Λ of the theory is

$$m_{\text{Pl}} \gtrsim f_\phi \gtrsim \Lambda \gtrsim 4\pi v_H \sim 1 \text{ TeV}. \quad (\text{VI.44})$$

Also, for a generic back-reaction potential which does not change the late time cosmology, the range of reappearance temperatures is

$$v_H \gtrsim T_{\text{ra}} \gtrsim T_{\text{BBN}} \sim 10 \text{ MeV}. \quad (\text{VI.45})$$

For masses below the eV scale, the relaxion can further mediate long-range forces. Experiments looking for such interactions (fifth force experiments, inverse-square-law and equivalence-principle tests) constrain the coupling of the relaxion to ordinary matter [174–180], which is induced by the relaxion-Higgs mixing angle given in Eq. (VI.4). In a similar manner, for masses up to the keV range, the mixing is constrained from stellar cooling [181–184], as it induces relaxion-mediated contributions to the energy loss in stars. Slightly weaker limits on the mixing angle can furthermore be obtained from bounds on the solar relaxion flux as constrained by XENON1T and other dark-matter direct detection experiments [185].

Additional constraints arise when coupling the relaxion to a dark photon field, with the coupling here chosen to saturate the trapping condition, i.e. $\alpha = \xi/(2\delta)$. In order for the dark photon induced friction to trap the relaxion, reappearance has to occur sufficiently late for the dark photon to be produced, i.e. $H_{\text{pp}} > H_{\text{ra}}$. This sets a lower bound on the relaxion mass, $m_\phi \gtrsim \sqrt{10} \delta H_{\text{ra}}$, for which the dark photon scenario can be applied.

If this condition is satisfied, throughout its evolution from reheating to reappearance, the relaxion continuously produces dark photons, depositing energy density into the latter. At the time of trapping, t_{ra} , the dark photon energy-density can be estimated as in Eq. (VI.15)

$$\rho_X(t_{\text{ra}}) = \frac{1}{2} m_\phi^2 f_\phi^2. \quad (\text{VI.46})$$

After T_{ra} , dark photon production stops and their energy density redshifts as that of radiation.

The dark photons contribute to N_{eff} and are therefore constraint by CMB measurements as discussed in Section V.5. This leads to a lower limit on the reappearance temperature as a function of the relaxion mass and decay constant

$$T_{\text{ra}} \gtrsim 2.5 g_{s,\text{ra}}^{-1/3} \sqrt{m_\phi f_\phi}, \quad (\text{VI.47})$$

where $g_{s,\text{ra}}$ is the number of entropic degrees of freedom at reappearance.

If we assume that the relaxion accounts for the full DM abundance, then plugging

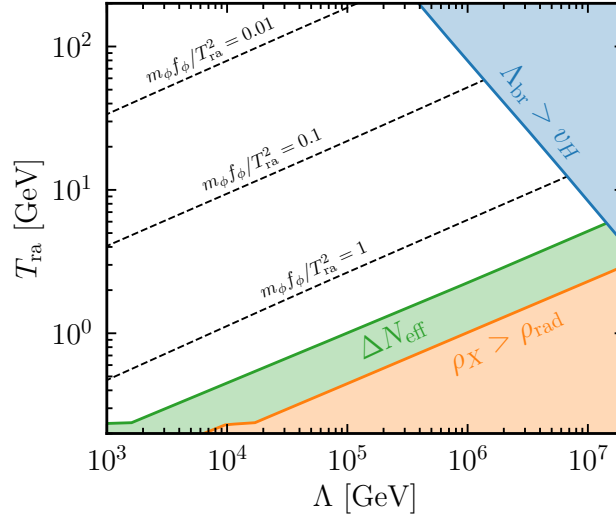


Figure VI.3: Allowed range of reappearance temperatures T_{ra} as a function of the cut-off scale Λ , while fixing f_ϕ to the value reproducing the measured DM abundance, Eq. (VI.40), assuming $T_{\text{osc}} = T_{\text{ra}}$. The blue shaded region is excluded since $\Lambda_{\text{br}} > v_H$, while in the green shaded regions, the CMB bound on ΔN_{eff} , Eq. (VI.48), is violated. In the orange shaded region, the dark photon energy density further dominates the Universe at reappearance. The dashed lines are contours of constant $m_\phi f_\phi / T_{\text{ra}}^2$, which sets the amplitude of the GW spectrum, cf. Eq. (VI.37). Figure created by A. Banerjee.

Eq. (VI.40) into Eq. (VI.47), we get,

$$T_{\text{ra}} \gtrsim 450 \text{ MeV} \left(\frac{67}{g_{*s,\text{ra}}} \right)^{\frac{1}{3}} \left(\frac{\Lambda}{10 \text{ TeV}} \right)^{\frac{4}{11}}. \quad (\text{VI.48})$$

Here, we also assume that the relaxion starts to oscillate at T_{ra} , which is only true for a sufficiently heavy relaxion. As we require $\Lambda \gtrsim 4\pi v_H \sim 1 \text{ TeV}$, this sets a lower bound of $T_{\text{ra}} \gtrsim 240 \text{ MeV}$ on the reappearance temperature for the relaxion DM scenario to be realized.² Upon the same assumptions, $\Lambda_{\text{br}} \lesssim v_H$ further sets an upper bound on the reappearance temperature,

$$T_{\text{ra}} \lesssim \min \left[v_H, 80 \text{ GeV} \left(\frac{10^6 \text{ GeV}}{\Lambda} \right) \left(\frac{96}{g_{*s,\text{ra}}} \right)^{\frac{1}{3}} \right]. \quad (\text{VI.49})$$

In Fig. VI.3 we show the minimal and maximal allowed reappearance temperature for relaxion DM as a function of the cut-off Λ of the theory. Combining $\Lambda_{\text{br}} < v_H$ (blue) and the N_{eff} constraint (green), we see that the highest Λ for which the relaxion can be realized as coherently oscillating DM is $\Lambda \lesssim 10^7 \text{ GeV}$, which is in accordance with the constraints for $T_{\text{ra}} \simeq 6 \text{ GeV}$. Due to the rapid change in the radiative degrees of freedom around the time of the QCD phase transition, the ΔN_{eff} limit on the reappearance temperature saturates at $T_{\text{ra}} \sim T_{\text{QCD}}$ for $\Lambda \lesssim 2 \text{ TeV}$. We also depict the weaker bound $\rho_X < \rho_{\text{rad}}$ that the energy in the dark sector may not dominate over the SM plasma in orange.

In Fig. VI.4, we depict the constraints on the relaxion parameters as a function of the relaxion mass m_ϕ and the mixing angle $\sin \theta_{h\phi}$, where we determined Λ and f_ϕ from the DM

²Note that, for this value of the reappearance temperature, the relaxion starts to oscillate directly after

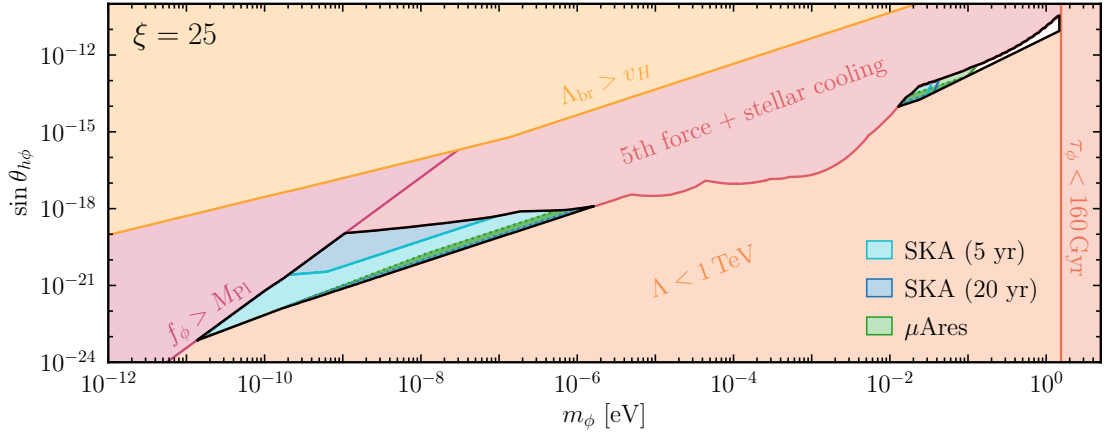


Figure VI.4: Available parameter space (black framed region) for relaxion DM in the relaxion mass m_ϕ vs. mixing angle $\sin \theta_{h\phi}$ plane. The red and orange shaded regions are excluded by the indicated constraints of combinations thereof. The colored regions inside the viable DM space can be probed via GWs in μ Ares (green) or SKA (blue/turquoise). The light shading and solid lines indicate points that can be probed for a subrange of reappearance temperatures, whereas the darker shaded parts enclosed by dotted lines are accessible for all valid T_{ra} . An animated version of the plot scanning the reappearance temperature is enclosed in the ancillary material of [6]. Figure created by A. Banerjee.

abundance using Eqs. (VI.4) and (VI.40). Scanning over all allowed values of T_{ra} , the full range of masses and mixing angles for which we can obtain coherently oscillating relaxion DM is indicated by the black-framed regions in Fig. VI.4. We obtain two separated islands of viable parameter space, one at low masses, $10^{-11} \text{ eV} \lesssim m_\phi \lesssim 10^{-6} \text{ eV}$, with mixing angles around $10^{-23} \lesssim \sin \theta_{h\phi} \lesssim 10^{-18}$, and another island at high masses, $10^{-2} \text{ eV} \lesssim m_\phi \lesssim 1 \text{ eV}$ with a narrow range of mixing angles around $10^{-14} \lesssim \sin \theta_{h\phi} \lesssim 10^{-11}$. Note that, in the high-mass island, the coupling to dark photons is required to trap the relaxion, whereas in most of the low-mass island, relaxion DM can be realized without dark photon friction [166]. It shall moreover be emphasized that the low-mass DM regions in the minimal and dark photon scenario are mostly separated in the reappearance temperature, since relaxion stopping via Hubble friction requires $m_\phi \lesssim \sqrt{40} \delta H_{\text{ra}}$, whereas dark photon production only occurs for $m_\phi \gtrsim \sqrt{10} \delta H_{\text{ra}}$.

VI.4 Discussion

At low frequencies the GW spectrum we found behaves as $\sim f^3$, in accordance with the expectations based on causality arguments using that the anisotropic stress of a causal source cannot be correlated at scales above the horizon size at the time of production [48, 157]. At high frequencies, the spectrum falls like $\sim f^{-4}$, allowing a simple distinction from the much steeper falling GW background generated from oscillating (Chapter IV) or rotating (Chapter V) axion-like fields. It should further be noted that, when the peak position is fixed, changing ξ barely affects the UV tail, while the IR tail goes as ξ^2 , potentially allowing to disentangle the reappearance temperature and ξ in the peak frequency Eq. (VI.34), and thereby facilitating the determination of the relaxion parameters from a hypothetical observed signal. Larger values of ξ further result in a flatter peak, although this may be

reappearance as long as $m_\phi \gtrsim 5 \times 10^{-10} \text{ eV}$.

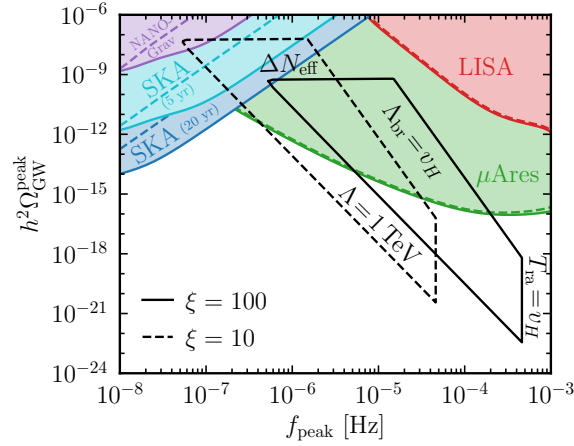


Figure VI.5: Values of the peak frequency and amplitude of the GW spectrum which can be obtained in the relaxion DM scenario. The edges of the polygon correspond to the minimal and maximal amplitudes which can be obtained for $\xi = 100$ (solid lines) and $\xi = 10$ (dashed lines), limiting to the case when the relaxion starts to oscillate immediately after barrier reappearance. Figure created by E. Madge.

an artefact of our analytic approximation, cf. Eq. (VI.38).

The range of peak frequencies and amplitudes that can be attained for coherently oscillating relaxion DM is displayed in Fig. VI.5, limiting to the case when the relaxion starts oscillating at the time the wiggles reappear. The polygons are obtained from the allowed range for the cut-off Λ , for T_{ra} between ~ 240 MeV and v_H , cf. Fig. VI.3. The solid and dashed lines assume $\xi = 100$ and $\xi = 10$, respectively. Peak positions inside the polygons can be realized. The sensitivities of μAres , LISA and PTAs are indicated as shaded regions. Note that the solid lines correspond to the sensitivity of the respective GW search for $\xi = 100$. For $\xi = 10$, the detection reach is degraded to the correspondingly-coloured dashed lines, due to the difference in the shape of the spectrum.

For a large part of the peak frequencies and amplitudes that can be realized with relaxion DM, an observable signal is obtained, although mostly requiring futuristic space-based interferometers such as μAres for observation. For low values of $\xi \sim 10$, a detection with SKA is possible. The present-day sensitivity of NANOGrav or expected reach of LISA are however insufficient for a detection. While NANOGrav is able to exclude parts of the parameter space if the DM assumption is relaxed (see below), the sensitivity of LISA will remain insufficient even in this more general case.

We also show the GW sensitivity for relaxion DM as coloured regions in Fig. VI.4, using the same colouring scheme as above. The (light) coloured regions enclosed by the solid green and blue lines here indicate the relaxion masses and mixing angles for which, at least in a sub-range of the reappearance temperatures in accordance with the constraints, an observable signal in μAres and SKA can be obtained. While μAres covers the full low-mass island as well as the range $m_\phi \lesssim 0.1$ eV in the high-mass island, the sensitivity of SKA is limited to slightly lower DM masses. Note that, as the GW spectrum strongly depends on the reappearance temperature, a non-observation in these experiments would in most cases not rule out the coloured parameter space, as a detection can be evaded by adjusting the reappearance temperature to shift the signal outside the experiment's reach. In the dark-green coloured region bounded by the dotted lines, however, the generated stochastic GW background is observable in μAres for the full range of allowed reappearance temperatures, guaranteeing a detectable signal in this region. The temperature dependence of

the relaxation constraints and GW limits can be seen explicitly in the animated version of the figure that can be found in the ancillary material of [6].

Last but not least, let us now dismiss the assumption that the relaxation constitutes all of DM, which leads to Fig. VI.6, where we again indicate the parameter regions in which the GW background can be observed in μ Ares (green), NANOGrav (purple) or SKA (blue/turquoise) by the respective colouring. The coloured regions respect the $f_\phi < m_{\text{Pl}}$ constraint. If we allow for super-Planckian decay constant, the regions extend to the dotted lines.

Regarding the GW sensitivity, the reader needs to be aware that the figure shows the projection of a four-dimensional plot, as T_{ra} and f_ϕ (or Λ) are not fixed. While red and orange shading mark the values of m_ϕ and $\sin\theta_{h\phi}$ for which it is not possible to evade the respective constraints by adjusting the remaining parameters (i.e. these coloured regions are definitely excluded), the GW contours (blue, turquoise, purple and green) correspond to the maximal reach of the respective experiments. They are obtained by taking the maximal SNR that can be achieved in each experiment for the given values of m_ϕ and $\sin\theta_{h\phi}$. Given the experimental sensitivities we assume here, a detection via GWs can be evaded in all of the viable parameter space. In particular, the purple colouring and lines do not indicate that the corresponding parameter points are excluded by NANOGrav data, but that NANOGrav constrains the reapparance temperature (and the decay constant) in this region. The same also applies to the projections for SKA and μ Ares. Furthermore, although the sensitivities overlap in the plot, μ Ares and PTAs operate in different frequency regimes and are therefore typically sensitive to different ranges of T_{ra} . Nonetheless, we can conclude that current and future GW experiments can potentially detect the stochastic GWs from relaxation-stopping via dark photon emission, and thereby constrain the parameter space.

In addition to the current and prospective exclusion range, we also work out the parameter range in which our model can account for the potential GW signal recently observed in NANOGrav [186] that has by now been detected by several PTAs [62–64]. Fitting our spectrum to the data using the same procedure as discussed in Chapter VII, where we keep ξ fixed and only fit the peak frequency and amplitude, we obtain the best-fit points and the corresponding 1σ and 2σ contours shown in Fig. VI.7. We further indicate the minimal peak frequency dictated by the lower bound on the reapparance temperature, $T_{\text{ra}} \gtrsim T_{\text{BBN}}$, as well as the maximal peak amplitude consistent with the constraint on ΔN_{eff} by dotted lines. While these bounds exclude an explanation of the observed stochastic process in terms of our model for large values of $\xi \sim 100$ (green), we can reach into the 1σ and 2σ regions for intermediate $\xi \sim 25$ (orange), and for $\xi \sim 10$ (blue) we can account for the NANOGrav best-fit point. We also carried out the same fit for the scenarios discussed in the previous two chapters and found that there it is not possible to explain the signal without being in tension with the ΔN_{eff} bound. Due to the prolonged emission of GWs in the setup considered here, it is however possible to have the characteristic scale of the source closer to the horizon at emission $\xi = \mathcal{O}(10)$, while in the previous cases this was limited at $\mathcal{O}(100)$ (e.g. $\theta_\alpha \approx 100$ in Chapter IV). The efficiency of GW emission is therefore enhanced in the case at hand as can be seen from the naive dimensional analysis Eq. (IV.14).

In the $\xi = 10$ (lower) panel of Fig. VI.6, we indicate the values of m_ϕ and $\sin\theta_{h\phi}$ for which we can attain the best-fit point ($f_{\text{peak}} = 3.3 \text{ nHz}$, $h^2\Omega_{\text{GW}}^{\text{peak}} = 1.2 \times 10^{-9}$) by the grey shaded region. Note that, as we fix ξ and f_{peak} , this also fixes the reapparance temperature to $T_{\text{ra}} \sim 20 \text{ MeV}$, while the peak amplitude then fixes f_ϕ as a function of m_ϕ . Hence, in the grey shaded region, Λ can be adjusted within the constraints to obtain the

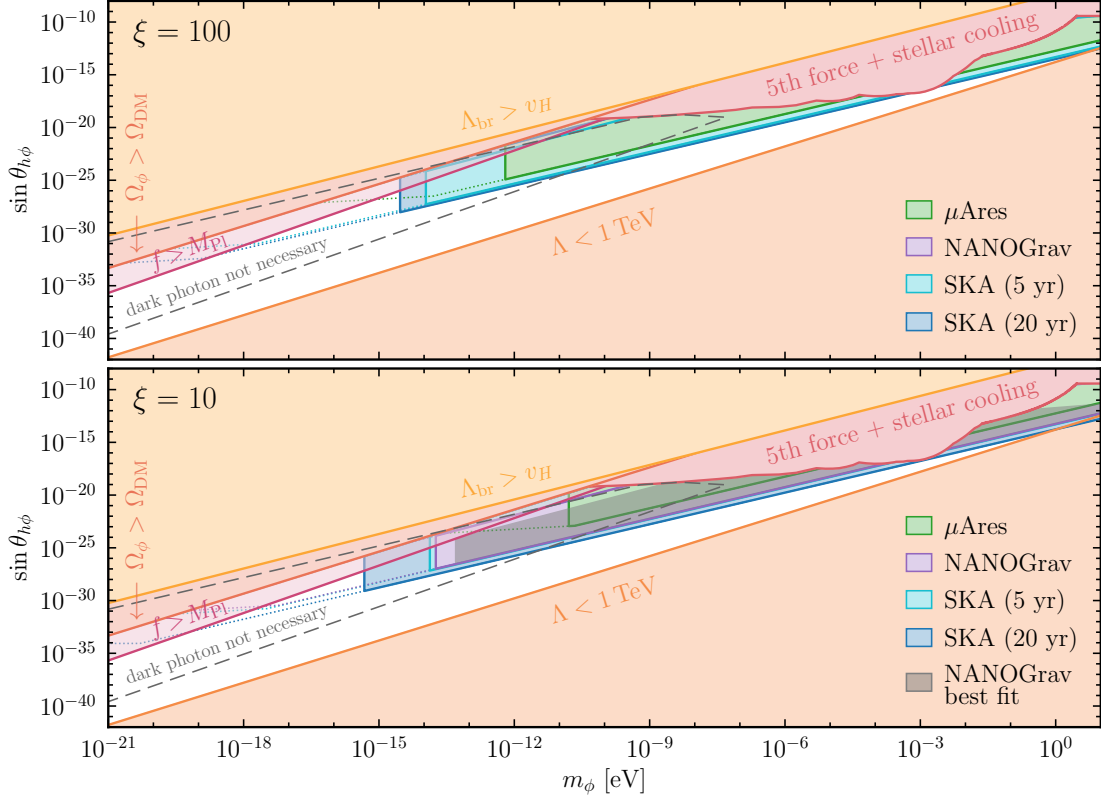


Figure VI.6: Available parameter space for $\xi = 100$ (top), and for $\xi = 10$ (bottom). The red and orange shaded regions are excluded by the indicated constraints or combinations thereof. Above the red solid line, the relaxation decay constant becomes super-Planckian. The grey dashed line encloses the parameter space in which re-trapping can be realized without dark photon friction such that the dark photon is not necessary for a viable relaxation scenario. The prospective GW sensitivity of μ Ares (green) as well as SKA after an observation period of 5 years (turquoise) and 20 years (blue) is indicated by the respective coloured regions. In the purple coloured region, a sub-range of the viable reappearance temperatures can be excluded using current NANOGrav data from the 11-year data set. The regions bounded by the coloured dotted lines need super-Planckian decay constants to be probed by the respective experiment. In the lower panel, the grey shaded region can reproduce our best-fit spectrum (at $T_{\text{ra}} \sim 20$ MeV) to the potential stochastic GW background seen in the recent NANOGrav data. Figure created by A. Banerjee.

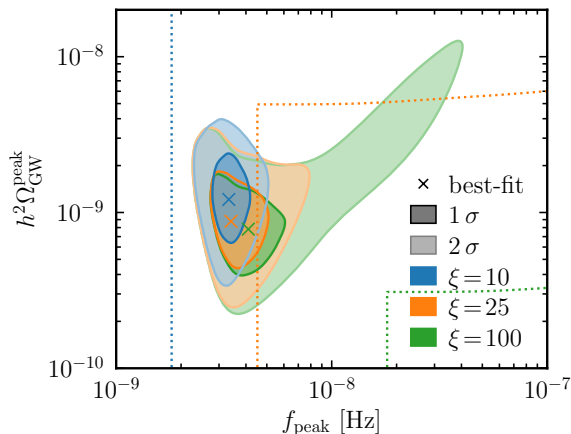


Figure VI.7: Best fit point (cross) to the NANOGrav 12.5-year data, as well as 1σ (dark) and 2σ (light) regions, fixing ξ to 10 (blue), 25 (orange) and 100 (green). The dotted lines enclose the region that can be obtained without being in tension with ΔN_{eff} or BBN at the respective value of ξ . Figure created by E. Madge.

respective value of the mixing angle.

VI.5 Conclusion

In this chapter, we have considered the possibility of probing the relaxion, which was proposed to ameliorate the Higgs hierarchy problem, via gravitational waves. A coupling to dark photons tames the relaxion excursion after reheating, and thus in turn opens up a large fraction of the parameter space which was excluded in the minimal scenario without dark photons. Furthermore, dark photon production after reheating can act as a source for the generation of a stochastic gravitational wave background. The gravitational waves are sourced by the anisotropies that are induced by the tachyonic production of dark photons between the electroweak phase transition and BBN. Hence, instead of the inflationary dynamics responsible for solving the hierarchy problem, we are here probing the late-time dynamics of the relaxion.

We have shown that this stochastic gravitational wave background can be probed by various current (NANOGrav) and future (SKA, μ Ares) gravitational wave detectors. In addition, we also highlight the parameter range in which our gravitational wave signal can account for the common-spectrum process observed in the most recent NANOGrav data [186]. Alongside the existing theoretical constraints, we have presented the relaxion parameter space which can be detected or excluded by the gravitational wave observatories in Fig. VI.6.

We find that the spectral shape of the gravitational wave signal in our model falls as the fourth power of the frequency above the peak, unlike the steeper falling gravitational wave signals generated by the other axion-like field dynamics considered in the previous chapters, whereas it behaves like f^3 in the infra-red, as expected based on causality arguments. An observation of the spectrum in the range around the peak should allow for a determination of the reappearance temperature, while the amplitude can be used to determine the product of the relaxion mass and decay constant.

Furthermore, we have shown that the relaxion can constitute dark matter in the present Universe in the mass range of $10^{-11} \text{ eV} \lesssim m_\phi \lesssim 10^{-6} \text{ eV}$ and $10^{-2} \text{ eV} \lesssim m_\phi \lesssim 1 \text{ eV}$.

While this scenario cannot be constrained with current NANOGrav data, most of the dark matter parameter space will be accessible by SKA and/or μ Ares in the future. Hence, with the advent of gravitational wave astronomy, we are now facing promising prospects for probing the relaxation of the electroweak scale via the stochastic gravitation wave background generated when stopping the relaxion, independently of whether the relaxion constitutes dark matter or not.



**Main part III:
Interplay of PTAs and
Spectral Distortions**

NANOGrav detection

VII.1 Introduction

GWs waves travel freely through the early universe and are therefore a possible messenger of new physics as we discussed in Section II.2. Pulsar Timing Arrays (PTAs) such as EPTA [187], PPTA [188] and NANOGrav [60] are sensitive to GWs with frequencies of 10^{-8} Hz and below. A stochastic background of such low frequency GWs could be produced in the early universe by a variety of processes, such as inflation, cosmic strings, phase transitions, or scalar field dynamics [48]. The recent data release of the NANOGrav collaboration [186] for the first time shows evidence for such a stochastic GW background, which is well described by a $f^{-2/3}$ power law spectrum with a GW strain amplitude of 2×10^{-15} , or equivalently a GW energy density $\Omega_{\text{GW}}h^2$ of order 10^{-10} . By now all other operating PTAs have released data in line with the NANOGrav observation [62–64]. While the inspirals of super massive black hole binaries (SMBHBs) are expected to source GWs at those frequencies, most astro-physical models predict smaller amplitudes than the observed one [189].

However, the signal is indeed consistent with the GW density one expects from a variety of cosmological sources, as was discussed for the case of cosmic strings [190–192], phase transitions [193, 194], or primordial black hole formation [195, 196].

So far these studies have focused on demonstrating that a sufficiently large GW density can be achieved in these models in the required frequency range. Here we perform a fit to the frequency binned NANOGrav data. Since most cosmological sources of GWs have specific spectral features, it is important to verify that indeed they agree well with the data. In doing this, we are able to obtain best fit parameter regions for two classes of models that produce primordial GWs, namely phase transitions in the early universe [197–201] and audible axions as discussed in Part II. We also show that the NANOGrav data already puts constraints on the parameter space of these models, which are comparable to the ones coming from other astrophysical observations such as big bang nucleosynthesis (BBN) or the constraint on the number of relativistic degrees of freedom, N_{eff} .

With more precise data it will become possible to distinguish between different cosmological sources and from the expected background due to supermassive black hole binaries. Our work presents a first step in this direction. It is organised as follows: In the next section, we give a brief introduction into the operation of a PTA and the current status of observations. This is followed up with a description of our effort at recasting the NANOGrav data, and re-derive the best fit regions for single power law fits. In the next two sections we investigate the possibility that the signal stems from one of the audible axion models discussed in Part II or a cosmological phase transition (PT), respectively, and we present the best fit regions for the model parameters, before we conclude.

VII.2 The Observation

Pulsars emit electromagnetic radiation along a rotating axis, effectively acting as a light house. The rotation frequency of the axis is linked to the rotation of the pulsar, which due to conservation of angular momentum is very stable. If the beam axis swipes earth, the light pulses arriving in regular intervals can therefore be used as a clock. Naturally the pulsars with the highest rotation frequency act as the best clocks. So called millisecond pulsars rotate close to a thousand times per second, which together with the immense stability of their rotation leads to their timing precision coming close to atomic clocks [202]. This gives rise to a unique opportunity of GW observations, since GWs distort the path of light traveling from the pulsar to earth. When comparing the arrival time of pulses on earth with an atomic clock, this leads to timing residuals. As a gravity wave passes between earth and the pulsar the “pulsar clock” will switch between running ahead and behind the atomic clock with the gravity waves frequency. Since the effect the gravity wave has is the same for all pulsars at the same position on the sky, large sensitivity can be achieved when cross-correlating the timing residuals of different pulsars, as this leads to the intrinsic timing noise of each single pulsar dropping out [203]. A PTA therefore measures the timing residuals of a number of millisecond pulsars to extract information about GWs. Since these pulsars are hundreds of light years away, PTAs are not limited by the size of the detector like interferometers, when it comes to observing low frequency GWs. It is rather the observation time that limits the frequencies to $\mathcal{O}(1/10 \text{ yr}) = \mathcal{O}(10^{-8} \text{ Hz})$.

All running PTAs have reported hints for a common signal among their observed pulsars [60, 62–64] and we discuss the strength of the observed signal based on the NANOGrav data below. The only missing piece that keeps any of the PTAs from claiming the detection of GWs is insufficient evidence for the quadrupolar signature of the signal. A gravity wave effects the path between pulsars at distinct locations on the sky differently over time. This effect is illustrated in the bottom panel of Section VII.2, where the effect of a +-polarized gravity wave propagating orthogonal to a plane with two pulsars (blue stars) on a circle of freely falling test bodies is shown. As one can see the circle is stretched in one direction while being compressed in the opposite one. If both pulsars lie in the same or opposite direction, the effect of the wave on the apparent distance to earth is therefore the same and one expects a correlated signal in their timing residuals. On the other hand, if the pulsars are separated by an angle of ≈ 90 degree, the signal is anti-correlated. For a stochastic GW background all propagation directions and polarization have to be taken into account, which leads to the Hellings-Downs curve for the angular cross-correlation between pulsars [203]. This curve is shown in blue in the upper panel of Section VII.2. A clock error on the otherhand would introduce a monopolar signal, shown in orange, while an ephemeris error results in a dipolar one. Evidence of the Hellings-Downs curve is therefore crucial to rule out possible errors. The gray violins in Section VII.2 give the probability for a particular correlation for seven bins of angular separation on the sky, as inferred from the NANOGrav 12.5yr dataset [186]. A definite distinction between the different scenarios is not possible at this point, but we will in the following assume that the signal is indeed caused by GWs.

The magnitude of a stochastic GW background is typically described by the dimensionless, frequency dependent characteristic strain amplitude $h_c(f)$. For a single power law it can be written as

$$h_c(f) = A_{\text{GW}} \left(\frac{f}{f_y} \right)^\alpha, \quad (\text{VII.1})$$

where A_{GW} is the amplitude, α is the slope and $f_y = 1/\text{year}$ is the pivot frequency at which

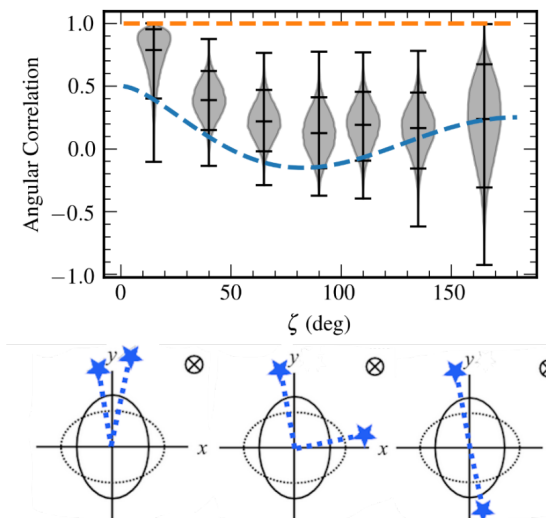


Figure VII.1: Top panel: The gray violins give the Bayesian reconstruction of interpulsar spatial correlations for seven bins of angular separation on the sky. The orange and blue line give the expected result in case of a monopolar and quadrupolar nature of the signal. Bottom panel: Illustration of difference in cross-correlation for pulsar pairs (blue) caused by different angles between the positions of the pulsars on the sky as a gravity wave with + polarization passes through. Figure borrowed from [186] with modifications by the author.

the amplitude is fixed. Throughout this thesis we have been using the related quantity $\Omega_{\text{GW}}(f)h^2$, which is the energy density in GWs as a fraction of the critical energy density, which is given by [60]

$$\Omega_{\text{GW}}(f)h^2 = \frac{2\pi^2}{3H_{100}^2} f^2 h_c^2(f), \quad (\text{VII.2})$$

where $H_{100} = 100 \text{ km/s/Mpc}$ and $H_0 = h H_{100}$ is the Hubble rate today with $h \approx 0.7$. In Fig. 1 of Ref. [186] the NANOGrav collaboration provides the results of different fits to the data, namely a free spectrum fit of the individual frequency bins, a fit of a single power law to the lowest 5 frequency bins or to all 30 bins, and a broken power law with different slopes for the low and high frequency part of the data. The high frequency bins are expected to be dominated by white noise with slope $\alpha = 3/2$, which is corroborated by the broken power law fit. Instead the 5 lowest frequency bins contribute 99.98% of the significance of the potential GW signal.

In the following, we will therefore fit our signal models to the 5 lowest frequency bins, assuming that the remaining data points are explained by white noise. The results of the free spectrum fit are given in terms of the timing residual cross-power spectral density, which is related to the characteristic strain via

$$S(f) = \frac{h_c^2(f)}{12\pi^2} \left(\frac{f}{f_y} \right)^{-3} f_y^{-3}. \quad (\text{VII.3})$$

Using the formulas above we will convert the data and carry out all of the following analysis in terms of $\Omega_{\text{GW}}(f)h^2$. In the next section we outline our hierarchical Bayesian approach of fitting signals based on the free spectrum result by the NANOGrav collaboration. We compare our result of a power law fit to the one obtained by starting from the residuals themselves. We then move on to fitting the free spectrum with signal templates motivated by concrete new physics scenarios.

VII.3 Refitting the NANOGrav data

Let us start with a brief description of the Bayesian approach to fitting the timing residuals. The observed data has to be explained by considering various sources of noise as well as the GW background. Every model m therefore has a set of parameters characterizing the noise \mathbf{n} as well as a set of parameters characterizing the signal \mathbf{s} . In total the model is given as the sum of the two $m = (\mathbf{n}, \mathbf{s})$. Using a timing software it is then possible to calculate the likelihood $p(D|m)$ that we get the observed data D given that the model m is realized by nature. If we furthermore have a prior believe $p(m)$ on whether m is the correct model, we can update this believe with Bayes theorem to get the posterior

$$p(m|D) \propto p(D|m)p(m). \quad (\text{VII.4})$$

In the following we will assume that the prior factorizes $p(m) = p(\mathbf{n})p(\mathbf{s})$, as is the case for all PTA analysis. Since the parameter space has a lot of dimensions, a Monte Carlo Markov Chain (MCMC) has to be used to update our believe. The parameter points in the resulting chain will follow the posterior distribution, which is identical with the likelihood up to a normalization, if the priors are taken to be flat as the NANOGrav collaboration does. For parameters where the order of magnitude is not known the distribution of the log is chosen to be flat (e.g. the amplitude A_{GW} in the simple power law).

This approach allows one to marginalize over parameters/ parts of the model one is not interested in. As we are not interested in the noise \mathbf{n} but only in the signal \mathbf{s} , we can boil down the information in the chain by ignoring the information about the noise \mathbf{n} . Mathematically this corresponds to integrating them out

$$p(\mathbf{s}|D) \propto \int_{\mathbf{n}} d\mathbf{n} p(m|D) = \int_{\mathbf{n}} d\mathbf{n} p(\mathbf{n}, \mathbf{s}|D). \quad (\text{VII.5})$$

We are then left with a chain of parameter points \mathbf{s} that are distributed according to $p(\mathbf{s}|D)$.

The Free Spectrum as a General Model

Given the time of observation T_{obs} in a PTA the free spectral model allows for an independent GW amplitude $\Omega_i = \Omega_{\text{GW}}(f_i)h^2$ for each frequency $f_i = i/T_{\text{obs}}$, $i \in \mathbb{N}$ such that the set of parameters is $\mathbf{s}_{\text{free}} = (\Omega_1, \Omega_2, \dots)$.

Now lets assume we have a model motivated by physics. For concreteness we will consider the simple power law given above. Such a model only has a few parameters, in our case the slope α and the amplitude A_{GW} : $\mathbf{s}_{\text{PL}} = (\alpha, A_{\text{GW}})$. Furthermore the model will specify a function to calculate the timing residuals in terms of the parameters, in our case

$$\Omega_i(\alpha, A_{\text{GW}}) = \frac{2\pi^2}{3H_{100}^2} f_i^2 A_{\text{GW}}^2 \left(\frac{f_i}{f_y} \right)^{2\alpha}, \quad (\text{VII.6})$$

where $f_{\text{yr}} = 1/\text{year}$. In short we can write $\mathbf{s}_{\text{free}}(\mathbf{s}_{\text{PL}})$. The likelihoods of the free and specific model are therefore related by

$$p(D|\mathbf{n}, \mathbf{s}_{\text{PL}}) = p(D|\mathbf{n}, \mathbf{s}_{\text{free}}(\mathbf{s}_{\text{PL}})). \quad (\text{VII.7})$$

We then find for the marginalized posterior of the specific model

$$p(\mathbf{s}_{\text{PL}}|D) \propto \int d\mathbf{n} p(D|\mathbf{s}_{\text{PL}})p(\mathbf{s}_{\text{PL}})p(\mathbf{n}) \quad (\text{VII.8})$$

$$= \int d\mathbf{n} p(D|\mathbf{n}, \mathbf{s}_{\text{free}}(\mathbf{s}_{\text{PL}}))p(\mathbf{s}_{\text{PL}})p(\mathbf{n}) \quad (\text{VII.9})$$

$$= \frac{p(\mathbf{s}_{\text{PL}})}{p(\mathbf{s}_{\text{free}}(\mathbf{s}_{\text{PL}}))} \int d\mathbf{n} p(D|\mathbf{n}, \mathbf{s}_{\text{free}}(\mathbf{s}_{\text{PL}}))p(\mathbf{s}_{\text{free}}(\mathbf{s}_{\text{PL}}))p(\mathbf{n}) \quad (\text{VII.10})$$

$$= \frac{p(\mathbf{s}_{\text{free}}(\mathbf{s}_{\text{PL}}|D))}{p(\mathbf{s}_{\text{free}}(\mathbf{s}_{\text{PL}}))}p(\mathbf{s}_{\text{PL}}). \quad (\text{VII.11})$$

So the posterior of \mathbf{s}_{PL} is given as the ratio of the marginalized posterior and prior for the free spectrum $\mathbf{s}_{\text{free}}(\mathbf{s}_{\text{PL}})$. With a flat prior $p(\mathbf{s}_{\text{free}}) = \text{const.}$ we find the simpler version

$$p(\mathbf{s}_{\text{PL}}|D) \propto p(\mathbf{s}_{\text{free}}(\mathbf{s}_{\text{PL}}|D))p(\mathbf{s}_{\text{PL}}). \quad (\text{VII.12})$$

We exploit this relation here to fit the power law and physical models below. To do so we have to reconstruct $p(\mathbf{s}_{\text{free}}(\mathbf{s}_{\text{PL}}|D))$ from the Markov chain provided by the NANOGrav collaboration. Given that we are considering the first 5 frequency bins, this is a distribution over a 5-dimensional space. Therefore, a chain containing a huge number of points would be required to accurately recover all the features of this distribution. We therefore make the simplifying assumption that the distribution factorizes

$$p(\mathbf{s}_{\text{free}}|D) = p(\Omega_1|D) \cdot p(\Omega_2|D) \cdot \dots, \quad (\text{VII.13})$$

neglecting any possible cross-correlation between the frequency bins. The separate posteriors $p(\Omega_i|D)$ are then reconstructed by taking a histogram of the points in the chain.¹ In Fig. VII.3, we show the posterior distribution extracted in this way for the first 5 frequency bins as gray violins. In Fig. VII.2 we show a comparison of the 68% and 95% confidence regions (in the following also referred to as the 1σ and 2σ regions) from our hierarchical method and the original, direct approach for the simple power law. We find that both regions are stretched out along the same diagonal line, which corresponds to both of them agreeing well on the amplitude of the GWs at $f \approx f_y/10$, as one can easily show. The region of the original fit extends to larger α , however. Crucially the expected value of $\alpha = -2/3$ from super massive black hole inspirals marked by the dotted line lies inside the 1σ region of the original fit and only the 2σ region inferred by our method. This discrepancy might be caused by neglecting the cross-correlation between the frequency bins. On the other hand there is still a large overlap of the inferred regions compared to their size. Our simple method only takes a fraction of the time needed for the full analysis and therefore has its place as a quick estimate that still goes beyond only matching the amplitude.

VII.4 Audible Axions and NANOGrav

We studied the prospect of sourcing a stochastic GW background after inflation from an axion coupled to a dark photon in great detail in Part II. For some of the scenarios we already briefly commented on the possibility that these might explain the NANOGrav signal.

The GWs in these models are sourced when the energy is transferred from the axion to the dark photon modes. After this process the majority of the energy remains in the dark photon and red-shifts like radiation.² It therefore contributes to the number of relativistic

¹For the original publication [7] we obtained the distributions by digitizing the violin plot Fig. 1 of Ref. [186]. This induced a sizeable error, which resulted in wider confidence regions for all subsequent fits.

²The remaining energy in the axion is initially suppressed, but comes to dominate eventually due to

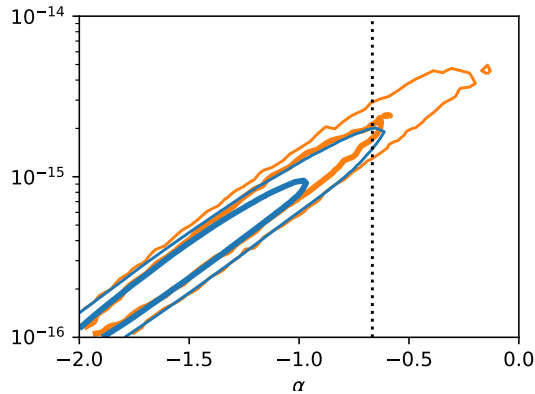


Figure VII.2: Comparison of 1σ and 2σ contours for a single power law fit to the 5 lowest frequency bins. Our results using the hierarchical method are shown in blue and the original result in orange. The black dotted line sits at $\alpha = -2/3$, the expected slope for the signal of SMBHBs.

degrees of freedom N_{eff} . As one can see from Fig. IV.9 the 2σ region (purple) for the minimal model with the misalignment angle of $\theta = 1$ and a coupling $\alpha = 100$ falls just into the region excluded by the Planck 2018 dataset at 95% confidence level. We find that the same holds true for the kinetically misaligned axion discussed in Chapter V. In this case the initial value of the saxion field S_i even has to be chosen super-Planckian in order to provide with enough energy to source a strong enough signal.

Only the relaxion model discussed in Chapter VI can match the signal without being in conflict with the N_{eff} bound. Due to the continuous emission of GWs in this scenario the ratio $\xi = k_{\text{ra}}/(a_{\text{ra}}H_{\text{ra}})$ between the typical scale of the fluctuations k_{ra} and the horizon at time of emission $a_{\text{ra}}H_{\text{ra}}$ can be reduced to $\mathcal{O}(10)$, while in the other scenarios it is typically $\mathcal{O}(100)$. From the estimate of the GW amplitude based on naive dimensional analysis that we used throughout this thesis (e.g. Eq. (IV.14)) it becomes clear that a reduction of this ratio leads to an enhancement in GW emission. In Fig. VI.7 we show the resulting 1 and 2σ regions of the fit using $\xi = 10, 25$ and 100 in terms of the resulting peak amplitude and peak frequency. As expected the region for $\xi = 100$ is excluded by the N_{eff} bound as well as the barriers of the relaxion reappearing before BBN. The regions for $\xi = 10$ are, however, not restricted by these bound with $\xi = 25$ being a middling case. It should however be said that small values of ξ require exponentially large values of the coupling α . In Fig. VII.3 we show the GW spectrum of the best fit parameters for $\xi = 10$ in green.

Another interesting aspect is that parameter points resulting in stronger signals than the ones in the best fit regions, can be excluded by the NANOGrav data. While at present all of these points are already excluded by the N_{eff} bound, these bounds can be expected to become relevant soon, as more PTA data becomes available.

VII.5 Phase transitions and NANOGrav

It has been known for many years that a cosmological phase transition (PT), such as from the spontaneous breaking of a global or gauge symmetry through a scalar field that acquires

only red-shifting like matter.

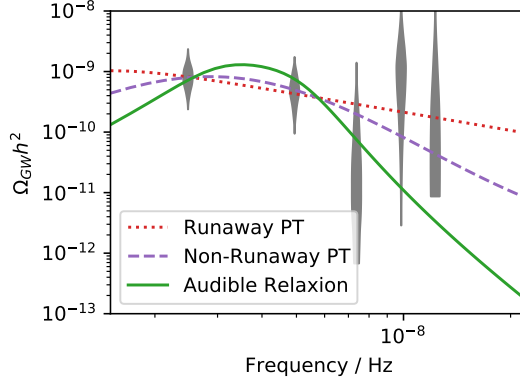


Figure VII.3: Signal of the best fits of a runaway and a non-runaway phase transition discussed in this chapter as well as the audible relaxation from Chapter VI with $\xi = 10$ compared to the first frequency bins of NANOGrav in the frequency- $\Omega_{\text{GW}}h^2$ plane.

a vacuum expectation value, produces a stochastic GW background if the transition is strongly first order [197–199]. While a large variety of models exists that predict such a transition at different scales, the GW signal of a strong first order PT is universally described by only four parameters, the ratio between the vacuum and total energy density $\alpha = \rho_{\text{vac}}/\rho_{\text{tot}}$, the time scale of the transition β/H , where H is the Hubble scale at the time of the transition, the temperature T_* at which the transition takes place and the bubble wall velocity v_w [200, 204].

We use the signal templates in terms of these parameters as given in [59]. The peak frequencies and amplitudes of the two most important contributions to the signal scale as

$$f_p \approx 2 \times 10^{-7} \text{Hz} \left(\frac{\beta}{H} \right) \left(\frac{T_*}{\text{GeV}} \right), \quad (\text{VII.14})$$

$$\Omega_{\text{GW}}h^2 \approx 10^{-6} v_w \left(\frac{\beta}{H} \right)^{-n} \left(\frac{\alpha}{1+\alpha} \right)^2, \quad (\text{VII.15})$$

where $n = 1$ for the sound wave contribution and $n = 2$ for the scalar field contribution, and we neglect order one numbers which are not relevant for the qualitative discussion. Very strong transitions are characterised by $\alpha > 0.1$ and a wall speed approaching the speed of light, $v_w \rightarrow 1$. The NANOGrav signal corresponds to an energy density $\Omega_{\text{GW}}h^2 > 10^{-10}$ at a frequency around 10^{-8} Hz, so that only a strong transition will be able to explain the data. Furthermore we immediately see that T_* should be of order $10^{-3} - 10^{-2}$ GeV, i.e. the PT should happen at a very low scale. The implications of this for concrete models will be discussed in more detail below.

We consider two scenarios. If the PT takes place at a temperature significantly below the critical temperature, the Universe will be dominated by vacuum energy, i.e. the α dependence drops out of Eq. (VII.15). In such a supercooled PT, no friction acts on the bubble wall, so that $v_w = 1$. Furthermore in the absence of a plasma, the only source of GWs is the scalar field itself, i.e. $n = 2$ in Eq. (VII.15). In that case, a good fit to the data requires relatively small values of $\beta/H \lesssim 100$, and transition temperatures around or below the MeV scale, as shown in Fig. VII.4. Above the peak frequency, the GW strain amplitude of the PT signal falls as $f^{-3/2}$. Therefore if the peak frequency lies below the lowest frequency probed by NANOGrav, the signal will look like a single power law to the detector. This explains the flat direction in the fit towards lower temperatures and lower

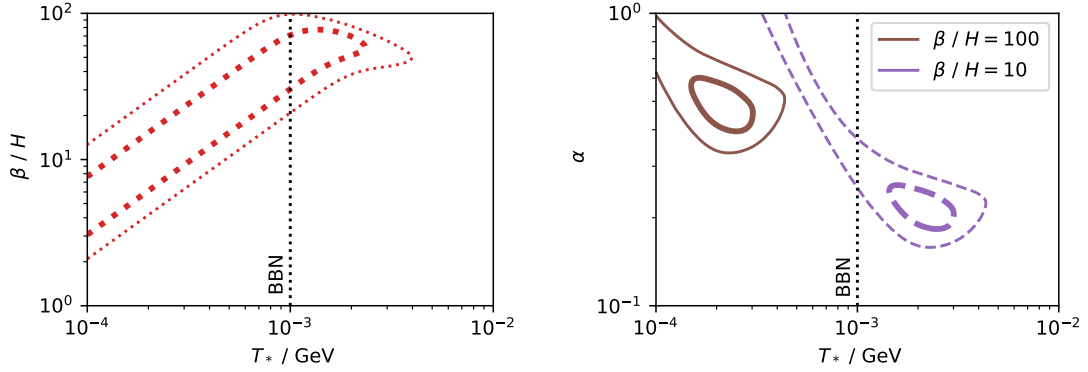


Figure VII.4: Left: Regions favoured by the NANOGrav signal for a vacuum PT, with $v_w = 1$, shown as a function of the transition temperature T_* and the PT timescale β/H . Right: Same for a strong first order PT in a plasma, with $v_w = 1$ and fixed values of β/H , as function of T_* and the energy budget α . The vertical line at one MeV indicates the onset of BBN, below which strong constraints apply to any models that alter the expansion rate of the Universe.

values of β/H . However lower values of β/H are increasingly difficult to obtain in realistic models, therefore this region should be considered less favoured.

If the PT is very strong but not supercooled, the bubble walls will still reach a relativistic terminal velocity, so for simplicity we again set $v_w = 1$. In this case sound waves in the plasma induced by the PT are the dominant source of GWs, and the amplitude is only suppressed by one power of β/H . As expected, in Fig. VII.4 we see that a good fit to the data in the $T_* - \alpha$ plane is found both for $\beta/H = 10$ and $\beta/H = 100$, where in the second case the suppression of the signal is compensated by a larger energy budget α . Again we also find a flat direction, where the peak of the PT signal is shifted below the NANOGrav frequency range, and data is fit by the high frequency tail. The strain amplitude in the UV tail falls off considerably faster though as f^{-3} than in the supercooled case, which is why the points along this flat direction are disfavoured.

In both scenarios, we find that the PT should happen at a temperature around 1 MeV. Since extensions of the SM at such low scales are almost impossible to hide from laboratory experiments, it is clear that the PT should take place in a dark sector, with only very weak interactions with the SM [59, 205–211].

Nevertheless it was shown in [59] that also PTs in a dark sector are subject to strong constraints, in particular if they happen close to the scale of BBN. The reason is that BBN is a sensitive probe of the Hubble scale at temperatures below the MeV scale, which in turn depends on the total energy density in the Universe, since gravity is universal. Either the energy density in the hidden sector should be transferred to the SM before the onset of BBN at $T \sim 1$ MeV, which essentially prohibits PTs below that scale [212], or the energy should be converted into dark radiation, in which case the dark sector temperature is constrained by N_{eff} .

Viable models should therefore have few degrees of freedom, and still feature a very strong first order PT. The simplest scenario is probably a single scalar field with a non-renormalizable potential, such as a very light radion or dilaton. Indeed for these models it is known that a strongly supercooled first order PT can occur and produce a large GW background [213–217]. For renormalizable scenarios, the most minimal models that were found in [59] consist of either two real singlet scalars or a $U(1)$ gauge boson with a

complex scalar charged under the gauge symmetry. While the majority of the parameter space of these models features a weaker PT, there are benchmark points with $\alpha > 0.5$ and $\beta/H \lesssim 100$, while still being consistent with constraints from BBN or N_{eff} .

Finally also here it should be noted that PTs with $T_* \sim 1$ MeV which produce a GW signal stronger than the observed one are now excluded by the NANOGrav data. We are therefore finding the first non-trivial constraints on the dynamics of potential dark sectors around these scales. Of course, to obtain robust limits on concrete models, a reduction of the large theoretical uncertainties in the prediction of the GW signals would be desirable. For some recent progress in this heroic task, see e.g [218–221].

VII.6 Discussion and Outlook

The first hint of a GWB observed by NANOGrav is very intriguing. While the data can be well explained with a single power law, consistent with the expected background from supermassive black hole binaries (SMBHBs), we show here that also broken power law spectra, which are predicted in various extensions of the SM, can well describe the signal. In both new physics scenarios we considered, the peak of the GW signal is strongly correlated with the relevant mass scale of the new physics, either the reappearance temperature of the relaxation barriers or the mass scale of the new sector that undergoes a phase transition. The PTA data therefore already allows us to narrowly constrain the potential mass range.

Since the data suggests very light new physics, it is already clear that these new particles have to be part of a dark sector that is only very weakly coupled to the SM, otherwise laboratory experiments would have uncovered them already. Yet astrophysical data on BBN and N_{eff} constrain the parameter space of such dark sectors.

For the audible realxion scenario, we find parameter regions consistent with N_{eff} if the ratio between the typical scale of the fluctuations and the horizon at reappearance can be brought down to $\xi = \mathcal{O}(10)$.

A first order PT can explain the data if the transition is very strong and happens at temperatures between 1-10 MeV, or slightly below, if BBN and N_{eff} constraints can be evaded. We have briefly illustrated some dark sector models that are known to satisfy all requirements. Here it will of course be interesting to ask whether concrete realizations can also explain the observed dark matter abundance, and whether they leave observable imprints elsewhere. One such imprint might be spectral distortions of the CMB, as we discuss in great detail in the next chapter.

Already this first hint of a stochastic GW background in the PTA range provides us with a deep insight into possible new physics explanations of the signal. With more precise frequency binned data it will be possible to distinguish between different models and astrophysical backgrounds such as the one from SMBHBs. It would also be interesting to directly fit a broader range of GW templates to the pulsar timing data, possibly including polarized signals such as the one expected from audible relaxions.

Spectral Distortions

VIII.1 Introduction

In the previous chapters we studied the dynamics of purely gravitationally coupled dark sectors that emit a primordial gravitational wave (GW) signal. These GWs can then be detected, if the amplitude is large enough and the red-shifted frequency falls into the range of one of the detectors. As possible detectors we discussed so far earth and space based interferometers that in the future will cover the frequency range $\approx 10^{-7} - 10^3$ Hz and pulsar timing arrays (PTAs). PTAs cover frequencies $\approx 10^{-9} - 10^{-7}$ Hz. At the lower end they are limited by the observation time, which is given by ≈ 10 yr. After this time a radio telescope is typically taken down either by a tropical storm or a Bond villain. At much lower frequencies $\approx 10^{-18} - 10^{-16}$ Hz gravity waves become detectable again by the imprint they leave on the CMB polarization, so called B-modes.

While this thesis was conceived, Ref. [25] pointed out that this gap in detectable frequencies could be closed by using CMB spectral distortions. The GW travels through space filled with the SM plasma. This plasma is a non-perfect fluid and therefore friction converts some of the GW energy into heat. This heat leads to a deviation of the CMB spectrum from a black body spectrum, if there are no processes to reach thermal equilibrium again. If the GW was generated during inflation and therefore “always” has been around that is surely the end of the story. But in the mechanisms of production discussed in this thesis the GW is only sourced in the post inflationary universe. In particular the dark sector with its energy fluctuations is still present when the spectral distortions are caused. A natural question to ask is, therefore, whether this is the dominant way a purely gravitationally sector causes spectral distortions or, if the effects mediated by the gravitational potential dominate.

In this chapter we indeed identify such a second way. It relies on the fact that the gravitational potential couples the dark sector to the baryon-photon fluid. The energy fluctuations in the dark sector therefore cause fluctuations in the the baryon-photon fluid, which propagate as acoustic waves. Due to photon diffusion these acoustic waves are eventually damped, at which point their energy is turned into heat. This heat also contributes to the distortion.

Before going into the details of this mechanism let us briefly recall, what a spectral distortion is and under which circumstances it gets sourced. It is well known that the CMB spectrum is to good approximation a black body spectrum. Any deviation of the spectrum from this shape, so called spectral distortions, therefore, encode valuable information about physics in the early universe. In principal any injection or removal of energy from the photons causes such a distortion. Whether a distortion is observable depends, aside from the size of the distortion, on whether efficient processes to thermalize the spectrum

again are present.

At high red-shift and correspondingly large temperatures processes changing the photons momentum, like Compton scattering, as well as photon number changing processes, like double Compton scattering, are present. This changes for redshifts $z \lesssim 2 \times 10^6$ when the photon number changing processes become ineffective. From this point onwards the photon number is a conserved quantity and one has to introduce a chemical potential μ to capture the equilibrium distribution. μ becomes non-zero if energy is injected into the plasma at this point. Below red-shifts of $z \lesssim 5 \times 10^4$ Compton scattering also becomes inefficient at redistributing the momentum beneath the photons, such that any distortion sourced now is directly imprinted onto the CMB spectrum.

The source of energy injection we are interested in this chapter is the damping of sound waves in the baryon-photon fluid. Any sound wave in the plasma is rapidly damped once its wavelength falls below the diffusion scale, which is the distance a photon covers by random walking between scattering events. For modes in the range $8 \times 10^3 \text{ Mpc}^{-1} \lesssim k \lesssim 2 \times 10^3 \text{ Mpc}^{-1}$ this happens while $5 \times 10^4 \lesssim z \lesssim 2 \times 10^6$ leading to a μ -distortion (see Fig. VIII.1). For longer-wave length modes where the damping occurs for $z \lesssim 5 \times 10^4$ the photon momenta are not redistributed, such that one observes the superposition of multiple black body spectra with slightly different temperatures $\delta T/\bar{T} = 4\delta\rho/\bar{\rho}$, where $\bar{\rho}$ and $\delta\rho$ denote the mean density and density fluctuations in the fluid respectively. The resulting distortion is called a y -distortion and differs in its frequency dependents from a μ -distortion. y -distortions are however also produced during the re-ionization era by the Sunyaev-Zeldovich effect [222, 223], which limits there use for studies of new primordial physics. We therefore only concentrate on μ -distortions hereafter.

In the inflationary paradigm the primordial fluctuations, measured at the largest scales as CMB fluctuations and in structure formation, are predicted to be approximately flat and therefore extend to the small scales sourcing μ -distortions. Here we however investigate dark sectors with turbulent dynamics which, through their gravitational coupling to the photon fluid, lead to additional fluctuations at smaller scales. Consequently the μ -distortions get enhanced, while leaving the scales relevant for CMB fluctuations and structure formation untouched. For some specific dark sector models these considerations have been made before [224, 225]. We present a general and easy-to-use framework for estimating and calculating these effects as well as comparing the contribution to the distortion from GWs and acoustic waves.

In Section VIII.2 we show that induction of sound waves in the photon fluid through the dark sector can be decoupled from the subsequent damping and production of distortions as well as presenting the relevant details to calculate the μ -distortion. In Section VIII.3 the induction of sound waves is discussed analytically and compared in Section VIII.4 to the numerical results of a particular dark sector. We recommend the impatient reader to jump to Section VIII.5, where we apply our techniques to various dark sectors that are well known GW sources.

VIII.2 Source of μ -distortions through gravitational interaction

The generic setup we have in mind is a dark sector that only comprises a subdominant amount of the total energy $\Omega_d \ll 1$ but develops large anisotropies at some point $\delta\rho_d/\bar{\rho}_d = \delta_d \approx 1$. Since $\Omega_d \ll 1$ metric and density fluctuations in other sectors present in the universe are still small, which allows us to treat them perturbatively, linearizing their dynamics. It is then beneficial to work in Fourier space. We use the following definitions

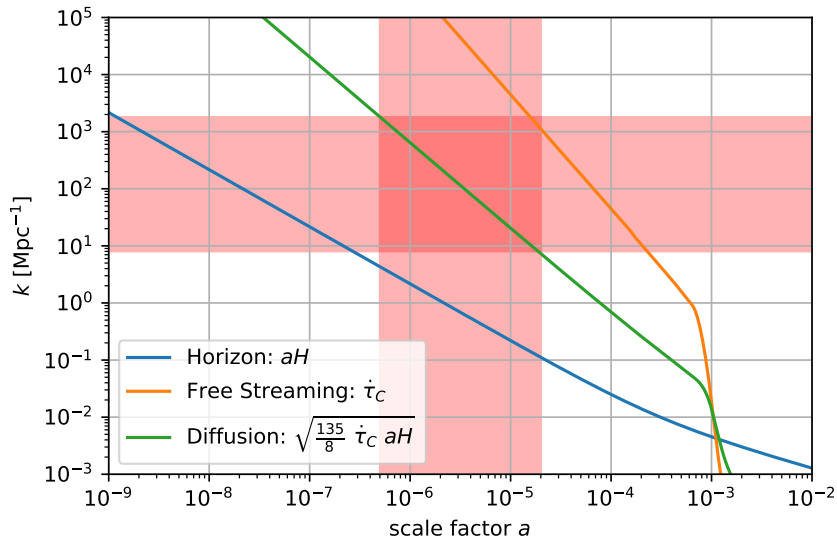


Figure VIII.1: The evolution of the horizon scale (blue), the scale a photon free streams between consecutive scattering events and diffusion scale that is approximately the distance traveled by a photon in a random walk as a result of all the scattering events in one Hubble time. Once a mode passes the diffusion scale the energy stored in the acoustic oscillation is damped. If this happens during the red-shifts marked in red on the x-axis a μ -distortion is sourced, singling out the modes marked in red on the y-axis as the dominant messengers of new physics. These modes enter the Horizon as early as $a \approx 10^{-9}$ allowing us to probe new physics back to when the photon temperature was ≈ 1 MeV.

for the Fourier transform and the dimensionless power spectrum \mathcal{P}

$$\delta(\mathbf{k}) = \int d^3x \delta(\mathbf{x}) \exp(-i\mathbf{k}\mathbf{x}); \quad \langle \delta(\mathbf{k}) \delta^*(\mathbf{k}') \rangle = \frac{2\pi^2}{k^3} \mathcal{P}_\delta(k) (2\pi)^3 \delta^{(3)}(\mathbf{k} - \mathbf{k}'). \quad (\text{VIII.1})$$

We furthermore use the conformal Newtonian gauge for the scalar metric perturbations

$$ds^2 = a^2(\tau) [(1 + 2\Psi(\mathbf{x}, \tau))d\tau^2 - (1 + 2\Phi(\mathbf{x}, \tau))d\mathbf{x}^2], \quad (\text{VIII.2})$$

where the equations of motion for the potentials Φ, Ψ are given by

$$3aH (\dot{\Phi} - aH\Psi) + k^2\Phi = \frac{3a^2H^2}{2} (\Omega_\gamma\delta_\gamma + \Omega_n\delta_n + \Omega_d\delta_d) \quad (\text{VIII.3})$$

$$\Phi + \Psi = -\frac{2Aa^2H^2}{k^2} \left(\Omega_\gamma\sigma_\gamma + \Omega_n\sigma_n + \frac{3}{4}(1 + w_d)\Omega_d\sigma_d \right). \quad (\text{VIII.4})$$

Here overdots denote derivatives with respect to conformal time τ , and δ and σ denote the energy fluctuation and shear in the respective sectors. For times well before matter-radiation equality, $a \ll a_{\text{eq}}$, the three relevant sectors are the baryon-photon fluid γ , the neutrinos n and the dark sector d . The shear is defined as the longitudinal traceless part of the energy momentum tensor $\sigma = -(\hat{\mathbf{k}}_i\hat{\mathbf{k}}_j - \frac{1}{3}\delta_{ij})T_j^i/(\bar{\rho} + \bar{p})$. Finally w_d is the equation of state parameter of the dark sector.

It is clearly visible that the scalar metric perturbations induced by δ_d are suppressed by Ω_d , thus justifying the linearised treatment. Furthermore since all other sectors only couple to the dark sector via gravity, also their perturbations induced by δ_d are suppressed by Ω_d . This also allows one to neglect the back-reaction effects of gravity onto the dark sector since $\Omega_d\delta_d \ll \delta_d$ and one can therefore study its dynamics independently. In the following we will assume that all fluctuations in the baryon-photon fluid and the neutrinos as well as the potentials are initially zero. The effects of other, uncorrelated fluctuations like e.g. inflationary ones can be studied independently, as usual in linear perturbation theory.

For modes deep inside the horizon, $k \gg aH$, one can solve for the gravitational potentials directly by neglecting the first term on the right side of Eq. (VIII.3). One finds that the gravitational potentials decay as $\Phi, \Psi \propto a^2H^2/k^2$ if the fluctuations don't keep growing after their generation, which is a reasonable assumption during radiation domination. The gravitational coupling between the sectors therefore quickly becomes negligible after horizon entry. For our specific case, it suggests that the amplitude of fluctuations in the baryon-photon fluid is set within about one Hubble time after horizon entry or after the fluctuations in the dark sector have been created, whichever happens later for a given mode. We can also anticipate the strength of the gravitational interaction being suppressed for modes that are deep inside the horizon when the dark sector develops its fluctuations. The details of this suppression are discussed in the next section.

For the times well before recombination, the baryon-photon fluid is well described by the tight-coupling approximation (TCA, e.g. [226, 227]) and the energy density in baryons can be neglected, leading to

$$\dot{\delta}_\gamma + \frac{4}{3}kv_\gamma = -4\dot{\Phi} \quad (\text{VIII.5})$$

$$\dot{v}_\gamma - k \left(\frac{1}{4}\delta_\gamma - \sigma_\gamma \right) = k\Psi \quad (\text{VIII.6})$$

$$\sigma_\gamma = \frac{16}{45} \frac{k}{\dot{\tau}_C} v_\gamma, \quad (\text{VIII.7})$$

where $v_\gamma = i\hat{\mathbf{k}}_i T_{\gamma,0}^j / (\bar{\rho}_\gamma + \bar{p}_\gamma)$ is the longitudinal part of the fluids velocity relative to the cosmological rest frame. The TCA takes advantage of the fact that all moments of the photon distribution past the velocity are suppressed by the high Compton scattering rate $\dot{\tau}_C = an_e\sigma_C \gg k$, where σ_C is the Compton cross-section and n_e the free electron density, which can be approximated as $\dot{\tau}_C = a^{-2} 4.5 \times 10^{-7} \text{ Mpc}^{-1}$ well before recombination. When solving these equations numerically we also take into account the free streaming neutrinos, see Section VIII.4.2.

To make progress with the analytic treatment one combines the equations for the baryon-photon fluid to get a damped harmonic oscillator. We will first do so in the limit that the mode is already deep inside the horizon and neglect the gravitational potentials

$$\ddot{\delta}_\gamma + k^2 \left(\frac{16}{45} \frac{1}{\dot{\tau}_C} \dot{\delta}_\gamma + \frac{1}{3} \delta_\gamma \right) = 0. \quad (\text{VIII.8})$$

In the given limit that $aH \ll k \ll \dot{\tau}_C$ the general solution to this problem is approximated as

$$\delta_\gamma = \left[A \sin \left(\frac{k\tau}{\sqrt{3}} \right) + B \cos \left(\frac{k\tau}{\sqrt{3}} \right) \right] \exp \left(-\frac{k^2}{k_D^2(\tau)} \right). \quad (\text{VIII.9})$$

This solution is interpreted as damped acoustic waves traveling in the baryon photon fluid with the relativistic speed of sound of $c_s = 1/\sqrt{3}$. The diffusion scale k_D appearing here is determined by the equation $\frac{d}{d\tau} k_D^{-2} = \frac{8}{45} \frac{1}{\dot{\tau}_C}$ and during radiation domination given as $k_D = \sqrt{\frac{135}{8} \dot{\tau}_C aH}$ as long as the free electron density is constant up to dilution by expansion. This effect is also known as Silk damping [228] and is attributed to photons performing a random walk with typical step length $\Delta x \approx 1/\dot{\tau}_C$ while doing $N \approx \frac{\dot{\tau}_C}{aH}$ steps per Hubble time. The diffusion scale is then the distance typically traversed by a photon $1/k_D \approx \Delta x \sqrt{N}$ in a Hubble time. Due to the direct energy exchange, the fluctuations quickly get erased.

From the discussion so far two important scales have emerged: the Horizon scale at which the gravitational coupling is strongest and we, therefore, expect the dark sector to efficiently source acoustic waves, and the diffusion scale. As can be seen in Fig. VIII.1, the modes of interest, marked in red on the y-axis, pass these two scales at scale factors a that are always separated by about two orders of magnitude or more. This allows one to separately discuss the two effects with the amplitude of the sound waves A, B being approximately constant in between. The important physical quantity that is constant during those times is the energy in acoustic waves. Relative to the total energy in the relativistic baryon-photon fluid it is given as

$$\epsilon_{ac} = \frac{\rho_{ac}}{\bar{\rho}_\gamma} = \frac{1}{V} \int_V d^3x \left[\frac{1}{8} \delta_\gamma^2(\mathbf{x}) + \frac{2}{3} v_\gamma^2(\mathbf{x}) \right] = \int d \log k \epsilon_{ac}(k), \quad (\text{VIII.10})$$

where we defined the spectral acoustic energy in the last step which is given as

$$\epsilon_{ac}(k) = \frac{1}{8} \mathcal{P}_{\delta_\gamma}(k) + \frac{2}{3} \mathcal{P}_{v_\gamma}(k) = \frac{1}{8} [\mathcal{P}_A(k) + \mathcal{P}_B(k)] \quad (\text{VIII.11})$$

in terms of the power spectra for δ_γ, v_γ and A, B respectively.

When the acoustic waves get damped by diffusion, this energy becomes part of the photon bulk energy. If this happens between $a_{dc} = 5 \times 10^{-7}$, when photon number changing processes such as Double Compton scattering becomes inefficient, and $a_{\mu,y} = 2 \times 10^{-5}$,

when Compton scattering stops redistributing the momentum between the photons, a μ -distortion gets sourced besides an increase in the bulk temperature. The approximation commonly used to determine the μ -parameter is

$$\mu \approx 1.4 \int d \log k \int_{a_{\mu,y}}^{\infty} d \log a \frac{d\epsilon_{ac}(k)}{d \log a} \exp \left(- \left(\frac{a_{dc}}{a} \right)^{5/2} \right), \quad (\text{VIII.12})$$

where $\frac{d\epsilon_{ac}(k)}{d \log a}$ is the acoustic “power” transmitted to the bulk energy. It is given as [226]

$$\frac{d\epsilon_{ac}(k)}{d \log a} = \frac{15}{4} \frac{\dot{\tau}_C}{aH} \mathcal{P}_{\sigma\gamma} = \frac{64}{135} \frac{k^2}{\dot{\tau}_C a H} \mathcal{P}_{v\gamma} = \frac{8}{3} \mathcal{P}_{v\gamma} \frac{d}{d \log a} \left(\frac{k^2}{k_D^2} \right) \approx 2\epsilon_{ac}(k, a) \frac{d}{d \log a} \left(\frac{k^2}{k_D^2} \right), \quad (\text{VIII.13})$$

where we used in the last step that due to virialization $\epsilon_{ac} \approx \frac{4}{3} \mathcal{P}_{v\gamma}$. In the limit that the acoustic energy takes on a constant value $\epsilon_{ac}^{\text{lim}}(k)$ before diffusion damping becomes active, we have $\epsilon_{ac}(k, a) = \epsilon_{ac}^{\text{lim}}(k) \exp(-2k^2/k_D^2(a))$ during the period of damping, such that we can write the μ -parameter as

$$\mu = \int d \log k \epsilon_{ac}^{\text{lim}}(k) \mathcal{W}(k), \quad (\text{VIII.14})$$

where we have introduced the window function [229]

$$\mathcal{W}(k) \approx 1.4 \int_{a_{\mu,y}}^{\infty} d \log a \exp \left(- \left(\frac{a_{dc}}{a} \right)^{5/2} \right) \frac{d}{d \log a} \exp \left(-2 \frac{k^2}{k_D^2(a)} \right) \quad (\text{VIII.15})$$

$$\approx 1.4 \left(\exp \left[- \left(\frac{k}{1360 \text{ Mpc}^{-1}} \right)^2 \left(1 + \left(\frac{k}{260 \text{ Mpc}^{-1}} \right)^{0.3} + \frac{k}{340 \text{ Mpc}^{-1}} \right)^{-1} \right] \right. \quad (\text{VIII.16})$$

$$\left. - \exp \left[- \left(\frac{k}{32 \text{ Mpc}^{-1}} \right)^2 \right] \right).$$

This remarkable easy expression allows one to calculate the μ -distortion a dark sector causes, given the spectral acoustic energy before damping.¹ This value can then be compared to current bounds and the detection threshold of future experiments.

In Fig. VIII.2 we show the numerical results of a toy model that neatly summarize this section. The dark sector is assumed to be radiation like such that $\Omega_d = \text{const.}$ while the sound waves are sourced, and the fluctuations are modeled as being zero until $a_* = 10^{-7}$ and as $\delta_d = \sin(k\tau)$ afterwards². The shear in the dark sector is set to zero. We show the evolution for one mode that is still outside the horizon at $a = a_*$ on the left and one that is already inside on the right.

¹In the literature the window function is commonly defined with respect to a primordial spectrum rather than the acoustic energy spectrum and therefore represents a convolution of the dynamics of horizon entry and damping (e.g. [229]). Our definition is universally applicable, although one would have to discuss horizon entry separately.

²As we will argue in Section VIII.4.3, $\dot{\delta}_d(k\tau)$ only changes on time scales $1/k$ for subhorizon modes making this an unphysical choice with $\delta_d(k\tau)$ being discontinuous at a_* . We only use this ansatz here for demonstration as well as for rough estimates in the following section.

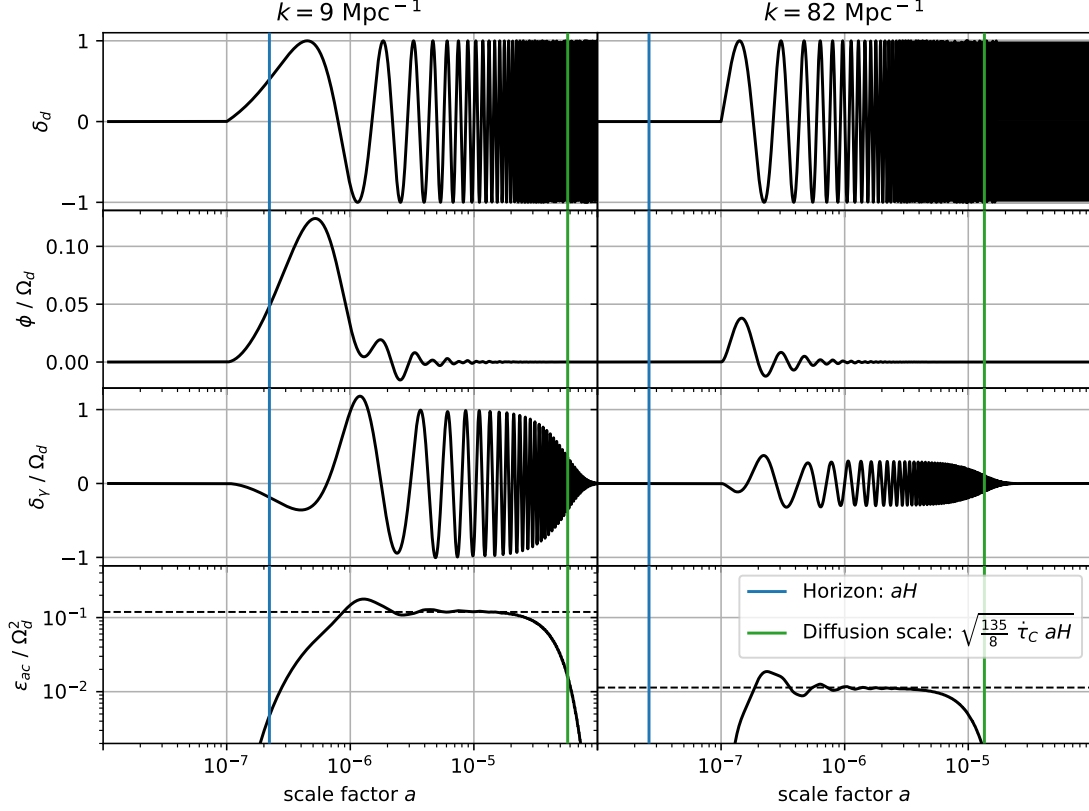


Figure VIII.2: Sourcing of acoustic waves through a gravitationally coupled dark sector and consequent damping by diffusion. The toy dark sector here is radiation like ($\Omega_d = \text{const.} \ll 1$) and its density fluctuations are zero until $a_* = 10^{-7}$ before evolving as $\delta_d = \sin(k\tau)$ (top row). The resulting gravitational potential (second row) causes acoustic oscillations in the baryon-photon fluid (third row). Since the gravitational potential rapidly decays after a mode has entered the horizon (vertical blue line) the amplitude of the acoustic oscillations quickly levels off resulting in an approximately constant acoustic energy $\epsilon_{ac}^{\text{lim}}(k)$ (bottom row, dashed line). The same effect also leads to the acoustic oscillations being suppressed for the high k mode (right side) that is already inside the horizon when the fluctuations in the dark sector develop. Subsequently the acoustic oscillations are damped for both modes once they cross the diffusion scale (green line). At this point the acoustic energy is injected into the bulk photon energy, leading to a sizeable μ -distortion for modes where this happens between $5 \times 10^{-7} \lesssim a \lesssim 2 \times 10^{-5}$.

VIII.3 Analytic Estimation of the Induced Acoustic Energy

We now obtain an analytic estimate for the acoustic energy ϵ_{ac}^{\lim} caused by fluctuations in a dark sector. We assume that the fluctuations are generated at a fixed time $a = a_*$. For modes that enter the horizon around or after a_* ($k \lesssim a_* H_*$), we find that the contribution of the photons and neutrinos to the gravitational potentials is of the same order as the one from the dark sector ($\Omega_d \delta_d \approx \Omega_\gamma \delta_\gamma \approx \Omega_n \delta_n$). The coupled system of equations can therefore only be solved numerically. As previously mentioned, for the modes already inside the horizon $k > a_* H_*$ the amplitudes of δ_γ and δ_n remain further suppressed by some power of $a_* H_*/k$. They can therefore be neglected when solving for the gravitational potentials. We therefore restrict our analytic treatment to $k > a_* H_*$.

To make further progress we again combine Eq. (VIII.5) and Eq. (VIII.6) but this time keeping the potentials and dropping the diffusion damping, since we now want to solve for times well before the mode crosses the damping scale, to find

$$\ddot{\delta}_\gamma + \frac{1}{3}k^2 \delta_\gamma = -4\ddot{\Phi} - \frac{4}{3}k^2 \Psi. \quad (\text{VIII.17})$$

To get rid of the second time derivative of Φ , we define $\tilde{\delta}_\gamma = \delta_\gamma + 4\Phi$. Since the gravitational potential decays, at late times we have $\tilde{\delta}_\gamma \approx \delta_\gamma$. Since we consider a sub-horizon mode, we can continue with only the last term on the left-hand side of Eq. (VIII.3), which allows us to solve for the potentials, the driving force of the harmonic oscillator $S(\tau)$, in terms of δ_d and σ_d directly

$$\ddot{\tilde{\delta}}_\gamma + \frac{1}{3}k^2 \tilde{\delta}_\gamma = 4a^2 H^2 \Omega_d [\delta_d + 6(1 + w_d)\sigma_d] \equiv S(\tau). \quad (\text{VIII.18})$$

The Greens function for this differential equation is $G(\tau) = \sqrt{3}/k \sin(k\tau/\sqrt{3})$, such that we can formally solve the above equation (adapted from e.g. []) and find

$$\epsilon_{ac}^{\lim}(k) = \frac{1}{8}\mathcal{P}_{\delta_\gamma}(k, \tau_{\text{lim}}) + \frac{2}{3}\mathcal{P}_{v_\gamma}(k, \tau_{\text{lim}}) \quad (\text{VIII.19})$$

$$= \frac{3}{8} \frac{1}{k^2} \int_{\tau_*}^{\tau_{\text{lim}}} d\tau' \int_{\tau_* - \tau'}^{\tau_{\text{lim}} - \tau'} d\tau'' \cos\left(\frac{k\tau''}{\sqrt{3}}\right) \mathcal{P}_S(k, \tau', \tau' + \tau''), \quad (\text{VIII.20})$$

where τ_{lim} is chosen large enough, such that ϵ_{ac}^{\lim} has approached a quasi constant value and $\tilde{\delta}_\gamma \approx \delta_\gamma$ holds. We have furthermore introduced the unequal time correlation spectrum of the source $\mathcal{P}_S(k, \tau, \tau')$, defined as

$$\langle S(\mathbf{k}, \tau) S^*(\mathbf{k}', \tau') \rangle = \frac{2\pi^2}{k^3} \mathcal{P}_S(k, \tau, \tau') (2\pi)^3 \delta^{(3)}(\mathbf{k} - \mathbf{k}'). \quad (\text{VIII.21})$$

Assuming that the equation of state of the dark sector w_d is known then so is the time dependence of $\Omega_d \propto a^{1-3w_d}$. We will hereafter assume that the dark sector behaves radiation-like such that $\Omega_d = \Omega_{d,*} = \text{const.}$. The time dependence of $\delta_d(\tau)$ and $\sigma_d(\tau)$ is, however, more intricate and closely related to the spatial structure of the dark source. We discuss these features for a general dark sector below.

VIII.3.1 Spatial Structure

It is reasonable to assume that the mechanism that causes the fluctuations in the dark sector has an intrinsic length scale or at least a finite range of scales over which sizeable fluctuations get produced. We assume here that there is only one characteristic scale k_*

that due to causality has to lie within the horizon when the fluctuations get produced, $a_* H_* < k_*$. Generalisation of our results is however straight forward as long as one may consider the different length scales independently. Since there is only one characteristic scale, the fluctuations that become separated by distances greater than $1/k_*$ are uncorrelated.

$$\langle \delta_d(\mathbf{x}) \delta_d(\mathbf{y}) \rangle \approx 0; \quad |\mathbf{x} - \mathbf{y}| > 1/k_*. \quad (\text{VIII.22})$$

Distributions where there is no correlation past a certain scale are commonly referred to as “white”. For concreteness we will use

$$\langle \delta_d(\mathbf{x}) \delta_d(\mathbf{y}) \rangle = A_{\delta_d} \exp\left(-\frac{|\mathbf{x} - \mathbf{y}|^2 k_*^2}{2}\right); \quad \mathcal{P}_{\delta_d}(k) = A_{\delta_d} \sqrt{\frac{2}{\pi}} \frac{k^3}{k_*^3} \exp\left(-\frac{k^2}{2k_*^2}\right), \quad (\text{VIII.23})$$

where A_{δ_d} parameterises the size of the fluctuations. The common feature of white distributions in three dimensions is that their power spectrum falls off as k^3 in the infrared, while the UV behavior depends on the exact shape. Had we chosen a distribution with compact support in position space, the power spectrum would fall off as a power-law in the UV instead of exponentially. The power spectrum gives the value of the unequal time correlation spectrum when one chooses both times to be the same $\mathcal{P}_{\delta_d}(k, \tau) = \mathcal{P}_{\delta_d}(k, \tau, \tau)$ and therefore gives the amplitude of the fluctuations at a given time. Since, the power spectrum falls for $k > k_*$ and the gravitational interaction for modes deeper inside the horizon is weaker, we can already anticipate that the acoustic energy becomes dominated for modes with $k \lesssim k_*$. For this reason, we only consider these modes in the following i.e. we only deal with length scales that are large enough such that there are no correlations past them.

VIII.3.2 Time Evolution

For this discussion we will make the Ansatz that the energy fluctuations and the shear of the dark sector can be described as a stationary statistical process past τ_* . This means that the unequal time correlation spectra can be factorized into a time autocorrelation function and a power spectrum. The power spectrum becomes constant past τ_* and the autocorrelation function \mathcal{A} only depends on the difference in time

$$\mathcal{P}(k, \tau, \tau') = \mathcal{P}(k) \mathcal{A}(k, \tau - \tau') \theta(\tau - \tau_*) \theta(\tau' - \tau_*). \quad (\text{VIII.24})$$

Let us start by considering a dark sector with relativistic dynamics. In this case, one naively expects that the only relevant time scales are $1/k_*$ and $1/k$. There is an important distinction to be emphasised between the energy fluctuations and the shear: Energy is a conserved quantity. A change of δ_k corresponds to a displacement of energy over a distance of $\approx 1/k$. This is why the only time scale for the energy fluctuations to change is given by $\approx c_d/k$, where $c_d \leq 1$ is the typical velocity of energy transport in the dark sector.

Since the energy fluctuations have this universal behavior, we are going to limit the discussion in the following to them and drop the shear σ_d from the source S . In general we expect the shear to be of the same size as the density fluctuations δ_d and this approximation therefore introduces an $\mathcal{O}(1)$ uncertainty.

Below we calculate the acoustic energy for two examples. In the first the energy fluctuations exhibit a stochastic behavior and the auto-correlation therefore decays as $\mathcal{A}_{\delta_d}(k, \Delta\tau) \rightarrow 0$, $|\Delta\tau| \rightarrow \infty$. For the other, we take a periodic, deterministic behavior as one expects if the dark sector comprises a fluid with waves itself.

Stochastic Source: Free Scalar Field

For a relativistic scalar field with Gaussian fluctuations, the auto-correlation function of the energy fluctuations for $k \ll k_*$ is given by

$$\mathcal{A}_{\delta_\phi}(k, \Delta\tau) = \text{sinc}(k\tau), \quad (\text{VIII.25})$$

as we show explicitly in Appendix C. Since the auto-correlation decays much faster than a Hubble time if $k \gg a_* H_*$ we approximate $\epsilon_{ac}^{\text{lim}}$ as

$$\epsilon_{ac}^{\text{lim}}(k) = \Omega_{d,*}^2 \mathcal{P}_{\delta_d}(k) \frac{6}{k^2} \int_{\tau_*}^{\infty} d\tau' a^4(\tau') H^4(\tau') \int_{-\infty}^{\infty} d\tau'' \cos\left(\frac{k\tau''}{\sqrt{3}}\right) \text{sinc}(k\tau) \quad (\text{VIII.26})$$

$$= \Omega_{d,*}^2 \mathcal{P}_{\delta_d}(k) 2\pi \left(\frac{a_* H_*}{k}\right)^3, \quad (\text{VIII.27})$$

where we used $a = \tau H_* a_*^2$ during radiation domination to solve the first integral. This estimate holds only for modes that are inside the horizon at a_* . The numerical results we present below suggest that for super horizon modes the efficiency of inducing acoustic waves is directly proportional to the amplitude $\mathcal{P}_{\delta_d}(k)$. This justifies using

$$\epsilon_{ac}^{\text{lim}}(k) \approx \Omega_{d,*}^2 \mathcal{P}_{\delta_d}(k) \frac{\pi}{2\pi + (k/a_* H_*)^2} \frac{1}{1 + k/(2a_* H_*)}, \quad (\text{VIII.28})$$

to estimate the acoustic energy also for superhorizon modes with $\mathcal{O}(1)$ accuracy.

Deterministic Source: Fluid

If the dark sector is comprised of a fluid itself with speed of sound c_d the auto-correlation is

$$\mathcal{A}_{\delta_\phi}(k, \Delta\tau) = \cos(c_d k \Delta\tau). \quad (\text{VIII.29})$$

In this case there is no sensible approximation that allows one to factorize the double integral in Eq. (VIII.20). Therefore we directly use the results from solving the full equations of motion numerically, including backreaction from photons and neutrinos, to discuss the behaviour. To do so we model the fluctuations in the dark sector as 0 up to τ_* and as $\delta_d = \sin(c_d k(\tau - \tau_*))$ afterwards. This corresponds to $\mathcal{P}_{\delta_d}(k) = \langle \sin^2 \rangle = 1/2$. In Fig. VIII.3 we show the results for $\epsilon_{ac}^{\text{lim}}$ normalized by $\Omega_{d,*}^2 \mathcal{P}_{\delta_d}$ for various dark speeds of sound. As one can see the efficiency of inducing acoustic waves takes on a constant $\mathcal{O}(1)$ value in all cases for modes outside the horizon at a_* . For modes inside the horizon the efficiency falls off as $(a_* H_*/k)^2$ and as $(a_* H_*/k)^4$ once the potential offset in frequency between the driving force $c_d k$ and $k/\sqrt{3}$ of the driven oscillator δ_γ becomes relevant $(\sqrt{3} - c_d)k/(a_* H_*) \gtrsim 1$. We therefore suggest using

$$\epsilon_{ac}^{\text{lim}}(k) \approx \Omega_{d,*}^2 \mathcal{P}_{\delta_d}(k) \frac{\pi}{2\pi + (k/a_* H_*)^2} \frac{1}{1 + (1/3 - c_d^2)(k/a_* H_*)^2}, \quad (\text{VIII.30})$$

which matches the numerical result up to a factor of $\lesssim 2$ for the cases shown in Fig. VIII.3. One can interpret the results Eq. (VIII.28) and Eq. (VIII.30) as follows: Naively one expects a suppression by $(a_* H_*/k)^4$ for modes inside the horizon $k > a_* H_*$ that stems from the potentials decaying as $\Phi, \Psi \propto (a_* H_*/k)^2$. The strength of the potentials is however approximately constant and keeps driving the acoustic oscillation in the baryon-photon fluid for the whole Hubble time after a_* corresponding to many oscillations $N_{\text{osc}} \propto k/a_* H_* \gg 1$ of the mode. The energy of a harmonic oscillator driven by a stochastic source or in resonance grows as $\propto N_{\text{osc}}$ or $\propto N_{\text{osc}}^2$ which leads to a milder suppression by $(a_* H_*/k)^3$ and $(a_* H_*/k)^2$ respectively.

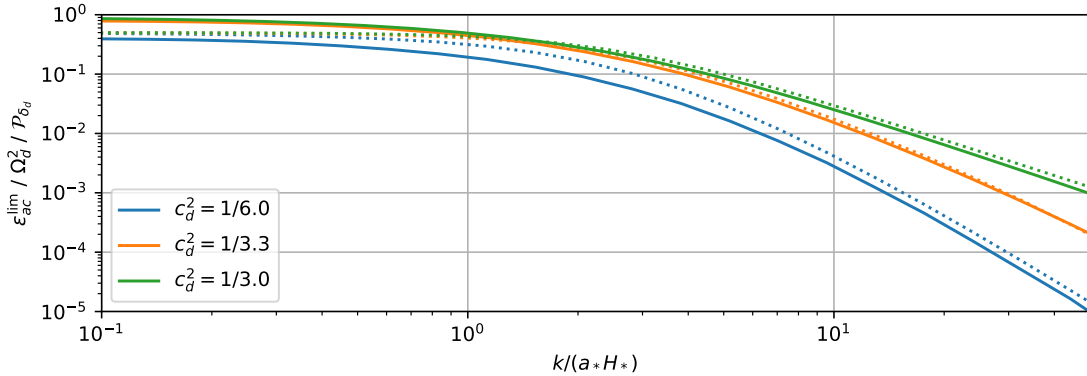


Figure VIII.3: Suppression of the induced acoustic energy for modes that are inside the horizon $k \gtrsim a_*H_*$ when the fluctuations develop at a_* . The fluctuations here are taken to evolve deterministically as $\propto \sin(c_d k(\tau - \tau_*))$ past a_* . The straight lines show the result from a numerical simulation including the contributions of the neutrinos and baryon-photon fluid to the gravitational potentials, while the dotted lines show the estimate $Eq.$ (VIII.30). For $k \gg a_*H_*$ the suppression falls as $\propto (a_*H_*/k)^2$ in the resonant case $c_d = c_\gamma = 1/\sqrt{3}$ (green) and as $\propto (a_*H_*/k)^4$ in the off-resonant cases, once the discrepancy in frequency becomes relevant.

VIII.4 Detailed analysis of a simple model: $\lambda\phi^4$ -Theory

To confirm the validity of our analytic estimates, we now consider a toy model for which a full numerical treatment is feasible. We have chosen a model consisting of two real scalar fields ϕ, ψ with the potential

$$V(\phi, \psi) = \frac{1}{4}\lambda\phi^4 + \frac{1}{2}g^2\phi^2\psi^2. \quad (\text{VIII.31})$$

This model has been studied in great detail in the context of preheating e.g. [49, 230–234]. We consider $\langle\phi\rangle = \phi_i \ll m_{\text{Pl}}$ and $\langle\psi\rangle = \langle\dot{\phi}\rangle = \langle\dot{\psi}\rangle = 0$ as the initial conditions. In this case, the energy density of the fields is always subdominant $\Omega_d \ll 0$ in contrast to the preheating scenario where the field ϕ with $\phi_i > m_{\text{Pl}}$ initially drives inflation.

In addition to deriving all the parameters needed to estimate the acoustic energy analytically as described above, we solve the dynamics of the model from first principles using a lattice simulation, which allows us to extract $\delta_d(k, \tau)$ and $\sigma_d(k, \tau)$. Using these we solve for $\delta_\gamma(k, \tau)$ and arrive at the acoustic energy. We recommend the reader only interested in the application of the estimate to skip forward to the next section.

We follow [49, 234] in our analysis and define the angular frequency $\omega_* = \sqrt{\lambda}\phi_i$ giving the typical curvature of the potential as well as the resonance parameter $q = g^2/\lambda$. For simplicity, we fix the latter at $q = 1$ in this work. Furthermore, we assume that both ϕ and ψ possess Gaussian fluctuations originating from inflation that are frozen before a mode enters the horizon

$$\mathcal{P}_{\phi, \psi} = \left(\frac{H_I}{2\pi}\right)^2; \quad \mathcal{P}_{\dot{\phi}, \dot{\psi}} \approx 0, \quad (\text{VIII.32})$$

where $H_I \gg \omega_*$ denotes the Hubble parameter during inflation. We assume that after inflation the universe reheats and undergoes the same evolution as in the standard Λ CDM case, with our dark sector acting as a purely gravitationally coupled spectator. At the times relevant for spectral distortions the universe is still radiation dominated.

VIII.4.1 Analytic Estimate

The field ϕ starts to oscillate once the Hubble rate drops to $H_{\text{osc}} = \omega_*$. The energy in the field ϕ is initially $\omega_*^2 \phi_i^2/4$ and dominates the dark sector such that one can estimate $\Omega_{d,\text{osc}} \propto (\phi_i/m_{\text{Pl}})^2$. Past a_{osc} the dark sector behaves like radiation such that $\Omega_d \approx \text{const}$. To go beyond an order of magnitude estimate, one has to solve the equation of motion for the homogeneous component of ϕ and finds

$$\Omega_{d,\text{osc}} \simeq 0.2 \left(\frac{\phi_i}{m_{\text{Pl}}} \right)^2. \quad (\text{VIII.33})$$

The oscillations of ϕ lead to a time-dependent effective mass of the field ψ , which causes its fluctuations to grow exponentially. This instability is very similar to the one discussed in Chapter III. As shown in e.g. [230] the equation of motion for the Fourier modes of the field ψ can be recast into the *Lamé* equation. From the corresponding instability chart, one can read off that the modes with $k \lesssim \omega_* a_{\text{osc}}$ experience exponential growth. The mode growing the fastest is $k_* \approx \omega_* a_{\text{osc}}/\sqrt{2}$ with its energy density growing as $\propto \exp(0.3 \omega_* a_{\text{osc}} \tau)$. The energy in the fluctuations is initially $\approx \omega_*^2 H_I^2/(2\pi)^2$ while the energy in the homogeneous ϕ field is $\approx \omega_*^2 \phi_i^2/4$. Due to the exponential growth this difference is overcome around

$$a_* \approx a_{\text{osc}} \frac{2}{0.3} \log \left(\frac{\pi \phi_i}{H_I} \right). \quad (\text{VIII.34})$$

At this point, the energy in the fluctuations starts to dominate, causing the energy density to become fully inhomogeneous in line with the definition of a_* in the previous chapters. This allows us to calculate $a_* H_* = a_{\text{osc}} \omega_* \cdot a_{\text{osc}}/a_*$. For the simulations presented in the following we fixed $H_I/\phi_i = 10^{-4}$, which gives $a_* \approx 70 a_{\text{osc}}$ and $a_* H_* \approx a_{\text{osc}} \omega_*/70$.

Once the fluctuations dominate, the energy gets split between the two fields and their respective kinetic and gradient contributions. If the system virializes quickly, the energy will be distributed evenly between the four, and there will be no correlations between them. If each separate contribution has $\mathcal{O}(1)$ fluctuations we find $\langle \delta_d^2 \rangle = A_{\delta_d} = 1/4$. We now have all necessary ingredients to estimate $\mathcal{P}_{\delta_d}(k)$ using Eq. (VIII.23).

As a final step, we need to make an assumption about the temporal behavior of $\delta_d(k, \tau)$. Similar to the case of the free scalar field, the energy fluctuations are due to the random interference of the field modes. If anything, one expects the potentially turbulent interaction of the field modes at a_* to lead to a faster decrease in the autocorrelation function. We, therefore, use Eq. (VIII.28) with the parameters derived above to analytically estimate the induced acoustic energy.

VIII.4.2 Numerical Treatment

Application of the Lattice Method

Using CosmoLattice [235, 236] we solve the full equations of motion of the interacting ϕ and ψ -field on a discretized space-time using a second-order velocity Verlet algorithm (equivalent to using a leapfrog algorithm). The evolution of the background metric is set to behave like a radiation dominated universe, independently of the dark sector. We simulate a box with $N = 1024$ sites along each spatial direction with a comoving length of $L = 2\pi a_{\text{osc}}/(0.015 \omega_*)$ and periodic boundary conditions. The fields in this box are evolved by time steps of $d\tau = 0.05 a_{\text{osc}}/\omega_*$. While this choice compromises between covering the dynamics close to the horizon at a_* and resolving the UV dynamics, once the system becomes fully non-perturbative, we ran simulations with higher spatial resolution

and smaller time steps to ensure that none of our results are affected by the poor UV resolution of the run presented here.

We start the simulation at $a_i = a_{\text{osc}}/10$ and use the initial conditions given above. We cut the inflationary spectrum for $k > 1.3 a_{\text{osc}}\omega_*$ to cover the full instability band in ψ , while at the same time only including modes with $k \ll aH|_{a=a_i} = 10 a_{\text{osc}}\omega_*$ such that $\mathcal{P}_{\dot{\phi},\dot{\psi}} \approx 0$ holds. After fixing $q = 1$ and $H_I/\phi_i = 10^{-4}$, the only remaining free parameters are ϕ_i and λ , or equivalently ϕ_i and ω_* . The dependence on these two is however fully covered by the scaling relations discussed above, with ϕ_i controlling Ω_d and ω_* the typical momentum scale k_* . We keep these relations explicit when showing our results below.

We modified `CosmoLattice` to calculate and save $\delta_d(k, \tau)$ and $\tilde{\sigma}_d(k, \tau)$ in time-intervals of $\Delta\tau = 0.5 a_{\text{osc}}/\omega_*$, where we defined

$$\tilde{\sigma}_d(k, \tau) = (1 + w)\sigma_d(k, \tau). \quad (\text{VIII.35})$$

This is more convenient for numerics, since it does not require knowledge of \bar{p}_d . The details of how we calculated these quantities can be found in Appendix B. To get power spectra from these quantities, we group them in radial bins of width $k_{IR} = 0.015 \omega_*$ and average over them. To keep the computational cost and required storage down, we limit us however to 70 bins that are spaced out linearly at low k and logarithmically at high k and only use up to 1000 modes per bin³. By interpolating between the saved values of $\delta_d(k, \tau)$ and $\tilde{\sigma}_d(k, \tau)$ as well as $\Omega_d(\tau)$ one can solve for the perturbations in the visible sector for each single mode like we describe below. With this approach one doesn't have to make any assumptions about the time evolution like we did in Section VIII.3.2. To obtain the induced acoustic energy $\epsilon_{ac}^{\text{lim}}$ or μ -distortion we then take the power spectra of $\mathcal{P}_{\delta_\gamma}(k, \tau)$ and $\mathcal{P}_{v_\gamma}(k, \tau)$ by averaging over the modes in one bin again and use Eqs. (VIII.11) and (VIII.13).

Acoustic Waves from Gravitational Coupling

To find the μ -distortion and/or acoustic energy $\epsilon_{ac}^{\text{lim}}$ we solve the Eqs. [VIII.3-VIII.6] numerically, supplemented with the free streaming neutrinos. To describe the neutrinos we have to go past the first three moments of the phase-space distribution δ, v and σ . We adopt the conventions used in [238] and write density fluctuations as deviations in temperature $\Theta(\mathbf{x}, \hat{\mathbf{p}}, \tau) = \frac{\delta T}{T}(\mathbf{x}, \hat{\mathbf{p}}, \tau)$. After Fourier transforming $\mathbf{x} \rightarrow \mathbf{k}$ the momenta of the distribution are defined as

$$\theta_l = i^l \int_{-1}^1 \frac{d\eta}{2} P_l(\eta) \theta(\eta), \quad (\text{VIII.36})$$

where P_l is the l th Legendre polynomial and $\eta = \hat{\mathbf{k}} \cdot \hat{\mathbf{p}}$. The first three moments can be related via $\delta = 4\theta_0$, $v = 3\theta_1$ and $\theta_2 = 2\sigma$ to the definitions used in the main text. For free streaming neutrinos the dynamics of $\Theta_n(\mathbf{x}, \hat{\mathbf{p}}, \tau)$ are described by the Boltzmann equation without a scattering term, which in the expansion introduced above becomes [227, 238]

$$\dot{\theta}_{n,0} + k\theta_{n,1} = -\dot{\phi} \quad (\text{VIII.37})$$

$$\dot{\theta}_{n,1} - k \left(\frac{1}{3}\theta_{n,0} - \frac{2}{3}\theta_{n,2} \right) = \frac{k}{3}\psi \quad (\text{VIII.38})$$

³Our method is equivalent to the type II, version 1 powerspectrum from the `CosmoLattice` technical note [237], except for limiting the number of modes per bin. `CosmoLattice` includes modes up to $\sqrt{3}/2 Nk_{IR}$, while we limited ourselves to $1/2 Nk_{IR}$, which explains why the spectra calculated by `CosmoLattice` directly extend to slightly higher momenta than the once calculated by our methods in Fig. VIII.5.

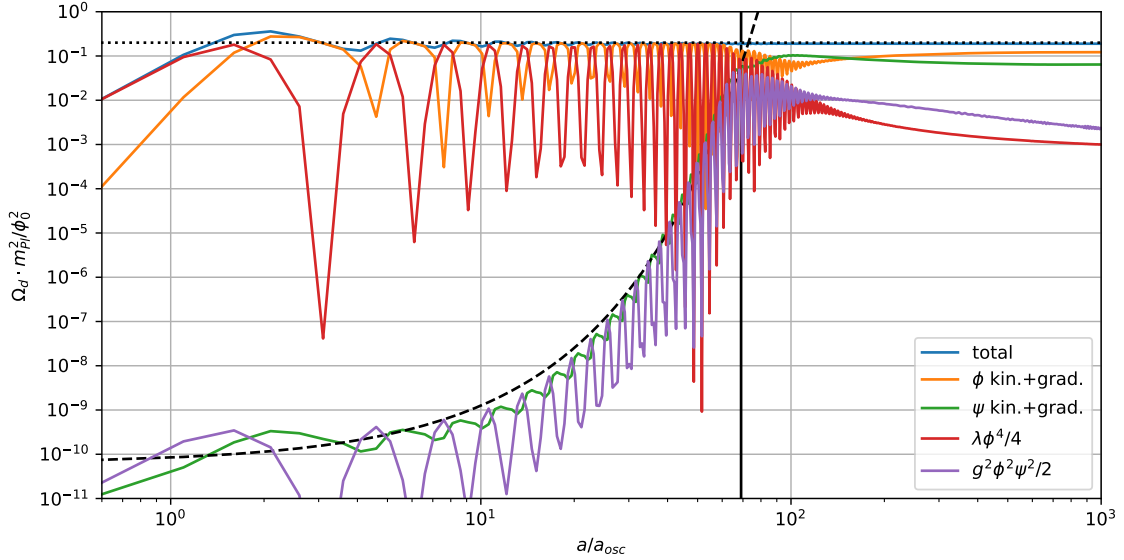


Figure VIII.4: Evolution of energy components in the dark sector. Around a_{osc} the ϕ -field starts oscillating and the energy initially stored in the quartic potential (red) starts going back and forth between the potential and kinetic energy (orange). The dark sector transitions from vacuum to radiation like scaling and its total energy (blue) asymptotes to the value given in Eq. (VIII.33) (dotted, black). The instabilities induced by the coupling (purple) in ψ lead to its energy (green) growing exponentially past a_{osc} . The mode functions of ψ can be approximated by solutions to the *Lamé* equation, leading to the estimate given by the dashed black line. The horizontal black line marks a_* , the time when the energy in the homogeneous ϕ field equals the energy in inhomogeneities of ψ as estimated in Eq. (VIII.34). At this point the perturbative treatment breaks down, making the lattice analysis necessary. Past this point the majority of energy is stored in fluctuations of ϕ and ψ .

$$\dot{\theta}_{n,l} - k \left(\frac{l}{2l+1} \theta_{n,l-1} - \frac{l+1}{2l+1} \theta_{n,l+1} \right) = 0; \quad l \geq 2. \quad (\text{VIII.39})$$

We truncate this hierarchy by neglecting moments $l > l_{\text{max}} = 4$ and follow [227] to close the system of equations using

$$\theta_{n,l_{\text{max}}+1} = \frac{2l_{\text{max}} + 1}{k\tau} \theta_{n,l_{\text{max}}} - \theta_{n,l_{\text{max}}-1}. \quad (\text{VIII.40})$$

As initial conditions we consider the gravitational potentials as well as all the fluctuations in the visible sector to be zero and supply the fluctuations of the dark sector either as an analytic Ansatz or as an interpolation of the values we get from the lattice simulation. To calculate $\epsilon_{\text{ac}}^{\text{lim}}$ we set $\dot{\tau}_C^{-1} = 0$ to decouple the generation of the acoustic energy completely from the damping. When calculating the μ -distortion directly without the approximation derived in Section VIII.2, one needs to include $\dot{\tau}_C$ when solving the differential equations and calculate the time integral in Eq. (VIII.12) numerically using the solutions.

VIII.4.3 Numerical Results

In Fig. VIII.4 we show the evolution of various energy components in the dark sector. Up to a_{osc} the energy is almost exclusively stored in the quartic potential while the dynamics

of ϕ remains overdamped by Hubble friction. Around a_{osc} , ϕ starts to oscillate and the energy in the dark sector red-shifts like radiation, resulting in Ω_d taking on the value given in Eq. (VIII.33). The fluctuations stored in ψ are subdominant around a_{osc} but start growing exponentially due to the instability caused by the coupling to the oscillating ϕ -field. The black, dashed line shows the analytic estimate obtained by looking up the growth coefficient in the instability chart of the *Lamé* equation

$$\Omega_\psi(\tau) \approx \frac{1}{3} \left(\frac{H_I}{2\pi m_{\text{Pl}}} \right)^2 \exp(0.3\omega_* a_{\text{osc}}(\tau - \tau_{\text{osc}})). \quad (\text{VIII.41})$$

Once the energy in fluctuations of ψ catches up to the energy in the ϕ -field, there is a back-reaction that decreases the amplitude of oscillations of the homogeneous part of ϕ while at the same time introducing sizeable inhomogeneities in ϕ . Shortly after a_* the energy becomes dominated by fluctuations of ϕ and ψ .

The evolution of the fluctuations in the fields can be seen directly from the top row of Fig. VIII.5. While the fluctuations in the ϕ field only oscillate as they enter the horizon, leading to the fringe pattern, the fluctuations in the ψ field grow exponentially in the instability band $k \lesssim a_{\text{osc}}\omega_*$ with the modes around k_* , marked by the vertical dashed line, growing the fastest. At $a/a_{\text{osc}} = 60$, as the system approaches a_* , we can see first signs of a back-reaction in the form of additional induced fluctuations in ϕ . Past $a_*/a_{\text{osc}} = 70$ both spectra feature a primary peak that keeps moving to higher k as time progresses. This can be understood as the onset of thermalization as ϕ and ψ particles/waves scatter of one another [75–77]. Somewhat surprisingly there forms a secondary peak in the spectrum of ψ around $k \approx 0.1 a_{\text{osc}}\omega_*$. We can only speculate that this might be the result of the homogeneous part of ϕ being damped and the instability band therefore moving to lower k .

In the second row of Fig. VIII.5 we show the evolution of power spectra of the density fluctuations in the dark sector as well as the shear. Initially the spectrum of density fluctuations is due to the interference of fluctuations of ϕ with its homogeneous part, dominating the energy. The spectrum is therefore also initially flat, as expected, and shows a similar oscillatory pattern as the modes enter the horizon. As fluctuations of ψ and ϕ come to dominate the energy around a_* , the fluctuations in the energy density are well described by the analytic estimate Eq. (VIII.23) with the parameters derived in Section VIII.4.1 (straight, black line). Our estimate describes the energy fluctuations well for the Hubble time following a_* , which is when we expect most of the acoustic energy in the baryon-photon fluid to be sourced. At later times the peak moves to higher k as a result of the scattering processes discussed above. The evolution of the shear is similar although it develops a much more pronounced secondary peak than the energy fluctuations at late times.

In Fig. VIII.6 we show the evolution of the energy fluctuation $\delta_d(k, \tau)$ and the shear $\tilde{\sigma}_d(k, \tau)$ for two modes in the infrared tail of the spectrum. We furthermore show the average amplitude of modes in the respective bin. As there is no clear pattern visible between the two different realisations for the same k , a stochastic description seems to be in place. We want to furthermore stress the difference in the evolution of $\delta_d(k, \tau)$ and $\tilde{\sigma}_d(k, \tau)$ around a_* . The shear shows $\mathcal{O}(1)$ variations on time scales $\Delta a/a_{\text{osc}} \approx 1 \approx k_* \Delta\tau$ that can be related to the characteristic scale $\Delta\tau \approx k_*$. The energy fluctuations on the otherhand only grow as $\propto [k(\tau - \tau_*)]^2$ and take on their late time amplitude after $\Delta\tau \approx 1/k$. This can also be seen from Fig. VIII.5 where the infrared tail of the power spectrum of the energy fluctuations is given as $\propto k^3 \cdot [k(\tau - \tau_*)]^4 \propto k^7$ at the times $a/a_{\text{osc}} = 80 - 100$ shortly after a_* before asymptoting to the final $\propto k^3$. This behavior can be understood as the

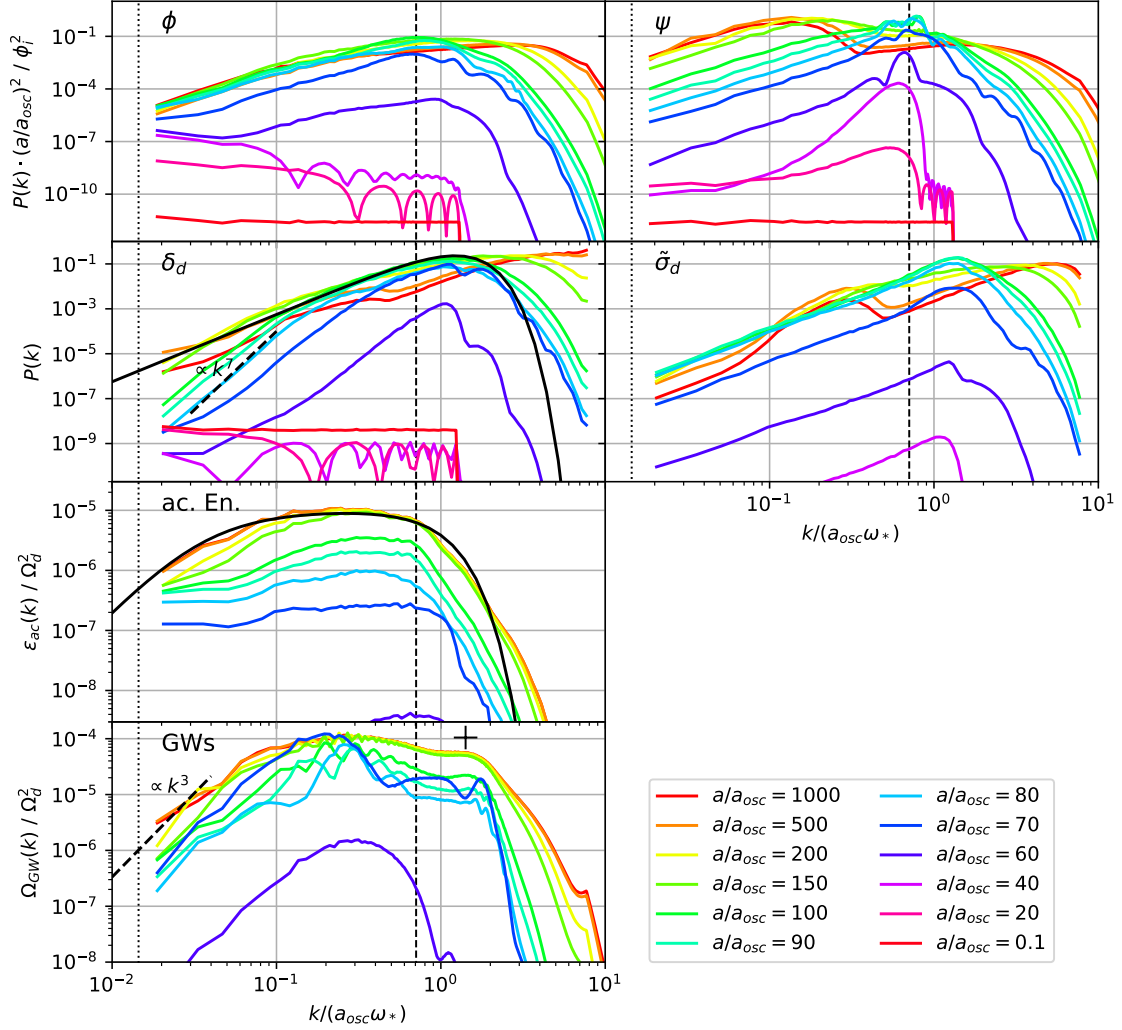


Figure VIII.5: Evolution of power spectra of the ϕ and ψ -field (top row) as well as energy fluctuations δ_d and shear $\tilde{\sigma}_d$ in the dark sector (second row). In the third row we show the induced acoustic energy in the baryon-photon fluid through gravitational coupling. See Section VIII.4.3 for discussion. In the bottom row we furthermore show the resulting spectrum of gravitational waves as discussed in Section VIII.5.1. The vertical, black, dotted line marks the horizon scale at a_* , $k \approx a_{\text{osc}}\omega_*/70$, and the dashed line gives our estimate for the fastest growing mode in ψ , $k_* \approx a_{\text{osc}}\omega_*/\sqrt{2}$. The thick, black, straight and dashed lines give analytic estimates discussed in the text.

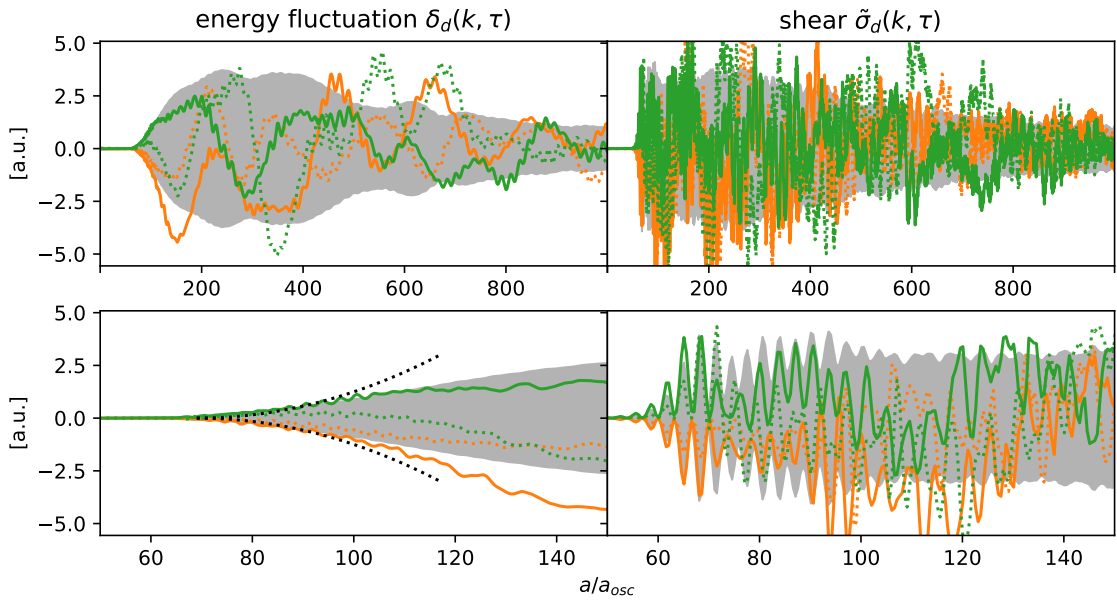


Figure VIII.6: Evolution of the energy fluctuation $\delta_d(k, \tau)$ and the shear $\tilde{\sigma}_d(k, \tau)$ for two modes (orange and green) in the infrared tail of the spectrum ($k = 0.05 a_{\text{osc}}\omega_*$). The straight and dotted line give the real and imaginary part respectively. The gray envelope indicates the evolution of the power spectrum $\propto \sqrt{\mathcal{P}(k, \tau)}$ as calculated by averaging the amplitude of all mode-functions in the respective bin. In the close-up on the Hubble time past $a_* \approx 70 a_{\text{osc}}$ in the bottom panel, we have indicated the amplitude of the energy fluctuations growing $\propto [k(\tau - \tau_*)]^2$ by the black dotted lines.

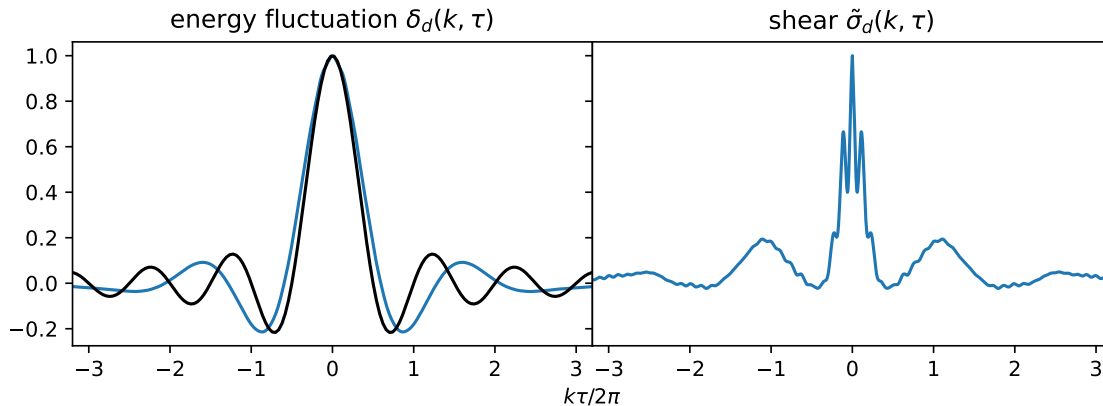


Figure VIII.7: Autocorrelation of the energy fluctuation $\delta_d(k, \tau)$ and the shear $\tilde{\sigma}_d(k, \tau)$ for same momentum as in Fig. VIII.6 ($k = 0.05 a_{\text{osc}}\omega_*$). For the energy fluctuation we show for comparison the sinc that we find analytically in Appendix C for a free scalar field (black).

energy density is conserved on subhorizon scales and we therefore have $\dot{\rho}(k, \tau) = ikj_\rho(k, \tau)$, which leads to $\rho(k, \tau) \propto k(\tau - \tau_*)$ assuming that the corresponding current $j_\rho(k, \tau)$ jumps to its final amplitude around a_* . Since the current $j_\rho(k, \tau)$ is however the momentum density and itself conserved, one finds $\rho(k, \tau) \propto [k(\tau - \tau_*)]^2$.⁴

In Fig. VIII.7 we show the autocorrelation function of $\delta_d(k, \tau)$ and $\tilde{\sigma}_d(k, \tau)$ for the same k calculated by averaging over the modes in the respective bin and times between $a/a_{\text{osc}} = 200 - 1000$. For comparison we also show the sinc we find in the case of a free scalar field (Appendix C) for the energy fluctuations. As one can see there is good qualitative agreement in that they both have a central peak of width $\approx 1/k$. As argued in Section VIII.3.2 this is also expected from energy conservation. Finding these two features makes us confident that our lattice version of the energy density indeed resembles the continuum one⁵. We also find qualitative agreement for the autocorrelation of the shear from the lattice simulation and the free scalar field. Both have features on small time scales related to the peak momentum k_* and on time scales related to k . It should however be mentioned that the autocorrelation function of the shear varies much more when varying the momentum k .

Given the evolution of fluctuations in the dark sector as shown in Fig. VIII.6, we can numerically solve the equations for fluctuations in the baryon-photon fluid on a mode per mode basis. This allows us to calculate the acoustic energy and the result is shown in the third row of Fig. VIII.5. As expected the majority of acoustic energy is induced in the Hubble time after a_* ($a/a_{\text{osc}} \approx 70 - 150$) and the energy becomes constant shortly after. Our analytic estimate in Eq. (VIII.28) with the parameters derived in Section VIII.4.1, shown in black, accurately estimates the main features of this final spectrum: A steep fall of

⁴Note that since the radiation dominated FRW universe possesses no time-like Killing vector field, there is no global energy conservation. On super-horizon scales modifications of energy conservation by pressure fluctuations become relevant as e.g. observed in models of cosmic seeds [239, 240].

⁵We first tried to do this analysis for an axion coupled to a vector, using the same code as for Chapter IV. This model and its lattice implementation is more complicated since it involves vectors. We were not able to construct an energy density on the lattice that showed these characteristics of energy conservation without decreasing the time step of the simulation by a lot, making the simulation unfeasible. We leave a systematic investigation of this issue for future work and recommend checking these features when running similar simulations.

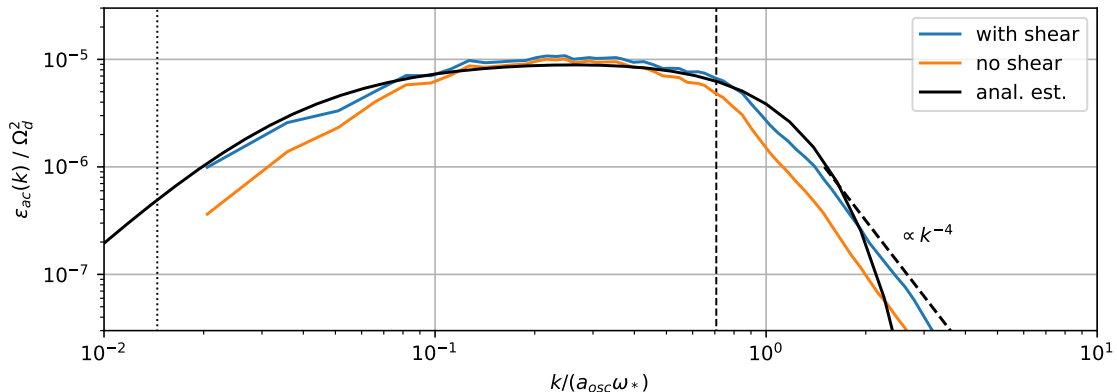


Figure VIII.8: Close-up of the acoustic energy spectrum at the final time of the simulation. The blue line represents the physical result, while the orange line stems from a simulation in which the shear of the dark sector was neglected. The straight black line gives the analytical estimate, with the black dashed line indicating a k^{-4} power law that seems more appropriate to describe the UV tail than the exponential decay of the analytic estimate. The vertical, black dotted and dashed line give the horizon at a_* and the estimate of the fastest growing mode in the ψ -field, k_* .

for modes larger than the peak momentum k_* , a flat plateau for momenta between k_* and the horizon at a_* (vertical, dotted, black line) and a k^3 infrared tail for momenta outside the horizon at a_* . Unfortunately our simulation does not properly cover superhorizon scales, but from what we can see the spectrum becomes steeper at the horizon in good agreement with our estimate.

In Fig. VIII.8 we show a close-up of the acoustic energy spectrum at the final time of the simulation. We furthermore show the result of a calculation in which we neglected the shear of the dark sector, when solving for the perturbations in the baryon-photon fluid. We find that both calculations as well as the analytic estimate agree to within $\approx 20\%$ in the plateau region. Neglecting the shear, however, results in underestimating the acoustic energy by a factor of $\approx 2 - 3$ in the IR and UV tail of the spectrum. Furthermore we find that in the UV the spectrum falls off as k^{-4} rather than the exponential suppression suggested by the analytic estimate.

VIII.5 Application to sources of GWs

Our mechanism of sourcing μ -distortions is only efficient if the dark sector features a sizeable amount of energy $\Omega_d \lesssim 1$ that has $\mathcal{O}(1)$ perturbations on scales close to the horizon. If the dynamics of the dark sector are furthermore relativistic, they efficiently produce gravitational waves as we have already seen throughout this thesis. In the following, we want to compare the reach of searches for GWs and spectral distortions for some of these models.

Before doing so, let us clarify that the opposite statement, all sources of primordial GWs take the aforementioned shape, is not necessarily true. An example would be strings originating from breaking of a local $U(1)$ gauge symmetry. In this case the majority of GWs are produced from the tiniest string loops, only populating a small fraction of the Hubble volume at a given time. In that sense the source is point-like, whereas for the dark sectors we are considering, GWs get sourced over the whole Hubble volume.

For these sectors the resulting GW spectrum is peaked around the characteristic scale k_* . The peak amplitude can be estimated by naive dimensional analysis as we have seen in Section III.7 and throughout Part II. We here consider an extended version of this estimate that also takes the size of the fluctuations into account [155, 156, 241]

$$\Omega_{\text{GW,peak}} \propto \Omega_d^2 \cdot \left(\frac{a_* H_*}{k_*} \right)^\alpha \cdot \mathcal{P}_{\delta_d}^2(k_*). \quad (\text{VIII.42})$$

Just like the induced acoustic energy, the energy in GWs is suppressed by Ω_d^2 . The suppression originating from the characteristic scale being inside the horizon potentially differs though from Equations VIII.28 and VIII.30, with the model dependent power α taking the values 1 and 2. If the new physics comprising the dark sector does not feature spin-2 degrees of freedom, gravitational waves can only get sourced in second-order processes resulting in the suppression by $\mathcal{P}_{\delta_d}^2 \lesssim 1$. Further suppression of the GW signal occurs if the dynamics are non-relativistic, but we are not considering this case below.

Experiments and Cosmological Bounds

At the lowest frequencies and correspondingly largest scales, the amount of GWs becomes limited by the non-detection of B -modes in the CMB polarization by Planck + BICEP2 + Keck [242], and we show the resulting limit in cyan in the following plots. Furthermore, the gravitationally induced scalar fluctuations would alternate the resulting CMB perturbation pattern. In our age of precision cosmology, deriving such bounds is done by refitting the angular perturbations from scratch. However, such an analysis is beyond this work. Instead, we take inspiration from searches of symmetry-breaking relics carried out in e.g [243–245]. They find that the fraction in the angular power spectrum stemming from the new physics is limited to a couple of percent over a wide range of angular scales l . To visualize the remaining uncertainty, we show an aggressive bound, limiting the amount of induced fluctuations to 2% of the inflationary ones up to the CMB pivot scale $\mathcal{P}_{\delta_\gamma} < 0.02 \mathcal{P}_{\delta_\gamma}^{\text{inf}}$ for $k < 0.05 \text{ Mpc}^{-1}$, as well as a more conservative bound corresponding to 10% out to scales of $k < 0.005 \text{ Mpc}^{-1}$. $\mathcal{P}_{\delta_\gamma}^{\text{inf}} \approx \mathcal{P}_\xi \cdot 16 \approx 2 \times 10^{-9} \cdot 16$ is the amount of inflationary fluctuations inferred from the Planck 2018 dataset [46]. We calculate $\mathcal{P}_{\delta_\gamma} \approx 4\epsilon_{ac}$ using the formulas given in Section VIII.3. The resulting bound is shown in red.

At smaller scales, we use the results from Section VIII.2 and Section VIII.3 to calculate the μ -distortions resulting from induced acoustic waves and show the results in green. We furthermore calculate the μ -distortions stemming from the interaction of the GWs emitted by the dark sector with the baryon-photon fluid [25, 246, 247]. We show the resulting bound in pink. The actual observable distortion would perhaps be the sum of these two effects, but we show them separately as to highlight their respective strength. As thresholds for the detection of a μ -distortion we consider the existing bound from COBE/FIRAS $\mu < 9 \times 10^{-5}$ at 95% confidence level [248] as well as the sensitivity of the future missions PIXIE $\mu \lesssim 3 \times 10^{-8}$ [249] and Voyage2050 $\mu \lesssim 1.9 \times 10^{-9}$ [250].

At even tinier scales, we fit the GW spectrum to the to-be-confirmed detection by pulsar timing arrays [61–64] using the first 5 frequency bins from the NANOGrav 12.5yr dataset [61] and the method proposed in Chapter VII. We show the resulting 2σ region of the fit as an orange area. We furthermore show the reach of the planned square kilometer array (SKA) after taking data for 20 years [58, 59, 251] as an orange line.

Since we consider dark sectors with relativistic dynamics, they will inadvertently act as a form of radiation not interacting with the baryon-photon fluid and therefore contribute to

the effective number of neutrinos N_{eff} . At recombination its contribution is given as

$$\Delta N_{\text{eff}} = \frac{8}{7} \left(\frac{11}{4} \right)^{\frac{4}{3}} \frac{\rho_d}{\rho_\gamma} \Big|_{T=T_{\text{rec}}}. \quad (\text{VIII.43})$$

The Planck 2018 dataset constrains $\Delta N_{\text{eff}} < 0.3$ at 95% confidence level [46] and the next generation of ground-based telescopes (CMB Stage-4) is expect to achieve a sensitivity of $\Delta N_{\text{eff}} < 0.03$ [252], which we show as a gray surface and line respectively. The details of how to redshift the abundances and length/frequency scales in order to compare to the sensitivity of the respective experiments can be found in Appendix A.

VIII.5.1 $\lambda\phi^4$ -Theory

Let's start with the model we already considered in great detail in Section VIII.4. In Fig. VIII.5 we show in the bottom row the evolution of the energy density spectrum of gravitational waves. As one can see, similar to the acoustic energy the energy in gravity waves is sourced in the Hubble time following the back-reaction of the ψ -field on ϕ , $a/a_{\text{osc}} \approx 70 - 150$. One might therefore try to estimate the peak amplitude with Eq. (VIII.42) and $\alpha = 2$, which has been observed to give a decent estimate for similar models. Very roughly one can set $\mathcal{P}_{\delta_d}(k_*) \approx 1$. It has also been observed that the peak of the GW spectrum lies typically about a factor 2 higher than the characteristic scale of the source $k_{\text{peak}} \approx 2k_*$ (see e.g. [3]). We show the resulting estimate as a black cross in Fig. VIII.5. Somewhat surprisingly the actual peak of the GW spectrum lies a factor ≈ 4 below the characteristic scale k_* and the estimate only corresponds to a secondary peak at higher k . The peak amplitude is however estimated to within a factor of 2. In Fig. VIII.5 we have further more indicated the k^3 powerlaw that one expects $\Omega_{\text{GW}}(k)$ to asymptote to for scales outside the horizon at a_* from causality [48, 157] (dotted, black line).

To derive the bounds and reach of future experiments we use the spectra found in our lattice simulation and extrapolate them as $\propto k^3$ in the infrared and conservatively as 0 in the UV. The relic abundance, the energy in GWs and wave vectors k are redshifted taking into account the changing number of relativistic degrees of freedom in the SM plasma in order to compare them to the future and present bounds mentioned above. The results are shown in Fig. VIII.9. We find that the at low effective masses $\omega_* \lesssim 10^{-22}$ eV the model is constraint by the non-observation of B-modes in the CMB (cyan). At intermediate values 10^{-23} eV $\lesssim \omega_* \lesssim 10^{-13}$ eV the spectral distortions induced by acoustic waves will be detectable by future missions. We find that for this model as for all other ones that we discuss the contribution from the GWs to the distortion is negligible. At even larger masses the model can be tested by SKA, but in the parameter space still allowed by the N_{eff} constraints the signal is too weak to explain the recent findings of today's PTAs.

The main reason, why all bounds relying on scalar fluctuations are rather weak compared to the following examples, is that the characteristic scale lies deep inside the horizon when the perturbations arise ($k_*/(a_*H_*) = \mathcal{O}(100)$). This factor enters with a power of -3 in the estimate Eq. (VIII.28). In the case of an axion coupled to a dark photon discussed in Part II this ratio is typically of the same order (possibly with the exception of the relaxion case in Chapter VI) and we expect comparable results. The situation is different for the related scenario of axion fragmentation discussed in Part I, where this ratio can be of $\mathcal{O}(1 - 10)$ and we expect that the spectral distortions could be much larger than recently estimated in [71], where only the GWs were considered.

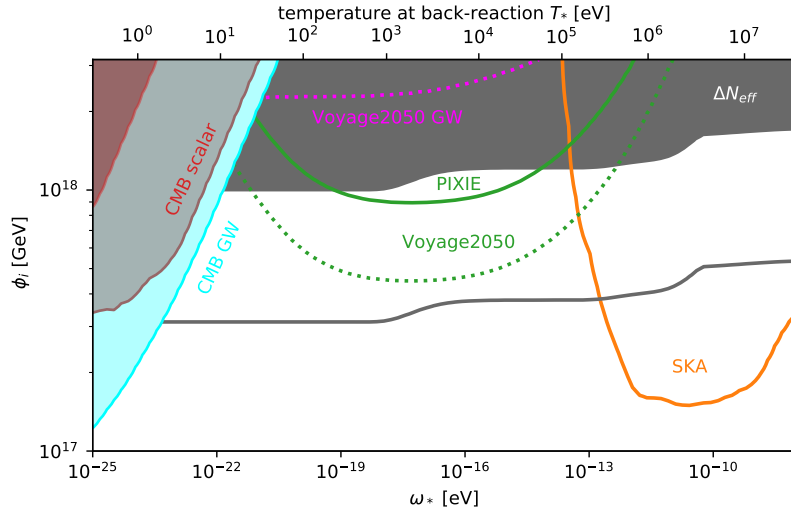


Figure VIII.9: Constraints and future probes of the $\lambda\phi^4$ -model introduced in Section VIII.4. ω_* determines the temperature T_* at which the fluctuations come to dominate the energy in the dark sector and the initial amplitude ϕ_i gives the energy in the dark sector Ω_d scaling the signal strength. The gray area and line give the current and future bound resulting from Ω_d increasing the effective number of neutrinos at recombination. For T_* below $\mathcal{O}(10^2 \text{ eV})$ the scenario is constraint by fits to CMB fluctuations (red) as well as the non-observation of B-polarization modes (cyan). For the wide range of annihilation temperatures of $10^2 - 10^7 \text{ eV}$ spectral distortions are able to probe the scenario with the future missions PIXIE (straight) and Voyage2050 (dotted). We show the bound including only the contribution from scalar acoustic waves in green and the one from only considering GWs in pink. At temperatures above 10^5 eV the model becomes testable by the future pulsar timing array SKA (orange line) and in the range $T_* \approx 10^6 - 10^7 \text{ eV}$ can possibly explain the NANOGrav signal with the 2σ region of the fit given by the orange area. Since this model is particularly efficient at emitting GWs, the corresponding probes dominate in all of the shown parameter space.

VIII.5.2 Remnants of post-inflationary Symmetry Breaking

Symmetry breaking in the early universe is one of the most anticipated predictions for BSM physics, emerging in many extensions of the standard model e.g. [253, 254]. Here we will assume that the symmetry breaking takes place after inflation resulting in a universe filled with topological defects or a network of scaling seeds. We restrict ourselves to the study of domain walls from the breaking of a discrete symmetry as well as cosmic strings resulting from the breaking of a global $U(1)$, like they can be found in axion-like particle (ALP) scenarios with post-inflationary Peccei-Quinn breaking.

VIII.5.2.1 Domain Walls

Domain walls (DWs) [255–257] are topological defects with sheet-like structure that emerge from the breaking of a discrete symmetry. The parameter controlling the DWs dynamics after formation is the surface tension σ . By considering that every Hubble patch with volume $1/H^3$ contains a sheet of DW with area $1/H^2$ one can show that

$$\Omega_{DW} \simeq 0.5 \frac{\sigma}{m_{\text{Pl}}^2 H}, \quad (\text{VIII.44})$$

where the $\mathcal{O}(1)$ prefactor is inferred from simulations during radiation domination [258]. This picture furthermore suggests that the system has $\mathcal{O}(1)$ density fluctuations at the horizon scale. As one can see the relative amount of energy in DWs grows as the universe cools down, leading to strict bounds on σ in order to not over-close the universe. Observability therefore motivates a scenario in which the degeneracy of the vacua related by the symmetry is broken by an additional term in the potential V_{bias} . The introduction of V_{bias} causes the walls to experience volume pressure, that leads to the annihilation of the network once the energy in the volume becomes comparable to the energy in the surface area of the DWs. In a radiation dominated universe the time of DW annihilation corresponds to the following temperature [258]

$$T_{\text{ann}} \approx 10 \text{ MeV} \left(\frac{\sigma}{\text{TeV}^3} \right)^{-\frac{1}{2}} \left(\frac{V_{\text{bias}}}{\text{MeV}^4} \right)^{\frac{1}{2}}. \quad (\text{VIII.45})$$

The GWs from annihilating DWs were first studied analytically [259, 260] and later on quantitatively using lattice simulations [258, 261–264]. On the lattice one finds that the GW spectrum is peaked at $k_{\text{peak}} = 2\pi a_{\text{ann}} H_{\text{ann}}$ and the peak amplitude at emission is given as [261]

$$\Omega_{GW, \text{peak, ann}} \simeq 0.02 \Omega_{DW, \text{ann}}^2. \quad (\text{VIII.46})$$

This is exactly what one expects from Eq. (VIII.42) for a source with dynamics on the horizon scale and $\mathcal{O}(1)$ density fluctuations. The shape of the spectrum is $\propto k^3$ for $k < k_{\text{peak}}$ and $\propto k^{-1}$ for $k > k_{\text{peak}}$.

To estimate the acoustic energy induced by the DWs we use the spectrum given in Eq. (VIII.23) and set the normalisation to $A_{\delta_d} = 1$. Since the spectrum peaks at $\approx 2k_*$ we set $k_* = k_{\text{peak}}/2$. We have no reason to expect that the energy fluctuations $\delta_d(k, \tau)$ show a deterministic behavior and therefore use Eq. (VIII.28). The DWs are expected to source acoustic energy for the whole time that the network exist with the biggest contribution stemming from the time of annihilation when the relative energy in the network is largest. As a conservative estimate we only take this contribution into account and set $a_* H_* = a_{\text{ann}} H_{\text{ann}}$ and $\Omega_{d,*} = \Omega_{DW, \text{ann}}$ in Eq. (VIII.28).

For the relic abundance of the DW network we assume that the oscillations of the system around the true minimum are quickly damped by the emission of dark, massless or light particles that consequently contribute to N_{eff} . We take into account the appropriate redshift to arrive at the results shown in Fig. VIII.10. We again find that the spectral distortions are dominantly produced through the damping of acoustic waves. The amount of acoustic energy and gravity waves is approximately the same $\epsilon_{\text{ac}} \sim \Omega_{\text{GW}} \propto \Omega_d^2$, but only a small fraction of the energy in gravity waves is injected into the photons, while all of the acoustic energy is dumped when the modes cross the diffusion scale.

On the right side of Fig. VIII.10 we sketch the GW spectrum for two benchmark points A and B along side the power law integrated noise of SKA.⁶ Since PTAs are only sensitive to the UV tail of the spectrum, if the annihilation temperature is below $T_{\text{ann}} \lesssim 10^7$ eV, SKA is not able to distinguish between the two benchmarks. On the bottom we show the acoustic energy density spectra in relation to $\mu_{\text{thr,PIXIE}}/\mathcal{W}(k)$, where $\mu_{\text{thr,PIXIE}} = 3 \times 10^{-8}$ is the threshold for detection by PIXIE and $\mathcal{W}(k)$ is the window function given in Eq. (VIII.15). Broadly speaking the overlap of the acoustic spectra with $\mu_{\text{thr,PIXIE}}/\mathcal{W}(k)$ gives how large the signal is compared to the threshold in accordance with Eq. (VIII.14). It becomes clear that the benchmarks, although indistinguishable by the SKA measurement, lead to drastically different μ -distortions. This goes to demonstrate the role spectral distortions might play in the upcoming age of multi-messenger cosmology.

⁶While for our parameter scan we use the exponential suppression in the UV from Eq. (VIII.23), for this sketch we show a power law that we think is more realistic. The majority of the signal is due to the peak such that this introduces only a small uncertainty only.

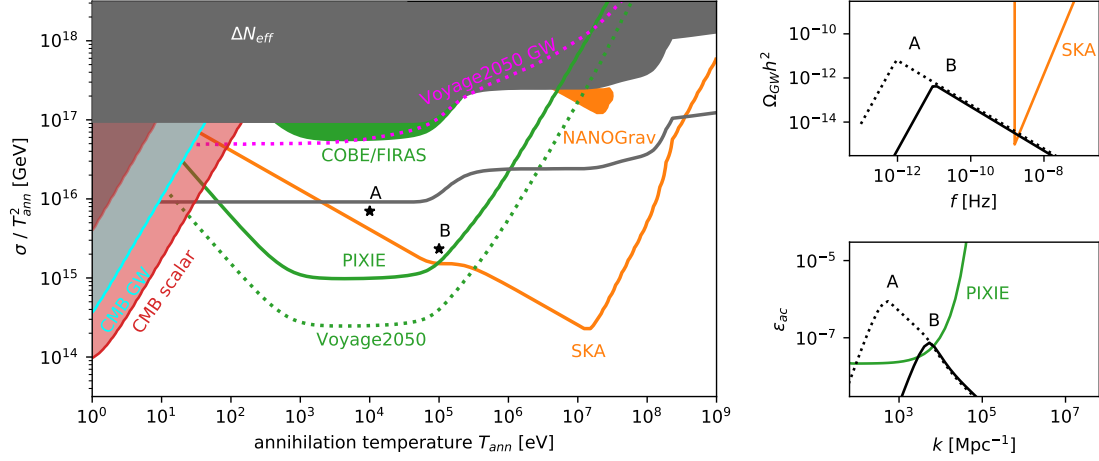


Figure VIII.10: Left: Constraints and future probes of domain walls in terms of the annihilation temperature of the network T_{ann} and the surface tension σ . Assuming that the domain walls relic density behaves as dark radiation after the annihilation leads to a contribution to N_{eff} with the present and future bound shown as the gray area and line respectively. At annihilation temperatures below $\mathcal{O}(10^2 \text{ eV})$ the scenario is constraint by fits to CMB fluctuations (red) as well as the non-observation of B-polarization modes (cyan). For the wide range of annihilation temperatures of $10^2 - 10^7 \text{ eV}$ spectral distortions as a result of the damping of acoustic waves (green) are able to probe the scenario, with current bounds from the COBE/FIRAS mission already in the same realm as the current N_{eff} bound in the range $T_{\text{ann}} = 10^3 - 10^5 \text{ eV}$ and future missions PIXIE and Voyage2050 going far beyond all other probes in this range. We also show the parameter space testable by the Voyage2050 mission taking into account only the contribution to the μ -distortion from gravity waves (pink dotted). This contribution is negligible in the parameter space still allowed by measurements of N_{eff} though. We have picked two benchmarks A and B. Right: On the top we show the GW signal for the benchmarks in relation to the power law integrated noise of SKA. While SKA can not distinguish the two scenarios, the induced spectral distortion is drastically different as can be seen from the bottom panel.

VIII.5.2.2 Global Strings (Axion-Like Particle)

Cosmic Strings (CSs) [256, 257], 1-D topological defects, are remnants of a spontaneous $U(1)$ symmetry breaking. The essential parameter controlling the dynamics of the strings is the symmetry breaking scale f_ϕ that determines the string tension μ . Since we are considering the breaking of a global $U(1)$ symmetry, the string tension and other relevant parameters might get enhanced by a time-dependent logarithmic factor $\log \equiv \log(f_\phi/H) = \mathcal{O}(100)$ in comparison to strings generated from the breaking of a local symmetry. The existence and extent of this logarithmic dependence still remains debated for observables like the emitted GWs [50, 245, 265, 266]. We will base our analysis in the following on the findings of [265] being aware of the uncertainties associated with this choice. [265] finds that the energy density in the string network is given as

$$\Omega_s \simeq 1.0 \cdot \log^2 \left(\frac{f_\phi}{m_{\text{Pl}}} \right)^2, \quad (\text{VIII.47})$$

during radiation domination once the system has entered the scaling regime. The energy of emitted GWs is given as

$$\Omega_{GW}(k) \simeq 0.2 \cdot \Omega_s^2|_{k=aH}. \quad (\text{VIII.48})$$

Similar to the example of domain walls, we will again consider the possibility that an explicit breaking of the $U(1)$ symmetry enforces the annihilation of the network. This breaking is parameterized by the mass m_ϕ of the pseudo Nambu-Goldstone boson. Once Hubble drops to $H_* = m_\phi$, the field settles in its true minimum resulting in the formation of domain walls that collapse the network. [265] finds that the GW spectrum features a peak at $k_{\text{peak}} = 2\pi a_* H_*$ with the amplitude at the peak and higher frequencies given by the formula above and falls off as k^3 for lower frequencies.

To determine the N_{eff} bound we use that the energy in relativistic Nambu-Goldstone bosons at emission is [265]

$$\Omega_\phi \approx 0.3 \cdot \log^3|_{a=a_*} \left(\frac{f_\phi}{m_{\text{Pl}}} \right)^2. \quad (\text{VIII.49})$$

Part of these bosons will become non-relativistic and contribute to the DM density. We refer the reader to [265] for the derivation of the DM abundance as well as other bounds arising from structure formation (see also [267, 268]).

To estimate the acoustic energy induced by strings, we employ largely the same arguments and procedures as shown for the DWs: As a conservative estimate, we limit ourselves to the contribution of the strings leaving aside the bosons. We therefore plug $k_* = k_{\text{peak}}/2$, $A_{\delta_d} = 1$ and Eq. (VIII.47) into Eq. (VIII.28) to get the estimate. To account for the continuous induction of acoustic energy during the scaling regime, we replace the exponential suppression for $k > k_{\text{peak}}$ by only a logarithmic dependence $\propto \log^4(k/k_{\text{peak}})$, in which we assumed that this is only due to the time dependence of Ω_s . The results are shown in Fig. VIII.11. We are additionally showing the reach of the future space-based interferometer LISA adopted from [265]. In the parameter space, in which the pseudo Nambu-Goldstone bosons contribution to DM is not overclosing the universe, SKA and LISA are capable of only probing the UV tail of the GW spectrum, which renders them insensitive to the decay of the network and therefore m_ϕ . Since for $m_\phi \gtrsim 10^{-22}\text{eV}$, the period in which acoustic waves remain sourced is cut short, spectral distortions offer an opportunity to estimate or at least constraint m_ϕ in most of the parameter space with detectable GWs.

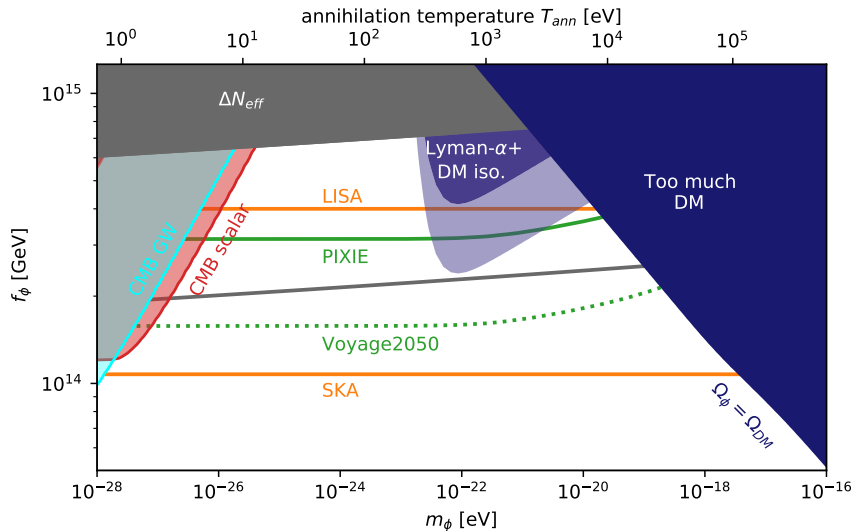


Figure VIII.11: Present and future constraints on string networks resulting from the breaking of a global $U(1)$ at the scale f_ϕ and annihilating at a temperature T_{ann} due to an explicit breaking of the symmetry parameterized by the mass of the resulting pseudo Nambu-Goldstone boson m_ϕ . The grey region and line correspond to the current and future bound of N_{eff} stemming from the emitted, relativistic axions. At a temperature of $T_{ann} = 1 - 10$ eV the scenario is constraint by fits to CMB fluctuations (red) as well as the non-observation of B-polarization modes (cyan). For $f_a \geq 10^{14}$ GeV a strong enough GW signal is emitted to be detectable by SKA, while for $f_a \geq 4 \times 10^{14}$ GeV LISA is also sensitive to the signal. PIXIE and Voyage2050 (green, straight and dotted) allow probing all of the parameter points testable by LISA and the majority accessible via SKA. Again the great complementarity between GWs and spectral distortion experiments shall be emphasized with the later being able to measure/constrain the mass. Further constraints on this parameter region arise due to the emitted axions making up a fraction of DM and featuring large isocurvature perturbations in conflict with Lyman- α observations (purple). For annihilation temperatures $T_{ann} \geq 10^5$ eV the most severe constraint comes from overproducing axion DM.

Before moving on, let us compare our results to the ones obtained in [224, 225] for non-decaying networks of scaling seeds. Both papers consider the spectral distortions due to gravitationally induced acoustic waves in the baryon-photon fluid, just as we do in this paper. [224] concerns the case of cosmic strings and found that only $\mu \approx 10^{-13}$ can be achieved without being in tension with CMB observations, while our analysis suggests that $\mu \approx 10^{-9}$ in the realm of detectability by Voyage2050 is possible. In [225] the breaking of an $\mathcal{O}(N)$ symmetry with $N \geq 4$ was studied that features no topological artefacts but a network of scaling seeds with quasi constant Ω and dynamics of horizon size. They find that present CMB bounds allow for $\mu \approx 10^{-9}$ for non-decaying networks in good agreement with our result.

VIII.5.3 Phase transitions

In theories for BSM physics, the prediction that first-order phase transitions could be present in the post-inflationary universe is very vast (see [152, 269–271]). Nevertheless, first-order phase transitions (FOPT) proceed through bubble nucleation that resolves in bubble collisions at relativistic speeds, [270, 272] therefore, this is a great source of GWs as large anisotropies in the momentum tensor are sourced by the presence of the bubbles. We consider the case in which the FOPT takes place in a purely gravitationally coupled sector as in [59, 211] and only consider the sound wave contribution to the GW spectrum. The parameters describing such a system are the energy density in the dark sector Ω_d that can readily be exchanged for the contribution to N_{eff} using Eq. (VIII.43), the amount of energy freed in the phase transition relative to the one in the dark fluid α_d ⁷, the time of the transition which we will give as the temperature T_* of the SM plasma at the time⁸, as well as the inverse time scale of the transition β . To keep our discussion simple we further set the wall velocity $v_w \simeq 1$ and restrict us to a speed of sound $c_d = 1/\sqrt{3}$ in the dark sector⁹ which allows us to estimate its acoustic energy relative to its total energy as

$$\epsilon_{\text{ac},d} = \frac{\rho_{\text{ac},d}}{\rho_d} = \frac{\kappa(\alpha_d)\alpha_d}{1 + \alpha_d}; \quad \kappa(\alpha_d) = \frac{\alpha_d}{0.73 + 0.083\sqrt{\alpha_d} + \alpha_d}, \quad (\text{VIII.50})$$

where κ gives the efficiency factor of turning the freed energy into sound waves as found in [273].

The energy density of GWs coming from the sound waves which are emitted from a dark sector with nucleated bubbles of sub-horizon size is [241]

$$\Omega_{\text{GW}}(k) \simeq 0.16 \left(\frac{k}{k_{\text{peak}}} \right)^3 \left(\frac{7}{4 + 3(k/k_{\text{peak}})} \right)^{7/2} \cdot \Omega_{d*}^2 \cdot \frac{H_*}{\beta} \cdot \left(\frac{\kappa(\alpha_d)\alpha_d}{1 + \alpha_d} \right)^2. \quad (\text{VIII.51})$$

The first term is again an $\mathcal{O}(1)$ prefactor for $k = k_{\text{peak}} = 2a_*\beta/\sqrt{3}$ and determines the shape of the spectrum, while we can identify the other terms with the factors in the rough estimate of Eq. (VIII.42).

The density fluctuations in the relativistic dark sector, just as in the baryon-photon fluid, are related to the acoustic energy via $A_{\delta_d} = \langle \delta_d^2 \rangle = 4\epsilon_{\text{ac},d}$ in the virial limit. Again we set $k_* = k_{\text{peak}}/2$, but in this case we use Eq. (VIII.30) to determine the gravitationally induced acoustic waves. This is justified, since one expects that δ_d only shows a stochastic behavior for a time $\approx 1/\beta$ while the walls are present and proceeds with the deterministic propagation of sound waves for the remaining Hubble time following the transition $1/H_* \gg 1/\beta$.

β/H_* determines if the PT completes mainly driven by the expansion of a few nucleated bubbles or by the nucleation of new bubbles everywhere in space. Large values of β/H_*

⁷The situation commonly discussed only concerns the case where the universe is filled with one fluid. When dealing with multiple fluids the introduction of α_d and Ω_d is necessary as opposed to only using $\alpha = \Omega_d\alpha_d/(1 + \alpha_d)$. Since the bubble walls only couple to the fluid in the dark sector, the matching conditions are only imposed on the dark sector and as a result the efficiency of generating sound waves depends on α_d as opposed to α [211].

⁸The dark sector, if it is thermal, must not have the same temperature as the SM plasma. If it possesses one relativistic degree of freedom its temperature is necessarily smaller. See [59, 211] for further details.

⁹In figure VIII.3 we show the effect of varying the sound velocity and find that the suppression in the amount of acoustic energy is small as long as the changes don't exceed $\approx k_*/(a_*H_*) \approx \beta/H_*$. It has recently been found though that even small changes can have a significant impact on the efficiency factor κ , entering both the GW and acoustic energy estimate. [273]

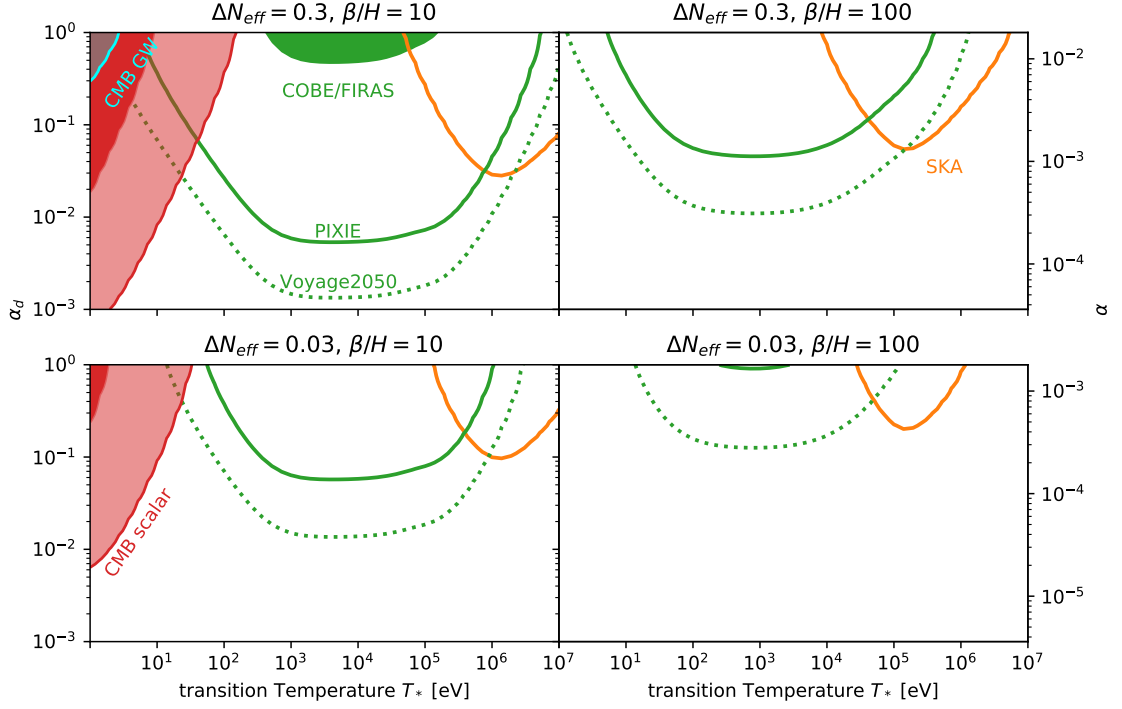


Figure VIII.12: Current and future constraints on a phase transition in a dark sector, in terms of the SM plasma temperature at the time of the transition, released energy relative to the energy in the dark fluid α_d , the ΔN_{eff} caused by the dark sector, and the inverse duration of the phase transition $\frac{\beta}{H}$. We only take into account the effects of the sound waves in the dark fluid caused by the transition. At temperatures $T_* = 1 - 10$ eV the scenario is constrained by CMB fluctuations in (red) and the non-observation of B-mode polarization in the CMB in (cyan). In the temperature range of $T_* = 10 - 10^6$ eV spectral distortions from acoustic waves (green) can probe the scenario. Strong phase transitions in a dark sector saturating the N_{eff} bound can already be constraint by the COBE/FIRAS results ($\alpha_d = \mathcal{O}(1)$, $\Delta N_{eff} = 0.3$, $\frac{\beta}{H} = 10$). At temperatures $T_* = 10^5 - 10^7$ eV the scenario can in the future be detected by SKA, while the present N_{eff} bound (top row) rules out the NANOGrav signal being generated this way. For convenience we have converted α_d to $\alpha = \Omega_d \alpha_d / (1 + \alpha_d)$ on the left y-axis.

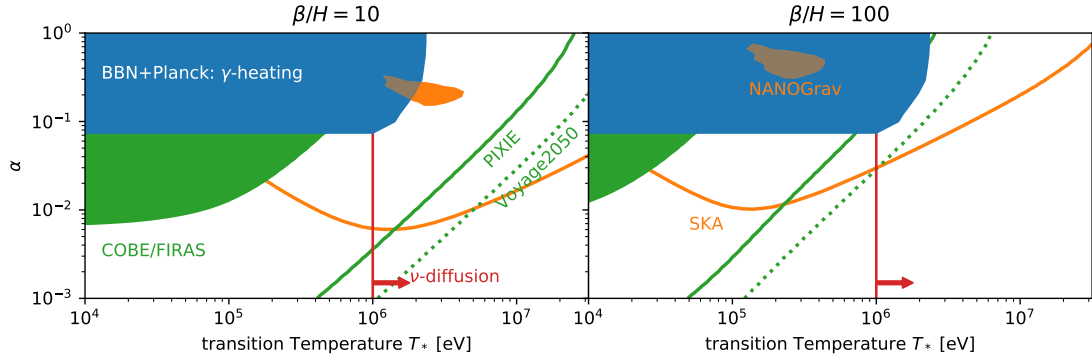


Figure VIII.13: Current and future constraints on a first order phase transition at temperature T_* releasing a relative energy α into the SM-plasma. For temperatures below ≈ 2 MeV the released energy α leads to tensions in BBN and CMB measurements of the baryon to photon ratio (blue). The sound waves caused by the phase transition source GWs that can explain the NANOGrav hint (orange, filled, same as right of Fig. VII.4) and in the future can be detected over a wide range of parameter space (orange line). The green area and lines show the current and future sensitivity to spectral distortions caused by the sound waves. At temperatures above ≈ 1 MeV the sound waves and therefore spectral distortions are expected to be reduced due to damping by neutrino diffusion.

mean faster nucleation rates which means that more bubbles will nucleate inside the Hubble horizon until the PT has completed, and hence their bubble radii get smaller. One expects an inverse relation between β/H_* and the amplitude of the GW spectrum in which β/H_* determines the peak frequency/momenta. For very strong FOPTs one might have to reformulate the definition of β/H_* as it may become inappropriate as was emphasized in [274, 275].

In Fig VIII.12 we show our results. Similar to the previous examples we find that spectral distortions bridge the gap between phase transitions detectable by CMB fluctuations ($T_* = 1 - 10$ eV) and by PTAs such as SKA ($T_* = 10^5 - 10^7$ eV). The probes relying on scalar mediation are however particularly strong for $\alpha_d \ll 1$. In this case the fluctuations in the dark sector are small $\mathcal{P}_{\delta_d} \ll 1$, which impacts the GWs heavier than the sourced acoustic waves, as one can see by comparing Eq. (VIII.42) with Eqs. (VIII.28) and (VIII.30).

VIII.5.4 Comment on Directly Coupled Sectors

Clearly, one can obtain stronger bounds from spectral distortions if there are further interactions between the new physics sector and SM plasma apart from the gravitational one. In this sense, the bounds presented above can be interpreted as lower limits, since gravity is always present as a coupling force. Furthermore, any study going beyond this has to make specific assumptions about the nature of the coupling and can therefore not be carried out in a model-independent way as we did in Section VIII.2 and Section VIII.3. Such studies have been carried out for cosmic strings [276, 277]. In light of the recent findings by PTAs discussed in Chapter VII, we here want to briefly comment on the case in which a phase transition directly causes sound waves in the SM plasma, and subsequently, GWs are emitted. As we already saw in the previous section, the GW signal emitted if the phase transition takes place in a completely decoupled sector can not explain the NANOGrav data without being in tension with the N_{eff} bound. If the signal stems from

sound waves caused by a phase transition, the only option is therefore that these are sound waves in the SM plasma.

To estimate the signal strength, we use the formulas from the previous section, setting $\Omega_d \rightarrow 1$ and replacing $\alpha_d \rightarrow \alpha$ as there is now only one fluid present.¹⁰ Since the walls now directly cause the acoustic energy in the baryon-photon fluid, we no longer rely on the gravitational coupling and therefore simply have

$$\epsilon_{\text{ac}}(k) = \frac{\kappa(\alpha)\alpha}{1+\alpha} \sqrt{\frac{2}{\pi}} \frac{k^3}{k_*^3} \exp\left(-\frac{k^2}{2k_*^2}\right), \quad (\text{VIII.52})$$

with $k_* = a_*\beta/\sqrt{3}$.

The results are shown in Fig. VIII.13. An energy injection around or after BBN at $T \approx 1$ MeV leads to a possible tension between the baryon to photon ratio obtained from BBN and CMB measurements. The resulting current bound on α and its temperature dependence has been investigated in [212], and we show it in blue. As can be seen, this bound already excludes a decent chunk of the 2σ -region to the NANOGrav fit (orange, filled). However we find that the remaining region can be probed by future distortion experiments, given that our estimate above holds. Furthermore we obtain a significant overlap of the parameter space testable by SKA and spectral distortions.

The previously mentioned conclusions come, however, with the following caveat: At the beginning of BBN around $T \approx 1$ MeV, the neutrinos decoupled from the rest of the SM plasma. Similar to the decoupling of photons, one has to expect that all perturbations on subhorizon scales might be significantly damped due to the diffusion of neutrinos. We anticipate that this effect would reduce the reach of distortion searches past temperatures of 1 MeV. The previously mentioned effect covers a significant region of the viable parameter space shown by the red line in Fig. VIII.13. For transition temperatures close to 1 MeV, in that region, it can further lead to a reduction in the GW amplitude as their emission and the damping by ν -diffusion are taking place simultaneously. We leave a detailed study of these effects to future work.

VIII.6 Conclusion

In this chapter we showed that spectral distortions caused by gravitationally induced acoustic waves in the baryon-photon fluid provide a powerful probe of new physics. We derived the already known fact that the damping of the acoustic waves due to diffusion of photons and generation of spectral distortions is independent of their origin. The μ -distortion can therefore be calculated solely from the amplitude or equivalently the energy of the waves (Eq. (VIII.12)).

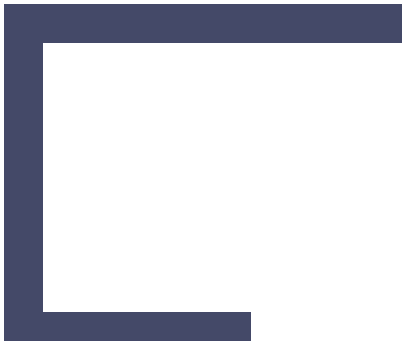
We here for the first time presented an analytic estimate of this acoustic energy caused by a purely gravitationally coupled sector (Eqs. (VIII.28) and (VIII.30)). This estimate only relies on a few parameters describing the dynamics of the dark sector. The most important amongst them are the amount of energy constituted by the dark sector, the amplitude of its energy fluctuations as well as the ratio between the typical length scale of the fluctuations and the horizon when the fluctuations are generated.

We continued by studying a particularly easy model consisting only out of two scalars in great detail. Solving for the dynamics in the dark sector using a lattice method and afterwards solving for the acoustic waves numerically, allowed us to calculate the acoustic

¹⁰For transition temperatures below ≈ 1 MeV the neutrinos are decoupled and there are technically two sectors. Since the energy in the baryon-photon fluid is still $\Omega_\gamma \approx 1$, we make this simplifying assumption.

energy from first principles. We compared the result obtained in this way to our analytic estimate and found agreement to within $\mathcal{O}(1)$ factors, in the peak region even to within 20%.

Finally we compared the reach of present and future spectral distortion experiments to other probes relying only on gravitational coupling for a number of possible dark sectors. For the sectors we considered the spectral distortions sourced by damping of acoustic waves always dominated the contribution from GWs. We were able to demonstrate that dark sectors where the energy fluctuations are present at temperatures between $\approx 10 - 10^6$ eV are either already constrained by the non-observation of spectral distortions or can be probed in the future. A particular interesting opportunity lies in the possible interplay with GW observations by PTAs. Here spectral distortions might be key in lifting observational degeneracies on the parameter space of various models.



Aftermath



Summary and Conclusion

In this thesis we studied models motivated by dissonances in the SM, so called tuning problems. Some of them are further able to provide light scalar and vector DM or generate the observed cosmological baryon asymmetry. Of special interest is the ability of new physics to source a detectable gravitational wave (GW) signal. We further showed that a wide class of GW sources also leads to a detectable μ -distortion of the CMB spectrum.

In the first part of this thesis we studied the process of axion fragmentation. This phenomenon occurs when an axion rolls over many periods of its potential. The effective mass, the curvature of the potential, thus varies, which leads to the exponential amplification of fluctuations in the field. While this process was studied before, we carried out a lattice simulation to investigate the role of non-linearities. We found that those enhance the efficiency of the energy transfer from the homogeneous part to the fluctuations. The effect is however too small to significantly alter the conclusions about the *self-stopping* relaxation.

We further investigated the possibility that the universe finds itself in different minima after the stopping process. Patches of the universe in different minima would lead to the formation of bubbles with walls separating them. We found that the size of the fluctuations caused by the stopping mechanism itself are too small to cause this phenomenon. Inflationary fluctuations are however large enough, if inflation proceeds at high enough energies. In the relaxation case these bubbles are not cosmologically viable and we were therefore able to put a bound on the scale of inflation in this case.

While the energy density of the system is initially homogeneous, it develops large inhomogeneities when fluctuations start to dominate. It is easy to see that this process is associated with energy currents and therefore also anisotropic stress, which itself leads to the emission of GWs. We gave a simple argument based on naive dimensional analysis, why this signal can not be detectable without the axion dark matter overclosing the universe. In part two of the thesis we then continued to study a system of an axion coupled to a dark photon, that features a similar instability. In this case it is the dark photon modes that grow exponentially. This process suppresses the axion DM abundance by itself, since the energy is transferred to the dark photon, which is why it can emit a detectable GW signal without being in tension with cosmological bounds. The dark photon could furthermore constitute vector DM itself. The lattice analysis that we carried out largely confirms the results of our previous linear approach. One of the main differences we found is that the maximal achievable suppression only reduces the axion abundance by two orders of magnitude compared to the regular misalignment mechanism. This limits the GW signal strength in the minimal scenario to only be detectable by future pulsar timing arrays like SKA.

We therefore studied more involved scenarios, namely the kinetically misaligned axion and the post inflationary evolution of the relaxation. In the first scenario the axion has an initial

velocity. The resulting phenomenology has recently gained a lot of attention. It can lead to the axion being a viable DM candidate over a wide range of parameter space accessible by direct detection experiments. It also features a viable scenario for baryogenesis as well as an enhancement of existing GW backgrounds if the axion leads to a period dominated by kinetic energy. We showed that even, if the axions energy is sub-dominant at all times, it can source a detectable GW signal by itself, if it couples to a dark photon. This signal can be strong enough to be detected by pulsar timing arrays (PTAs) and interferometers without being in tension with cosmological constraints. For the post-inflationary evolution of the relaxion we found that the coupling to a dark photon not only leads to a detectable GW signal, but also that the friction provided by the production of photons keeps the relaxion from overshooting its original minimum. This is a necessary condition not to ruin the relaxion solution to the hierarchy problem and therefore opens new viable parameter space.

Finally we studied dark sectors with sizeable energy fluctuations more broadly. We asked the question whether such new physics can source a strong enough GW signal to explain the recent hint by today's PTAs, such as NANOGrav. To answer this question we developed a quick fitting method that allows for the estimation of the model parameters. We found that especially the existing N_{eff} bound from CMB and BBN measurements limits the ability to explain the hint by a purely gravitationally coupled sector severely. For example in the case of an ALP coupled to dark photons, only extreme parameter points in the specific case where the ALP is the relaxion are able to produce a strong enough signal. It is intriguing however that the sensitivity of PTAs is already in the same realm as other cosmological measurements. Our studies highlighted the important role that these observations will take in the future as PTAs are constantly taking more data.

Further we showed that distortions in the CMB spectrum present a new possibility to search for purely gravitationally coupled sectors. Energy fluctuations in the dark sector lead to scalar metric fluctuations that themselves cause acoustic waves in the baryon-photon fluid. These acoustic waves are eventually damped due to diffusion of photons at which point the energy of the wave is converted to heat. If this damping takes place when the photon number is conserved but otherwise thermalization is achieved, this leads to a μ -distortion. We showed that a wide variety of new physics processes such as the above mentioned instabilities, but also first order phase transitions and scaling seed networks, can lead to detectable distortions. It is especially intriguing that some of the models that are able to explain the recent PTA data might also lead to a detectable spectral distortion. In the future a combination of spectral distortions and PTA measurements might not only detect such a sector but due to the complementary nature of the signals also be able to fully determine its parameters.

Acknowledgments

First, I would like to thank my supervisor. He kept me on track during my master and doctoral studies, even though I broke my hand, a pandemic struck and I nearly got lost in Paris. It was always a pleasure to work with him and discuss research ideas in the institute as well as betas at Blockwerk. Further, I want to thank my second supervisor who has also been with me since my master studies and the other committee members who took their time to read and evaluate my PhD thesis.

My collaborators also deserve a lot of praise for helping me with my research. Our discussion always lead to new insights and inspired new ideas.

During my 4.5 year long journey of master and PhD studies I had the pleasure to experience the friendly atmosphere in the THEP group. Thanks to all of you for very nice coffee and lunch breaks, whiskey tastings, hikes, bouldering sessions and lots more.

Moreover I want to especially thank all people who helped proof reading this thesis.

Finally, I want to thank my friends and family for all their various ways of supporting me. First and foremost my parents, who invested loads of time and effort into my education and always provided me with good advice.

Redshifting Abundances and Scales

Sectors that only interact gravitationally are nowadays constraint by precise cosmological and astrophysical observations. We here give the relations to find the present day abundances once the energy of the sector has taken on the scaling a^{-3} and a^{-4} for dark matter and dark radiation respectively. One of the strongest hints for dark matter is its aiding role in structure formation which requires it to be 'cold'. This means that its momentum has to be small compared to its mass. We derive the corresponding bound below. We furthermore give the formulas that relate the length and frequency scales of fluctuations or GWs at the time of their production to the present day value.

A.1 Dark Matter

Relic Abundance

Given that the dark matter abundance is set at a_* and from thereon only redshift $\propto a^{-3}$ has to be taken into account, the relic abundance can be calculated as

$$\Omega_\phi^0 = \Omega_\phi^* \frac{g_{\rho,*}}{g_{s,*}} \frac{g_{s,\text{eq}}}{g_{\rho,\gamma}} \frac{T_{\text{osc}}}{T_0} \Omega_\gamma^0, \quad (\text{A.1})$$

with $g_{s,\text{eq}} = 2 + 2N_{\text{eff}}(7/8)(4/11) = 3.938$, $g_{\rho,\gamma} = 2$, $T_0 = 2.73$ K. g_ρ and g_s denote the effective relativistic degrees of freedom in the SM plasma in terms of energy density and entropy. For temperatures above 10 MeV when all species are in equilibrium these two coincide.

If the dark matter is produced with a momentum k_* larger than its mass $k_*/a_* > m$, it redshifts like radiation before the momentum becomes negligible at $a_{\text{mat}} \simeq k_*/m$ leading to a suppression of $k_*/(a_*m)$ compared to the equation above.

Cold enough

Secondly a non-zero momentum leads to a finite velocity of the dark matter at matter radiation equality

$$\beta = \frac{k_*}{a_{\text{eq}}m} = \frac{k_*}{a_*m} \frac{T_{\text{eq}}}{T_*} \left(\frac{g_{s,\text{eq}}}{g_{s,*}} \right)^{1/3}. \quad (\text{A.2})$$

If this velocity is sizeable, structure formation will be suppressed leading to tensions with observations of the Lyman- α forest. We infer the bound on the velocity from studies of sterile neutrino dark matter produced through freeze out, where the average neutrino momentum is given by the temperature. From Refs. [278, 279] we find

$$\beta \lesssim 1.1 \times 10^{-4}. \quad (\text{A.3})$$

A.2 Dark Radiation

Relic Abundance

Any effectively massless degree of freedom changes the number of effective relativistic degrees of freedom (N_{eff}). At the epoch of recombination, the dark radiation contribution to N_{eff} is given by

$$\Delta N_{\text{eff}} = \frac{8}{7} \left(\frac{11}{4} \right)^{\frac{4}{3}} \frac{\rho_d}{\rho_\gamma} \Big|_{T=T_{\text{rec}}}, \quad (\text{A.4})$$

where the energy densities of SM photons and dark radiation are ρ_γ and ρ_d , respectively. Since both species scale as radiation, the fraction ρ_d/ρ_γ only changes when SM fields become non-relativistic and transmit their entropy to the photon bath. As stated above the dark radiation abundance is set at a_* resulting in the following contribution to ΔN_{eff}

$$\Delta N_{\text{eff}} = \frac{8}{7} \left(\frac{11}{4} \right)^{\frac{4}{3}} \left(\frac{g_{s,\text{eq}}}{g_{s,*}} \right)^{\frac{4}{3}} \left(\frac{g_{\rho,*}}{g_{\rho,\gamma}} \right) \Omega_d^*. \quad (\text{A.5})$$

The Planck 2018 TT,TE,EE,lowE+lensing+BAO dataset constrains $\Delta N_{\text{eff}} < 0.3$ at 95% confidence level [172]. Future CMB observations are expected to improve this bound by an order of magnitude.

A.3 Gravitational Waves

Relic Abundance

Gravitational waves constitute also a form of dark radiation and therefore in principal also contribute to N_{eff} . As discussed in the main text, however, the energy density in GWs is negligible compared to the one in the sector sourcing them for all mechanisms of GW production discussed in this work.

In the thesis we stress however that GWs can be used to search for new exotic dark sectors. To determine the detectability of a signal in a pulsar timing array or laser interferometer its present day energy density needs to be known. Assuming that the GW production takes place at a_* it is calculated as

$$\Omega_{\text{GW}}^0 = \Omega_{\text{GW}}^* \left(\frac{g_{s,\text{eq}}}{g_{s,*}} \right)^{\frac{4}{3}} \left(\frac{g_{\rho,*}}{g_{\rho,\gamma}} \right) \Omega_\gamma^0. \quad (\text{A.6})$$

A.4 Redshifting Scales

The mechanism that we considered in this work for the production of GWs or fluctuations can be associated with a typical wavelength/length scale at the time of production. When comparing the signal to the sensitivity of an experiment, the present day length scale needs to be known. Given a scale at production k/a_* the redshifted value is determined via

$$\frac{k}{a_0} = \left(\frac{g_{s,\text{eq}}}{g_{s,*}} \right)^{1/3} \frac{T_0}{T_*} \frac{k}{a_*}. \quad (\text{A.7})$$

Chapter B

Lattice Implementation

The main focus of this chapter is the implementation of the axion-dark photon coupling on the lattice that was used to produce the results of Chapter IV. The much simpler algorithm that one obtains when getting rid of the dark-photon and its coupling, leaving only scalars, is however what was used in Chapters III and VIII. For the axion and dark photon dynamics we closely followed Refs. [72, 73] while for the gravitational waves we adhere to Refs. [111, 112]. While for Chapters III and IV we used a code written from scratch, for Chapter VIII we used the implementation given by the package `CosmoLattice` and only implemented the energy density and the shear of scalar fields ourselves. These expressions are given at the end of the chapter.

B.1 Lattice Action

We use a staggered grid algorithm to solve the dynamics of the axion coupled to the dark photon. At the heart of these algorithms lies the notion of some fields lying between lattice sites. For example, the axion field, as it is parity odd, is displaced half a time step forward. We will denote this by $\phi(x + dx_0/2) = \phi|_{x+dx_0/2}$, where $x = (x_0, x_1, x_2, x_3)$ is a point on the lattice. Furthermore, we use a non-compact formulation of the $U(1)$ gauge dynamics, meaning that we use the field strength as our variable instead of Wilson lines. Since the gauge field X_μ is associated with the Wilson line linking neighboring lattice sites, it naturally is displaced by $+dx_\mu/2$ ($X_\mu|_{x+dx_\mu/2}$). We define the forward and backward derivative of a quantity $f(x)$ as

$$\Delta_\mu^\pm f(x \pm dx_\mu/2) = \frac{\pm f(x \pm dx_\mu) \mp f(x)}{dx_\mu}. \quad (\text{B.1})$$

This reproduces the continuum derivative up to $\mathcal{O}(dx_\mu^2)$, but only if one expands around the natural lattice site $x \pm dx_\mu/2$ as one can easily check

$$\Delta_\mu^\pm f(x \pm dx_\mu/2) = \partial_\mu f(x \pm dx_\mu/2) + \mathcal{O}(dx_\mu^2). \quad (\text{B.2})$$

The last rule needed for building the discretized version of the action in Eq. (IV.1) is that the product of two operators that reproduce their continuum version up to second order is only of second order if the operators lie on the same lattice site.

We work in conformal time and assume that the contribution of the axion and dark photon to the total energy density is negligible, i.e. that the evolution of the scale factor is independent of the dynamics. We assume the scale factor is a given function $a(\tau)$ that can be evaluated to get $a|_\tau$ and $a|_{\tau+d\tau/2}$. The action we want to discretize reads:

$$S = \int d^4x \left[\frac{a^2}{2} \partial_\mu \phi \partial_\nu \phi \eta^{\mu\nu} - a^4 V(\phi) - \frac{1}{4} X_{\mu\nu} X_{\alpha\beta} \eta^{\mu\alpha} \eta^{\nu\beta} + \frac{\alpha}{8f} \phi X_{\mu\nu} X_{\alpha\beta} \epsilon^{\mu\nu\alpha\beta} \right], \quad (\text{B.3})$$

where $\partial_\mu = (\partial_\tau, \partial_{x_i})$ denotes the derivative with respect to comoving coordinates, $\eta^{\mu\nu} = \text{diag}(1, -1, -1, -1)$ is the inverse Minkowski metric, $X_{\mu\nu} = \partial_\mu X_\nu - \partial_\nu X_\mu$ is the dark photon field strength and $\epsilon^{\mu\nu\alpha\beta}$ is the totally antisymmetric tensor with sign convention $\epsilon^{0123} = 1$. The discretized version of the axion part of the action is

$$S \supset d\tau dx^3 \sum_x \left[\frac{(a|_\tau)^2}{2} \Delta_0^- \phi \Delta_0^- \phi \Big|_x - \frac{(a|_{\tau+d\tau/2})^2}{2} \sum_i \Delta_i^+ \phi \Delta_i^+ \phi \Big|_{x+d\tau/2+dx_i/2} + (a|_{\tau+d\tau/2})^4 V(\phi) \Big|_{x+d\tau/2} \right], \quad (\text{B.4})$$

where we have indicated the exact lattice site of the displaced operators. The lattice version of the dark photon field strength is

$$X_{\mu\nu}|_{x+dx_\mu/2+dx_\nu/2} = \Delta_\mu^+ X_\nu - \Delta_\nu^+ X_\mu, \quad (\text{B.5})$$

which is invariant under the gauge transformation

$$X_\mu \rightarrow X_\mu + \Delta_\mu^+ \alpha, \quad (\text{B.6})$$

where $\alpha(x)$ is an arbitrary function of the lattice site. It is convenient to introduce the electric and magnetic fields as

$$E_i = X_{0i}|_{x+d\tau/2+dx_i/2} \quad (\text{B.7})$$

$$B_i = \frac{1}{2} \epsilon_{ijk} X_{jk}|_{x+dx_j/2+dx_k/2}, \quad (\text{B.8})$$

as this allows us to write the gauge kinetic term on the lattice as

$$S \supset d\tau dx^3 \sum_{x,i} \frac{1}{2} \left[E_i E_i \Big|_{x+d\tau/2+dx_i/2} - B_i B_i \Big|_{x+dx_j/2+dx_k/2} \right]. \quad (\text{B.9})$$

Finding a lattice version of the interaction piece is more challenging, since the electric and magnetic field strengths are associated with different sites on the lattice and therefore the first guess

$$S \supset d\tau dx^3 \sum_x \frac{\alpha}{f} \phi \sum_i E_i B_i, \quad (\text{B.10})$$

does not reproduce the continuum action up to second order. The solution to this problem is to introduce averages of operators between lattice sites, since these reproduce the operator to second order on the site in between. In principle there are several averaging schemes, but one also needs to check that the shift symmetry $\phi \rightarrow \phi + \epsilon$ is respected and that the resulting equations of motion allow for an iterative solution. These issues are discussed in detail in Ref. [72], and we use the scheme found there, employing the following averages:

$$E_i^{(2)}|_{x+d\tau/2} = \frac{1}{2} (E_i|_{x+d\tau/2+dx_i/2} + E_i|_{x+d\tau/2-dx_i/2}) \quad (\text{B.11})$$

$$B_i^{(4)}|_x = \frac{1}{4} (B_i|_{x+dx_j/2+dx_k/2} + B_i|_{x+dx_j/2-dx_k/2} + B_i|_{x-dx_j/2+dx_k/2} + B_i|_{x-dx_j/2-dx_k/2}). \quad (\text{B.12})$$

With these definitions, the interaction piece becomes

$$S \supset d\tau dx^3 \sum_x \frac{\alpha}{f} \phi \frac{1}{2} \sum_i E_i^{(2)} (B_i^{(4)} + B_i^{(4)}|_{+d\tau}) \Big|_{x+d\tau/2}. \quad (\text{B.13})$$

B.2 Equations of Motion and Integration Scheme

We work in temporal gauge where $X_0 = 0$. The dynamical degrees of freedom are $\Pi_\phi = \Delta_0^- \phi$ and X_i given at time τ as well as ϕ and $E_i = \Delta_0^+ X_i$ at time $\tau + d\tau/2$. We use the defining equation of E_i to find X_i at $\tau + d\tau$

$$X_i \Big|_{x+d\tau} = X_i \Big|_x + d\tau E_i \Big|_{x+d\tau/2}. \quad (\text{B.14})$$

By varying the action with respect to ϕ one finds the equation of motion

$$\begin{aligned} \Delta_0^+(a^2 \Pi_\phi) &= a^2 \sum_i \Delta_i^- \Delta_i^+ \phi - a^4 V'(\phi) \\ &+ \frac{\alpha}{2f} \sum_i E_i^{(2)} (B_i^{(4)} + B_i^{(4)}|_{x+d\tau}), \end{aligned} \quad (\text{B.15})$$

that is used to evolve Π_ϕ

$$\begin{aligned} a^2(\tau + d\tau) \Pi_\phi|_{x+d\tau} &= a^2(\tau) \Pi_\phi + d\tau \left[a^2|_{\tau+d\tau/2} \sum_i \Delta_i^- \Delta_i^+ \phi \right. \\ &\left. - a^4|_{\tau+d\tau/2} V'(\phi) + \frac{\alpha}{2f} \sum_i E_i^{(2)} (B_i^{(4)} + B_i^{(4)}|_{x+d\tau}) \right]. \end{aligned} \quad (\text{B.16})$$

Note that since X_i is known at τ and $\tau + d\tau$, the calculation of B_i and $B_i^{(4)}$ at these times is straightforward and the interaction term can be calculated explicitly. Now that $\Pi_\phi(\tau + d\tau)$ is known, ϕ can be evolved

$$\phi|_{x+d\tau \cdot 3/2} = \phi|_{x+d\tau/2} + d\tau \Pi_\phi|_{x+d\tau}. \quad (\text{B.17})$$

Finally, we have the equation of motion of X_i to evolve E_i

$$\begin{aligned} \Delta_0^- E_i &= - \sum_{j,k} \epsilon_{ijk} \Delta_j^- B_k - \frac{\alpha}{2f} \left(\Pi_\phi B_i^{(4)} + \Pi_\phi|_{x+dx_i} B_i^{(4)}|_{x+dx_i} \right) \\ &+ \frac{\alpha}{8f} (2 - d\tau \Delta_0^-) \sum_{\pm} \epsilon_{ijk} (2 + dx \Delta_i^+) \left(\Delta_j^\pm \phi E_k^{(2)}|_{x \pm dx_j} \right). \end{aligned} \quad (\text{B.18})$$

Notice however, that the evolved E_i appears not only on the left-hand side of the equation but also on the right-hand side in the interaction piece. Furthermore, the interaction piece features E_i not only at different times but also at different spatial positions due to the averages, making an explicit solution impossible. We therefore use the following implicit method. First, we approximate the $E_i|_{x+d\tau \cdot 3/2}$ by the already known $E_i|_{x+d\tau/2}$ in the interaction piece to get

$$\begin{aligned} E_i|_{x+d\tau \cdot 3/2,1} &= E_i|_{x+d\tau/2} + d\tau \left[- \sum_{j,k} \epsilon_{ijk} \Delta_j^- B_k \right. \\ &- \frac{\alpha}{2f} \left(\Pi_\phi B_i^{(4)} + \Pi_\phi|_{x+dx_i} B_i^{(4)}|_{x+dx_i} \right) \\ &\left. + \frac{\alpha}{4f} \sum_{\pm} \epsilon_{ijk} (2 + dx \Delta_i^+) \left(\Delta_j^\pm \phi|_{x+d\tau/2} E_k^{(2)}|_{x \pm dx_j + d\tau/2} \right) \right]. \end{aligned} \quad (\text{B.19})$$

This first approximation only satisfies the equation of motion up to $\mathcal{O}(d\tau)$ and we therefore have to at least do one more iteration, where we use the $E_i|_{x+d\tau\cdot 3/2,1}$ we just found to approximate $E_i|_{x+d\tau\cdot 3/2}$.

$$\begin{aligned}
 E_i|_{x+d\tau\cdot 3/2,2} &= E_i|_{x+d\tau\cdot 3/2,1} \\
 &+ d\tau \left[\frac{\alpha}{8f} \sum_{\pm} \epsilon_{ijk} (2 + dx\Delta_i^+) \left(\Delta_j^{\pm} \phi|_{x+d\tau\cdot 3/2} E_k^{(2)}|_{x\pm dx_j+d\tau\cdot 3/2,1} \right) \right. \\
 &\left. - \frac{\alpha}{8f} \sum_{\pm} \epsilon_{ijk} (2 + dx\Delta_i^+) \left(\Delta_j^{\pm} \phi|_{x+d\tau/2} E_k^{(2)}|_{x\pm dx_j+d\tau/2} \right) \right].
 \end{aligned} \tag{B.20}$$

While this approximation is now correct up to $\mathcal{O}(d\tau^2)$, it still poses a violation to the shift symmetry $\phi \rightarrow \phi + \epsilon$. This violation can be suppressed via higher order approximations such as

$$\begin{aligned}
 E_i|_{x+d\tau\cdot 3/2,n+1} &= E_i|_{x+d\tau\cdot 3/2,n} \\
 &+ d\tau \left[\frac{\alpha}{8f} \sum_{\pm} \epsilon_{ijk} (2 + dx\Delta_i^+) \left(\Delta_j^{\pm} \phi|_{x+d\tau\cdot 3/2} E_k^{(2)}|_{x\pm dx_j+d\tau\cdot 3/2,n} \right) \right. \\
 &\left. - \frac{\alpha}{8f} \sum_{\pm} \epsilon_{ijk} (2 + dx\Delta_i^+) \left(\Delta_j^{\pm} \phi|_{x+d\tau\cdot 3/2} E_k^{(2)}|_{x\pm dx_j+d\tau\cdot 3/2,n-1} \right) \right].
 \end{aligned} \tag{B.21}$$

This concludes one time step in the evolution of the fields. To integrate the equations of motion, one repeats these steps. One can obtain one more equation of motion, the Gauss constraint, by varying the action with respect to X_0

$$\sum_i \Delta_i^- E_i = -\frac{\alpha}{4f} \sum_i \sum_{\pm} \Delta_i^{\pm} \phi (2 + d\tau\Delta_0^+) B_i^{(4)}|_{x\pm dx_i}. \tag{B.22}$$

Given the fields at the same times as in the beginning of the step, checking this equation is straightforward, since $B_i|_{x+d\tau}$ can be calculated using Eq. (B.14). One has to choose the initial field configuration such that the Gauss constraint is fulfilled. Evolving the fields using the exact equations of motion then ensures that it stays fulfilled at all times. It can therefore be used to check the accuracy of the implicit method solving for $E_i|_{x+d\tau\cdot 3/2}$.

B.3 Fourier Transformation and Polarization

We define the Fourier transformation of fields not spatially displaced from a lattice site (e.g. ϕ and Π_{ϕ}) as

$$\phi(\tau, \mathbf{k}) = \frac{L^{3/2}}{N^3} \sum_{\mathbf{x}} \phi(\tau, \mathbf{x}) \exp(-i\mathbf{k} \cdot \mathbf{x}). \tag{B.23}$$

For fields that are spatially displaced, we take the displacement into account in the exponential. For example for the Fourier transform of X_i which is displaced by $+dx_i/2$ we have

$$X_i(\tau, \mathbf{k}) = \frac{L^{3/2}}{N^3} \sum_{\mathbf{x}} X_i(\tau, \mathbf{x} + dx_i/2) \exp(-i\mathbf{k} \cdot (\mathbf{x} + dx_i/2)). \tag{B.24}$$

Note that this also means that a field and its derivatives transform differently since the derivative is displaced. The benefit of this convention is that the relation between a field and its derivative in Fourier space is simply

$$\mathcal{F}(\Delta_i^{\pm} \phi)(\tau, \mathbf{k}) = i p_i(k_i) \phi(\tau, \mathbf{k}), \quad p_i(k_i) \equiv \frac{2}{dx} \sin\left(\frac{dx}{2} k_i\right). \tag{B.25}$$

Note that $p_i(k_i)$ is real, making the discussion of polarization easier as shown in Ref. [112]. It allows us to define the polarization with respect to the behavior under rotations around $\mathbf{p}(\mathbf{k})$, as in the continuum case

$$\sum_{j,k} \epsilon_{ijk} p_j(k_j) X_k^\pm(\mathbf{k}) = \mp i |\mathbf{p}(\mathbf{k})| X_i^\pm(\mathbf{k}). \quad (\text{B.26})$$

B.4 Initial Conditions

We investigate the process of particle production during a period of radiation domination, where the scale factor takes the form $a(\tau) = m\tau$. We start the simulation at $\tau_0 = 0.1/m$ when $H_0 = 100m$, such that the axion is pinned by Hubble friction and $\Pi_{\phi,0} = 0$, and assume the axion is displaced by $\phi_0 = \theta f$ from the minimum of the potential. The dark photon field is in the Bunch-Davies vacuum at the start of the simulation. This corresponds to $X_i(\tau_0, \mathbf{k})$ and $E_i(\tau_0, \mathbf{k})$ being drawn from a Gaussian distribution with widths $1/\sqrt{2|\mathbf{p}(\mathbf{k})|}$ and $\sqrt{|\mathbf{p}(\mathbf{k})|/2}$, respectively. Afterwards, the projector

$$P_{ij} = \delta_{ij} - \frac{p_i(k_i)p_j(k_j)}{|\mathbf{p}(\mathbf{k})|^2}, \quad (\text{B.27})$$

is applied to ensure that the Gauss constraint Eq. (B.22) is initially fulfilled. We then take the inverse Fourier transform to arrive at $X_i(\tau_0, \mathbf{x})$ and $E_i(\tau_0, \mathbf{x})$.

B.5 Lattice Dimensions and Number of Iterations

We choose the time step of our simulations as

$$d\tau = \frac{1}{4} \min\{dx, 1/(ma(\tau))\}, \quad (\text{B.28})$$

in order to avoid instabilities as a result of the discretization. We varied the side lengths of the simulated volume L and the number of lattice sites along each direction N as well as the number of iterations used when implicitly solving for E_i . In Fig. IV.1, we show the evolution of the comoving number density of the axion and dark photon for a variety of choices for the above mentioned parameters. Except for the two runs where the length was chosen particularly small $L = \pi/(4 \cdot m)$, the results agree up to $\approx 10\%$ fluctuations. Aside from the physical quantities we also monitored violations in the Gauss constraint (B.22). We introduce the quantity

$$\frac{\left\langle \left| \sum_i \Delta_i^- E_i + \frac{\alpha}{4f} \sum_i \sum_{\pm} \Delta_i^\pm \phi (2 + d\tau \Delta_0^+) B_i^{(4)} \Big|_{x \pm dx_i} \right| \right\rangle}{\langle \sum_i |E_i| / dx \rangle}, \quad (\text{B.29})$$

where $\langle \dots \rangle$ denote averages over all lattice sites, to measure the relative error in the Gauss constraint. In Fig. B.1 we show the evolution of this quantity. We note that the relative error starts out around 10^{-15} at $a = a_{osc}$ independently of the lattice parameters, close to the precision of a double precision float of $2^{-53} \approx 10^{-16}$. This goes to show that our procedure to initialize the dark photon indeed respects the Gauss constraint as expected. During the linear regime, when the dark photon energy is negligible compared to the axion, the relative error stays around 10^{-15} and only jumps up once the system enters the non linear regime, when the energy in the axion and dark photon becomes comparable and the axion field is fully inhomogeneous. As we can see from Fig. B.1, the size of the

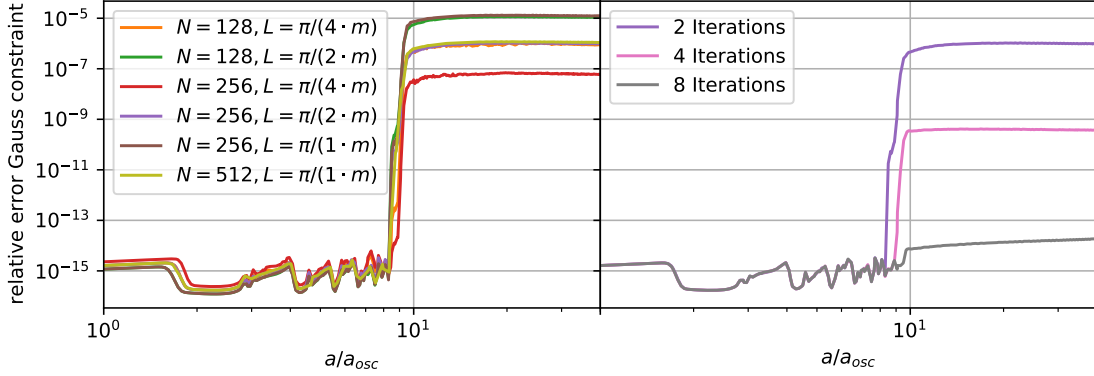


Figure B.1: Evolution of the relative error in the Gauss constraint Eq. (B.29) for different choices of the number of lattice sites along each direction N and the side length of the simulated box L with fixed $\alpha = 60$, $\theta = 1$. The number of iterations used in the implicit scheme is fixed at 2 for the left panel while it is varied in the right panel with $N = 256$, $L = \pi/(2 \cdot m)$ held fixed. In all cases, the error stays close to machine precision $\approx 10^{-16}$ up to $a/a_{osc} \approx 8$, when the dark photon production backreacts on the axion. Thereafter, the error is minimized for small lattice spacings $dx = L/N$ and a high number of iterations.

violation of the Gauss error depends on the lattice spacing $dx = L/N$ and (as expected) on the number of iterations. It should be noted that already for $n = 8$ iterations the error in the Gauss constraint does not exceed 10^{-14} significantly and we expect it to stay at machine precision with only a few more iterations.

Since none of the physical quantities showed significant dependence on the number of iterations n for $n \geq 2$, which is necessary to ensure convergence at $\mathcal{O}(dx^2)$, we set $n = 2$ for all the simulations discussed in the main text to minimize the computational effort. The choices for N and L listed in Section IV.3 were thus motivated by getting reliable results for the physical quantities, covering the relevant range of momenta and keeping computational costs down.

B.6 Gravitational Waves

Following Ref. [111], we calculate the gravitational wave spectrum by solving for the transverse traceless (TT) fluctuations of the metric

$$\frac{1}{a^2} \partial_\tau (a^2 \partial_\tau h_{ij}) - \nabla^2 h_{ij} = \frac{2}{M_P^2} \Pi_{ij}. \quad (\text{B.30})$$

We note that this equation as well as the TT projection is linear, and for practical purposes we therefore solve

$$\frac{1}{a^2} \partial_\tau (a^2 \partial_\tau \tilde{h}_{ij}) - \nabla^2 \tilde{h}_{ij} = \frac{2}{M_P^2} S_{ij}, \quad (\text{B.31})$$

where S_{ij} is the TT part of the energy-momentum tensor

$$S_{ij} = \partial_i \phi \partial_j \phi - \frac{1}{a^2} (E_i E_j + B_i B_j). \quad (\text{B.32})$$

The metric fluctuation h_{ij} can then be obtained by applying the TT projection Π

$$\Pi(\tilde{h}_{ij}) = h_{ij}. \quad (\text{B.33})$$

From the source term we can immediately see that the corresponding fields on the lattice are not located on the same lattice site and an averaging scheme has to be employed. An important criterion when choosing this scheme, aside from practicality, is that it should allow for coherent interpretation of the TT conditions

$$\partial_i h_{ij} = 0, \quad h_{ii} = 0. \quad (\text{B.34})$$

There exist many such schemes as discussed in Ref. [112]. Therein the authors find that the choice of scheme has only marginal influence on the results. In the scheme we employ, h_{ij} sits at $x + d\tau/2$. Since the position of h_{ij} is independent of i and j , the trace can be calculated at each site $x + d\tau/2$. To find a local interpretation of the condition for transversality, we introduce the symmetric lattice derivative

$$\Delta_\mu^{\text{sym}} \phi = \frac{\phi(x + dx_\mu) - \phi(x - dx_\mu)}{2dx_\mu}. \quad (\text{B.35})$$

The symmetric derivative reproduces the continuum derivative with $\mathcal{O}(dx_\mu^2)$ accuracy and is located at the same site as the field ϕ in contrast to the one-sided derivatives Δ^\pm . With this, the transverse condition also takes a local form

$$\sum_i \Delta_i^{\text{sym}} h_{ij} \Big|_{x+d\tau/2} = 0, \quad \sum_i h_{ii} \Big|_{x+d\tau/2} = 0. \quad (\text{B.36})$$

The equation of motion on the lattice reads

$$\frac{1}{a^2} \Delta_\tau^- (a^2 \Delta_\tau^+ \tilde{h}_{ij}) - \Delta_k^- \Delta_k^+ \tilde{h}_{ij} = \frac{2}{M_P^2} S_{ij}. \quad (\text{B.37})$$

Since the left side of the equation is located at the lattice site $x + d\tau/2$, we have to employ an averaging scheme such that S_{ij} is located on the same site. To do so, we introduce

$$B_i^{(8)} \Big|_{x+d\tau/2} = \frac{1}{2} \left(B_i^{(4)} \Big|_x + B_i^{(4)} \Big|_{x+d\tau} \right), \quad (\text{B.38})$$

and define on the lattice

$$S_{ij} = \Delta_i^{\text{sym}} \phi \Delta_j^{\text{sym}} \phi - \frac{1}{a^2} \left(E_i^{(2)} E_j^{(2)} + B_i^{(8)} B_j^{(8)} \right). \quad (\text{B.39})$$

With this explicit expression for the source term S_{ij} , Eq. (B.37) can be solved in a leap frog scheme to find \tilde{h}_{ij} . The associated momentum of the symmetric derivative is

$$\mathcal{F}(\Delta_i^{\text{sym}} \phi)(\tau, \mathbf{k}) = i p_i^{\text{sym}}(k_i) \phi(\tau, \mathbf{k}); \quad p_i^{\text{sym}}(k_i) \equiv \frac{1}{dx} \sin(dx k_i). \quad (\text{B.40})$$

By replacing \mathbf{k} in the continuum with $\mathbf{p}^{\text{sym}}(\mathbf{k})$, the discussion of polarization and the TT projection is analogous to the continuum. Therefore, the two polarizations are defined by

$$\sum_{k,l} p_k^{\text{sym}}(k_k) [\epsilon_{ikl} h_{lj}^\pm(\mathbf{k}) + \epsilon_{jkl} h_{il}^\pm(\mathbf{k})] = \mp 2i |\mathbf{p}^{\text{sym}}(\mathbf{k})| h_{ij}^\pm(\mathbf{k}). \quad (\text{B.41})$$

B.7 Energy Density and Shear

For Chapter VIII we furthermore need the energy density and the shear of the simulated system. Since there we only consider scalars two scalars ϕ and ψ , we will restrict our discussion to them from now on. Again we will need to employ an averaging scheme. Otherwise the kinetic energy will be displaced from the potential and gradient ones. In the scheme we employ the velocities are brought half a time step forward, which is equivalent to using $\Pi_\phi^{(2)}|_{x+d\tau/2} = (\Pi_\phi|_x + \Pi_\phi|_{x+d\tau})/2$. From these one can calculate the total energy as discussed in e.g. [235]

$$\bar{\rho}_{\text{tot}} = \left\langle \frac{1}{2} \sum_{\Phi \in \{\phi, \psi\}} \left[\Pi_\Phi^{(2)} \Pi_\Phi^{(2)} + \frac{1}{2} \sum_{i=1}^3 (\Delta_i^+ \Phi \Delta_i^+ \Phi + \Delta_i^- \Phi \Delta_i^- \Phi) \right] + V(\phi, \psi) \right\rangle. \quad (\text{B.42})$$

In principle a generalization to an energy density is straight forward. The only term one has to treat carefully is the gradient energy. These reproduce $\nabla_i \phi(\mathbf{x})$ only up to $\mathcal{O}(dx)$ but $\nabla_i \phi(\mathbf{x} \pm dx/2 \hat{\mathbf{e}}_i)$ to $\mathcal{O}(dx^2)$. We therefore employ the following averaging scheme to get an energy density that is correct up to $\mathcal{O}(dx^2)$

$$\rho_{\text{tot}}(\mathbf{x}) = \frac{1}{2} \sum_{\Phi \in \{\phi, \psi\}} \left[\Pi_\Phi^{(2)} \Pi_\Phi^{(2)} + \frac{1}{2} \sum_{i=1}^3 (\Delta_i^+ \Phi \Delta_i^+ \Phi + \Delta_i^- \Phi \Delta_i^- \Phi) \right] + V(\phi, \psi). \quad (\text{B.43})$$

This scheme has the added benefit of reproducing the energy that is used in `CosmoLattice` when consistently evolving the scale factor or checking energy conservation

$$E_{\text{tot}} = \frac{N^3}{L^3} \sum_{\mathbf{x}} \rho_{\text{tot}}(\mathbf{x}). \quad (\text{B.44})$$

This is opposed to a scheme where one uses the symmetric spacial derivative

$$\Delta_i^{\text{sym}} \phi(\mathbf{x}) = \frac{1}{2} \frac{\phi(\mathbf{x} + dx \hat{\mathbf{e}}_i) - \phi(\mathbf{x} - dx \hat{\mathbf{e}}_i)}{dx}. \quad (\text{B.45})$$

The expressions given here and below only hold in a flat space-time but can easily be generalized to expanding backgrounds using the α -time concept of `CosmoLattice` [235, 236].

The shear is the longitudinal-traceless component of the anisotropic stress. We again use the pseudo-stress given in Eq. (B.39), but only keep the scalars. To obtain the longitudinal part we apply the following projector

$$(\bar{\rho} + \bar{p})\sigma(\mathbf{k}) = \sum_{i,j=0}^3 \left(\hat{\mathbf{p}}_i^{\text{sym}}(\mathbf{k}) \hat{\mathbf{p}}_j^{\text{sym}}(\mathbf{k}) - \frac{1}{3} \delta_{ij} \right) T_{ij}(\mathbf{k}). \quad (\text{B.46})$$

Free Scalar Field

Below we calculate the energy fluctuations and their autocorrelation functions for a single relativistic scalar field ϕ with Gaussian fluctuations

$$\mathcal{P}_\phi(k) = A_\phi \sqrt{\frac{2}{\pi}} \frac{k^3}{\tilde{k}_*^3} \exp\left(-\frac{k^2}{2\tilde{k}_*^2}\right), \quad (\text{C.1})$$

where $1/\tilde{k}_*$ is the characteristic length scale of fluctuations in the field as opposed to the energy density. We assume that the modes of the field are virialized such that $\mathcal{P}_\phi(k) = \omega_k^2 \mathcal{P}_\phi(k)$, where $\omega_k^2 = k^2 + m^2$ is the frequency of the respective mode. For a free scalar field the mode functions follow the equation of motion of an unperturbed harmonic oscillator, which is why the autocorrelation of both ϕ and $\dot{\phi}$ is given as $\cos(\omega_k t)$, while the cross-correlation is given as

$$\langle \phi(\mathbf{k}, t) \dot{\phi}^*(\mathbf{k}', t') \rangle = \frac{2\pi^2}{k^3} \mathcal{P}_\phi(k) \omega_k \sin(\omega_k(t - t')) (2\pi)^3 \delta^{(3)}(\mathbf{k} - \mathbf{k}'). \quad (\text{C.2})$$

Energy Fluctuations

The energy density of the field is

$$\rho_\phi = \frac{1}{2} \left(\dot{\phi}^2 + \nabla\phi^2 + m^2\phi^2 \right) \quad (\text{C.3})$$

and its Fourier coefficients are given as

$$\rho_\phi(\mathbf{k}) = \frac{1}{2} \int \frac{d^3p}{(2\pi)^3} \dot{\phi}(\mathbf{p}) \dot{\phi}(\mathbf{k} - \mathbf{p}) + [m^2 - \mathbf{p} \cdot (\mathbf{k} - \mathbf{p})] \phi(\mathbf{p}) \phi(\mathbf{k} - \mathbf{p}). \quad (\text{C.4})$$

The mean energy density can be calculated as

$$\bar{\rho}_\phi = \frac{1}{V} \langle \rho_\phi(\mathbf{k} = 0) \rangle = \begin{cases} 3A_\phi \tilde{k}_*^2 & \omega_k \approx k \\ A_\phi m^2 & \omega_k \approx m \end{cases} \quad (\text{C.5})$$

for the relativistic and non-relativistic case respectively and V denotes the volume one is averaging over. When calculating the correlation of energy fluctuations $\langle \rho_\phi(\mathbf{k}) \rho_\phi^*(\mathbf{k}') \rangle$ we will face the following kind of correlators between Gaussian variables

$$= \langle \phi(\mathbf{p}) \phi(\mathbf{k} - \mathbf{p}) \phi^*(\mathbf{p}') \phi^*(\mathbf{k}' - \mathbf{p}') \rangle \quad (\text{C.6})$$

$$= \langle \phi(\mathbf{p}) \phi^*(\mathbf{p}') \rangle \langle \phi(\mathbf{k} - \mathbf{p}) \phi^*(\mathbf{k}' - \mathbf{p}') \rangle + \langle \phi(\mathbf{p}) \phi^*(\mathbf{k}' - \mathbf{p}') \rangle \langle \phi(\mathbf{k} - \mathbf{p}) \phi^*(\mathbf{p}') \rangle \quad (\text{C.7})$$

$$= (2\pi)^3 \delta^3(\mathbf{k} - \mathbf{k}') \left[(2\pi)^3 \delta^3(\mathbf{p} - \mathbf{p}') + (2\pi)^3 \delta^3(\mathbf{p} - (\mathbf{k}' - \mathbf{p}')) \right] \frac{2\pi^2}{p^3} \mathcal{P}_\phi(\mathbf{p}) \frac{2\pi^2}{|\mathbf{k} - \mathbf{p}|^3} \mathcal{P}_\phi(\mathbf{k} - \mathbf{p}), \quad (\text{C.8})$$

where we assumed $\mathbf{k} \neq 0$ and therefore $\langle \phi(\mathbf{p})\phi(\mathbf{k} - \mathbf{p}) \rangle = 0$. Putting it all together we arrive at

$$\begin{aligned} \mathcal{P}_{\rho_\phi}(k, t, t + \Delta t) &= \frac{k^3}{2\pi^2} \frac{1}{2} \int \frac{d^3 p}{(2\pi)^3} \frac{2\pi^2}{p^3} \mathcal{P}_\phi(p) \frac{2\pi^2}{|\mathbf{k} - \mathbf{p}|^3} \mathcal{P}_\phi(k - p). \quad (\text{C.9}) \\ &\left[(\omega_p^2 \omega_{k-p}^2 + (m^2 - \mathbf{p} \cdot (\mathbf{k} - \mathbf{p}))^2) \cos(\omega_p \Delta t) \cos(\omega_{k-p} \Delta t) + \right. \\ &\quad \left. 2\omega_p \omega_{k-p} (m^2 - \mathbf{p} \cdot (\mathbf{k} - \mathbf{p})) \sin(\omega_p \Delta t) \sin(\omega_{k-p} \Delta t) \right]. \end{aligned}$$

We can further evaluate this expression for $k \ll \tilde{k}_*$. In this case approximate $\mathbf{p} = \mathbf{p} - \mathbf{k}$ except sine and cosine, since we want to keep track of the time evolution. The p -integral is dominated by modes with $p \approx \tilde{k}_*$ and we therefore approximate

$$\Delta\omega = \omega_p - \omega_{k-p} \approx \begin{cases} \mathbf{k} \cdot \mathbf{p}/|\mathbf{p}| & \omega_{\tilde{k}_*} \approx \tilde{k}_* \\ \mathbf{k} \cdot \mathbf{p}/m & \omega_{\tilde{k}_*} \approx m. \end{cases} \quad (\text{C.10})$$

We then find by using trigonometric identities

$$\mathcal{P}_{\rho_\phi}(k, t, t + \Delta t) \approx \frac{k^3}{2\pi^2} \int_0^\infty d \log p \frac{2\pi^2}{p^3} \mathcal{P}_\phi^2(p) \omega_p^4 \int_{S^2} \frac{d\Omega_p}{4\pi} \cos(\Delta\omega \Delta t). \quad (\text{C.11})$$

The last integral in this expression is the autocorrelation function of the energy fluctuations. In the relativistic case it does not depend on $|\mathbf{p}|$, while in the non-relativistic we can approximate $|\mathbf{p}| \approx \tilde{k}_*$ and introduce the typical velocity of energy transport in the dark sector as $c_d = \tilde{k}_*/m$ to find

$$\mathcal{A}_{\delta_\phi}(k, \Delta t) = \begin{cases} \text{sinc}(kt) & \omega_{\tilde{k}_*} \approx \tilde{k}_* \\ \text{sinc}(c_d kt) & \omega_{\tilde{k}_*} \approx m. \end{cases} \quad (\text{C.12})$$

We argued in the main text that the only relevant time scale for the autocorrelation of the energy density is c_d/k , with c_d the typical velocity of energy transport. Here we showed this explicitly.

Shear

The space-space part of the energy momentum tensor of a scalar field is given by

$$T_{ij} \approx \nabla_i \phi \nabla_j \phi, \quad (\text{C.13})$$

where we neglected contributions proportional to g_{ij} that exclusively contribute to the trace. We find the shear by going to Fourier space and projecting out the longitudinal traceless component

$$\sigma_\phi(\mathbf{k}) = \frac{1}{\bar{\rho}_\phi + \bar{p}_\phi} \left[\frac{1}{k^2} k_i T_{ij}(\mathbf{k}) k_j - \frac{1}{3} T_{ii}(\mathbf{k}) \right]. \quad (\text{C.14})$$

From there the steps are the same as for the energy density and we arrive at

$$\mathcal{P}_{\sigma_\phi}(k, t, t + \Delta t) = \frac{1}{(\bar{\rho}_\phi + \bar{p}_\phi)^2} \frac{k^3}{2\pi^2} 2 \int \frac{d^3 p}{(2\pi)^3} \frac{2\pi^2}{p^3} \mathcal{P}_\phi(p) \frac{2\pi^2}{|\mathbf{k} - \mathbf{p}|^3} \mathcal{P}_\phi(k - p). \quad (\text{C.15})$$

$$\left[\left(\hat{\mathbf{k}} \mathbf{p} \right) \left(\hat{\mathbf{k}} (\mathbf{p} - \mathbf{k}) \right) - \frac{1}{3} \mathbf{p} (\mathbf{p} - \mathbf{k}) \right]^2 \cos(\omega_p \Delta t) \cos(\omega_{k-p} \Delta t).$$

When we expand the cosines again for $k \ll \tilde{k}_*$, we find

$$\cos(\omega_p \Delta t) \cos(\omega_{k-p} \Delta t) = \frac{1}{2} \left(\cos\left(2\omega_{\tilde{k}_*} t\right) + \cos(\Delta\omega t) \right). \quad (\text{C.16})$$

To arrive at the autocorrelation function one would need to carry out the integration. But we are content here with only showing that for a non-conserved quantity like the shear indeed both time scales $1/\tilde{k}_*$ and $1/k$ enter. This can already be seen from the above expression with the $\cos\left(2\omega_{\tilde{k}_*} t\right)$ term not canceling.

List of Figures

Chapter II

- II.1 Polarized gravitational wave hitting a circle of freely falling particles. The circle lies in the blue plane orthogonal to the propagation direction. The solid line with blue dots shows the perturbed circle while the dotted line with white dots is the unperturbed circle before the arrival of the wave. The circle is shown at different times. $P = 2\pi/k$ is the period of the gravitational wave. Illustration borrowed from [47]. 13

Chapter III

- III.1 Field evolution with slope $\mu = 0$ and no expansion for different initial velocities and decay constants f . All simulations were run with $N = 128^3$ lattice sides and length $L = 20/m$ along each side. Top: We clearly see how the stopping process consists of two parts i) a phase where the modes that are initially enhanced by parametric resonance grow from vacuum to an energy density $\rho \approx m^2 f^2$ in a time δt_{amp} and ii) a nonlinear part that lasts a time of $2.3 t_{\text{nl}}$ (marked by the red dotted line). Bottom: We see that in the non-linear regime the fields roll a distance $\approx \phi_{\text{nl}} \cdot 1.5$ (blue dashed line), in the limit of large f and $\dot{\phi}_0$ 24
- III.2 Average axion velocity for $f = 10^3 m$, $\mu = 0$, and no expansion as obtained from linear analysis (Eq. (III.9)) and from different realizations of the lattice. 25
- III.3 Evolution of the axion field with $\mu = 0$, $f = 10^{10} m$, $\dot{\phi}_0 = 10 m f$, and no expansion for different initial energy spectra. The dark colors correspond to a flat initial energy spectrum (as expected if fluctuations are enhanced during inflation) where the energy in the initial resonance band is enhanced by a factor $d\rho/d\log k(k_{\text{cr},0}) \approx 10^8 d\rho_{\text{BD}}/d\log k(k_{\text{cr},0})$ as compared to the Bunch-Davies vacuum (light colors). The gray and black dashed lines mark δt_{amp} and $\delta t_{\text{amp}}^{\text{mod}}$, respectively (see Eq. (III.19)), while the thin and thick red dashed lines correspond to $\delta t_{\text{amp}} + z t_{\text{nl}}$ and $\delta t_{\text{amp}}^{\text{mod}} + z t_{\text{nl}}$. Both simulations were run with $N = 256^3$ lattice sides and length $L = 80/m$ along each side. 26
- III.4 Average axion velocity varying the slope in the range $0.70 < \mu/\mu_{\text{max}} < 1.10$, for $f/m = 10^3$ (top) and 10^{10} (bottom), and $\dot{\phi}_0 = 5 m f$ (left) and $10 m f$ (right). The red dotted line is at $(t - \delta t_{\text{amp}})/t_{\text{nl}} = 2.3$ 27

III.5	Early evolution of the axion energy spectrum for $f/m = 10^{10}$, $\dot{\phi}_0 = 10mf$. The blue shaded lines show the spectrum as obtained from a lattice with $N = 512^3$ sites and side length $L = 40/m$. The bottom black line is the analytic expression for the initial Bunch Davies vacuum $\propto k^4$ and the orange lines give the analytic NLO estimate Eq. (III.37) for $t = 0.7 - 1.0 \cdot t_{\text{amp}}$. On the right we magnified the region around the peak $k_{\text{cr}} = 5m$ and show for comparison the analytic LO estimate Eq. (III.6) for $t = 0.1 - 1.0 \cdot t_{\text{amp}}$ in red.	31
III.6	Evolution of the axion energy spectrum past δt_{amp} for $f/m = 10^{10}$, $\dot{\phi}_0 = 10mf$. The blue shaded lines show the spectrum as obtained from the same lattice as in Fig. III.5. The black line shows the spectrum from the linear analysis given in Eq. (III.38).	32
III.7	Dependence of the number density of bubbles with a volume bigger than V_0 for different f and $\dot{\phi}_0$ at three different times. The dashed lines show the fit of an exponential decay $n(V_0) \propto \exp(-\Gamma V_0)$ to the last few data points for each time.	36
III.8	Spread of the minima the field stops in for $f = 10^{10}m$ and $\dot{\phi}_0 = 10mf$ in different lattice configurations. The y -axis is centered around the average final minimum $\mu_{\phi, \text{frag}}$. Importantly, the spread of the minima $\sigma_{\phi, \text{frag}}$ decreases as the size of the box L is increased.	36
III.9	Dependence of the spread in the final position of the zero-mode of the field $\sigma_{\phi, \text{frag}}$ on the length of the sides of the simulated box L . The different color crosses represent simulations with different numbers of lattice sites, all with $f = 10^{10}m$ and $\dot{\phi}_0 = 10mf$. The solid line corresponds to the analytic estimate of Eq. (III.61), which seems to underestimate the spread by $\mathcal{O}(10)$ but captures the decrease of the spread with increasing length L correctly.	39
III.10	Evolution of the axion RMS field value caused by modes with $k > m$ as computed by integration of the axion power spectrum obtained from a lattice computation with $N = 256^3$ lattice sites, $L = 40/m$, and $f = 10^{10}m$ (solid lines). The dotted horizontal lines show the analytic estimate from Eq. (III.64). The horizontal, dotted, red line marks the time around which the axion stops as estimated in Sec. III.3.	40
III.11	Parameter space of the relaxion model including the results of this paper (in red), compared to the results of Ref. [44] (in gray, dashed lines). Top: Relaxation during inflation. Center: Relaxation after inflation, with $g/g' = 1$. Bottom: Relaxation after inflation, with $g/g' = 1/(4\pi)^2$. In the center and bottom rows, we superimpose the contours of $\log_{10} H_I^{\text{max}}$, defined according to Eq. (III.48).	43
IV.1	Comoving axion (solid) and dark photon (dotted) number densities for different choices of the lattice parameters with $\alpha = 60$ and $\theta = 1$ held fixed. In the left panel, L and N are varied while the number of iterations in the implicit scheme is held fixed at 2. Similarly, the right panel fixes $N = 256$, $L = \pi/(2m)$ and varies the number of iterations in the implicit scheme. The different choices agree to within $\sim 10\%$ except in the case of the smallest length $L = \pi/(4m)$.	54
Chapter IV		
IV.2	Early evolution of the dark photon (left) and axion (right) spectra. The model parameters are $\alpha = 60$ and $\theta = 1$. The “+” polarization is the first to experience tachyonic instability.	55

IV.3	Evolution of the spectra in the non-linear regime. The model parameters are $\alpha = 60$ and $\theta = 1$. The “+” polarization is the first to experience tachyonic instability. The dark photon and axion panels correspond to those in Fig. IV.2 but within a much smaller range of energy densities.	56
IV.4	Evolution of the comoving axion energy density for $\theta = 1$. Around $a = a_{osc}$, the axion starts oscillating and scaling like matter $\rho_\phi \approx a^{-3}m^2f^2$. Without particle production, this scaling would persist (blue dot-dashed line) yielding the standard abundance from misalignment. For $\alpha = 60$, the backreaction of dark photon production becomes strong around $a/a_{osc} \sim 9$. The thin gray line shows the result from the linear analysis, while the solid orange line gives the lattice result. The lattice result shows a suppression of the final axion abundance by $\approx 10^{-2}$ compared to the case with no particle production, in stark contrast to the linear analysis which suggests a much stronger suppression. The dotted lines show possible further suppression in case where the final mass is adiabatically reduced, while the brown dashed line corresponds to a time dependent potential that vanishes around $a/a_{osc} = 100$ (see Sec. IV.5 for details).	58
IV.5	Suppression of the axion relic abundance for different values of α and fixed $\theta = 1$ compared to the standard misalignment case where $\alpha = 0$ and there is no dark photon production. We see that $\theta\alpha \gtrsim 30$ is required for efficient dark photon production. For values of $\theta\alpha \gtrsim 200$, friction from particle production causes the axion to slow-roll and behave as vacuum energy, thus it will quickly come to dominate the energy density of the universe. As we ignore the effect of the axion-dark photon system on the gravitational background, this regime is beyond the scope of our simulation, and we simply sketch the expected sharp loss of suppression in this region with the dashed line.	58
IV.6	Gravitational wave spectra computed on the lattice for different values of α with $\theta = 1$ held fixed. The light dashed lines show the two polarizations (red, blue) when $\rho_X = \rho_\phi/2$ (roughly the end of the perturbative regime). The solid lines are the final spectra taken at $a/a_{osc} = 40$ when the GW spectrum has fully converged. The solid black line gives the sum of the two polarizations in the final spectrum and green crosses mark the NDA scaling relation from Eq. IV.14 with $c_{eff} = 1$. The source material includes the final spectra in tabulated form.	60
IV.7	Same as Fig. IV.6 except $\alpha = 40$ is held fixed while θ is varied. In the case of $\theta = 3$ we chose a smaller sized box $L = \pi/(3ma_{osc})$ to better resolve the UV part of the spectrum.	61
IV.8	Axion and ALP parameter space in the mass vs. inverse decay constant plane. Regions below the colored curves are in reach of future ground-based (ET) and satellite-based (LISA, BBO, DECIGO) GW detectors, or future pulsar timing arrays (SKA). Shaded regions are excluded by existing constraints, while unshaded regions show the sensitivity of various other planned experiments. Black hole superradiance excludes the grey shaded region, and future black hole observations could extend this region to the grey line. The location of the QCD axion band is indicated by the black dashed line.	63

IV.9 ALP parameter space in the mass vs. inverse decay constant plane with $\alpha = 100$ and $\theta = 1$ held fixed. The parameter space below the bright colored curves could be probed by future GW experiments, such as pulsar timing arrays (SKA) as well as space- (LISA, DECIGO, BBO, μ Ares) and Earth-based (ET) interferometers. In addition, we also show the region where LISA (dashed red) or ET (dashed blue) can potentially detect the chirality of the GW signal. The purple region is where the model could account for the recently reported NANOGrav signal. The gray region is excluded in case of a relativistic dark photon by bounds on N_{eff} , while in the green region a massive dark photon can be a viable DM candidate. The solid diagonal lines refer to axion dark matter scenarios in which, from left to right, there is no particle production (standard misalignment), only the suppression from particle production $\approx 10^{-2}$ (PP only), or further suppression η from model extensions (PP + η). In the blue shaded area, the axion is cool enough to be DM, assuming sufficient suppression of the relic abundance. 64

Chapter V

V.1 Comparison of rates and energy densities between a numerical simulation and analytic scaling relations for $S_i = 2 \times 10^{18}$ GeV, $m_{S,0} = 1$ GeV, $f_\phi = 5 \times 10^{13}$ GeV, $\alpha = 0.02$ and $\epsilon = 1$. We start the simulation when the Hubble rate coincides with the dark photon growth rate k_{peak}/a at $a = a_*$. In the top panel we show the growth rate in dark blue dominating over the Hubble rate. At $a_{\text{GW}}/a_* \approx 43$ marked by the black dotted line, the growth rate deviates from the analytic scaling behavior shown as the purple, dash-dotted line. The reason for this discrepancy can be found in the bottom panel, where we can see the dark photon energy becoming comparable to the one of the axion around this time. Friction from dark photon production becomes efficient and the growth rate, which is proportional to the axions velocity, decreases faster as by the scaling only considering Hubble friction. The dash-dotted black line marks the saxion field settling at its VEV f_ϕ at $a_{S=f_\phi}$. Afterwards the photon production quickly becomes inefficient and all quantities take on their respective scaling behaviors, although with the growth rate and axion energy reduced due to friction from the photons. The relic ALP abundance after dark photon production is well matched by the red dash-dotted line, which denotes a kination-like scaling starting at a_{GW} . Since we observe this behavior throughout all our simulations, we will use this as an analytic estimate of the minimum relic ALP abundance in Section V.5.1. Simulation and figure created by D. Schmitt. 73

V.2 GW spectrum as a function of the physical momentum k/a_{GW} normalized to the Hubble rate at emission calculated from the same simulation as Fig. V.1. The black dots indicates the estimate in Eq. (V.25). **Left:** GW spectrum at the time of emission. The solid blue curve depicts the total spectrum, whereas the dot-dashed orange and cyan curves correspond to positive and negative GW helicities, respectively. **Right:** Total GW spectrum at different times. Figure created by D. Schmitt. 76

V.3	Parameter space of the QCD axion for fixed benchmark parameters $S_i = 2 \times 10^{18}$ GeV and $\alpha = 10^{-7}$. On the blue lines the correct baryon symmetry is induced by weak sphaleron (WS) processes at the time of the electroweak phase transition. For large saxion masses this happens during or after the production of dark photons, where the predictability of our perturbative method is limited, which is why we show two limiting scenarios (straight and dash-dotted). In the future, the relevant parameter space may be probed by both direct axion searches such as the IAXO experiment (yellow shaded region), as well as the GW observatory LISA (green-shaded region) and potential follow-up experiments like μ ARES. Note that for the chosen parameters, the relic axion abundance corresponds to the one obtained from conventional misalignment and therefore only constitutes part of DM in the shown parameter region. Figure created by D. Schmitt.	79
V.4	The parameter regions in the $S_i - m_{S,0}$ plane that are testable in the future, for the benchmark parameters $f_\phi = 10^{12}$ GeV and $\alpha = 0.02$. Since the GW amplitude is independent of f_ϕ , the presented model provides detectable signals for any value of f_ϕ . Hence, also the parameter region that is subject to direct axion searches may be probed via GWs in the future. In the entire parameter space, the ALP can constitute DM, since the GW production is independent of m_ϕ . The blue shaded region marks where the dark photons, if they were massive, are sufficiently cold to be DM, but also do not overclose the Universe at T_{eq} . Figure created by D. Schmitt.	81
VI.1	Simulated (coloured lines) and expected (dashed black line) amplitude of the dark photon modes at different times. The deep (light) coloured lines correspond to the positive (negative) helicity. At each time, the expected peak momentum is indicated by the vertical dashed line in the corresponding colour, whereas the black-dashed vertical line indicates the upper bound $k < k_{\text{pp}}$ on the tachyonic dark photon momentum. Figure created by E. Madge.	87
Chapter VI		
VI.2	Simulation (full colours) and analytic approximation (light colours) of the GW spectrum for a reappearance temperature of $T_{\text{ra}} = 150$ GeV (blue) and 750 GeV (orange). The vertical dashed lines indicate the expected peak frequency, whereas the dash-dotted and dotted curves correspond to the positive and negative helicity contributions to the simulated spectrum. Figure created by E. Madge.	92
VI.3	Allowed range of reappearance temperatures T_{ra} as a function of the cut-off scale Λ , while fixing f_ϕ to the value reproducing the measured DM abundance, Eq. (VI.40), assuming $T_{\text{osc}} = T_{\text{ra}}$. The blue shaded region is excluded since $\Lambda_{\text{br}} > v_H$, while in the green shaded regions, the CMB bound on ΔN_{eff} , Eq. (VI.48), is violated. In the orange shaded region, the dark photon energy density further dominates the Universe at reappearance. The dashed lines are contours of constant $m_\phi f_\phi / T_{\text{ra}}^2$, which sets the amplitude of the GW spectrum, cf. Eq. (VI.37). Figure created by A. Banerjee.	94

VI.4	Available parameter space (black framed region) for relaxion DM in the relaxion mass m_ϕ vs. mixing angle $\sin\theta_{h\phi}$ plane. The red and orange shaded regions are excluded by the indicated constraints of combinations thereof. The colored regions inside the viable DM space can be probed via GWs in μ Ares (green) or SKA (blue/turquoise). The light shading and solid lines indicate points that can be probed for a subrange of reappearance temperatures, whereas the darker shaded parts enclosed by dotted lines are accessible for all valid T_{ra} . An animated version of the plot scanning the reappearance temperature is enclosed in the ancillary material of [6]. Figure created by A. Banerjee.	95
VI.5	Values of the peak frequency and amplitude of the GW spectrum which can be obtained in the relaxion DM scenario. The edges of the polygon correspond to the minimal and maximal amplitudes which can be obtained for $\xi = 100$ (solid lines) and $\xi = 10$ (dashed lines), limiting to the case when the relaxion starts to oscillate immediately after barrier reappearance. Figure created by E. Madge.	96
VI.6	Available parameter space for $\xi = 100$ (top), and for $\xi = 10$ (bottom). The red and orange shaded regions are excluded by the indicated constraints or combinations thereof. Above the red solid line, the relaxion decay constant becomes super-Planckian. The grey dashed line encloses the parameter space in which re-trapping can be realized without dark photon friction such that the dark photon is not necessary for a viable relaxation scenario. The prospective GW sensitivity of μ Ares (green) as well as SKA after an observation period of 5 years (turquoise) and 20 years (blue) is indicated by the respective coloured regions. In the purple coloured region, a sub-range of the viable reappearance temperatures can be excluded using current NANOGrav data from the 11-year data set. The regions bounded by the coloured dotted lines need super-Planckian decay constants to be probed by the respective experiment. In the lower panel, the grey shaded region can reproduce our best-fit spectrum (at $T_{\text{ra}} \sim 20$ MeV) to the potential stochastic GW background seen in the recent NANOGrav data. Figure created by A. Banerjee.	98
VI.7	Best fit point (cross) to the NANOGrav 12.5-year data, as well as 1σ (dark) and 2σ (light) regions, fixing ξ to 10 (blue), 25 (orange) and 100 (green). The dotted lines enclose the region that can be obtained without being in tension with ΔN_{eff} or BBN at the respective value of ξ . Figure created by E. Madge.	99

Chapter VII

VII.1	Top panel: The gray violins give the Bayesian reconstruction of interpulsar spatial correlations for seven bins of angular separation on the sky. The orange and blue line give the expected result in case of a monopolar and quadrupolar nature of the signal. Bottom panel: Illustration of difference in cross-correlation for pulsar pairs (blue) caused by different angles between the positions of the pulsars on the sky as a gravity wave with + polarization passes through. Figure borrowed from [186] with modifications by the author.	105
VII.2	Comparison of 1σ and 2σ contours for a single power law fit to the 5 lowest frequency bins. Our results using the hierarchical method are shown in blue and the original result in orange. The black dotted line sits at $\alpha = -2/3$, the expected slope for the signal of SMBHBs.	108

VII.3	Signal of the best fits of a runaway and a non-runaway phase transition discussed in this chapter as well as the audible relaxation from Chapter VI with $\xi = 10$ compared to the first frequency bins of NANOGrav in the frequency- $\Omega_{GW}h^2$ plane.	109
VII.4	Left: Regions favoured by the NANOGrav signal for a vacuum PT, with $v_w = 1$, shown as a function of the transition temperature T_* and the PT timescale β/H . Right: Same for a strong first order PT in a plasma, with $v_w = 1$ and fixed values of β/H , as function of T_* and the energy budget α . The vertical line at one MeV indicates the onset of BBN, below which strong constraints apply to any models that alter the expansion rate of the Universe.	110
Chapter VIII		
VIII.1	The evolution of the horizon scale (blue), the scale a photon free streams between consecutive scattering events and diffusion scale that is approximately the distance traveled by a photon in a random walk as a result of all the scattering events in one Hubble time. Once a mode passes the diffusion scale the energy stored in the acoustic oscillation is damped. If this happens during the red-shifts marked in red on the x-axis a μ -distortion is sourced, singling out the modes marked in red on the y-axis as the dominant messengers of new physics. These modes enter the Horizon as early as $a \approx 10^{-9}$ allowing us to probe new physics back to when the photon temperature was ≈ 1 MeV.	115
VIII.2	Sourcing of acoustic waves through a gravitationally coupled dark sector and consequent damping by diffusion. The toy dark sector here is radiation like ($\Omega_d = \text{const.} \ll 1$) and its density fluctuations are zero until $a_* = 10^{-7}$ before evolving as $\delta_d = \sin(k\tau)$ (top row). The resulting gravitational potential (second row) causes acoustic oscillations in the baryon-photon fluid (third row). Since the gravitational potential rapidly decays after a mode has entered the horizon (vertical blue line) the amplitude of the acoustic oscillations quickly levels off resulting in an approximately constant acoustic energy $\epsilon_{ac}^{\text{lim}}(k)$ (bottom row, dashed line). The same effect also leads to the acoustic oscillations being suppressed for the high k mode (right side) that is already inside the horizon when the fluctuations in the dark sector develop. Subsequently the acoustic oscillations are damped for both modes once they cross the diffusion scale (green line). At this point the acoustic energy is injected into the bulk photon energy, leading to a sizeable μ -distortion for modes where this happens between $5 \times 10^{-7} \lesssim a \lesssim 2 \times 10^{-5}$	119
VIII.3	Suppression of the induced acoustic energy for modes that are inside the horizon $k \gtrsim a_*H_*$ when the fluctuations develop at a_* . The fluctuations here are taken to evolve deterministically as $\propto \sin(c_d k(\tau - \tau_*))$ past a_* . The straight lines show the result from a numerical simulation including the contributions of the neutrinos and baryon-photon fluid to the gravitational potentials, while the dotted lines show the estimate Eq. (VIII.30). For $k \gg a_*H_*$ the suppression falls as $\propto (a_*H_*/k)^2$ in the resonant case $c_d = c_\gamma = 1/\sqrt{3}$ (green) and as $\propto (a_*H_*/k)^4$ in the off-resonant cases, once the discrepancy in frequency becomes relevant.	123

VIII.4 Evolution of energy components in the dark sector. Around a_{osc} the ϕ -field starts oscillating and the energy initially stored in the quartic potential (red) starts going back and forth between the potential and kinetic energy (orange). The dark sector transitions from vacuum to radiation like scaling and its total energy (blue) asymptotes to the value given in Eq. (VIII.33) (dotted, black). The instabilities induced by the coupling (purple) in ψ lead to its energy (green) growing exponentially past a_{osc} . The mode functions of ψ can be approximated by solutions to the *Lamé* equation, leading to the estimate given by the dashed black line. The horizontal black line marks a_* , the time when the energy in the homogeneous ϕ field equals the energy in inhomogeneities of ψ as estimated in Eq. (VIII.34). At this point the perturbative treatment breaks down, making the lattice analysis necessary. Past this point the majority of energy is stored in fluctuations of ϕ and ψ 126

VIII.5 Evolution of power spectra of the ϕ and ψ -field (top row) as well as energy fluctuations δ_d and shear $\tilde{\sigma}_d$ in the dark sector (second row). In the third row we show the induced acoustic energy in the baryon-photon fluid through gravitational coupling. See Section VIII.4.3 for discussion. In the bottom row we furthermore show the resulting spectrum of gravitational waves as discussed in Section VIII.5.1. The vertical, black, dotted line marks the horizon scale at a_* , $k \approx a_{\text{osc}}\omega_*/70$, and the dashed line gives our estimate for the fastest growing mode in ψ , $k_* \approx a_{\text{osc}}\omega_*/\sqrt{2}$. The thick, black, straight and dashed lines give analytic estimates discussed in the text. 128

VIII.6 Evolution of the energy fluctuation $\delta_d(k, \tau)$ and the shear $\tilde{\sigma}_d(k, \tau)$ for two modes (orange and green) in the infrared tail of the spectrum ($k = 0.05 a_{\text{osc}}\omega_*$). The straight and dotted line give the real and imaginary part respectively. The gray envelope indicates the evolution of the power spectrum $\propto \sqrt{\mathcal{P}(k, \tau)}$ as calculated by averaging the amplitude of all mode-functions in the respective bin. In the close-up on the Hubble time past $a_* \approx 70 a_{\text{osc}}$ in the bottom panel, we have indicated the amplitude of the energy fluctuations growing $\propto [k(\tau - \tau_*)]^2$ by the black dotted lines. 129

VIII.7 Autocorrelation of the energy fluctuation $\delta_d(k, \tau)$ and the shear $\tilde{\sigma}_d(k, \tau)$ for same momentum as in Fig. VIII.6 ($k = 0.05 a_{\text{osc}}\omega_*$). For the energy fluctuation we show for comparison the sinc that we find analytically in Appendix C for a free scalar field (black). 130

VIII.8 Close-up of the acoustic energy spectrum at the final time of the simulation. The blue line represents the physical result, while the orange line stems from a simulation in which the shear of the dark sector was neglected. The straight black line gives the analytical estimate, with the black dashed line indicating a k^{-4} power law that seems more appropriate to describe the UV tail than the exponential decay of the analytic estimate. The vertical, black dotted and dashed line give the horizon at a_* and the estimate of the fastest growing mode in the ψ -field, k_* 131

VIII.9 Constraints and future probes of the $\lambda\phi^4$ -model introduced in Section VIII.4. ω_* determines the temperature T_* at which the fluctuations come to dominate the energy in the dark sector and the initial amplitude ϕ_i gives the energy in the dark sector Ω_d scaling the signal strength. The gray area and line give the current and future bound resulting from Ω_d increasing the effective number of neutrinos at recombination. For T_* below $\mathcal{O}(10^2 \text{ eV})$ the scenario is constraint by fits to CMB fluctuations (red) as well as the non-observation of B-polarization modes (cyan). For the wide range of annihilation temperatures of $10^2 - 10^7 \text{ eV}$ spectral distortions are able to probe the scenario with the future missions PIXIE (straight) and Voyage2050 (dotted). We show the bound including only the contribution from scalar acoustic waves in green and the one from only considering GWs in pink. At temperatures above 10^5 eV the model becomes testable by the future pulsar timing array SKA (orange line) and in the range $T_* \approx 10^6 - 10^7 \text{ eV}$ can possibly explain the NANOGrav signal with the 2σ region of the fit given by the orange area. Since this model is particularly efficient at emitting GWs, the corresponding probes dominate in all of the shown parameter space. 134

VIII.10Left: Constraints and future probes of domain walls in terms of the annihilation temperature of the network T_{ann} and the surface tension σ . Assuming that the domain walls relic density behaves as dark radiation after the annihilation leads to a contribution to N_{eff} with the present and future bound shown as the gray area and line respectively. At annihilation temperatures below $\mathcal{O}(10^2 \text{ eV})$ the scenario is constraint by fits to CMB fluctuations (red) as well as the non-observation of B-polarization modes (cyan). For the wide range of annihilation temperatures of $10^2 - 10^7 \text{ eV}$ spectral distortions as a result of the damping of acoustic waves (green) are able to probe the scenario, with current bounds from the COBE/FIRAS mission already in the same realm as the current N_{eff} bound in the range $T_{\text{ann}} = 10^3 - 10^5 \text{ eV}$ and future missions PIXIE and Voyage2050 going far beyond all other probes in this range. We also show the parameter space testable by the Voyage2050 mission taking into account only the contribution to the μ -distortion from gravity waves (pink dotted). This contribution is negligible in the parameter space still allowed by measurements of N_{eff} though. We have picked two benchmarks A and B. Right: On the top we show the GW signal for the benchmarks in relation to the power law integrated noise of SKA. While SKA can not distinguish the two scenarios, the induced spectral distortion is drastically different as can be seen from the bottom panel. 137

VIII.11 Present and future constraints on string networks resulting from the breaking of a global $U(1)$ at the scale f_ϕ and annihilating at a temperature T_{ann} due to an explicit breaking of the symmetry parameterized by the mass of the resulting pseudo Nambu-Goldstone boson m_ϕ . The grey region and line correspond to the current and future bound of N_{eff} stemming from the emitted, relativistic axions. At a temperature of $T_{ann} = 1 - 10$ eV the scenario is constrained by fits to CMB fluctuations (red) as well as the non-observation of B-polarization modes (cyan). For $f_a \geq 10^{14}$ GeV a strong enough GW signal is emitted to be detectable by SKA, while for $f_a \geq 4 \times 10^{14}$ GeV LISA is also sensitive to the signal. PIXIE and Voyage2050 (green, straight and dotted) allow probing all of the parameter points testable by LISA and the majority accessible via SKA. Again the great complementarity between GWs and spectral distortion experiments shall be emphasized with the later being able to measure/constrain the mass. Further constraints on this parameter region arise due to the emitted axions making up a fraction of DM and featuring large isocurvature perturbations in conflict with Lyman- α observations (purple). For annihilation temperatures $T_{ann} \geq 10^5$ eV the most severe constraint comes from overproducing axion DM. 139

VIII.12 Current and future constraints on a phase transition in a dark sector, in terms of the SM plasma temperature at the time of the transition, released energy relative to the energy in the dark fluid α_d , the ΔN_{eff} caused by the dark sector, and the inverse duration of the phase transition $\frac{\beta}{H}$. We only take into account the effects of the sound waves in the dark fluid caused by the transition. At temperatures $T_* = 1 - 10$ eV the scenario is constrained by CMB fluctuations in (red) and the non-observation of B-mode polarization in the CMB in (cyan). In the temperature range of $T_* = 10 - 10^6$ eV spectral distortions from acoustic waves (green) can probe the scenario. Strong phase transitions in a dark sector saturating the N_{eff} bound can already be constrained by the COBE/FIRAS results ($\alpha_d = \mathcal{O}(1)$, $\Delta N_{eff} = 0.3$, $\frac{\beta}{H} = 10$). At temperatures $T_* = 10^5 - 10^7$ eV the scenario can in the future be detected by SKA, while the present N_{eff} bound (top row) rules out the NANOGrav signal being generated this way. For convenience we have converted α_d to $\alpha = \Omega_d \alpha_d / (1 + \alpha_d)$ on the left y-axis. 141

VIII.13 Current and future constraints on a first order phase transition at temperature T_* releasing a relative energy α into the SM-plasma. For temperatures below ≈ 2 MeV the released energy α leads to tensions in BBN and CMB measurements of the baryon to photon ratio (blue). The sound waves caused by the phase transition source GWs that can explain the NANOGrav hint (orange, filled, same as right of Fig. VII.4) and in the future can be detected over a wide range of parameter space (orange line). The green area and lines show the current and future sensitivity to spectral distortions caused by the sound waves. At temperatures above ≈ 1 MeV the sound waves and therefore spectral distortions are expected to be reduced due to damping by neutrino diffusion. 142

B.1 Evolution of the relative error in the Gauss constraint Eq. (B.29) for different choices of the number of lattice sites along each direction N and the side length of the simulated box L with fixed $\alpha = 60$, $\theta = 1$. The number of iterations used in the implicit scheme is fixed at 2 for the left panel while it is varied in the right panel with $N = 256$, $L = \pi/(2 \cdot m)$ held fixed. In all cases, the error stays close to machine precision $\approx 10^{-16}$ up to $a/a_{osc} \approx 8$, when the dark photon production backreacts on the axion. Thereafter, the error is minimized for small lattice spacings $dx = L/N$ and a high number of iterations. 158

Chapter B

List of abbreviations

Λ CDM - standard model of cosmology

ALP - axion-like particle

BAO - baryonic acoustic oscillation

BAU - baryon asymmetry of the Universe

BBN - big bang nucleosynthesis

BSM - beyond the Standard Model

CDM - cold dark matter

CMB - cosmic microwave background

DM - dark matter

EM - electromagnetism

EW - electroweak

EWSB - electroweak symmetry breaking

FRW - Friedmann-Robertson-Walker

GW - gravitational wave

IR - infrared

NGB - Nambu-Goldstone boson

PNGB - pseudo Nambu-Goldstone boson

PTA - pulsar timing array

PQ - Peccei-Quinn

QCD - quantum chromodynamics

QED - quantum electrodynamics

SM - Standard Model (of particle physics)

SMBH - super massive black hole

SMBHB - super massive black hole binary

TR - thermal relic

TCA - tight coupling approximation

UV - ultra violet

VeV - vacuum expectation value

Bibliography

- [1] E. Morgante, W. Ratzinger, R. Sato, and B. A. Stefanek, *Axion fragmentation on the lattice*, *JHEP* **12** (2021) 037, [[arXiv:2109.13823](#)].
- [2] C. S. Machado, W. Ratzinger, P. Schwaller, and B. A. Stefanek, *Gravitational wave probes of axionlike particles*, *Phys. Rev. D* **102** (2020), no. 7 075033, [[arXiv:1912.01007](#)].
- [3] C. S. Machado, W. Ratzinger, P. Schwaller, and B. A. Stefanek, *Audible Axions*, *JHEP* **01** (2019) 053, [[arXiv:1811.01950](#)].
- [4] W. Ratzinger, P. Schwaller, and B. A. Stefanek, *Gravitational Waves from an Axion-Dark Photon System: A Lattice Study*, *SciPost Phys.* **11** (2021) 001, [[arXiv:2012.11584](#)].
- [5] E. Madge, W. Ratzinger, D. Schmitt, and P. Schwaller, *Audible axions with a booster: Stochastic gravitational waves from rotating ALPs*, *SciPost Phys.* **12** (2022), no. 5 171, [[arXiv:2111.12730](#)].
- [6] A. Banerjee, E. Madge, G. Perez, W. Ratzinger, and P. Schwaller, *Gravitational wave echo of relaxation trapping*, *Phys. Rev. D* **104** (2021), no. 5 055026, [[arXiv:2105.12135](#)].
- [7] W. Ratzinger and P. Schwaller, *Whispers from the dark side: Confronting light new physics with NANOGrav data*, [arXiv:2009.11875](#).
- [8] S. L. Glashow, *Partial Symmetries of Weak Interactions*, *Nucl. Phys.* **22** (1961) 579–588.
- [9] S. Weinberg, *A Model of Leptons*, *Phys. Rev. Lett.* **19** (1967) 1264–1266.
- [10] A. Salam, *Weak and Electromagnetic Interactions*, *Conf. Proc. C* **680519** (1968) 367–377.
- [11] G. 't Hooft and M. J. G. Veltman, *Regularization and Renormalization of Gauge Fields*, *Nucl. Phys. B* **44** (1972) 189–213.
- [12] ATLAS Collaboration, G. Aad et al., *Observation of a new particle in the search for the Standard Model Higgs boson with the ATLAS detector at the LHC*, *Phys. Lett. B* **716** (2012) 1–29, [[arXiv:1207.7214](#)].
- [13] CMS Collaboration, S. Chatrchyan et al., *Observation of a New Boson at a Mass of 125 GeV with the CMS Experiment at the LHC*, *Phys. Lett. B* **716** (2012) 30–61, [[arXiv:1207.7235](#)].
- [14] F. Zwicky, *Die Rotverschiebung von extragalaktischen Nebeln*, *Helv. Phys. Acta* **6** (1933) 110–127.

- [15] J. F. Navarro, C. S. Frenk, and S. D. M. White, *The Structure of cold dark matter halos*, *Astrophys. J.* **462** (1996) 563–575, [[astro-ph/9508025](#)].
- [16] M. Persic, P. Salucci, and F. Stel, *The Universal rotation curve of spiral galaxies: 1. The Dark matter connection*, *Mon. Not. Roy. Astron. Soc.* **281** (1996) 27, [[astro-ph/9506004](#)].
- [17] D. Clowe, M. Bradac, A. H. Gonzalez, M. Markevitch, S. W. Randall, C. Jones, and D. Zaritsky, *A direct empirical proof of the existence of dark matter*, *Astrophys. J. Lett.* **648** (2006) L109–L113, [[astro-ph/0608407](#)].
- [18] Particle Data Group Collaboration, P. A. Zyla et al., *Review of Particle Physics*, *PTEP* **2020** (2020), no. 8 083C01.
- [19] C. Cornella, D. A. Faroughy, J. Fuentes-Martin, G. Isidori, and M. Neubert, *Reading the footprints of the B-meson flavor anomalies*, *JHEP* **08** (2021) 050, [[arXiv:2103.16558](#)].
- [20] A. G. Riess et al., *A 2.4% Determination of the Local Value of the Hubble Constant*, *Astrophys. J.* **826** (2016), no. 1 56, [[arXiv:1604.01424](#)].
- [21] J. D. Bowman, A. E. E. Rogers, R. A. Monsalve, T. J. Mozdzen, and N. Mahesh, *An absorption profile centred at 78 megahertz in the sky-averaged spectrum*, *Nature* **555** (2018), no. 7694 67–70, [[arXiv:1810.05912](#)].
- [22] C. Abel et al., *Measurement of the Permanent Electric Dipole Moment of the Neutron*, *Phys. Rev. Lett.* **124** (2020), no. 8 081803, [[arXiv:2001.11966](#)].
- [23] Event Horizon Telescope Collaboration, K. Akiyama et al., *First M87 Event Horizon Telescope Results. I. The Shadow of the Supermassive Black Hole*, *Astrophys. J. Lett.* **875** (2019) L1, [[arXiv:1906.11238](#)].
- [24] Event Horizon Telescope Collaboration, K. Akiyama et al., *First Sagittarius A* Event Horizon Telescope Results. I. The Shadow of the Supermassive Black Hole in the Center of the Milky Way*, *Astrophys. J. Lett.* **930** (2022), no. 2 L12.
- [25] T. Kite, A. Ravenni, S. P. Patil, and J. Chluba, *Bridging the gap: spectral distortions meet gravitational waves*, [arXiv:2010.00040](#).
- [26] E. Witten, *Some Properties of $O(32)$ Superstrings*, *Phys. Lett. B* **149** (1984) 351–356.
- [27] P. Svrcek and E. Witten, *Axions In String Theory*, *JHEP* **06** (2006) 051, [[hep-th/0605206](#)].
- [28] A. Arvanitaki, S. Dimopoulos, S. Dubovsky, N. Kaloper, and J. March-Russell, *String Axiverse*, *Phys. Rev. D* **81** (2010) 123530, [[arXiv:0905.4720](#)].
- [29] D. J. E. Marsh, *Axion Cosmology*, *Phys. Rept.* **643** (2016) 1–79, [[arXiv:1510.07633](#)].
- [30] P. Agrawal, J. Fan, and M. Reece, *Clockwork Axions in Cosmology: Is Chrononatural Inflation Chrononatural?*, *JHEP* **10** (2018) 193, [[arXiv:1806.09621](#)].
- [31] Y. Bai and B. A. Stefanek, *Natural millicharged inflation*, *Phys. Rev. D* **91** (2015), no. 9 096012, [[arXiv:1405.6720](#)].
- [32] N. Kitajima, J. Soda, and Y. Urakawa, *Gravitational wave forest from string axiverse*, *JCAP* **10** (2018) 008, [[arXiv:1807.07037](#)].
- [33] J. Jaeckel, V. M. Mehta, and L. T. Witkowski, *Monodromy Dark Matter*, *JCAP* **01** (2017) 036, [[arXiv:1605.01367](#)].

- [34] J. Preskill, M. B. Wise, and F. Wilczek, *Cosmology of the Invisible Axion*, *Phys. Lett. B* **120** (1983) 127–132.
- [35] G. 't Hooft, C. Itzykson, A. Jaffe, H. Lehmann, P. K. Mitter, I. M. Singer, and R. Stora, eds., *Recent Developments in Gauge Theories. Proceedings, Nato Advanced Study Institute, Cargese, France, August 26 - September 8, 1979*, vol. 59, 1980.
- [36] R. Peccei and H. R. Quinn, *CP Conservation in the Presence of Instantons*, *Phys. Rev. Lett.* **38** (1977) 1440–1443.
- [37] F. Wilczek, *Problem of Strong P and T Invariance in the Presence of Instantons*, *Phys. Rev. Lett.* **40** (1978) 279–282.
- [38] G. Grilli di Cortona, E. Hardy, J. Pardo Vega, and G. Villadoro, *The QCD axion, precisely*, *JHEP* **01** (2016) 034, [[arXiv:1511.02867](#)].
- [39] J. E. Kim, *Weak Interaction Singlet and Strong CP Invariance*, *Phys. Rev. Lett.* **43** (1979) 103.
- [40] M. A. Shifman, A. I. Vainshtein, and V. I. Zakharov, *Can Confinement Ensure Natural CP Invariance of Strong Interactions?*, *Nucl. Phys. B* **166** (1980) 493–506.
- [41] S. Koren, *The Hierarchy Problem: From the Fundamentals to the Frontiers*. PhD thesis, UC, Santa Barbara, 2020. [arXiv:2009.11870](#).
- [42] P. W. Graham, D. E. Kaplan, and S. Rajendran, *Cosmological Relaxation of the Electroweak Scale*, *Phys. Rev. Lett.* **115** (2015), no. 22 221801, [[arXiv:1504.07551](#)].
- [43] N. Fonseca, E. Morgante, R. Sato, and G. Servant, *Axion fragmentation*, *JHEP* **04** (2020) 010, [[arXiv:1911.08472](#)].
- [44] N. Fonseca, E. Morgante, R. Sato, and G. Servant, *Relaxion Fluctuations (Self-stopping Relaxion) and Overview of Relaxion Stopping Mechanisms*, *JHEP* **05** (2020) 080, [[arXiv:1911.08473](#)]. [Erratum: *JHEP* **01**, 012 (2021)].
- [45] A. D. Linde, *ETERNAL CHAOTIC INFLATION*, *Mod. Phys. Lett. A* **1** (1986) 81.
- [46] Planck Collaboration, N. Aghanim et al., *Planck 2018 results. VI. Cosmological parameters*, *Astron. Astrophys.* **641** (2020) A6, [[arXiv:1807.06209](#)]. [Erratum: *Astron. Astrophys.* **652**, C4 (2021)].
- [47] N. T. Bishop and L. Rezzolla, *Extraction of Gravitational Waves in Numerical Relativity*, *Living Rev. Rel.* **19** (2016) 2, [[arXiv:1606.02532](#)].
- [48] C. Caprini and D. G. Figueroa, *Cosmological Backgrounds of Gravitational Waves*, *Class. Quant. Grav.* **35** (2018), no. 16 163001, [[arXiv:1801.04268](#)].
- [49] D. G. Figueroa and F. Torrenti, *Gravitational wave production from preheating: parameter dependence*, *JCAP* **10** (2017) 057, [[arXiv:1707.04533](#)].
- [50] D. G. Figueroa, M. Hindmarsh, J. Lizarraga, and J. Urrestilla, *Irreducible background of gravitational waves from a cosmic defect network: update and comparison of numerical techniques*, *Phys. Rev. D* **102** (2020), no. 10 103516, [[arXiv:2007.03337](#)].
- [51] E. Thrane and J. D. Romano, *Sensitivity curves for searches for gravitational-wave backgrounds*, *Phys. Rev. D* **88** (2013), no. 12 124032, [[arXiv:1310.5300](#)].

- [52] P. Brady, G. Losurdo, and H. Shinkai, *LIGO, VIRGO, and KAGRA as the International Gravitational Wave Network*, pp. 1205–1225. Springer Nature Singapore, Singapore, 2022.
- [53] M. Punturo et al., *The Einstein Telescope: A third-generation gravitational wave observatory*, *Class. Quant. Grav.* **27** (2010) 194002.
- [54] LISA Collaboration, P. Amaro-Seoane et al., *Laser Interferometer Space Antenna*, [arXiv:1702.00786](#).
- [55] T. Robson, N. J. Cornish, and C. Liu, *The construction and use of LISA sensitivity curves*, *Class. Quant. Grav.* **36** (2019), no. 10 105011, [[arXiv:1803.01944](#)].
- [56] A. Sesana et al., *Unveiling the Gravitational Universe at μ Hz Frequencies*, [arXiv:1908.11391](#).
- [57] J. Crowder and N. J. Cornish, *Beyond LISA: Exploring future gravitational wave missions*, *Phys. Rev. D* **72** (2005) 083005, [[gr-qc/0506015](#)].
- [58] G. Janssen et al., *Gravitational wave astronomy with the SKA*, *PoS AASKA14* (2015) 037, [[arXiv:1501.00127](#)].
- [59] M. Breitbach, J. Kopp, E. Madge, T. Opferkuch, and P. Schwaller, *Dark, Cold, and Noisy: Constraining Secluded Hidden Sectors with Gravitational Waves*, *JCAP* **07** (2019) 007, [[arXiv:1811.11175](#)].
- [60] NANOGrav Collaboration, Z. Arzoumanian et al., *The NANOGrav 11-year Data Set: Pulsar-timing Constraints On The Stochastic Gravitational-wave Background*, *Astrophys. J.* **859** (2018), no. 1 47, [[arXiv:1801.02617](#)].
- [61] NANOGrav Collaboration, Z. Arzoumanian et al., *The NANOGrav 12.5 yr Data Set: Search for an Isotropic Stochastic Gravitational-wave Background*, *Astrophys. J. Lett.* **905** (2020), no. 2 L34, [[arXiv:2009.04496](#)].
- [62] B. Goncharov et al., *On the evidence for a common-spectrum process in the search for the nanohertz gravitational-wave background with the Parkes Pulsar Timing Array*, [arXiv:2107.12112](#).
- [63] S. Chen et al., *Common-red-signal analysis with 24-yr high-precision timing of the European Pulsar Timing Array: Inferences in the stochastic gravitational-wave background search*, *Mon. Not. Roy. Astron. Soc.* **508** (2021), no. 4 4970–4993, [[arXiv:2110.13184](#)].
- [64] J. Antoniadis et al., *The International Pulsar Timing Array second data release: Search for an isotropic gravitational wave background*, *Mon. Not. Roy. Astron. Soc.* **510** (2022), no. 4 4873–4887, [[arXiv:2201.03980](#)].
- [65] R. Flauger, L. McAllister, E. Pajer, A. Westphal, and G. Xu, *Oscillations in the CMB from Axion Monodromy Inflation*, *JCAP* **06** (2010) 009, [[arXiv:0907.2916](#)].
- [66] J. Berges, A. Chatrchyan, and J. Jaeckel, *Foamy Dark Matter from Monodromies*, *JCAP* **08** (2019) 020, [[arXiv:1903.03116](#)].
- [67] A. Chatrchyan and J. Jaeckel, *Gravitational waves from the fragmentation of axion-like particle dark matter*, [arXiv:2004.07844](#).
- [68] R. T. Co, L. J. Hall, and K. Harigaya, *Axion Kinetic Misalignment Mechanism*, *Phys. Rev. Lett.* **124** (2020), no. 25 251802, [[arXiv:1910.14152](#)].
- [69] C.-F. Chang and Y. Cui, *New Perspectives on Axion Misalignment Mechanism*,

- Phys. Rev. D* 102 (2020), no. 1 015003, [[arXiv:1911.11885](#)].
- [70] L. Di Luzio, B. Gavela, P. Quilez, and A. Ringwald, *Dark matter from an even lighter QCD axion: trapped misalignment*, [arXiv:2102.01082](#).
- [71] C. Eröncel, R. Sato, G. Servant, and P. Sørensen, *ALP Dark Matter from Kinetic Fragmentation: Opening up the Parameter Window*, [arXiv:2206.14259](#).
- [72] D. G. Figueroa and M. Shaposhnikov, *Lattice implementation of Abelian gauge theories with Chern–Simons number and an axion field*, *Nucl. Phys. B* 926 (2018) 544–569, [[arXiv:1705.09629](#)].
- [73] J. R. C. Cuissa and D. G. Figueroa, *Lattice formulation of axion inflation. Application to preheating*, *JCAP* 06 (2019) 002, [[arXiv:1812.03132](#)].
- [74] L. Di Luzio, B. Gavela, P. Quilez, and A. Ringwald, *An even lighter QCD axion*, *JHEP* 05 (2021) 184, [[arXiv:2102.00012](#)].
- [75] D. Boyanovsky, C. Destri, and H. J. de Vega, *The Approach to thermalization in the classical ϕ^4 theory in (1+1)-dimensions: Energy cascades and universal scaling*, *Phys. Rev. D* 69 (2004) 045003, [[hep-ph/0306124](#)].
- [76] R. Micha and I. I. Tkachev, *Turbulent thermalization*, *Phys. Rev. D* 70 (2004) 043538, [[hep-ph/0403101](#)].
- [77] C. Destri and H. J. de Vega, *Ultraviolet cascade in the thermalization of the classical ϕ^4 theory in 3+1 dimensions*, *Phys. Rev. D* 73 (2006) 025014, [[hep-ph/0410280](#)].
- [78] G. I. Rigopoulos and E. P. S. Shellard, *The separate universe approach and the evolution of nonlinear superhorizon cosmological perturbations*, *Phys. Rev. D* 68 (2003) 123518, [[astro-ph/0306620](#)].
- [79] Z. Lalak, S. Lola, and P. Magnowski, *Dynamics of domain walls for split and runaway potentials*, *Phys. Rev. D* 78 (2008) 085020, [[arXiv:0710.1233](#)].
- [80] M. Ibe, Y. Shoji, and M. Suzuki, *Fast-Rolling Relaxion*, *JHEP* 11 (2019) 140, [[arXiv:1904.02545](#)].
- [81] N. Kitajima, T. Sekiguchi, and F. Takahashi, *Cosmological abundance of the QCD axion coupled to hidden photons*, *Phys. Lett. B* 781 (2018) 684–687, [[arXiv:1711.06590](#)].
- [82] P. Agrawal, N. Kitajima, M. Reece, T. Sekiguchi, and F. Takahashi, *Relic Abundance of Dark Photon Dark Matter*, *Phys. Lett. B* 801 (2020) 135136, [[arXiv:1810.07188](#)].
- [83] N. Kitajima, J. Soda, and Y. Urakawa, *Nano-Hz gravitational wave signature from axion dark matter*, [arXiv:2010.10990](#).
- [84] P. Agrawal, J. Fan, M. Reece, and L.-T. Wang, *Experimental Targets for Photon Couplings of the QCD Axion*, *JHEP* 02 (2018) 006, [[arXiv:1709.06085](#)].
- [85] B. Salehian, M. A. Gorji, S. Mukohyama, and H. Firouzjahi, *Analytic study of dark photon and gravitational wave production from axion*, [arXiv:2007.08148](#).
- [86] P. Agrawal, G. Marques-Tavares, and W. Xue, *Opening up the QCD axion window*, *JHEP* 03 (2018) 049, [[arXiv:1708.05008](#)].
- [87] B. Holdom, *Two $U(1)$'s and Epsilon Charge Shifts*, *Phys. Lett.* 166B (1986) 196–198.

- [88] S. Dubovsky and G. Hernández-Chifflet, *Heating up the Galaxy with Hidden Photons*, *JCAP* **1512** (2015), no. 12 054, [[arXiv:1509.00039](#)].
- [89] J. Jaeckel and A. Ringwald, *The Low-Energy Frontier of Particle Physics*, *Ann. Rev. Nucl. Part. Sci.* **60** (2010) 405–437, [[arXiv:1002.0329](#)].
- [90] J. Jaeckel and A. Ringwald, *A Cavity Experiment to Search for Hidden Sector Photons*, *Phys. Lett.* **B659** (2008) 509–514, [[arXiv:0707.2063](#)].
- [91] S. A. Abel, J. Jaeckel, V. V. Khoze, and A. Ringwald, *Illuminating the Hidden Sector of String Theory by Shining Light through a Magnetic Field*, *Phys. Lett.* **B666** (2008) 66–70, [[hep-ph/0608248](#)].
- [92] S. A. Abel, M. D. Goodsell, J. Jaeckel, V. V. Khoze, and A. Ringwald, *Kinetic Mixing of the Photon with Hidden $U(1)$ s in String Phenomenology*, *JHEP* **07** (2008) 124, [[arXiv:0803.1449](#)].
- [93] M. Ahlers, J. Jaeckel, J. Redondo, and A. Ringwald, *Probing Hidden Sector Photons through the Higgs Window*, *Phys. Rev.* **D78** (2008) 075005, [[arXiv:0807.4143](#)].
- [94] J. Redondo, *Bounds on Very Weakly Interacting Sub-eV Particles (WISPs) from Cosmology and Astrophysics*, in *Proceedings, 4th Patras Workshop on Axions, WIMPs and WISPs (AXION-WIMP 2008): Hamburg, Germany, June 18-21, 2008*, pp. 23–26, 2008. [arXiv:0810.3200](#).
- [95] J. Redondo, *Helioscope Bounds on Hidden Sector Photons*, *JCAP* **0807** (2008) 008, [[arXiv:0801.1527](#)].
- [96] A. Mirizzi, J. Redondo, and G. Sigl, *Microwave Background Constraints on Mixing of Photons with Hidden Photons*, *JCAP* **0903** (2009) 026, [[arXiv:0901.0014](#)].
- [97] R. Essig, P. Schuster, and N. Toro, *Probing Dark Forces and Light Hidden Sectors at Low-Energy $e+e-$ Colliders*, *Phys. Rev.* **D80** (2009) 015003, [[arXiv:0903.3941](#)].
- [98] B. Batell, M. Pospelov, and A. Ritz, *Exploring Portals to a Hidden Sector Through Fixed Targets*, *Phys. Rev.* **D80** (2009) 095024, [[arXiv:0906.5614](#)].
- [99] A. Afanasev, O. K. Baker, K. B. Beard, G. Biallas, J. Boyce, M. Minarni, R. Ramdon, M. Shinn, and P. Slocum, *New Experimental Limit on Photon Hidden-Sector Paraphoton Mixing*, *Phys. Lett.* **B679** (2009) 317–320, [[arXiv:0810.4189](#)].
- [100] J. Jaeckel and J. Redondo, *Searching Hidden-sector Photons inside a Superconducting Box*, *EPL* **84** (2008), no. 3 31002, [[arXiv:0806.1115](#)].
- [101] S. N. Gninenko and J. Redondo, *On search for eV hidden sector photons in Super-Kamiokande and CAST experiments*, *Phys. Lett.* **B664** (2008) 180–184, [[arXiv:0804.3736](#)].
- [102] M. Baryakhtar, J. Huang, and R. Lasenby, *Axion and hidden photon dark matter detection with multilayer optical haloscopes*, *Phys. Rev.* **D98** (2018), no. 3 035006, [[arXiv:1803.11455](#)].
- [103] J. E. Kim, *Weak-interaction singlet and strong CP invariance*, *Phys. Rev. Lett.* **43** (Jul, 1979) 103–107.
- [104] M. Shifman, A. Vainshtein, and V. Zakharov, *Can confinement ensure natural cp*

- invariance of strong interactions?, *Nuclear Physics B* **166** (1980), no. 3 493 – 506.
- [105] J. I. Kapusta and C. Gale, *Finite-temperature field theory: Principles and applications*. Cambridge Monographs on Mathematical Physics. Cambridge University Press, 2011.
- [106] U. Kraemmer, A. K. Rebhan, and H. Schulz, *Hot scalar electrodynamics as a toy model for hot QCD*, in *From thermal field theory to neural networks: A day to remember Tanguy Altherr. Proceedings, Meeting, Geneva, Switzerland, November 4, 1994*, pp. 13–23, 1995.
[hep-ph/9505307](#).
- [107] A. Linde, *Infrared problem in the thermodynamics of the yang-mills gas*, *Physics Letters B* **96** (1980), no. 3 289 – 292.
- [108] D. J. Gross, R. D. Pisarski, and L. G. Yaffe, *Qcd and instantons at finite temperature*, *Rev. Mod. Phys.* **53** (Jan, 1981) 43–80.
- [109] J. R. Espinosa, M. Quiros, and F. Zwirner, *On the nature of the electroweak phase transition*, *Phys. Lett.* **B314** (1993) 206–216, [[hep-ph/9212248](#)].
- [110] V. Domcke and K. Mukaida, *Gauge Field and Fermion Production during Axion Inflation*, *JCAP* **11** (2018) 020, [[arXiv:1806.08769](#)].
- [111] J.-F. Dufaux, D. G. Figueroa, and J. Garcia-Bellido, *Gravitational Waves from Abelian Gauge Fields and Cosmic Strings at Preheating*, *Phys. Rev. D* **82** (2010) 083518, [[arXiv:1006.0217](#)].
- [112] D. G. Figueroa, J. Garcia-Bellido, and A. Rajantie, *On the Transverse-Traceless Projection in Lattice Simulations of Gravitational Wave Production*, *JCAP* **11** (2011) 015, [[arXiv:1110.0337](#)].
- [113] P. Adshead, J. T. Giblin, and Z. J. Weiner, *Gravitational waves from gauge preheating*, *Phys. Rev. D* **98** (2018), no. 4 043525, [[arXiv:1805.04550](#)].
- [114] F. Marchesano, G. Shiu, and A. M. Uranga, *F-term Axion Monodromy Inflation*, *JHEP* **09** (2014) 184, [[arXiv:1404.3040](#)].
- [115] R. Blumenhagen and E. Plauschinn, *Towards Universal Axion Inflation and Reheating in String Theory*, *Phys. Lett. B* **736** (2014) 482–487, [[arXiv:1404.3542](#)].
- [116] A. Hebecker, S. C. Kraus, and L. T. Witkowski, *D7-Brane Chaotic Inflation*, *Phys. Lett. B* **737** (2014) 16–22, [[arXiv:1404.3711](#)].
- [117] L. McAllister, E. Silverstein, A. Westphal, and T. Wrase, *The Powers of Monodromy*, *JHEP* **09** (2014) 123, [[arXiv:1405.3652](#)].
- [118] E. Silverstein and A. Westphal, *Monodromy in the CMB: Gravity Waves and String Inflation*, *Phys. Rev. D* **78** (2008) 106003, [[arXiv:0803.3085](#)].
- [119] L. McAllister, E. Silverstein, and A. Westphal, *Gravity Waves and Linear Inflation from Axion Monodromy*, *Phys. Rev. D* **82** (2010) 046003, [[arXiv:0808.0706](#)].
- [120] N. Kaloper and L. Sorbo, *A Natural Framework for Chaotic Inflation*, *Phys. Rev. Lett.* **102** (2009) 121301, [[arXiv:0811.1989](#)].
- [121] N. Kaloper and L. Sorbo, *Where in the String Landscape is Quintessence*, *Phys. Rev. D* **79** (2009) 043528, [[arXiv:0810.5346](#)].

- [122] E. Witten, *Dyons of Charge $e\theta/2\pi$* , *Phys. Lett. B* **86** (1979) 283–287.
- [123] M. Kawasaki, F. Takahashi, and M. Yamada, *Suppressing the QCD Axion Abundance by Hidden Monopoles*, *Phys. Lett. B* **753** (2016) 677–681, [[arXiv:1511.05030](#)].
- [124] R. Namba and M. Suzuki, *Implications of Gravitational-wave Production from Dark Photon Resonance to Pulsar-timing Observations and Effective Number of Relativistic Species*, *Phys. Rev. D* **102** (2020) 123527, [[arXiv:2009.13909](#)].
- [125] M. J. Baker, M. Breitbach, J. Kopp, and L. Mittnacht, *Dynamic Freeze-In: Impact of Thermal Masses and Cosmological Phase Transitions on Dark Matter Production*, *JHEP* **03** (2018) 114, [[arXiv:1712.03962](#)].
- [126] V. Cardoso, O. J. C. Dias, M. Hartnett, Gavin S. and Middleton, P. Pani, and J. E. Santos, *Constraining the mass of dark photons and axion-like particles through black-hole superradiance*, *JCAP* **1803** (2018), no. 03 043, [[arXiv:1801.01420](#)].
- [127] A. Arvanitaki, M. Baryakhtar, and X. Huang, *Discovering the QCD Axion with Black Holes and Gravitational Waves*, *Phys. Rev. D* **91** (2015), no. 8 084011, [[arXiv:1411.2263](#)].
- [128] Z. J. Weiner, P. Adshead, and J. T. Giblin, *Constraining early dark energy with gravitational waves before recombination*, [[arXiv:2008.01732](#)].
- [129] A. Papageorgiou, *Gravitational Wave Signatures from Warm Dark Energy*, [[arXiv:2011.06312](#)].
- [130] J. A. Dror, K. Harigaya, and V. Narayan, *Parametric Resonance Production of Ultralight Vector Dark Matter*, *Phys. Rev. D* **99** (2019), no. 3 035036, [[arXiv:1810.07195](#)].
- [131] R. T. Co, A. Pierce, Z. Zhang, and Y. Zhao, *Dark Photon Dark Matter Produced by Axion Oscillations*, *Phys. Rev. D* **99** (2019), no. 7 075002, [[arXiv:1810.07196](#)].
- [132] M. Bastero-Gil, J. Santiago, L. Ubaldi, and R. Vega-Morales, *Vector dark matter production at the end of inflation*, *JCAP* **04** (2019) 015, [[arXiv:1810.07208](#)].
- [133] N. Seto and A. Taruya, *Measuring a Parity Violation Signature in the Early Universe via Ground-based Laser Interferometers*, *Phys. Rev. Lett.* **99** (2007) 121101, [[arXiv:0707.0535](#)].
- [134] N. Seto and A. Taruya, *Polarization analysis of gravitational-wave backgrounds from the correlation signals of ground-based interferometers: Measuring a circular polarization mode*, *Phys. Rev. D* **77** (2008) 103001, [[arXiv:0801.4185](#)].
- [135] T. L. Smith and R. Caldwell, *Sensitivity to a Frequency-Dependent Circular Polarization in an Isotropic Stochastic Gravitational Wave Background*, *Phys. Rev. D* **95** (2017), no. 4 044036, [[arXiv:1609.05901](#)].
- [136] N. Seto, *Prospects for direct detection of circular polarization of gravitational-wave background*, *Phys. Rev. Lett.* **97** (2006) 151101, [[astro-ph/0609504](#)].
- [137] N. Seto, *Quest for circular polarization of gravitational wave background and orbits of laser interferometers in space*, *Phys. Rev. D* **75** (2007) 061302, [[astro-ph/0609633](#)].
- [138] V. Domcke, J. Garcia-Bellido, M. Peloso, M. Pieroni, A. Ricciardone, L. Sorbo, and G. Tasinato, *Measuring the net circular polarization of the stochastic gravitational wave background with interferometers*, *JCAP* **05** (2020) 028, [[arXiv:1910.08052](#)].

- [139] S. G. Crowder, R. Namba, V. Mandic, S. Mukohyama, and M. Peloso, *Measurement of Parity Violation in the Early Universe using Gravitational-wave Detectors*, *Phys. Lett. B* **726** (2013) 66–71, [[arXiv:1212.4165](#)].
- [140] R. T. Co and K. Harigaya, *Axiogenesis*, *Phys. Rev. Lett.* **124** (2020), no. 11 111602, [[arXiv:1910.02080](#)].
- [141] R. T. Co, L. J. Hall, K. Harigaya, K. A. Olive, and S. Verner, *Axion Kinetic Misalignment and Parametric Resonance from Inflation*, *JCAP* **08** (2020) 036, [[arXiv:2004.00629](#)].
- [142] B. Barman, N. Bernal, N. Ramberg, and L. Visinelli, *QCD Axion Kinetic Misalignment: Observational Aspects*, [arXiv:2111.03677](#).
- [143] V. Domcke, Y. Ema, K. Mukaida, and M. Yamada, *Spontaneous Baryogenesis from Axions with Generic Couplings*, *JHEP* **08** (2020) 096, [[arXiv:2006.03148](#)].
- [144] R. T. Co, L. J. Hall, and K. Harigaya, *Predictions for Axion Couplings from ALP Cogenesis*, *JHEP* **01** (2021) 172, [[arXiv:2006.04809](#)].
- [145] R. T. Co, N. Fernandez, A. Ghalsasi, L. J. Hall, and K. Harigaya, *Lepto-Axiogenesis*, *JHEP* **21** (2020) 017, [[arXiv:2006.05687](#)].
- [146] R. T. Co, K. Harigaya, Z. Johnson, and A. Pierce, *R-Parity Violation Axiogenesis*, [arXiv:2110.05487](#).
- [147] R. T. Co, D. Dunskey, N. Fernandez, A. Ghalsasi, L. J. Hall, K. Harigaya, and J. Shelton, *Gravitational Wave and CMB Probes of Axion Kination*, [arXiv:2108.09299](#).
- [148] Y. Gouttenoire, G. Servant, and P. Simakachorn, *Revealing the Primordial Irreducible Inflationary Gravitational-Wave Background with a Spinning Peccei-Quinn Axion*, [arXiv:2108.10328](#).
- [149] Y. Gouttenoire, G. Servant, and P. Simakachorn, *Kination cosmology from scalar fields and gravitational-wave signatures*, [arXiv:2111.01150](#).
- [150] R. T. Co, K. Harigaya, and A. Pierce, *Gravitational Waves and Dark Photon Dark Matter from Axion Rotations*, [arXiv:2104.02077](#).
- [151] I. Affleck and M. Dine, *A New Mechanism for Baryogenesis*, *Nucl. Phys. B* **249** (1985) 361–380.
- [152] V. A. Kuzmin, V. A. Rubakov, and M. E. Shaposhnikov, *On the Anomalous Electroweak Baryon Number Nonconservation in the Early Universe*, *Phys. Lett. B* **155** (1985) 36.
- [153] Planck Collaboration, Y. Akrami et al., *Planck 2018 results. X. Constraints on inflation*, *Astron. Astrophys.* **641** (2020) A10, [[arXiv:1807.06211](#)].
- [154] J. E. Kim, H. P. Nilles, and M. Peloso, *Completing natural inflation*, *JCAP* **01** (2005) 005, [[hep-ph/0409138](#)].
- [155] W. Buchmüller, V. Domcke, K. Kamada, and K. Schmitz, *The Gravitational Wave Spectrum from Cosmological $B - L$ Breaking*, *JCAP* **10** (2013) 003, [[arXiv:1305.3392](#)].
- [156] J. T. Giblin and E. Thrane, *Estimates of maximum energy density of cosmological gravitational-wave backgrounds*, *Phys. Rev. D* **90** (2014), no. 10 107502, [[arXiv:1410.4779](#)].

- [157] C. Caprini, R. Durrer, T. Konstandin, and G. Servant, *General Properties of the Gravitational Wave Spectrum from Phase Transitions*, *Phys. Rev. D* **79** (2009) 083519, [[arXiv:0901.1661](#)].
- [158] M. P. Hertzberg, M. Tegmark, and F. Wilczek, *Axion Cosmology and the Energy Scale of Inflation*, *Phys. Rev. D* **78** (2008) 083507, [[arXiv:0807.1726](#)].
- [159] P. Fox, A. Pierce, and S. D. Thomas, *Probing a QCD string axion with precision cosmological measurements*, [hep-th/0409059](#).
- [160] A. Ayala, I. Domínguez, M. Giannotti, A. Mirizzi, and O. Straniero, *Revisiting the bound on axion-photon coupling from Globular Clusters*, *Phys. Rev. Lett.* **113** (2014), no. 19 191302, [[arXiv:1406.6053](#)].
- [161] IAXO Collaboration, E. Armengaud et al., *Physics potential of the International Axion Observatory (IAXO)*, *JCAP* **06** (2019) 047, [[arXiv:1904.09155](#)].
- [162] A. Banerjee, H. Kim, O. Matsedonskyi, G. Perez, and M. S. Safronova, *Probing the Relaxed Relaxion at the Luminosity and Precision Frontiers*, *JHEP* **07** (2020) 153, [[arXiv:2004.02899](#)].
- [163] T. Flacke, C. Frugiuele, E. Fuchs, R. S. Gupta, and G. Perez, *Phenomenology of relaxion-Higgs mixing*, *JHEP* **06** (2017) 050, [[arXiv:1610.02025](#)].
- [164] D. S. Salopek, J. R. Bond, and J. M. Bardeen, *Designing Density Fluctuation Spectra in Inflation*, *Phys. Rev. D* **40** (1989) 1753.
- [165] D. Bödeker and W. Buchmüller, *Baryogenesis from the weak scale to the grand unification scale*, [arXiv:2009.07294](#).
- [166] A. Banerjee, H. Kim, and G. Perez, *Coherent relaxion dark matter*, *Phys. Rev. D* **100** (2019), no. 11 115026, [[arXiv:1810.01889](#)].
- [167] K. Choi, H. Kim, and T. Sekiguchi, *Dynamics of the cosmological relaxation after reheating*, *Phys. Rev. D* **95** (2017), no. 7 075008, [[arXiv:1611.08569](#)].
- [168] K. Choi, H. Kim, and S. Yun, *Natural inflation with multiple sub-Planckian axions*, *Phys. Rev. D* **90** (2014) 023545, [[arXiv:1404.6209](#)].
- [169] K. Choi and S. H. Im, *Realizing the relaxion from multiple axions and its UV completion with high scale supersymmetry*, *JHEP* **01** (2016) 149, [[arXiv:1511.00132](#)].
- [170] D. E. Kaplan and R. Rattazzi, *Large field excursions and approximate discrete symmetries from a clockwork axion*, *Phys. Rev. D* **93** (2016), no. 8 085007, [[arXiv:1511.01827](#)].
- [171] G. F. Giudice and M. McCullough, *A Clockwork Theory*, *JHEP* **02** (2017) 036, [[arXiv:1610.07962](#)].
- [172] Planck Collaboration, N. Aghanim et al., *Planck 2018 results. VI. Cosmological parameters*, [arXiv:1807.06209](#).
- [173] B. Audren, J. Lesgourgues, G. Mangano, P. D. Serpico, and T. Tram, *Strongest model-independent bound on the lifetime of Dark Matter*, *JCAP* **12** (2014) 028, [[arXiv:1407.2418](#)].
- [174] C. A. J. O'Hare and E. Vitagliano, *Cornering the axion with CP-violating interactions*, *Phys. Rev. D* **102** (2020), no. 11 115026, [[arXiv:2010.03889](#)].
- [175] W.-H. Tan et al., *Improvement for Testing the Gravitational Inverse-Square Law at the Submillimeter Range*, *Phys. Rev. Lett.* **124** (2020), no. 5 051301.

- [176] J. Bergé, P. Brax, G. Métris, M. Pernot-Borràs, P. Touboul, and J.-P. Uzan, *MICROSCOPE Mission: First Constraints on the Violation of the Weak Equivalence Principle by a Light Scalar Dilaton*, *Phys. Rev. Lett.* **120** (2018), no. 14 141101, [[arXiv:1712.00483](#)].
- [177] Y. J. Chen, W. K. Tham, D. E. Krause, D. Lopez, E. Fischbach, and R. S. Decca, *Stronger Limits on Hypothetical Yukawa Interactions in the 30–8000 nm Range*, *Phys. Rev. Lett.* **116** (2016), no. 22 221102, [[arXiv:1410.7267](#)].
- [178] D. J. Kapner, T. S. Cook, E. G. Adelberger, J. H. Gundlach, B. R. Heckel, C. D. Hoyle, and H. E. Swanson, *Tests of the gravitational inverse-square law below the dark-energy length scale*, *Phys. Rev. Lett.* **98** (2007) 021101, [[hep-ph/0611184](#)].
- [179] S. Schlamminger, K. Y. Choi, T. A. Wagner, J. H. Gundlach, and E. G. Adelberger, *Test of the equivalence principle using a rotating torsion balance*, *Phys. Rev. Lett.* **100** (2008) 041101, [[arXiv:0712.0607](#)].
- [180] J. K. Hoskins, R. D. Newman, R. Spero, and J. Schultz, *Experimental tests of the gravitational inverse square law for mass separations from 2-cm to 105-cm*, *Phys. Rev. D* **32** (1985) 3084–3095.
- [181] J. A. Grifols, E. Masso, and S. Peris, *Energy Loss From the Sun and RED Giants: Bounds on Short Range Baryonic and Leptonic Forces*, *Mod. Phys. Lett. A* **4** (1989) 311.
- [182] D. Cadamuro and J. Redondo, *Cosmological bounds on pseudo Nambu-Goldstone bosons*, *JCAP* **02** (2012) 032, [[arXiv:1110.2895](#)].
- [183] G. Raffelt, *Limits on a CP-violating scalar axion-nucleon interaction*, *Phys. Rev. D* **86** (2012) 015001, [[arXiv:1205.1776](#)].
- [184] E. Hardy and R. Lasenby, *Stellar cooling bounds on new light particles: plasma mixing effects*, *JHEP* **02** (2017) 033, [[arXiv:1611.05852](#)].
- [185] R. Budnik, O. Davidi, H. Kim, G. Perez, and N. Priel, *Searching for a solar relaxion or scalar particle with XENON1T and LUX*, *Phys. Rev. D* **100** (2019), no. 9 095021, [[arXiv:1909.02568](#)].
- [186] NANOGrav Collaboration, Z. Arzoumanian et al., *The NANOGrav 12.5-year Data Set: Search For An Isotropic Stochastic Gravitational-Wave Background*, [[arXiv:2009.04496](#)].
- [187] L. Lentati et al., *European Pulsar Timing Array Limits On An Isotropic Stochastic Gravitational-Wave Background*, *Mon. Not. Roy. Astron. Soc.* **453** (2015), no. 3 2576–2598, [[arXiv:1504.03692](#)].
- [188] M. Kerr et al., *The Parkes Pulsar Timing Array Project: Second data release*, *Publ. Astron. Soc. Austral.* **37** (2020) e020, [[arXiv:2003.09780](#)].
- [189] A. Sesana, F. Haardt, P. Madau, and M. Volonteri, *Low - frequency gravitational radiation from coalescing massive black hole binaries in hierarchical cosmologies*, *Astrophys. J.* **611** (2004) 623–632, [[astro-ph/0401543](#)].
- [190] S. Blasi, V. Brdar, and K. Schmitz, *Has NANOGrav found first evidence for cosmic strings?*, [[arXiv:2009.06607](#)].
- [191] J. Ellis and M. Lewicki, *Cosmic String Interpretation of NANOGrav Pulsar Timing Data*, [[arXiv:2009.06555](#)].

- [192] W. Buchmuller, V. Domcke, and K. Schmitz, *From NANOGrav to LIGO with metastable cosmic strings*, [arXiv:2009.10649](#).
- [193] Y. Nakai, M. Suzuki, F. Takahashi, and M. Yamada, *Gravitational Waves and Dark Radiation from Dark Phase Transition: Connecting NANOGrav Pulsar Timing Data and Hubble Tension*, [arXiv:2009.09754](#).
- [194] A. Addazi, Y.-F. Cai, Q. Gan, A. Marciano, and K. Zeng, *NANOGrav results and Dark First Order Phase Transitions*, [arXiv:2009.10327](#).
- [195] V. Vaskonen and H. Veermae, *Did NANOGrav see a signal from primordial black hole formation?*, [arXiv:2009.07832](#).
- [196] V. De Luca, G. Franciolini, and A. Riotto, *NANOGrav Hints to Primordial Black Holes as Dark Matter*, [arXiv:2009.08268](#).
- [197] E. Witten, *Cosmic Separation of Phases*, *Phys. Rev.* **D30** (1984) 272–285.
- [198] C. J. Hogan, *NUCLEATION OF COSMOLOGICAL PHASE TRANSITIONS*, *Phys. Lett.* **133B** (1983) 172–176.
- [199] C. J. Hogan, *Gravitational radiation from cosmological phase transitions*, *Mon. Not. Roy. Astron. Soc.* **218** (1986) 629–636.
- [200] C. Caprini et al., *Science with the space-based interferometer eLISA. II: Gravitational waves from cosmological phase transitions*, *JCAP* **1604** (2016) 001, [[arXiv:1512.06239](#)].
- [201] A. Mazumdar and G. White, *Review of cosmic phase transitions: their significance and experimental signatures*, *Rept. Prog. Phys.* **82** (2019), no. 7 076901, [[arXiv:1811.01948](#)].
- [202] J. G. Hartnett and A. Luiten, *Colloquium: Comparison of Astrophysical and Terrestrial Frequency Standards*, *Rev. Mod. Phys.* **83** (2011) 1–9, [[arXiv:1004.0115](#)].
- [203] R. w. Hellings and G. s. Downs, *UPPER LIMITS ON THE ISOTROPIC GRAVITATIONAL RADIATION BACKGROUND FROM PULSAR TIMING ANALYSIS*, *Astrophys. J. Lett.* **265** (1983) L39–L42.
- [204] C. Caprini et al., *Detecting gravitational waves from cosmological phase transitions with LISA: an update*, *JCAP* **2003** (2020) 024, [[arXiv:1910.13125](#)].
- [205] P. Schwaller, *Gravitational Waves from a Dark Phase Transition*, *Phys. Rev. Lett.* **115** (2015), no. 18 181101, [[arXiv:1504.07263](#)].
- [206] J. Jaeckel, V. V. Khoze, and M. Spannowsky, *Hearing the signal of dark sectors with gravitational wave detectors*, *Phys. Rev.* **D94** (2016), no. 10 103519, [[arXiv:1602.03901](#)].
- [207] A. Addazi, *Limiting First Order Phase Transitions in Dark Gauge Sectors from Gravitational Waves experiments*, *Mod. Phys. Lett.* **A32** (2017), no. 08 1750049, [[arXiv:1607.08057](#)].
- [208] I. Baldes, *Gravitational waves from the asymmetric-dark-matter generating phase transition*, *JCAP* **1705** (2017) 028, [[arXiv:1702.02117](#)].
- [209] A. Addazi and A. Marciano, *Gravitational waves from dark first order phasetransitions and dark photons*, *Chin. Phys.* **C42** (2018), no. 2 023107, [[arXiv:1703.03248](#)].

- [210] D. Croon, V. Sanz, and G. White, *Model Discrimination in Gravitational Wave spectra from Dark Phase Transitions*, *JHEP* **08** (2018) 203, [[arXiv:1806.02332](#)].
- [211] M. Fairbairn, E. Hardy, and A. Wickens, *Hearing without seeing: gravitational waves from hot and cold hidden sectors*, *JHEP* **07** (2019) 044, [[arXiv:1901.11038](#)].
- [212] Y. Bai and M. Korwar, *Cosmological constraints on first-order phase transitions*, *Phys. Rev. D* **105** (2022), no. 9 095015, [[arXiv:2109.14765](#)].
- [213] P. Creminelli, A. Nicolis, and R. Rattazzi, *Holography and the electroweak phase transition*, *JHEP* **03** (2002) 051, [[hep-th/0107141](#)].
- [214] L. Randall and G. Servant, *Gravitational waves from warped spacetime*, *JHEP* **05** (2007) 054, [[hep-ph/0607158](#)].
- [215] T. Konstandin and G. Servant, *Cosmological Consequences of Nearly Conformal Dynamics at the TeV scale*, *JCAP* **1112** (2011) 009, [[arXiv:1104.4791](#)].
- [216] E. Megias, G. Nardini, and M. Quiros, *Cosmological Phase Transitions in Warped Space: Gravitational Waves and Collider Signatures*, *JHEP* **09** (2018) 095, [[arXiv:1806.04877](#)].
- [217] P. Baratella, A. Pomarol, and F. Rompineve, *The Supercooled Universe*, *JHEP* **03** (2019) 100, [[arXiv:1812.06996](#)].
- [218] S. Hoeche, J. Kozaczuk, A. J. Long, J. Turner, and Y. Wang, *Towards an all-orders calculation of the electroweak bubble wall velocity*, [[arXiv:2007.10343](#)].
- [219] D. Cutting, E. G. Escartin, M. Hindmarsh, and D. J. Weir, *Gravitational waves from vacuum first order phase transitions II: from thin to thick walls*, [[arXiv:2005.13537](#)].
- [220] J. Ellis, M. Lewicki, and V. Vaskonen, *Updated predictions for gravitational waves produced in a strongly supercooled phase transition*, [[arXiv:2007.15586](#)].
- [221] D. Croon, O. Gould, P. Schicho, T. V. I. Tenkanen, and G. White, *Theoretical uncertainties for cosmological first-order phase transitions*, [[arXiv:2009.10080](#)].
- [222] Y. B. Zeldovich and R. A. Sunyaev, *The Interaction of Matter and Radiation in a Hot-Model Universe*, *Astrophys. Space Sci.* **4** (1969) 301–316.
- [223] J. Chluba and R. A. Sunyaev, *The evolution of CMB spectral distortions in the early Universe*, *Mon. Not. Roy. Astron. Soc.* **419** (2012) 1294–1314, [[arXiv:1109.6552](#)].
- [224] H. Tashiro, E. Sabancilar, and T. Vachaspati, *CMB Distortions from Damping of Acoustic Waves Produced by Cosmic Strings*, *JCAP* **08** (2013) 035, [[arXiv:1212.3283](#)].
- [225] M. A. Amin and D. Grin, *Probing early-universe phase transitions with CMB spectral distortions*, *Phys. Rev. D* **90** (2014), no. 8 083529, [[arXiv:1405.1039](#)].
- [226] W. Hu and N. Sugiyama, *Small scale cosmological perturbations: An Analytic approach*, *Astrophys. J.* **471** (1996) 542–570, [[astro-ph/9510117](#)].
- [227] C.-P. Ma and E. Bertschinger, *Cosmological perturbation theory in the synchronous and conformal Newtonian gauges*, *Astrophys. J.* **455** (1995) 7–25, [[astro-ph/9506072](#)].
- [228] W. Hu, N. Sugiyama, and J. Silk, *The Physics of microwave background anisotropies*, *Nature* **386** (1997) 37–43, [[astro-ph/9604166](#)].

- [229] J. Chluba and D. Grin, *CMB spectral distortions from small-scale isocurvature fluctuations*, *Mon. Not. Roy. Astron. Soc.* **434** (2013) 1619–1635, [[arXiv:1304.4596](#)].
- [230] P. B. Greene, L. Kofman, A. D. Linde, and A. A. Starobinsky, *Structure of resonance in preheating after inflation*, *Phys. Rev. D* **56** (1997) 6175–6192, [[hep-ph/9705347](#)].
- [231] L. Kofman, A. D. Linde, and A. A. Starobinsky, *Reheating after inflation*, *Phys. Rev. Lett.* **73** (1994) 3195–3198, [[hep-th/9405187](#)].
- [232] Y. Shtanov, J. H. Traschen, and R. H. Brandenberger, *Universe reheating after inflation*, *Phys. Rev. D* **51** (1995) 5438–5455, [[hep-ph/9407247](#)].
- [233] L. Kofman, A. D. Linde, and A. A. Starobinsky, *Towards the theory of reheating after inflation*, *Phys. Rev. D* **56** (1997) 3258–3295, [[hep-ph/9704452](#)].
- [234] D. G. Figueroa and F. Torrenti, *Parametric resonance in the early Universe - a fitting analysis*, *JCAP* **1702** (2017), no. 02 001, [[arXiv:1609.05197](#)].
- [235] D. G. Figueroa, A. Florio, F. Torrenti, and W. Valkenburg, *The art of simulating the early Universe – Part I*, *JCAP* **04** (2021) 035, [[arXiv:2006.15122](#)].
- [236] D. G. Figueroa, A. Florio, F. Torrenti, and W. Valkenburg, *CosmoLattice*, [[arXiv:2102.01031](#)].
- [237] D. G. Figueroa and A. Florio, “Technical note 1: Power spectra.” https://cosmolattice.net/assets/technical_notes/CosmoLattice_TechnicalNote_PowerSpectrum.pdf, 06, 2022.
- [238] S. Dodelson, *Modern Cosmology*. Academic Press, Amsterdam, 2003.
- [239] R. Durrer, M. Kunz, and A. Melchiorri, *Cosmic structure formation with topological defects*, *Phys. Rept.* **364** (2002) 1–81, [[astro-ph/0110348](#)].
- [240] R. Durrer, M. Kunz, C. Lineweaver, and M. Sakellariadou, *Cosmic microwave background anisotropies from scaling seeds: Fit to observational data*, *Phys. Rev. Lett.* **79** (1997) 5198–5201, [[astro-ph/9706215](#)].
- [241] M. Hindmarsh, S. J. Huber, K. Rummukainen, and D. J. Weir, *Numerical simulations of acoustically generated gravitational waves at a first order phase transition*, *Phys. Rev. D* **92** (2015), no. 12 123009, [[arXiv:1504.03291](#)].
- [242] T. J. Clarke, E. J. Copeland, and A. Moss, *Constraints on primordial gravitational waves from the Cosmic Microwave Background*, *JCAP* **10** (2020) 002, [[arXiv:2004.11396](#)].
- [243] Planck Collaboration, P. A. R. Ade et al., *Planck 2013 results. XXV. Searches for cosmic strings and other topological defects*, *Astron. Astrophys.* **571** (2014) A25, [[arXiv:1303.5085](#)].
- [244] T. Charnock, A. Avgoustidis, E. J. Copeland, and A. Moss, *CMB constraints on cosmic strings and superstrings*, *Phys. Rev. D* **93** (2016), no. 12 123503, [[arXiv:1603.01275](#)].
- [245] A. Lopez-Eiguren, J. Lizarraga, M. Hindmarsh, and J. Urrestilla, *Cosmic Microwave Background constraints for global strings and global monopoles*, *JCAP* **07** (2017) 026, [[arXiv:1705.04154](#)].
- [246] A. Ota, T. Takahashi, H. Tashiro, and M. Yamaguchi, *CMB μ distortion from*

- primordial gravitational waves*, *JCAP* **10** (2014) 029, [[arXiv:1406.0451](#)].
- [247] J. Chluba, L. Dai, D. Grin, M. Amin, and M. Kamionkowski, *Spectral distortions from the dissipation of tensor perturbations*, *Mon. Not. Roy. Astron. Soc.* **446** (2015) 2871–2886, [[arXiv:1407.3653](#)].
- [248] D. J. Fixsen, E. S. Cheng, J. M. Gales, J. C. Mather, R. A. Shafer, and E. L. Wright, *The Cosmic Microwave Background spectrum from the full COBE FIRAS data set*, *Astrophys. J.* **473** (1996) 576, [[astro-ph/9605054](#)].
- [249] A. Kogut et al., *The Primordial Inflation Explorer (PIXIE): A Nulling Polarimeter for Cosmic Microwave Background Observations*, *JCAP* **07** (2011) 025, [[arXiv:1105.2044](#)].
- [250] J. Chluba et al., *New horizons in cosmology with spectral distortions of the cosmic microwave background*, *Exper. Astron.* **51** (2021), no. 3 1515–1554, [[arXiv:1909.01593](#)].
- [251] A. Weltman et al., *Fundamental physics with the Square Kilometre Array*, *Publ. Astron. Soc. Austral.* **37** (2020) e002, [[arXiv:1810.02680](#)].
- [252] CMB-S4 Collaboration, K. N. Abazajian et al., *CMB-S4 Science Book, First Edition*, [[arXiv:1610.02743](#)].
- [253] M. Dine, L. Randall, and S. D. Thomas, *Supersymmetry breaking in the early universe*, *Phys. Rev. Lett.* **75** (1995) 398–401, [[hep-ph/9503303](#)].
- [254] D. Kazanas, *Dynamics of the Universe and Spontaneous Symmetry Breaking*, *Astrophys. J. Lett.* **241** (1980) L59–L63.
- [255] A. Vilenkin, *Cosmic Strings and Domain Walls*, *Phys. Rept.* **121** (1985) 263–315.
- [256] A. Vilenkin and A. E. Everett, *Cosmic Strings and Domain Walls in Models with Goldstone and PseudoGoldstone Bosons*, *Phys. Rev. Lett.* **48** (1982) 1867–1870.
- [257] T. W. B. Kibble, *Topology of Cosmic Domains and Strings*, *J. Phys. A* **9** (1976) 1387–1398.
- [258] K. Saikawa, *A review of gravitational waves from cosmic domain walls*, *Universe* **3** (2017), no. 2 40, [[arXiv:1703.02576](#)].
- [259] A. Vilenkin, *Gravitational Field of Vacuum Domain Walls and Strings*, *Phys. Rev. D* **23** (1981) 852–857.
- [260] J. Preskill, S. P. Trivedi, F. Wilczek, and M. B. Wise, *Cosmology and broken discrete symmetry*, *Nucl. Phys. B* **363** (1991) 207–220.
- [261] T. Hiramatsu, M. Kawasaki, and K. Saikawa, *On the estimation of gravitational wave spectrum from cosmic domain walls*, *JCAP* **02** (2014) 031, [[arXiv:1309.5001](#)].
- [262] T. Hiramatsu, M. Kawasaki, and K. Saikawa, *Gravitational Waves from Collapsing Domain Walls*, *JCAP* **05** (2010) 032, [[arXiv:1002.1555](#)].
- [263] M. Kawasaki and K. Saikawa, *Study of gravitational radiation from cosmic domain walls*, *JCAP* **09** (2011) 008, [[arXiv:1102.5628](#)].
- [264] K. Saikawa, *Gravitational waves from cosmic domain walls: a mini-review*, *J. Phys. Conf. Ser.* **1586** (2020), no. 1 012039.
- [265] M. Gorghetto, E. Hardy, and H. Nicolaescu, *Observing invisible axions with gravitational waves*, *JCAP* **06** (2021) 034, [[arXiv:2101.11007](#)].

- [266] C.-F. Chang and Y. Cui, *Gravitational waves from global cosmic strings and cosmic archaeology*, *JHEP* **03** (2022) 114, [[arXiv:2106.09746](#)].
- [267] R. Murgia, G. Scelfo, M. Viel, and A. Raccanelli, *Lyman- α Forest Constraints on Primordial Black Holes as Dark Matter*, *Phys. Rev. Lett.* **123** (2019), no. 7 071102, [[arXiv:1903.10509](#)].
- [268] K. K. Rogers and H. V. Peiris, *Strong Bound on Canonical Ultralight Axion Dark Matter from the Lyman-Alpha Forest*, *Phys. Rev. Lett.* **126** (2021), no. 7 071302, [[arXiv:2007.12705](#)].
- [269] S. W. Hawking, I. G. Moss, and J. M. Stewart, *Bubble Collisions in the Very Early Universe*, *Phys. Rev. D* **26** (1982) 2681.
- [270] C. Grojean and G. Servant, *Gravitational Waves from Phase Transitions at the Electroweak Scale and Beyond*, *Phys. Rev. D* **75** (2007) 043507, [[hep-ph/0607107](#)].
- [271] M. Geller, S. Lu, and Y. Tsai, *B modes from postinflationary gravitational waves sourced by axionic instabilities at cosmic reionization*, *Phys. Rev. D* **104** (2021), no. 8 083517, [[arXiv:2104.08284](#)].
- [272] M. Kamionkowski, A. Kosowsky, and M. S. Turner, *Gravitational radiation from first order phase transitions*, *Phys. Rev. D* **49** (1994) 2837–2851, [[astro-ph/9310044](#)].
- [273] J. R. Espinosa, T. Konstandin, J. M. No, and G. Servant, *Energy Budget of Cosmological First-order Phase Transitions*, *JCAP* **06** (2010) 028, [[arXiv:1004.4187](#)].
- [274] S. J. Huber and T. Konstandin, *Production of gravitational waves in the nMSSM*, *JCAP* **05** (2008) 017, [[arXiv:0709.2091](#)].
- [275] R. Jinno, S. Lee, H. Seong, and M. Takimoto, *Gravitational waves from first-order phase transitions: Towards model separation by bubble nucleation rate*, *JCAP* **11** (2017) 050, [[arXiv:1708.01253](#)].
- [276] H. Tashiro, E. Sabancilar, and T. Vachaspati, *CMB Distortions from Superconducting Cosmic Strings*, *Phys. Rev. D* **85** (2012) 103522, [[arXiv:1202.2474](#)].
- [277] M. Anthonisen, R. Brandenberger, A. Laguë, I. A. Morrison, and D. Xia, *Cosmic Microwave Background Spectral Distortions from Cosmic String Loops*, *JCAP* **02** (2016) 047, [[arXiv:1509.07998](#)].
- [278] V. K. Narayanan, D. N. Spergel, R. Dave, and C.-P. Ma, *Constraints on the mass of warm dark matter particles and the shape of the linear power spectrum from the Ly α forest*, *Astrophys. J. Lett.* **543** (2000) L103–L106, [[astro-ph/0005095](#)].
- [279] S. H. Hansen, J. Lesgourgues, S. Pastor, and J. Silk, *Constraining the window on sterile neutrinos as warm dark matter*, *Mon. Not. Roy. Astron. Soc.* **333** (2002) 544–546, [[astro-ph/0106108](#)].